THE UNIVERSITY OF ALBERTA

Design and Performance Evaluation of Tunnels and Shafts

by

Chik Kwong Wong (Ron)

A THESIS

SUBMITTED TO THE FACULTY OF GRADUATE STUDIES AND RESEARCH

IN PARTIAL FULFILMENT OF THE REQUIREMENTS FOR THE DEGREE

OF Doctor of Philosophy

IN

Department of Civil Engineering

EDMONTON, ALBERTA

SPRING 1986

ISBN 0-315-30244-5

THE UNIVERSITY OF ALBERTA

RELEASE FORM

NAME OF AUTHOR Chik Kwong Wong (Ron)

TITLE OF THESIS Design and Performance Evaluation of Tunnels and Shafts

DEGREE FOR WHICH THESIS WAS PRESENTED Doctor of Philosophy

YEAR THIS DEGREE GRANTED SPRING 1986

Permission is hereby granted to THE UNIVERSITY OF ALBERTA LIBRARY to reproduce single copies of this thesis and to lend or sell such copies for private, scholarly or scientific research purposes only.

The author reserves other publication rights, and neither the thesis nor extensive extracts from it may be printed or otherwise reproduced without the author's written permission.

(SIGNED) ......Wong Chik Kwong......

PERMANENT ADDRESS:

......2009 ELAINE CIRCLE......

......FLORENCE, SC 29501......

......U.S.A.......

DATED ......DEC. 24, 1985...... 19

THE UNIVERSITY OF ALBERTA

FACULTY OF GRADUATE STUDIES AND RESEARCH

The undersigned certify that they have read, and recommend to the Faculty of Graduate Studies and Research, for acceptance, a thesis entitled Design and Performance Evaluation of Tunnels and Shafts submitted by Chik Kwong Wong (Ron) in partial fulfilment of the requirements for the degree of Doctor of Philosophy in Civil Engineering.

..................................(Dr. P.K. Kaiser)

Supervisor

..................................(Dr. K. Barron)

..................................(Dr. Z. Eisenstein)

..................................(Dr. N.R. Morgenstern)

..................................(Dr. A. Scanlon)

..................................(Dr. J.J.K. Daemen)

External Examiner

Date. DEC. 16, 1985

Abstract

The behaviour of tunnels and shafts in purely cohesionless and cohesive soils (elastic perfectly plastic) are studied by the use of the convergence confinement method (or ground reaction concept). The main objectives of this research work are to investigate the behavioral modes of tunnels and shafts in terms of yield initiation, propagation of yield zone and collapse mechanism, and to propose analytical techniques to predict the support stress-displacement relationship around these openings.

Tunnels

The excavation of a tunnel is simulated, in the two-dimensional plane strain model, by the proportional unloading of the initial insitu stress around the opening. The conditions and consequences of ground responses around the tunnel are analyzed using numerical techniques, e.g., continuum mechanics, finite element method and limit state theory. Several possible modes of yield initiation and yield zone propagation are identified. It was found that the occurrence and development of each mode is governed by such parameters as depth ratio (H/a), strength properties (ϕ, c), insitu stress coefficient (K_o) and internal support pressure (p_i, τ_i). Two modes, Modes I (localized yield zones at the tunnel shoulders) and II (continuous yield domain around the opening), are identified. They are commonly encountered in soft ground tunnelling. Experimental results of model tests (Atkinson *et al.*, 1974; Atkinson and Potts, 1977) confirm the existence of these modes (I and II). Furthermore,

analytical studies of Mode I and II behaviour reveal that a unique relationship exists between the support pressure and the displacement around the tunnel opening. The relationship can be interpreted by the use of the ground convergence curve. The approach proposed in this thesis is supported and verified by case histories of model tests and field measurements. It indicates a strong dependency among support pressure, mode of yielding and induced ground displacement, which is usually neglected in current design practice based on different semi-empirical approaches.

Shafts

Ground deformations around circular shafts cannot be determined from currently available design approaches which are mostly derived on the basis of limit equilibrium techniques. The convergence confinement method (usually only applied to tunnels) with consideration of the mechanism of the shaft behaviour as a three-dimensional problem, is proposed as an analytical tool to predict the formation pressure on a shaft and the ground displacements. It was found that the behaviour of a shaft is governed by: (1) the mode of yield initiation dominated by the insitu stress state and the soil strength, and (2) the extent of the yield zone generated by the wall displacements allowed during construction. Closed-form solutions for pressure-displacement relationships of cohesionless and cohesive grounds are presented. The results from the proposed technique compare well with those obtained from finite element analyses. The validity of the proposed technique is also evaluated by comparison of the predicted response with the observed behaviour of shafts in model tests and actual field measurements. It was shown that the well established limit equilibrium methods provide minimum support pressures that are required to maintain stability, but these pressures are only encountered in the field if relatively large ground movements are permitted during construction with relatively poor ground control.

Acknowledgements

The supports of the following persons and organizations during the preparation of this dissertation are gratefully acknowledged:

Prof. P.K. Kaiser, my supervisor, for giving me the opportunity to undertake a Ph.D. program and for his continuous supports (intellectual effort in problem-solving discussions, emotional help and endless encouragement) during the course of this project.

Prof. N.R. Morgenstern for his contribution to the shaft analysis and his supervision during Prof. Kaiser's leave.

Prof. Z. Eisenstein for his advice on the tunnel analysis.

Dr. D. Chan for his generous assistance on the computer analyses of this research.

AOSTRA, NSERC and Department of Civil Engineering, University of Alberta for financial supports.

Finally, I wish to specially thank to my wife, *Grace* and my parents for their moral supports throughout my studies.

Table of Contents

Chapter — Page

1. INTRODUCTION 1

1.1 Thesis Introduction 1

1.2 Convergence Confinement Method 3

1.2.1 Introduction 3

1.2.2 Ground Convergence Curve (GCC) 4

1.2.3 Support Confinement Curve (SCC) and Ground-Support Interaction 8

1.3 Objective and Scope of this Thesis 9

2. MECHANISM OF TUNNEL BEHAVIOUR 13

2.1 Introduction 13

2.2 Ground Responses 14

2.2.1 Simulation of Excavation 14

2.2.2 Stress Relief during Excavation and Modes of Yielding 14

2.2.3 Bifurcation Phenomena in Tunnelling 19

2.2.3.1 Introduction 19

2.2.3.2 Strategy 20

2.2.3.3 Examples 26

2.2.4 Formulation of Ground Response 27

2.2.4.1 Mode I 28

2.2.4.2 Mode II 37

2.2.4.3 Vertical Settlement Profiles above Tunnel (Modes I and II) 42

2.2.5 Numerical Examples (FEM) 47

2.2.5.1 Approach 47

2.2.5.2 Results 48

3. TUNNEL - CASE STUDIES 101

3.1 Introduction 101

3.2 Case Studies 101

3.2.1 Model Tests 101

3.2.2 Field Measurements 106

4. DESIGN OF SHAFT IN SOIL 122

4.1 Introduction 122

4.2 Review of conventional Shaft Design Techniques .124

4.2.1 Terzaghi's Method 124

4.2.2 Berezantzev's Method 125

4.2.3 Prater's Method 126

4.2.4 Convergence Confinement Method 127

4.2.4.1 Simulation of Horizontal Arching .129

4.2.4.2 Simulation of Vertical Arching (Gravity Effect) 129

4.3 Design Based on Convergence Confinement Method (CCM) 133

4.4 Mechanism of Shaft Behaviour 134

4.4.1 Effects of Variations of E and q along with Depth on Shape of Plastic Zone 142

4.5 Comparison of Proposed Solution with FE Analysis 144

4.5.1 FE Analysis 144

4.5.2 Results from Finite Element Analyses 145

5. SHAFT - CASE STUDY (FIELD MEASUREMENTS) 175

5.1 E. L. Smith Plant - Terwillegar Shaft 175

5.1.1 Introduction 175

5.1.2 Project Description 175

5.1.3 Field Instrumentation 176

5.2 Analysis of Shaft Performance 177

5.2.1 Comparison of Predicted (FEM) and Observed Performance 179

5.3 Comparison of Measurements with Predictions from other Methods 181

5.3.1 Earth Pressure 182

5.3.2 Discussion 182

6. SHAFT - CASE STUDIES (MODEL TESTS) 198

6.1 Berlin Model Tests (Mode A Yielding) 198

6.1.1 Introduction 198

6.1.2 Testing Apparatus and Procedure 198

6.1.3 Test Results 200

6.1.4 Interpretation of Model Test Results by CCM 201

6.2 Cambridge Centrifuge Model Tests (Mode B Yielding 206

6.2.1 Introduction 206

6.2.2 Testing Apparatus and Procedures 206

6.2.3 Test Results 207

6.2.4 Prediction of Model Test Behaviour by the CCM 208

7. SUMMARY AND CONCLUSIONS 226

7.1 Introduction 226

7.2 Conclusions on Tunnel 226

7.2.1 Tunnel Behaviour 226

7.2.2 Practical Implications 230

7.3 Recommendations for Further Studies (Tunnel) ...233

7.4 Conclusions on Shaft 233

7.4.1 Shaft Behaviour 233

7.4.2 Practical Implications 236

7.5 Recommendations for Further Studies (Shaft) 238

References 239

APPENDIX A - Notations 247

APPENDIX B - Tunnel Analyses 250

B.1 Schmidt's Equations of Stress Distribution around a Tunnel 250

B.2 Formulation of Mode II 252

B.3 Calculation of Coefficient K_r 255

B.4 Calculation of Tunnel Support Pressure p_{fc} 256

B.5 Analysis of 2-D Plane Strain Hole-in-Plate Problem (Ladanyi, 1974) 257

APPENDIX C - Tunnel Case Histories 266

APPENDIX D - Shaft Analyses 270

D.1 Vertical Arching 270

D.2 Mechanism of Shaft Behaviour in Cohesive Soil ..274

APPENDIX E - Shaft Case Histories 285

APPENDIX F - Computer Program 292

List of Tables

Table		Page
2.1	Input Data for FE Analyses (Tunnel)	61
2.2	Summary of FE Analyses (Tunnel)	62
2.3	Summary of p_{ys}, p_{ic}, p_{fc} (Tunnel)	63
3.1	Input Data for Constructions of GCC for EXP and LRT Tunnels	112
4.1	Input Data for FE Analyses (Shaft)	151
5.1	Input Data for FE Analyses (Terwillegar Shaft)	185
5.2	Convergence Curve Data	186
6.1	Centrifuge Model Test Data	213
6.2	Calculation of Displacement u_y	214
C.1	Tunnel Case Histories - Cohesionless Soils	267
C.2	Tunnel Case Histories - Cohesive Soils	268
E.1	Properties of Melinex (Shaft Lining)	286
E.2	Properties of Leigthon Buzzard Sand 120/220	287

List of Figures

Figure | Page

1.1 Convergence Confinement Method....................11

1.2 Conceptual Framework - Ground-Support Interaction...12

2.1 Modes of Yield Initiation..........................64

2.2 Propagation of Yield Zone..........................65

2.3 Possible Modes of Yielding near a Tunnel...........66

2.4 Modes of Yielding near a Tunnel....................67

2.5 Mode I...68

2.6 Modes of Yielding near a Tunnel ϕ=20°, c=0...........69

2.7 Modes of Yielding near a Tunnel ϕ=30°, c=0...........70

2.8 Modes of Yielding near a Tunnel ϕ=40°, c=0...........71

2.9 Formulation of GCC (roof) for Modes I and II........72

2.10 Direction of Propagation of Yield Zone (Mode I)....73

2.11 p_{ys} (and p_{ic}) as function of H/a and ϕ...........74

2.12 p_{fc} as function of H/a and ϕ.......................75

2.13 Types of Arching (a) Convex and (b) Inverted.......76

2.14 Hole-in-Plate Model for Mode II....................77

2.15 p_i-u-R Plot for Mode II...........................78

2.16 Surface Settlement Profile.........................79

2.17 Vertical Settlement Profiles above Tunnel for Modes I and II....80

2.18 Extent of Yield Zone - Cohesionless (ST1,ST2).......81

2.19 Extent of Yield Zone - Cohesionless (ST3)...........82

2.20 Extent of Yield Zone - Cohesionless (AP1)...........83

2.21 Extent of Yield Zone - Cohesionless (DT1,DT2).......84

2.22 Extent of Yield Zone - Cohesive (STC1,STC2).........85

2.23 Stress Distribution above Roof - Cohesionless (ST1,ST2)....86

Figure Page

2.24 Stress Distribution above Roof - Cohesive (STC1,STC2)....87

2.25 GCC - Cohesionless (ST1,ST2)....88

2.26 GCC - Cohesionless (ST3,AP1)....89

2.27 GCC - Cohesionless (DT1,DT2)....90

2.28 GCC - Cohesive (STC1,STC2)....91

2.29 Vertical Settlement Profile above Roof - Cohesionless (ST1,ST2)....92

2.30 Vertical Settlement Profile above Roof - Cohesionless (ST3,AP1)....93

2.31 Vertical Settlement Profile above Roof - Cohesionless (DT1,DT2)....94

2.32 Vertical Settlement Profile above Roof - Cohesive (STC1,STC2)....95

2.33 S_s/S_c Settlement Relations....96

2.34 Plots of p_i/p_o versus S_s/S_c....97

2.35 Surface Settlement-Cohesionless (ST1,ST2,AP1)....98

2.36 Surface Settlement-Cohesionless (DT1,DT2)....99

2.37 Surface Settlement-Cohesive (STC1,STC2)....100

3.1 Contours of Volume and Shear Strains in Sand (modified from Atkinson and Potts, 1977)....113

3.2 Contours of Shear Strains in Sand (modified from Cording et al. ,1976)....114

3.3 Contours of Volume and Shear Strains in Kaolin (modified from Atkinson et al., 1974)....115

3.4 Surface Settlement Profiles in Sand (modified from Potts, 1976)....116

3.5 GCC and Support Pressure-Extent of Yield Zone (EXP Tunnel)....117

3.6 GCC and Support Pressure-Extent of Yield Zone (LRT Tunnel)....118

3.7 Field Measurements (Cohesionless Soils)....119

Figure Page

3.8 Field Measurements (Cohesive Soils, c_u = 0 to 100kPa) 120

3.9 Field Measurements (Cohesive Soils, c_u >100kPa) 121

4.1 Earth Pressure as a function of Depth Ratio (H/a) 152

4.2 Mechanism of Shaft Behaviour 153

4.3 Gravity Effect due to Vertical Arching 154

4.4 Support Pressure due to Gravity Effect (Cohesionless) 155

4.5 Support Pressure due to Gravity Effect (Cohesive) 156

4.6 Shaft Design Approach - CCM with inclusion of Gravity Effect 157

4.7 Mode A and Mode B 158

4.8 Stress States (Mode A) 159

4.9 Stress States (Mode B) 160

4.10 Configurations of Plastic Zones with Depth for Cohesionless and Cohesive Soils 161

4.11 Comparison of Stress Distribution (u/a=0.3%, SM1); (a) σ_r (b) σ_t (c) σ_v 162

4.12 Comparison of Stress Distribution (u/a=0.5%, SM2); (a) σ_r (b) σ_t (c) σ_v 163

4.13 Comparison of Stress Distribution (u/a=0.56%, CM1); (a) σ_r (b) σ_t (c) σ_v 164

4.14 Comparison of Stress Distribution (h=3.789m, SM1) 165

4.15 Comparison of Stress Distribution (h=3.789m, SM2) 166

4.16 Comparison of Stress Distribution (h=3.789m, CM1) 167

4.17 Comparison of Pressure-Displacement-Plastic Zone (SM1, Cohesionless, Ko=0.41); a) h=1.789m b) h=3.789m c) h=5.789m d) h=7.789m 168

Figure | Page

4.18 Comparison of Pressure-Displacement-Plastic Zone (SM2, Cohesionless, Ko=0.98); a) h=1.789m b) h=3.789m c) h=5.789m d) h=7.789m....................169

4.19 Comparison of Pressure-Displacement-Plastic Zone (CM1, Cohesive, Ko=0.98); a) h=1.789m b) h=3.789m c) h=5.789m d) h=7.789m....................170

4.20 Comparison of Plastic Zone with Depth (SM1,SM2,CM1)171

4.21 Comparison of Pressure with Depth (SM1)............172

4.22 Comparison of Pressure with Depth (SM2)............173

4.23 Comparison of Pressure with Depth (CM1)............174

5.1 Subsurface Stratigraphy (at Terwillegar Shaft).....187

5.2 Layout of Field Instrumentation.....................188

5.3 Transverse Section showing Shaft Instrumentation (along Axis OA)....................189

5.4 Two-Dimensional Mesh for the FE Analyses of the Terwillegar Shaft...........................190

5.5 Comparison of Surface Settlements..................191

5.6 Comparison of Subsurface Settlements...............192

5.7 Comparison of Horizontal (Radial) Displacements....193

5.8 Comparison of Soil Pressures.......................194

5.9 Earth Pressures versus Depth.......................195

5.10 Convergence Curves................................196

5.11 Comparison of Shaft Design Methods................197

6.1 Pressure versus Depth - Model I (modified from Muller-Kirchenbauer et al., 1980)............215

6.2 Active Force versus Recess Parameter - Model I (modified from Muller-Kirchenbauer et al., 1980)..................216

6.3 Comparison of Active Pressures - Model II..........217

Figure		Page

6.4 Measurement of Stresses Before and After Excavation (modified from Muller-Kirchenbauer et al., 1980)....218

6.5 Measurement of Surface Settlement (modified from Muller-Kirchenbauer et al., 1980)....219

6.6 Predicted Plastic Zone with Depth 220

6.7 Radial Strains in Melinex Shafts versus Depth (modified from Lade et al., 1981) 221

6.8 Comparison of Pressures with Depth 222

6.9 Comparison of Stress Distribution 223

6.10 Young's Modulus versus Confining Pressure 224

6.11 Predicted Plastic Zone 225

B.1 Cauchy Problem....258

B.2 K_r-values....259

B.3 Finite Element Mesh for Tunnel Analysis....260

B.4 Displacement Vectors (ST1 and ST2)....261

B.5 Displacement Vectors (ST3 and AP1)....262

B.6 Displacement Vectors (DT1)....263

B.7 Displacement Vectors (DT2)....264

B.8 Displacement Vectors (STC1 and STC2)....265

C.1 Contours of Vertical and Horizontal Displacements around EXP Tunnel (modified from Eisenstein et al., 1981)....269

D.1 Terzaghi's Method (1943)....279

D.2 Berezantzev's Method (1958)....280

D.3 Prater's Method (1977)....281

D.4 Gravity Effect in Cohesive Soils....282

D.5 Coefficients of Vertical-Radial Stress (K_s, K_w)....283

D.6 Finite Element Mesh for Shaft Analysis....284

Figure | Page

E.1 Shaft Details (modified from Muller-Kirchenbauer et al., 1980) 288

E.2 Shaft Models-Types I and II (modified from Muller-Kirchenbauer et al., 1980) 289

E.3 Model Test Setup (modified from Lade et al., 1981) 290

E.4 Stress-Strain and Volume Change Curves from Triaxial Compression Tests on Leighton Buzzard Sand (modified from Lade et al., 1981) 291

1 . INTRODUCTION

1.1 Thesis Introduction

Due to rapid growth of population, underground construction has been active for the last 10 years in Edmonton, Alberta. Most underground projects have involved construction of shafts and tunnels for storm and sanitary sewer systems, power distribution systems, and light rail transportation.

The Geotechnical Section of the Civil Engineering Department at the University of Alberta have been aware of the benefits incurred from monitoring underground construction. This monitoring approach provides a method for validating empirical design techniques, evaluating stability and determining the mode of ground behaviour adjacent to the opening. Eisenstein and Thomson (1978) observed the geotechnical performance of a tunnel in till and predicted the field performance using the finite element method of analysis. Thomson and El-Nahhas (1980) measured the deformations of the temporary lining of two tunnels in till and clay shale. Medeiros (1979) studied the problem of magnitude and distribution of lateral pressure acting on a deep retaining structure excavated in till and sand by an approach integrating field measurement from a case history with finite element analysis. El-Nahhas (1980), Branco (1981) and Corbett (1984) carried out extensive field instrumentation to monitor the soil mass displacement and pressure formation around tunnel excavation. Kaiser *et al.* (1982) performed an investigation of a shaft in clay shale.

Korpach (1983) used stressmeters to measure stress changes near tunnel faces. Besides these field monitoring activities, Kaiser and Hutchinson (1982) studied the effects of construction procedure on tunnel performance using finite element methods. Eisenstein *et al*. (1984), Heinz (1985), and Eisenstein and Negro (1985) carried out finite element parametric studies on the ground responses near shallow tunnels.

Inspite of the above research work, there were few quantitative analyses of the ground response that follows the correct sequence of stress relief of insitu stress, i.e., passage from elastic behaviour through yielding to collapse. Few attempts were made to relate stress relief with displacements for the whole spectrum of responses. Support pressure and displacement observations were often interpreted separately. In reality, soil pressures on tunnel and shaft linings are highly dependent on the soil displacements permitted during construction. This interrelationship has been recognized by many, e.g., Rabcewicz and Golser (1973), Egger (1975), Daemen (1975), in relating tunnel wall movement and support pressure, and more recently by Eisenstein and Negro (1985) for surface settlement and support pressure relationship. Current design methods usually treat with these two aspects individually, separating pressure prediction from displacement prediction. For example, limit equilibrium methods proposed by Terzaghi (1943), Berezanztev (1958) and Prater (1977) yield minimum support pressures to maintain stability of a shaft and do not predict displacements. In the field displacements are usually controlled by selecting an appropriate factor of safety and through proper construction techniques. The current practice may lead to conservative or unsafe designs, as will be demonstrated later. Again, this aspect has been discussed for shallow tunnels by Eisenstein and Negro (1985).

In view of these limitations, a theoretical approach to solve this problem and to accommodate the dependency between stresses and displacements is attempted. This thesis is built on the concept of ground-support interaction or convergence confinement method which was originally proposed by Fenner (1938) and expanded later by Pacher (1964) and Rabcewicz and Golser (1973). This approach proposed and verified in this thesis is expanded to include various aspects as insitu stress, yield initiation and propagation, effect of gravity and collapse mechanism.

1.2 Convergence Confinement Method

1.2.1 Introduction

The convergence confinement method (CCM) will be used throughout this thesis, as a conceptual framework for understanding the ground-support interaction in underground openings. This method is applied by constructing two characteristic curves of fictitious radial pressure versus radial displacement defining the ground response and the support reaction. The former describes the ground convergence in terms of the internal pressure relief (Ground Convergence Curve, GCC) while the latter relates the confining pressure acting on the support to its deformation (Support Confinement Curve, SCC). The state of equilibrium of the ground-support interaction is given, in a simplified fashion, at the intersection of the GCC and SCC, as illustrated in Fig. 1.1.

1.2.2 Ground Convergence Curve (GCC)

The ground convergence curve gives the relationship between the radial displacements at the wall and a fictitious radial support pressure. This relationship at a specific point on the wall of the opening depends on (i) the initial insitu stresses, (ii) the strength-deformation properties of ground, (iii) the excavation method and (iv) the sequence of stress-relief for materials that are not linear elastic (see Fig. 1.2).

Fig. 1.1 shows a schematic ground convergence curve for a uniformly stressed circular opening in a homogeneous ground, along with the relationship between the extent of the plastic zone and the displacement. For $K_o=1$, all GCCs originate at a single point of radial support pressure corresponding to the initial insitu stress. For a non-uniform biaxial stress field, separate GCCs can be developed for each point along the circumference of the opening. For small stress relief, the ground response is elastic, and the GCC is linear with the slope being proportional to the shear modulus of the ground. Further stress relief might induce yielding around the opening, and the GCC becomes nonlinear. For sufficiently strong ground, the opening remains stable without any support (Curve 1 for elastic or Curve 2 for plastic ground). However, in weak ground yielding will propagate outward as the internal support stress decreases, and the pressure may reach a minimum value (Curve 3) or start to increase (Curve 4) after an optimum support pressure at Point A.

Several modes of yielding can possibly develop near an underground opening: (i) localized yield zones (or shear bands), (ii) separate yield zones (diffuse yielding), (iii) a continuous (global) yield zone and (iv) combinations of the above. The plastic zone development depends primarily on the boundary condition and ground properties. The prediction of the mode of yielding is an unresolved area of research, but might be handled by the bifurcation theory, Vardoulakis (1985). One of the main objectives of this thesis is to identify typical modes of yielding that develop around tunnels and shafts, and to derive techniques to predict the behaviour of these modes.

Excessive yielding around an opening may induce a kinematically possible collapse mechanism under the effect of gravity, especially near the free boundary surface. A minimum support stress p_g due to this gravity effect is required to maintain the stability of the opening. The opening will remain stable as long as p_i is greater or equal to p_g. The gravity effect becomes dominant when p_i reaches a critical value, p_{cr} (Fig. 1.1). For strain-hardening ground (no reduction in strength during yielding), p_g will be approached asymptotically (Curve 3). For strain-weakening ground, the strength reduction in the yield zone will accelerate the gravitational effect, and

p_g increases with growth of the yield zone (Curve 4).

For ground with time-dependent strength or deformation properties, the displacement will increase with time. These time-dependent aspects have been studied by Ladanyi (1980) and Panet and Guenot (1982), and will not be pursued further in this thesis.

For the design of underground openings, we are concerned with both the support pressure and the ground displacement (e.g., for ground control). For the GCC of type (1), design and construction are simple and little difficulties are to be expected. For GCC type (2), we may reduce the support pressure at the expense of permenant plastic displacements, and hence ground control criterion may govern the design. For ground where the gravity effect becomes dominant, the support pressure will not decrease to zero and may even increase with large or "excessive" displacements. In this type of ground, the design must concentrate on the determination of the critical displacements (u_{cr}) and the amount of gravity loading which depends on the type of collapse mechanism that is initiated. For good ground control, the displacements allowed during construction should be less than the critical in order to prevent excessive deformation that brings undesirable load increases and possibly destructive effect to surrounding structures.

Brown *et al.* (1983) presented a summary of currently available GCC formulations of different material models for the idealistic case of a circular opening in an isotropic stress field under two-dimensional plane strain condition.

Daemen (1975) included the gravity effect in his formulation. Application of these closed-form solutions to underground openings is very restrictive because of the inherent assumptions. For complicated boundary conditions and anisotropic stress fields as in shallow tunnels, the GCC can only be obtained by numerical simulation techniques (i.e., Eisenstein and Negro, 1985). However, severe problems are confronted in these approaches when excessive yielding takes place or the system approaches its limit state. Thus if the primary interest is the critical state (u_{cr}) or the limiting load, uses of these numerical simulation technique, e.g., FEM are not practically possible because the collapse of a geomechanical system is mostly associated with the formation and propagation of yield zones. Alternatively, the pressure required to prevent the collapse of an opening can be determined using analytical methods of the theory of limit state, but this approach requires the correct prediction of the formation of the yield zone and the mode of collapse. In this research, the mode of initiation and propagation of yield zones are studied and the collapse loads are determined.

Thus, the strategy used to determine the entire GCC is to obtain the initial portion using continuum mechanics techniques (closed-form solutions) or finite element method, where appropriate, and to combine it with a terminal portion determined from theory of limit state (Fig. 1.1).

1.2.3 Support Confinement Curve (SCC) and Ground-Support Interaction

The support confinement curve defines the relationship between radial support pressure and radial displacement at the support-ground interface (Curve 5, Fig. 1.1). The location at which the curve originates depends on the time of installation, construction techniques and face effects. These three-dimensional effects can be accounted for in a simplified way by considering either an equivalent radial displacement (u_o) or an initial stress change (p_{ro}) for the plane strain model. The shape of the SCC is associated with the strength-deformation properties of the support system and its activation. It is generally not a unique curve, except for $K_o = 1$, circular opening and no gravity effects.

Hence, the way to obtain the equilibrium state of ground-support interaction as shown in Fig. 1.1 (intersection of the GCC and SCC) is over-simplified. The final equilibrium state depends on K_o, and the ground and support parameters (Pender, 1979). The study of this aspect is beyond the scope of this thesis. However, one can approximately locate the equilibrium state by considering two possible extremes in pressure formation on the support. For very flexible supports, symmetrical pressure distribution around the tunnel opening is expected. Averaging the pressure formation at ground-support interaction points yields loci of the final equilibrium state (e.g., at the roof and floor). For very stiff supports, the final equilibrium state is comparable to the pre-support state. The uneven pressure around the support is balanced by shear at the ground/support interface. This simplified approach suggested by Peck *et al.* (1972) was expanded by Einstein and Schwartz (1979).

Hoek and Brown (1980) presented solutions for a number of support systems. For simplicity, we assume linear-elastic behaviour for the support system.

1.3 Objective and Scope of this Thesis

The objectives of this thesis are (i) to investigate the mechanisms of ground behaviour near shallow and deep tunnels and shafts, (ii) to develop an approach to assess behavioral modes of both shallow and deep tunnels and shafts, and (iii) to verify this approach by comparison with results of behavioral mode, support pressure and ground displacement from finite element analyses, field measurements and model tests.

The convergence confinement method, employed as a conceptual framework for this thesis, was introduced in this introductory chapter. Chapters 2 to 3 are concerned with the analysis of tunnels while Chapters 4 to 6 deal with shafts.

Chapter 2 is mainly concerned with the mechanism of tunnel behaviour and the formulation of the GCC. Numerical examples, generated by the finite element method, are compared with the proposed approach. Chapter 3 presents case histories from field and model test studies. The proposed technique is used to interpret some of the observations obtained in these case studies.

A review of limitations and assumptions of the currently available design methods for shafts is introduced in Chapter 4 and followed by a detailed study of the ground deformation mechanisms near shafts. The CCM with the inclusion of gravity effect is suggested as a theoretical approach to shaft design. In this fashion it is possible not only to predict the formation pressure but also the ground displacements. Numerical examples generated by finite element analyses are compared with results predicted by the proposed technique.

Chapter 5 describes a well documented case history of an instrumented shaft constructed in Edmonton. Field measurements of displacements and pressures around the shaft are included in this chapter. Results of back analyses using the proposed technique and the FEM are compared with those obtained from field observations.

Chapter 6 presents case histories of model tests for shafts. The proposed CCM technique has been used to interpret these test results.

Conclusions on tunnel and shaft behaviour are given in Chapter 7.

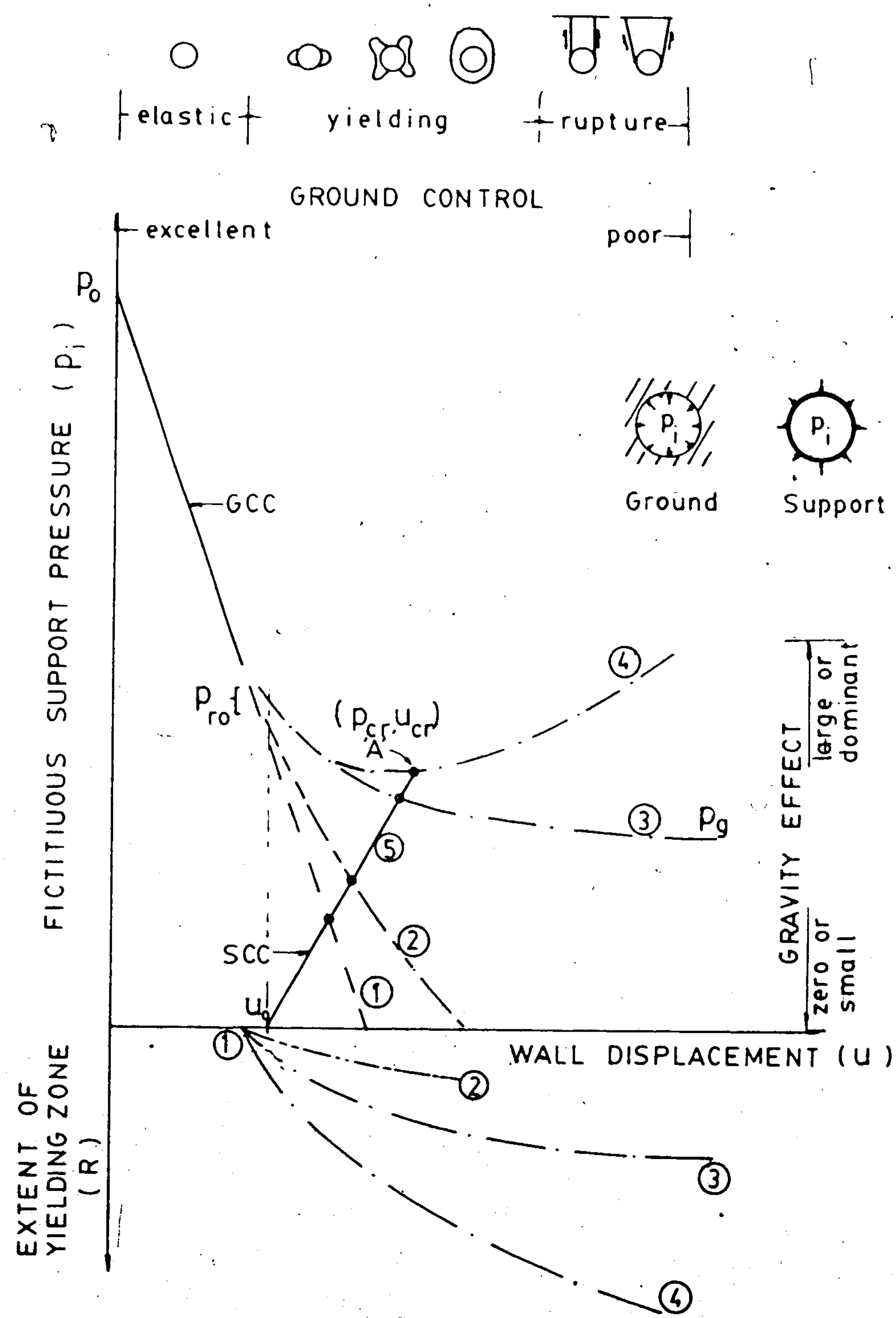

Figure 1.1 Convergence Confinement Method

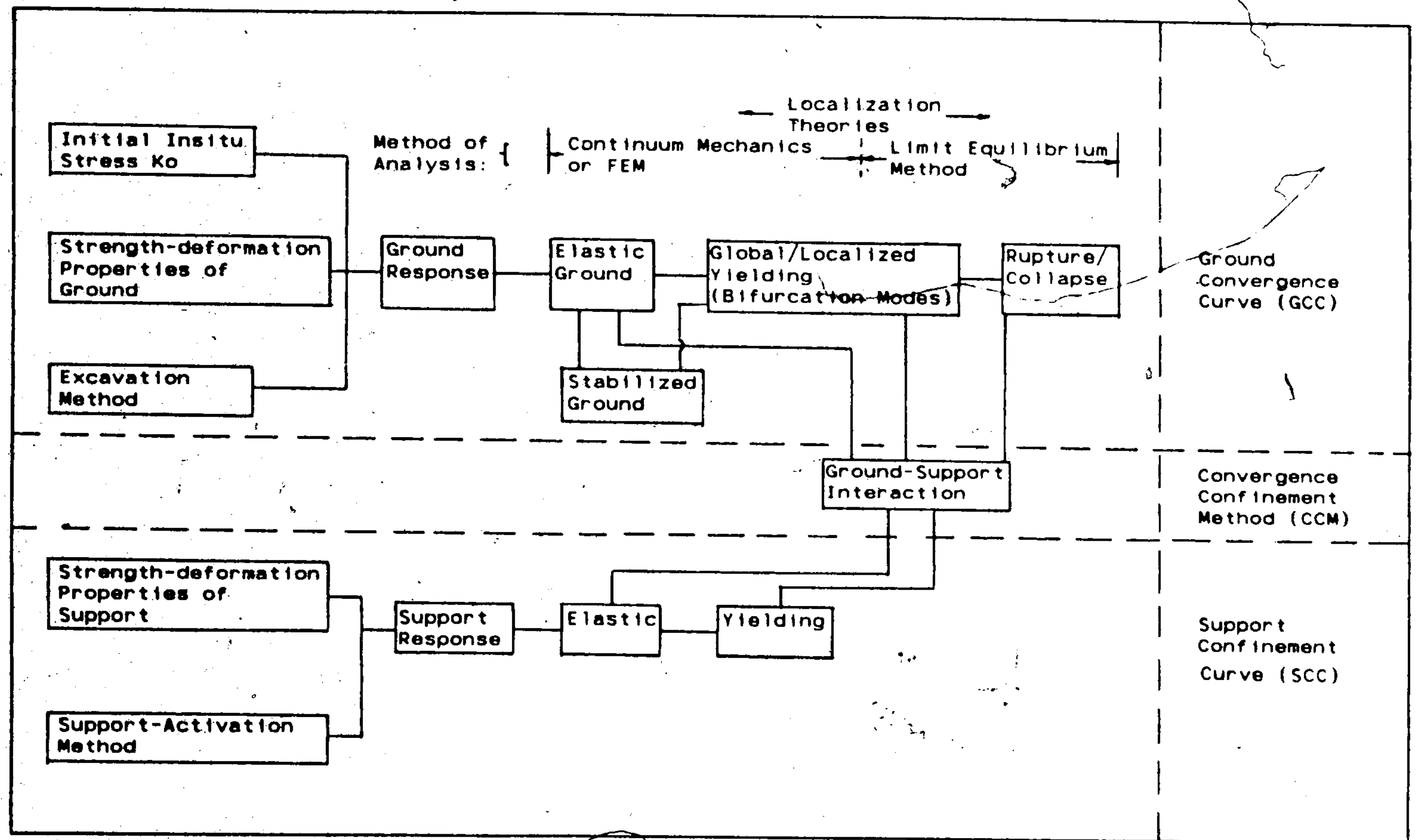

Figure 1.2 Conceptual Framework - Ground-Support Interaction

2 . MECHANISM OF TUNNEL BEHAVIOUR

2.1 Introduction

Driving a tunnel causes stress relief of initial insitu stress around an opening. The disturbed ground mass will displace and search for a new state of equilibrium. Depending on the insitu stress, the strength of the ground and the construction method, this new state of equilibrium might be reached after undergoing elastic or plastic deformation, or collapse. Excessive displacements around a tunnel are prevented by installing a support system. Hence, the mechanism of tunnel behaviour must be governed by the distribution and magnitude of stress relief permitted near the opening during construction.

Ground movements due to tunnelling may cause destructive distortion or settlement to adjacent structures. For shallow soft ground tunnels, prevention of damage due to surface settlements becomes of prime concern and many design and construction decisions may be directed toward preventing excessive damage to structures or utilities near the surface.

The objectives of this chapter are to identify possible behavioral modes of shallow and deep tunnels and to propose analytical techniques to assess these modes. The proposed techniques will be verified by comparison with results of finite element analyses, model tests and field measurements.

2.2 Ground Responses

2.2.1 Simulation of Excavation

Consider the case of a circular tunnel, to be excavated to an initial radius a (Fig. 2.1a). The length of the tunnel is assumed to be much greater than its diameter and the section is remote from the excavation face. The tunnel can be treated as a two-dimensional plane strain problem. Excavation removes the insitu stress existing at the periphery of the tunnel opening. It is assumed that the ground response to this excavation process can be simulated by successively reducing a fictitious internal support pressure (radial and shear components). For a deep tunnel under hydrostatic insitu stresses, this fictitious support pressure may be approximated by a uniform radial stress equal to the overburden pressure at the tunnel axis. But for a shallow tunnel with non-uniform initial insitu stresses ($K_o \neq 1$), the fictitious support pressure is no longer uniform (p(roof)≠p(floor)) and is composed of radial (normal) and shear stresses, p_i and τ_i (τ_i=0 at the roof, springline and floor).

2.2.2 Stress Relief during Excavation and Modes of Yielding

As the fictitious support pressure decreases, the wall will converge and stress redistribution involving a decrease in radial stress and an increase in tangential stress will take place. Arching action develops around the opening, as indicated by arrows in Fig. 2.1a. Yielding at the wall will be induced with a further decrease in support pressure if the stress difference between tangential and radial stresses violates the failure criterion.

The mode of yielding which is initiated at the wall depends solely on the initial insitu stress state, K_o. Fig. 2.1b shows two modes of yield initiation for (I) K_o=0.5 and (II) K_o=1.0. For Mode I, the initial radial stress is greater than the tangential stress at the roof, and vice versa at the springline. As p_i decreases, the stress differences $(\sigma_t - \sigma_r)$ becomes smaller at the roof (R) and larger at the springline (S). The soil element at the roof or floor always remains elastic while the soil element at the springline will fail. Thus the plastic zone will initiate at the springline for K_o=0.5. For K_o=1.0, the stress difference $(\sigma_t - \sigma_r)$ at the roof and springline will grow approximately at the same rate. Hence, yielding will initiate around the periphery simultaneously unless localization occurs. For K_o>1.0, the plastic zone will initiate at the roof and floor because of high initial horizontal stress. This mode of yielding corresponds to Mode I rotated by 90°.

Once yielding is initiated at the wall, further stress relief in p_i will cause propagation of the plastic zone. How the plastic zone propagates depends on the displacement boundary conditions. For a deep tunnel where the external boundaries are remote from the opening, the problem can be simplified as an opening subjected to a confined insitu stress field. The plastic zone will propagate symmetrically.

Near a shallow tunnel the free surface boundary affects the propagation of the plastic zone. Again, two

K_o conditions must be considered separately; for example, K_o=0.5 and K_o=1.0, as shown in Fig. 2.2. For K_o=0.5, the behaviour of the circular tunnel with plastic zones at the springline are comparable to a rectangular slot (trap door) of a width equal to the distance between two extremes of the plastic zones (w=2R). The weight of the soil block above the opening is supported by the shear resistance in the unyielded soil. Thus, resisting shear stress will be mobilized along some inclined surfaces due to the downward movement of the soil block. The state of stress on a soil element along the inclined plane is plotted in a Mohr diagram in Fig. 2.2. The induced shear stresses due to gravity increase the stress difference between two principal stresses (the diameter of the Mohr circle) until failure occurs. Thus, localized plastic zones propagate upward from the springline and toward the free surface. The direction of the propagation of the yield zones, denoted by the inclined angle (β) (e.g., Fig. 2.5) depends on the distance to the free surface (H/a), K_o and the stress boundary at the opening. This will be proved later (Section 2.2.3.3). It is interesting to notice that the soil elements at the roof may still remain in an elastic state when a limit state is approached. Roof and surface settlements will increase at a comparable rate at this point.

The tunnel behaviour for K_o=1.0 is different. After initial yielding, the opening becomes completely surrounded by the yielding ground. The maximum extent (w) of the plastic zones at the springlines is smaller than that for K_o=0.5, and the stress concentration is less severe.

Furthermore, because of relatively high initial horizontal stresses, the shear resistance against downward movements of a soil block is enhanced. Hence, the soil block above the opening has less tendency to displace downward (because the state of stress is farther from the yield surface) and high localized shear stresses do not develop to cause localized yielding. The plastic zone around the opening tends to propagate evenly outward. Its shape may be influenced by gravity causing more rapid propagation towards the free ground surface (Mode II).

The above illustration only shows two basic and idealized mechanisms of tunnel behaviour (I) formation of localized yield zones and (II) formation of a concentric (or an egg-shaped) plastic zone. However, other modes may also occur. Fig. 2.3 shows some possible modes which are of practical interest. It is assumed that in all these processes, the stress relief around the periphery of the tunnel opening is in proportional unloading of the insitu stress (p_i, τ_i) and yielding is induced by an active failure mode. Modes I and II have already been discussed in detail. A critical K-value (K_{cr}) should exist between 0.5 and 1.0 at which yielding may initiate at the springline and two localized shear zones may coalesce to form a continuous domain around the opening as further stress-relief is allowed, i.e., Mode I develops into Mode II.

A third mode, Mode III occurs at K_o>1.0 when yielding is initiated at the roof and floor, and a fourth mode, Mode IV similar to yielding in the 'trap-door' model test (Terzaghi, 1943), is observed if only vertical stress-relief or displacement is allowed.

These four modes of yield initiation (Modes I to IV) can develop into other sub-modes, depending on the boundary conditions and ground parameters. In this thesis, only Modes I and II are of the primary interest. For Mode I, two separate yield zones at the springline may propagate in forms of localized lobes, and they may (Mode I-1) or may not (Mode I-2) reach the free surface before yielding is initiated at the roof. Mode I-1 usually dominates at deep tunnels whereas Mode I-2 at shallow tunnels (Atkinson and Potts, 1977). The extent of yield zone at the roof propagates with further stress relief (i.e., Modes I-1.1 and I-2.1). At this stage, kinematic collapse may possibly occur at the roof. This collapse mechanism is governed by the formation of slip lines within the yield zone (i.e., upper bound solution). Mode I can also develop into a special Mode I-3 in which the yield lobes merge to form a ring with an unyielded core before the surface is reached. Mode II is common in situations where K_o is close to 1.0. The continuous yield zone will expand as stress relief proceeds, and two ear-shaped zones may be formed at the shoulders of the tunnel (El-Nahhas, 1980). Similarly to Mode I, two ear-shaped zones may or may not reach the free surface (i.e., Modes II-1 and II-2, respectively). In Modes I and II, the minimum fictitious support pressure around the tunnel opening is the one that prevents the kinematically possible collapse mechanism.

Various bifurcation processes discussed above govern the behaviour of tunnels in terms of their mode of yielding, required support load (e.g., collapse load), and soil displacement (e.g., surface and subsurface settlements). Hence, it is essential to investigate what conditions and parameters govern each possible mode before other aspects like load and displacement development can be quantified.

2.2.3 Bifurcation Phenomena in Tunnelling

2.2.3.1 Introduction

The main purposes of this section are:

1. to identify parameters governing the modes of yielding near tunnels;
2. to locate boundaries and regimes of each possible mode; and
3. to propose analytical techniques formulating the ground responses near the tunnel for different modes of yielding.

Formation of localized yield zones at the springline (e.g., Mode I) or a continuous plastic domain around the tunnel opening (Mode II) can be considered as a bifurcation problem. Bifurcation of a deformation process means that under certain critial states the deformation process may turn from one mode of behaviour to another entirely different mode.

Vardoulakis (1985) presented an excellent review of recent theoretical and experimental work done in the area of stability evaluation and bifurcation theory in soil mechanics. Some of the studies relevant to our objectives are briefly mentioned here. The study of bifurcation in continuous mechanics was pioneered by Hill (1962). Following this fundamental work, Palmer and Rice (1973) formulated conditions for localization in connection with shear-band development in overconsolidated clays. Rudnicki and Rice (1975) also derived conditions for localization in pressure-sensitive, dilatant materials. Bifurcation analyses in deformable materials under tests of ideal stress conditions were performed by Hill and Hutchinson (1975), Young (1976), and Vardoulakis (1978, 1979, 1981). Needleman (1979) and Molenkamp (1985) investigated the effects of constitutive relationships of materials on bifurcation processes.

Bifurcation modes are governed by the constitutive properties of the soil, boundary conditions (stress and displacement), and geometrical and/or material imperfections. The mode of yielding near a tunnel, as discussed in Section 2.2.2, is dictated by the boundary conditions, e.g., insitu stress, internal support pressure and the free surface. Transition of one mode to another mode is due to the bifurcation process. Formulation of this bifurcation process near a tunnel is difficult because of the complexity of the boundary conditions. Vardoulakis (1985) suggested to use finite element methods or semi-inverse methods to solve this complex boundary value problem.

2.2.3.2 Strategy

While the three-dimensional conditions near the tunnel face may actually dominate, only the two-dimensional plane strain conditions of a tunnel will be considered. Modes of yielding near a tunnel are linked by (i) strength parameters (ϕ,c), (ii) geometry and proximity of the free surface boundary (H/a), and (iii) boundary stress (K_o and p_i, τ_i). The main objectives of the following analyses are to investigate under what combinations of the above governing conditions each mode dominates and to categorize them into typical modes of yielding. Instead of deriving exact solution for each possible mode which involves complicated numerical formulations, a semi-theoretical approach coupled with finite element analyses and interpretation of results from model tests and field observations will be used to establish boundaries among various modes. Continued research will be needed to formulate the method of analysis for each individual mode.

It was shown in the previous section that two basic modes can be identified under different K_o conditions: (I) localized yielding from the springline for $K_o < K_{cr}$, and (II) continuous yielding around the opening for $K_o > K_{cr}$. Mode I was observed in model tests (Atkinson *et al.*, 1975; Potts, 1976; Cording *et al.*, 1976). Reyes and Deere (1966) and Smith (1973) investigated the mode of yielding around a circular cavity under biaxial stresses and found that localized yield zones developed for $K_o < 0.4$. Lo *et al.* (1984) made use of Mode II in predicting the crown settlement for tunnels in soft clay, and found that their predictions compared well with field observations. Atkinson and Potts (1977) also carried out model tests in overconsolidated kaolin (at

K_o =1.0) and reported that at collapse load high shear strains were concentrated at the springline, i.e., Mode I. Their findings seem to contradict the proposition that Mode II occurs at K_o =1.0. However, it will be shown (Fig. 2.4) that because of the bifurcation process the mode may change depending on how and to what level the boundary stress p_i is reduced. Hence, from these observations in model and field tests, it is postulated that two modes are possible near a tunnel where K_o is less than or equal to 1.0. It is further postulated that these two modes are mutually exclusive and independent events under given boundary conditions, i.e., there is no overlapping of the two modes. Transition from one mode to another is, however, possible if changes in boundary conditions occur.

All important parameters governing the bifurcation process near a tunnel are included in Fig. 2.4 which is a plot of p_i/p_o versus K_o for a given ϕ and H/a. Fig. 2.4 shows schematically regimes of possible modes. Steps in constructing the boundaries of the various regimes for different modes of behaviour are given below and followed by some numerical examples.

Regime A

Line a-b is the limiting value to K_o, equal to the active pressure coefficient, K_a. The K_o values within this regime are inadmissable if the initial state of the ground is assumed to be elastic (i.e., the initial deviatoric stress of the K_o condition must be less than that of the K_a).

Regime B

This regime corresponds to conditions where no yielding occurs on elastic unloading. Line c-d denotes the limit for initiation of yielding. Since we are primarily concerned with cases of $K_o<1.0$, yielding will be initiated at the springline. Line c-d is determined by comparing the tangential-radial stress difference at the springline with the available strength of the ground. Schmidt (1926) derived equations for stress distribution around a circular tunnel in a stress field where the pressure increases with depth (Appendix B.1). The internal support pressure is assumed to be uniform around the circumference instead of percentage of the original insitu stress. This assumption leads to an underestimation of p_i/p_o for $K_o<1.0$. The underestimation magnifies as K_o decreases to K_a.

Regimes C, D, E, F, G and H

When the internal support stresses are slightly below those of Line c-d, yielding occurs at the springline.

Regimes C and H correspond to conditions where initial yieldings are localized at the springline. But there exists a critical K_o-value, K_{cr} (Line g-j) which separates two different modes of yielding around the opening. Determination of Line g-j will be explained later.

For $K_o<K_{cr}$ (Regime C) the two localized plastic zones at the springline will develop into pairs of localized yield zones (Model I-1, Regime D). This development occurs at a p_i/p_o value defined by Line p-q which cannot be quantified at this stage. Further stress relief causes the top pair of

localized yield zones to propagate to the free surface. These yield zones may (Regime F) or may not (Regime D) reach the free surface before yielding is initiated at the roof. Line e-f separating Regime F from Regime D is determined by searching for the most critical case of limit equilibrium state around the tunnel opening as demonstrated in Fig. 2.5 for Mode I. In this critical state, the two localized yield zones intersect the free surface. The assumption that the states of stress along the inclined planes AB and CD are at ultimate strength (or residual for strain-weakening ground) may be made. Thus, the required support pressure (p_{ys}) (Line e-f, Fig. 2.4) to allow the localized yield zones to propagate to the free surface is determined using the limit equilibrium method. This approach will be given in details along with numerical examples in Section 2.2.4.1.

Line h-k signifies the point of yield initiation at the roof. Values of p_i/p_o for Line h-k could be determined using the same method as that for Line c-d, except for the roof instead of for the springline. Alternatively, the method presented by Detournay (1983) may be used. Hence, as a simplification it may be assumed that the elastic stress field around the tunnel is not affected by the yielding process at the springline. This effect of the yielding process is minimal as K_o is close to unity where the extent of yielding at the springline is narrow (e.g., Regime H). In Regime E (Mode I-1.1), yielding has been initiated at the roof but the yield zones at the shoulder do not reach to the free surface. In Regime G (Mode I-2.1), the mode of yielding is similar to that of Mode I-1.1, except that the yield zones at the shoulders have reached the surface.

Regimes J and K

In Regime H yielding only occurs at the springline. This localized yielding will develop into a continuous domain (Regime J, or Mode II) as p_i decreases below support pressures of Line h-k. Further stress relief may again induce ear-shaped yield zones at the shoulders of the tunnel, as shown in Regime K. (Model II-1).

Line i-l represents the boundary of the transition from Mode II into Mode II-1 where ears develop. Within Regime J, the opening is completely surrounded by a continuous plastic zone. The solution to determine the extent of this continuous plastic zone comprises (i) determining elastic and plastic stress distributions satisfying all boundary conditions and (ii) searching the elastic-plastic interface by stress continuity (Oda and Yamagami, 1979; Detournay, 1983). Within the plastic zone stress equilibrium and failure criteria must be satisfied. These requirements impose conditions to seek for values along Line i-l. Steps to obtain Line i-l are given in Appendix B.2.

Regime L

Once yielding occurs around the tunnel, kinematical collapse mechanisms bounded by slip lines within the yield zone can develop under the effect of gravity. The collapse mechanism becomes more obvious at the roof. Line m-n defines the minimum support pressure, p_{ic} required to prevent any kinematically possible collapse at roof. If

p_i is reduced to support pressure below p_{ic}, the collapse mechanism at the roof will be triggered and will propagate toward the free surface. Then, the state of stress above the roof has been disturbed and a new final equilibrium state must be reached. The required support stress to maintain this equilibrium state is designated as p_{fc}. This mode is not shown in Fig. 2.4, and will be explored in detail later (Section 2.2.4.1).

2.2.3.3 Examples

The approach described above (Fig. 2.4) is now used to investigate the modes of yielding near a tunnel in cohesionless soil. Governing parameters such as H/a, K_o and p_i/p_o are varied to investigate the modes of behaviour, and the results are shown in Figs. 2.6 to 2.8. The support stresses at the periphery of the tunnel are non-uniform, distributed in proportion of the insitu stress.

Comparisons among Figs. 2.6 to 2.8 reveal that areas for each regime are a function of H/a and ϕ. The area of the elastic unloading Regime B increases in size as expected with increasing ground strength (ϕ). Regimes denoting the first mode (Mode I) contract in general as ϕ increases. Regimes F and G diminish for most cases at H/a=18, i.e., for deep tunnels the localized yield zones will not reach to the free surface. The tendency of transforming from Mode II to Mode II-1 (area of Regime J) or the development of ears in the yield zone becomes less pronounced as ϕ and H/a increases. This implies that the behaviour of a tunnel is not properly approximated by the "hole-in-plate" theory unless the values of governing parameters fall within the area of Regime J.

On Fig. 2.7 (ϕ=30°) are also plotted results of some numerical examples calculated by FEM, which are presented in Section 2.2.5. As expected, the yield initiation point for K_o=0.5 obtained from FEM (empty circles) are higher (by 5-18%) than the predicted owing to the different stress distributions of internal support pressures assumed for two cases (percentage of p_o in FEM and uniform in closed-form solution). However, the FEM results agree better with the closed-form solution as K_o approaches unity. With regard to aspects such as mode of yielding and yield initiation at the springline, the FEM and the predicted results compare well. Similar consistence between results obtained from the FEM and the predicted are also found for the case of K_o=0.82.

Results obtained from field and model test monitoring (Chapter 3) are also plotted in Figs. 2.7 and 2.8 for comparison, which will be discussed in detail later.

2.2.4 Formulation of Ground Response

This section mainly explores analytical methods to depict the ground responses in stages from the state of yield initiation to collapse under the progressive stress relief in the excavation. We are interested not only in the ground convergence curve at the tunnel wall but also in the relationship among crown displacement, surface settlement and stress relief. Since two types of modes in ground behaviour, I and II have been identified, it is appropriate to investigate them separately. Although the following analyses are based on elastic perfectly plastic cohesionless ground, basic principles and reasonings can be applied to other types of ground with different constitutive laws.

2.2.4.1 Mode I

Fig. 2.9 presents a typical ground convergence curve at the roof for Mode I (Mode II also). On this figure are also plotted modes of yielding and methods of analysis. The changes in states of stress above the roof described by K-coefficient are also shown in Fig. 2.9. K is the average ratio of horizontal stress to vertical stress at soil elements above the crown. Each portion of the ground convergence curve is depicted in detail in the following.

Portion o-b

Portion o-a represents the elastic unloading response of the ground and Point a indicates the initiation of yielding at the springline. Portion a-b reflects the nonlinear ground response when the yield zones propagate outward with stress-relief.

Portion o-b may be determined using a continuum mechanics approach. But the influence of such factors as free surface boundary, gravity, non-hydrostatic loading and localized plastic zones must be considered. They impose numerical difficulties in obtaining closed-form solutions. Duddeck (1980), Eisenstein *et al.* (1984) and others suggested the finite element method as an analytical tool to evaluate the ground response to tunnel excavation. Eisenstein and Negro (1985) developed a two-dimensional finite element program to simulate the tunnel behaviour for ground of non-linear hyperbolic elastic stress-strain response with time-independent properties. For shallow tunnels in cohesionless soils, they encountered severe convergence problems in equilibrium iteration when the stress relief was more than 60% of the original insitu stress. This is one of the numerical inadequacy in finite element analysis when the limit state is approached. In reality, however, support pressure much less that 40% of insitu stress have been reported from field measurements (Eisenstein *et al.*, 1981; Branco, 1981; Corbett, 1984). Hence, it is fruitful if one can explore the ground response beyond this state.

Portion b-e

This portion describes the ground responses due to the stress relief from yielding to ultimate behaviour. Point c represents the state at which the yield zones just intersect the free surface, and the support pressure at this state is denoted by p_{ys}. At Point c, the soil block above the roof may or may not remain elastic. The support pressure can be further reduced to a lower p_{ic} (Point d) at which the collapse occurs at the roof. There exists a point between Points c and d corresponding to the point of yield initiation at the roof (i.e., Line h-k in Fig. 2.4). From the initial Point o to Point d, the tangential arching action above the roof (indicated by K-value) increases with stress-relief. But, beyond Point d the roof collapse mechanism is triggered and will propagate to the free surface. This mechanism will induce stress redistribution above the roof and the resultant K-value will drop. Hence, a sudden increase in support pressure from Point d to Point e results mainly from the decrease in tangential arching. For strain-weakening ground the whole portion a-e will be further shifted upward because of strength reduction associated with plastic straining in residual state.

With correct predicted modes of yielding, the support pressures at Points c, d and e can be determined by use of theory of limit state. Currently, no solution exists for the corresponding displacement at each point. Thus, some simplifications are required to construct Portion b-e. This can be done by extrapolating Portion a-b to Point d, i.e., following the negative slope at Point b. This assumption may lead to conservative design because Portion b-d should become flattened for yielding ground (i.e., the slope (negative) increases with displacement).

Portion b-e is of practical importance to tunnelling design because it provides information on marginal safety from collapse mechanism and also the ground control.

Point c (p_{ys})

At Point c, the yield zones just intersect the free surface forming a wedge as illustrated in Fig. 2.5a. The required support pressure p_{ys} can be estimated by limit equilibrium method.

Several assumptions regarding the failure surface and the stress destribution along it must be made such that an overall equation of equilibrium, in terms of stress resultants, can be written. Consider the equilibrium state of a soil block (ABCD) above a tunnel (Fig. 2.5a). Planes A-B and C-D inclined at β to the horizontal describe two failure surfaces giving the most critical condition of maximum required support pressure. Due to symmetry, no shear stress exists along Plane E-F. Considering the horizontal and vertical force components acting on the soil block, the equilibrium gives:

$$F_r + p_h a - (W - p_v a)\tan(\beta-\phi) = 0 \qquad 2.1$$

where: F_r - force acting on the plane E-F

p_h - equivalent uniform support pressure in horizontal direction (= $K_o[(H-a/2)\gamma]\eta$ where η is % of insitu stress)

p_v - equivalent uniform support pressure in vertical direction (= $[(H-a/2)\gamma]\eta$ where η is % of insitu stress)

Differentiation of Eqn. 2.1 with respect to variable β yields a maximum value for p_i. The angle β calculated in this manner should correspond to the direction of yield zone propagation from the springline to the surface.

Solution of Eqn. 2.1 requires knowledge of the force F_r. This force is equal to the resultant of the horizontal insitu stresses before tunnel excavation plus an increase in stress due to tangential arching resulting from stress-relief (see Fig. 2.5b). Thus F_r can be expressed as:

$$F_r = 1/2(K_r)\gamma(H-a)^2 \qquad 2.2$$

where: $K_r = K_o + \Delta K_r$. ΔK_r and K_r are coefficients used to approximate the increase in tangential stress and the resultant respectively (Figs. 2.5 and 2.9). It is important to note that the ratio of horizontal stress to vertical stress (K) actually varies along the depth above the crown.

Assuming even stress redistribution around the opening (Fig. 2.5b), the coefficient K_r can be calculated in terms of the variables H/a and K_o (see Appendix B.3). It is plotted in Fig. B.2. These K_r values depend on the percentage of stress-relief of the initial insitu stress. Thus, the maximum K_r is governed by the minimum support pressure, p_{ic}. Theoretically, K_r can reach the passive resistance coefficient, K_p (i.e., the whole soil block above the roof are in passive yielding). From Fig. B.2, it can be seen that the case of K_r approaching K_p only occurs near shallow tunnels and the maximum K_r is usually dictated by p_{ic}.

Eqn. 2.1 provides information not only on the support pressure, p_{ys} but also on the direction of the propagation of the yield zone, β. A computer program (TUN5, Appendix F) is written to calculate p_{ys} and β. Fig. 2.10 shows the angle β for ranges of H/a and ϕ values. It can be seen that this mode of yielding (Mode I-2) is only admissible at certain values of H/a, K_o and ϕ. The K_o-value has a limiting value of active pressure,

K_a. At high H/a (deep tunnel) and ϕ values (strong ground) the tendency of yield zone to propagate to the free surface is less pronounced. With K_o approaching to unity, the mode of yielding is Mode II. The angle β depends on K_o and H/a as well. For a shallow tunnel with high K_o, the yield zones are vertical.

The German Tunnelling guidelines (e.g., Duddeck, 1980 and 1982) differentiate between 'shallow' and 'deep' tunnels for H/a<5 and 'deep' tunnels for H/a>7. For 'shallow' tunnels, an equivalent continuum model (no embedding allowed at the crown, e.g., Duddeck and Erdmann, 1982) without reduction of ground pressure at the crown is recommended for lining dimensioning. For 'deep' tunnels, a continuum model (fully embedded, e.g., Muir-Wood, 1975) with some reduction of ground pressure may be appropriate. Careful examination on these guidelines reveals that one important factor governing the tunnel behaviour is neglected: the displacement permitted during construction, u_{con}. It has been proven that the ground pressure on a support and the behavioral mode of a tunnel depend on u_{con} and hence the structural model. Therefore, the structural models proposed in these guidelines are only valid under certain conditions. It is of practical importance to explore these conditions and to locate the limitations of these guidelines.

Limits between 'shallow' and 'deep' tunnels are plotted on Fig. 2.10 as 'A' and 'B' respectively. If Mode I-2 takes place (i.e., yield zones reach the ground surface), β are in ranges of 75° to 90° for 'shallow' tunnels and 60° to 80° for deep tunnels. The boundaries of these ranges depend on

ϕ. The structural model for 'shallow' tunnels recommended by the German guideline is conservative in terms of ground pressure. From Fig. 2.9 (GCC), full overburden pressure is only experienced if no displacement is permitted during construction. This condition is seldomly encountered in the field. Ground pressure may increase for $u_{con} > u_{ic}$ (beyond Point d, Fig. 2.9), but the induced pressure is still less than the overburden pressure. A partially embedded model (no embedding at the crown) is justified because in Mode I-2 the soil block bounded by two yield zones intersecting the ground surface has tendency to displace downward and exert pressure on the liner at the crown. Hence, the soil block above the crown should not be treated as part of embedding. For structural model of 'deep' tunnels, the ground pressure can be reduced with the increased displacement. The reduction depends on u_{con} and GCC. From Fig. 2.10, it is observed that the fully embedded model is only valid for Modes I-1 and II. If yield zones intersect the ground surface (e.g., ϕ=20°, K_o<0.60; ϕ=30°, K_o<0.40; ϕ=40°, K_o<0.30) or u_{con} is greater than u_{ic} (i.e., roof collapse has been initiated), then the partially embedded model instead of the fully embedded should be used.

It is interesting to observe that K_o of normally consolidated soils given by (1-sinϕ) (Brooker and Ireland, 1965) falls within limits 'A' and 'B' in Fig. 2.10. This suggests that the German Tunnelling guidelines are appropriately designed for normally consolidated soils provided that conditions stated above are satisfied.

Fig. 2.11 is a plot of normalized support pressure ($p_{ys}/\gamma h$) versus normalized depth (H/a) when the yield zone reaches the ground surface. This figure indicates that p_{ys} is a function of K_o and ϕ. p_{ys} decreases with increasing K_o and ϕ, implying that a small amount of stress relief of the insitu stress will cause the yield zones to reach the free surface in weak grounds under low K_o. Hence, tunnelling in these conditions is much more risky as intuitively expected. On Fig. 2.11 is also plotted the support pressure p_{ic} corresponding to the initiation of roof collapse mechanism. For conditions of $p_{ic}>p_{ys}$, Model I-1 is impossible, and Mode I-2 or Mode II-1 takes over depending on K_o (see bifurcation modes, Fig. 2.4).

Point d (Pic)

At this point yielding at the roof has occurred and possible collapse mechanisms defined by slip-lines within the yield zone may develop. The critical mechanism can be found by selecting any possible modes and performing an appropriate work rate calculation. The accuracy of this calculation (upper bound solution) will depend on the proximity of the assumed mechanism to the real one.

Atkinson *et al.* (1975) observed the configuration of the collapse mechanism in model tests and derived an upper bound solution.

$$p_{ic}/\gamma H = (a/2H\cos\phi)(1/\tan\phi+\phi-\pi/2) \qquad 2.3$$

provided that H/a is equal to or greater than $1/\sin(\phi)$. This equation is true only for material with an associated flow rule and $\psi=\phi$ where ψ is the angle of dilation (Hansen, 1958).

The values of p_{ic} normalized to overburden pressure (γH) are plotted in Fig. 2.11. Actually, p_{ic} are independent of the depth of overburden.

Point e (p_{fc})

Beyond Point d the roof collapse mechanism has been initiated. The extent of the propagation of this collapse mechanism depends on the displacement allowed at the roof. At the ultimate behaviour, the mechanism will reach the free surface and the soil block above the roof will be in the limit state. The support pressure p_{fc} at this state can be found by the use of the soil arching theory (Terzaghi, 1943). The arching action will be developed against both sides of the wedge (Fig. 2.5a). The mathematical treatment on arching is given in Appendix B.4.

Normalized support pressures p_{fc} are plotted against the depth ratio (H/a) for different shape of wedges (β) and friction angle (ϕ). The p_{fc} values also depend on the assumed earth pressure coefficient at the sides, K_s (Handy, 1985). Fig. 2.12 with $K_s=K_a$ shows that the p_{fc} becomes fairly constant for H/a>5. This agrees well again with the guidelines given in the German Tunnelling Handbook (suggesting full overburden at the crown if $u_{con}>u_{ic}$).

It is interesting to realize that two different types of arching action occur before and after this initiation of the roof collapse (Point d). For the state before Point d, the horizontal (tangential) stress is the major principal stress and the vertical (radial) is the minor within the yield zones above the roof. In this soil arching, the catenary must be convex upward as illustrated by Fig. 2.13a. In contrast to this, an inverted arch develops after excessive movements (Fig. 2.13b). This mode beyond Point d was well recognized and explained by Handy (1985). In this sagging state, soil arching may be depicted as a trajectory of minor principal stress that approximates a catenary (the vertical stress is major principal stress). For arching action to be supportive, the catenary must dip downward. The configuration of the catenary will change from convex upward to concave downward after passage of Point d. This transition signifies an abrupt increase in settlements above the roof.

From the GCC the relationship between the support stress and displacement at the roof can be obtained except for the ultimate state where the total displacement cannot be predicted. The next essential step then is to relate this to the roof settlement profile above the tunnel. This aspect will be discussed in detail together with Mode II.

2.2.4.2 Mode II

If yield initiation and propagation take place during unloading under K_o equal or close to unity, the tunnel opening becomes completely surrounded by a continuous, approximate concentric plastic zone. This situation follows the mechanism of a "hole-in-plate" model, and permits application of continuum mechanics and theory of plasticity to predict the internal pressure-convergence relationship. Daemen (1975) adopted this approach and included the gravity effect within the plastic zone to determine the ground convergence curves for deep rock tunnels. Lo *et al.* (1984) also used the same approach to predict the roof settlements due to tunnelling in soft clays.

In spite of the above studies, the continuum mechanics approach has not been used as an analytical tool to predict the behaviour of shallow tunnels, which are dominated by the gravity effect and complicated by the free surface boundary. In this thesis the technique proposed by Daemen (1975) will be adopted and expanded to include the effect of the free surface.

Considering a case of a tunnel as shown in Fig. 2.14a, i.e., a two-dimensional plane strain problem under $K_o=1.0$, a plastic zone of radius R will develop around the opening if the ground strength is exceeded. There exists a relationship between the internal support pressure p_i and the plastic zone R at the periphery of the opening.

For a shallow tunnel the true conditions can be replaced by a simplified model as shown in Fig. 2.14b. The stress distribution within the plastic zone are governed by the equilibrium equations.

$$\sigma_t - \sigma_r - r(d\sigma_r/dr) - d\tau/d\theta + r\gamma\cos\theta = 0 \qquad 2.4$$

$$d\sigma_t/d\theta + 2\tau + r(d\tau/dr) - r\gamma\sin\theta = 0 \qquad 2.5$$

Assuming $\tau=0$ at the roof, springline and floor, Eqns. 2.4 and 2.5 can be reduced to:

$$\sigma_t - \sigma_r - r(d\sigma_r/dr) \pm r\gamma = 0 \qquad 2.6$$

where: + for floor, - for roof and $r\gamma=0$ at springline.

For the ground that can be characterized by a cohesionless Mohr-Coulomb yield criterion:

$$\sigma_1/\sigma_3 = \sigma_t/\sigma_r = \tan^2(\pi/4+\phi/2) \qquad 2.7$$

Integration of Eqn. 2.6 along with Eqn. 2.7 and continuity of radial stress at the elastic-plastic boundary leads to the following relationships for (p_i).

$$p_i = p_o[(1-\sin\phi)(a/R)^{2\sin\phi/(1-\sin\phi)}] \pm a\gamma[(1-\sin\phi)/(1-3\sin\phi)][1-(a/R)]^{(3\sin\phi-1)/(1-\sin\phi)} \qquad 2.8$$

where: + for floor, - for roof and last term reduced to zero for springline.

In Eqn. 2.8, the parameter p_o is a function of R and varies at the roof, springline and floor as shown in Fig. 2.14b. Also, in Eqn. 2.8 it can be seen that the first term is primarily concerned with strength mobilization while the second term describes the effect of gravity within the plastic zone. This term is more significant in strain-weaking ground because less strength can be mobilized over the total extent of the plastic zone.

In the roof area the gravity acts against the internal pressure thereby increasing the internal pressure required to achieve equilibrium. Hence the gravity term is positive. In the floor area, gravity acts as a stabilizer and thus reduces the internal pressure. Hence the gravity term is negative. There is no gravity effect at the springline where the direction of the gravity is perpendicular to the radial pressure.

Integration of Eqn. 2.6 with known stress boundaries given by Eqn. 2.8 provides stress distributions at the roof, springline and floor. When these stress distributions are coupled with material deformation characteristics (Brown *et al.*, 1983), one can obtain separate ground convergence curves for the roof, springline and floor. These expressions for the GCCs depend on material properties and are quite lengthy. Formulations proposed by Ladanyi (1974) are considered in this thesis and details are given in Appendix B.5.

Fig. 2.15 presents a schematic plot of the pressure-displacement and pressure-extent of plastic zone relationships. Each GCC originates from its initial insitu stress state, i.e., the floor has the highest value. After an initial linear response it becomes non-linear with yield initiation. As the plastic zone increases, the gravity effect becomes dominant, reduces support stress at the floor and increases it at the roof. The floor may be left without support depending on soil strength. The same reasonings on the gravity effect can be applied to the p_i-R relationship (given by Eqn. 2.8) but the extent of plastic zone at the roof will stop when it reaches the ground surface at R=H.

Before the above technique is applied to determine the GCC, it is important to understand the limitations inherent in this method.

1. Simplifications have been made in the derivations of Eqn. 2.8. Based on the "hole-in-plate" theory, the equation is obtained from its own boundary stresses, independent of other boundary stresses as shown in Fig. 2.14b. In addition the assumption of $\tau=0$ is only valid along vertical axes at the roof and floor, and at a horizontal axis through the springline. This assumption leads to an overestimation of p_i at the roof, but an underestimation at the floor.
2. Eqn. 2.8 is formulated assuming a plastic zone of constant radius formed around the opening. The derivation of the p_i-u relationship follows the path (1) shown in Fig. 2.14. At excessive yielding, the support pressure distribution may result in a maximum at the roof and a minimum at the floor, which is in contrast to the assumed stress distribution in excavation simulation (stress-relief in a percentage of the original insitu stress). Hence the use of Eqn. 2.8 is restricted to a certain limited range of p_i values. This is further confirmed by the studies of the modes of yielding near tunnels. From Figs. 2.6 to 2.8, the mode of yielding with a continuous plastic zone is limited only to Regime J (Mode II). The area of this regime increases as H/a increases, implying that the proposed technique will yield better results for the

behaviour of deep tunnels.

3. It is of practical interest to find the extent of the plastic zone around the tunnel. For a rigid liner (Case 1), the plastic zone is fairly concentric, resulting in a differential support pressure between at the roof and at the floor. This unequal pressure may be transferred to the ground through shear at the support-ground interface. This shear effect will affect the shape of the GCC (Curtis, 1976), which is beyond the scope of this thesis. If flexible liners are used in tunnel supports, no bending action will be developed within the liner and symmetrically distributed support stress will result. This condition is similar to Case 2 in Fig. 2.15. Symmetrical support pressure distribution induces an egg-shaped plastic zone, i.e., large yielding occurred in the roof area.

From the above discussion, it can be seen that the application of the proposed technique (Mode II) is restricted by its inherent assumptions. Formulation of ground responses beyond the regime of Mode II requires techniques similar to Mode I (Fig. 2.9).

2.2.4.3 Vertical Settlement Profiles above Tunnel (Modes I and II)

Analytical prediction of the settlement profile above the roof is complicated by the proximity of the surface boundary. Finite element methods seem to provide the only approach to predict the displacement pattern around the tunnel, but several attempts using continuum mechanics have revealed that the surface settlements are normally underestimated, e.g., Atkinson and Potts (1977). Lo *et al.* (1984) used a semi-empirical approach to estimate the surface settlement and succeeded to predict the crown displacements using continuum mechanics. Because of these problems, a semi-theoretical approach supported by case histories is used here to predict the settlement profile above the crown.

So far discussed are the relationship between the crown convergence and support pressure. There exists also a similar relationship for the surface settlement, i.e., the surface settlement is governed by the crown settlement S_c and thus the internal pressure p_i. The p_i-S_c-S_s relationship is a steady changing function until kinematically possible collapse mechanism takes place (e.g., Point d, Fig. 2.9). The surface settlement beyond Point d increases abruptly and become excessive. A prediction of settlement after a collapse mechanism has been initiated is not dificult. Hence, the following analysis is concentrated only to states before collapse.

Considering only the vertical ground displacement at the ground surface, it is well established that the settlement profile may be represented by a Gaussian distribution curve of form (Fig. 2.16a)

$$S = S_s (\exp)[-(1/2)(x/i)^2] \qquad 2.9$$

where: i is the point of inflection.

For a given tunnel, the surface settlement profile (Eqn. 2.9) depends on p_i and S_c. Assuming the surface displacement profile outside a distance of w (between 2.5i and 3i, Cording *et al.*, 1976) remains uninfluenced by the progressive stress relief a relationship of S_s-i is derived by putting $S=S_o$ at x=w: (where $w=H(\cot\beta')+a$)

$$S_s/S_o = \exp\{1/2[(1+(H/a)\cot\beta')/(i/a)]^2\} \qquad 2.10$$

In Eqn. 2.10, the variable S_s is a measure of S_c or p_i, and the variable i is of the settlement profile. The parameter β' (approximately equal to β) defining the trough width is dependent on the mode of yielding or K_o as discussed earlier (Modes I or II).

Fig. 2.16b is a plot of normalized S_s versus i for H/a=3 to 10, ϕ=20° to 40° and β=70° to 80°. The β-values are extracted from Fig. 2.10 of Mode I. For shallow tunnels i decreases to a limiting value with a small increase in S_s, i.e., small crown displacement or stress relief causes the yield zone to propagate to the surface. At deep tunnels i also decreases with S_s, but at a slower rate. Fig. 2.16b indicates that the shape of the settlement trough for a given cohesionless ground is dependent on H/a and p_i (or S_c) as well. The ϕ parameter has less extent of influence.

It must be expected that Modes I and II display distinctly different and unique features in their settlement profiles because they represent different modes of yielding. Consider Modes I and II and allow a constant crown settlement

S_c in both cases (Fig. 2.17). If S_c is small, the extent of the yield zone is small. The vertical settlement profiles of Modes I and II are initially very similar, but the magnitude of settlement is larger in Mode I than in Mode II. Small displacement occurs in the elastic zone and large plastic straining within the yield zone (Fig. 2.17a and b). For excessive S_c (i.e., the yield zone reaching the surface), Modes I and II exhibit distinct differences in vertical settlement profile above the crown. In Mode I, two localized shear planes develop and the soil block displaces toward the opening as a rigid body. The soil block remains elastic so that the differential strain and displacement between the crown and the surface is small. Hence, the ratio of surface to crown displacement (S_s/S_c) is closer to and tends toward unity (Fig. 2.17d). In Mode II, a plastic zone develops around the opening and is surrounded by the elastic ground, the elastic zone area is small, and most of the straining will occur within the plastic zone. Thus, the settlement profile above the crown looks like the one plotted in Fig. 2.17b and the settlement ratio S_s/S_c must be much less than unity (Fig. 2.17d).

The shape of the surface settlement trough is defined by S_s and i. Eqn. 2.10 indicates a strong dependency between i and p_i (or S_c) which is shown diagrammatically in Fig. 2.17c. On this figure are also shown schematically two pairs of GCCs for a shallow and a deep tunnel, and S_c/a-i/a curves of Modes I and II for each tunnel. For the shallow tunnel the yield zones (Mode I-2 or II-1) will propagate to the surface with a comparatively small displacement. For Mode

I-2, i will displace toward the centre of the trough in a faster rate. The width of the settlement trough for Mode I must be related to the inclined angle β of the shear plane to horizontal (Fig. 2.10) and will be narrow for the shallow tunnel. For Mode II-1 the settlement trough will be wider because the strength mobilization and stress redistribution are distributed around the opening, instead of concentrated at localized zones. The inflection point will remain fairly stationary about at the initial state (i.e., no ear-shaped yield zone developed (Mode II)), and will decrease with progressive stress relief near collapse. Same reasoning is applicable to the deep tunnel. When the extent of yield zone around the tunnel is small, i for both modes may remain stationary. As the yield zones reach the surface, the i will drop significantly.

From Fig. 2.17d, the S_s/S_c ratio is fairly constant for Mode I, and seems to be almost independent of p_i. This is in contrast to Mode II where the S_s/S_c ratio is initially small and later increases with decrease in p_i. As the collapse mechanisms are approached the settlement ratio will tend toward unity for both cases, but at a faster rate for Mode I.

From the above analysis, if the same displacements are allowed in tunnel construction larger surface settlement and a narrower trough will be induced in Mode I than in Mode II. Ground with low K_o imposes more difficulties in ground controls than ground with K_o close to unity.

2.2.5 Numerical Examples (FEM)

2.2.5.1 Approach

Numerical examples generated by the finite element method are used to understand the tunnel behaviour and to investigate the applicability and validity of the proposed technique described in the previous section. Eight analyses were performed and the input data for each case are listed in Table 2.1. The behaviour of purely cohesionless and cohesive soils were investigated. For cohesionless soil, one set of typical soil parameters and a range of K_o-values from 0.5 to 1.3 were chosen to observe the effect of K_o on the yield zone localization. Behaviour near shallow and deep tunnels was studied by varying the free surface boundary parameter, H/a. It is important to realize that the cohesionless model with the assumed associated flow rule predicts larger dilation and displacement than the real soil model of non-associated flow rule. For the cohesive soil, only shallow tunnel behaviour was considered. For simplicity, the unconfined compression strength of the ground was assumed to be constant with depth and thus the K_o-value had to be set to unity. It was assumed that the excavation process could be simulated by proportional unloading of the original insitu stress (denoted by P* in Table 2.1). A case of an air-pressurized tunnel (Case AP1, Table 2.1) was studied by applying a uniform internal pressure to the periphery of the tunnel opening.

The finite element program SAFE, developed by Chan (1985), was used for all analyses. Fig. B.3 shows the finite element mesh for H/a=18, composing of 8-node quadrilateral iso-parametric elements outside the tunnel and 6-node triangular iso-parametric elements inside the tunnel. Zero lateral displacements are imposed along the two sides and zero vertical displacements at the bottom boundary. For H/a=5, the same mesh was used, but elements at the four top rows were deleted. Each analysis involved the following steps:

1. Apply gravity stress by switch-on-gravity method, i.e., $\sigma_v=\gamma y$, $\sigma_h=\nu/(1-\nu)\gamma y$,
2. Amend the Poisson's ratio, ν to a constant value.
3. Remove elements inside the tunnel and reinstate the initial insitu stress by applying equivalent nodel forces so that no displacemnts are induced.
4. Simulate the excavation process by reducing the nodal forces around the periphery of the tunnel in increments.
5. Continue step (4) until no numerical convergence in equilibrium iteration is possible for stress relief increments of 0.1% of insitu stress.

2.2.5.2 Results

Modes of Yielding

The extent of the yield zones at intermediate and final stress levels are plotted in Figs. 2.18 to 2.22 for eight cases. Table 2.2 summarizes the mode of initial yielding, the mode of yielding propagation, the applied stress at the yield initiation and at the last step (expressed in % of insitu stress). Some of these results are plotted in Figs.

2.7 to 2.8 for comparison, and they agree well with the predictions. Several important aspects on mode of yielding near tunnel are confirmed by these results of the finite element analyses:

(a) Cohesionless Soil (Figs. 2.18 to 2.21)

1. For K_o<1.0, yield initiation occurs at the springline. Depending on K_o, these localized yield zones at the springline develop into (1) localized lobes at both shoulders (K_o=0.5) or (2) continuous plastic domain around the opening (K_o=0.82). Fig. 2.18a (H/a=5.0 and K_o=0.5) shows the propagation of localized zones at the shoulder toward the free surface. On Fig. 2.18b (H/a=5.0, K_o=0.82), it can be seen than two ear-shaped lobes start to emerge from the continuous plastic domain, indicating the development of yield zone localization (Mode II-1). For K_o=1.3, yield zones are initiated at the roof and floor (Mode III) and merge to form a continuous zone.

   Yielding is observed near the ground surface. This is explained by the fact that Mohr circles of elements near the surface are ill-defined because of small overburden pressure. Small stress changes could induce yielding. This problem is one of numerical inadequacy of finite element analysis.

2. The influence of the free surface boundary on the yield zone can be observed by comparison of results of analyses of shallow and deep tunnels. For deep tunnels, the shape of plastic zones is symmetrical about the

horizontal tunnel axes. In shallow tunnels, the free surface has a tendency to displace downward, which accelerates the yielding process at the roof. Thus at equal percentage of stress-relief, the extent of the plastic zone at the roof is greater in shallow than in deep tunnels.

3. From Fig. 2.20 (Case AP1), it can be observed that the boundary stress around the periphery of the tunnel has a significant influence on the mode of yielding. Initially, application of a uniform pressure equivalent to overburden pressure (at the level of tunnel axis) induces yielding at the roof and floor. At 60kPa yielding occurs only in the roof and floor, and after a further pressure reduction to 20kPa (20% of overburden) the mode of yielding is similar to Case ST1. However, the extent of the yield zone at comparable stress level is much reduced. This finding is of great practical signifance. Most excavation modelers simulating pressures neglect this important aspect. It is also extremely important for back analysis or interpretation of field measurements.

4. From Fig. 2.7 it can be seen that the roof collapse mechanisms are dominant in the six FEM cases. Thus the minimum support stresses are the p_{ic} (upper bound solution). The required p_{ic} for roof collapse are calculated: 8% and 3% of overburden pressure at tunnel axis for H/a= 5 and 18 respectively. Comparisons between the applied stress at the last step (Table 2.1) and

p_{ic} imply that the tunnels are still far away from the kinematic collapse state. However, severe problems have been encountered at this stage in modelling, indicating the limitation of the FEM in exploring the limit state of this particular geomechanical system.

b) Cohesive Soil (Fig. 2.22)

1. For both cases (STC1 and STC2), under $K_o = 1.0$ localized yielding initiates at the floor and develops into a continuous zone around the tunnel propagating downward rather than toward to the free surface. This response is a result of the method by which the stress is relieved at the periphery of the tunnel.
2. The tunnel in ground with higher strength (Case STC 2) remains stable without any support. For Case ST1 the yield zone reaches the surface at 40% support stress. Fig. 2.22 shows that the configuration of the yield zone is influenced by the free surface, i.e., the shape of the yield zone is no longer circular. Various kinematically possible collapse mechanism could occur within the extensive yield zone. Davis *et al.* (1980) studied such possible collapse mechanisms of shallow tunnels in cohesive material and derived solutions of collapse loads using the upper bound theorem of plasticity. The collapse load for Case STC1 was calculated: 38% of insitu stress which is close to that from the FEM.

Stress Distribution (Figs. 2.23 and 2.24)

Fig. 2.23 shows the tangential and radial stress distributions above the roof for a shallow tunnel (H/a=5) under K_o=0.5 and 0.82 (i.e., cohesionless cases ST1 and ST2). For both cases, an increase in tangential stress is observed, denoting arching developed at the roof due to stress-relief inside the tunnel. The equivalent coefficients K_r, defined in Section 2.2.4 were calculated: K_r=0.81 for K_o=0.5 at 65% stress-relief, and K_r=1.31 for K_o=0.82 at 75% stress-relief. These K_r values compare well with those given by Eqn. B.8. implying that the earlier assumption of equal amount of stress redistributed to the roof and floor is valid.

For K_o=0.5, the mobilized tangential-radial stress difference is much less than the soil capacity and the soil above the crown remains elastic. However, for K_o=0.82, yielding has occurred and the tangential stress decreases to cope with the decrease in radial stress in order to satisfy the failure criterion.

Similar reasonings are applicable to cohesive soils, Cases STC1 and STC2 (Fig. 2.24). The K_r values calculated are: 1.38 for STC1 (60% stress-relief) and 1.62 for STC2 (unsupported), and they compare well with the predicted values given by Eqn. B.8. The tangential-radial stress difference within the plastic zone is governed by the unconfined compressive strength of the soil which is independent of overburden pressure.

Interpretation of K-values above the Roof (Terzaghi ,1943)

It is interesting to observe the horizontal to vertical stress ratio K along the depth above the roof. For K_o=0.5 (at 65% stress-relief) the K-value is close to unity above 3.0m depth and increases to 2.0 at the crown. For K_o=0.82 (at 75% stress-relief) the K values from 1.5 to 3.0.

Terzaghi (1943) derived a solution for the vertical stress distribution above a tunnel in cohesionless soil using the soil arching theory, and recommended that the K-value should be approximately unity. Hence, Terzaghi's case follows closely with Case ST1 (K_o=0.5). However, the K-value also depends on the amount of stress-relief or the displacement. Thus Terzaghi's case is only valid for a special case of tunnel behaviour.

Ground Responses (GCC)

Ground responses at the roof (Rf), springline (Sl) and floor (Fl), expressed in GCCs of normalized fictitious support stress versus normalized displacements, are shown in Figs. 2.25 to 2.28 for all eight cases.

For all cases except AP1, the ground initially responds to elastic unloading, and the displacement is proportional to the amount of stress-relief. For K_o=0.5 and 0.82, the amount of stress relief at the floor is greater than at the roof and springline, and thus the slope of the convergence curve is initially steeper for the floor. However, once yield zones are developed, the plastic deformation starts to dominate. Once yielding occurs, the support stress at the roof will remain fairly constant with a further increase in displacements. Similar reasoning can be applied to the cases with K_o=0.82 and 1.3.

The ground responses for Case AP1 (uniform internal pressure) are very different. The wall at the springline first displaces outward and then starts to converge as the uniform pressure decreases. The responses at the roof, springline and floor are almost linear even though plastic zones are formed first in the roof and then near the springline and the shoulders. This shows clearly that the approach of application of a constant fictitious p_i in simulation of excavation does not lead to a reasonable solution of ground response for K_o different from unity.

For case ST2 where K_o is close to unity, Eqns. 2.6 to 2.8 can be used to approximate the p_i/p_o-u/a relationship (Mode II). The results are plotted on Fig. 2.25 for comparison. These predicted values fall reasonably close to those of the FE analyses. The discrepancies can be attributed to the fact that Eqns. 2.6 to 2.8 assume Ko=1.0 and different stress boundary condition. A similar comparison for a deep tunnel (H/a=18, Fig. 2.27) shows that the gravity effect becomes less dominant, i.e., the three predicted GCC (roof, springline and floor) are close together.

The FEM only provides the results for the initial portion of the GCC up to the applied stress levels stated in Table 2.2. The subsequent portion of the GCC, where localization processes and transition to collapse modes dominate, cannot be currently predicted analytically. However, it is possible to estimate the required support stress for several states

(p_{ys}, p_{ic} and p_{fc}) which are of practical interest. These support pressures p_{ys}, p_{ic} and p_{fc} were calculated for each case and are listed in Table 2.2.

For the two cases with cohesive soil (Fig. 2.28), Eqns. 2.6 to 2.8 (with cohesive strength criteria) are used to calculate the predicted GCC. The predicted response corresponds well with those calculated by FEM for the stable case of STC2. It is interesting to note that for this case the GCC of the floor are higher than those of the springline and the roof. With proportional unloading greater deviatoric stresses are induced at the floor than at the roof and springline. This causes a deeper plastic zone and larger deformation at the floor because the strength of the cohesive soil is independent of confining pressure. From a comparison with Case STC1, agreement is only observed initially up to u/a<0.4% because the plastic zone influenced by the free surface is no longer circular. The GCC for the roof becomes horizontal, indicating that the collapse mechanism is approached. Eqns. 2.6 to 2.8. do no longer apply. The calculated collapse load of 38% is , however, close to the applied stress at the last step (40%). Despite these discrepancies it can be concluded that the models proposed earlier can be applied to predict the ground behaviour with reasonable accuracy.

Ground Deformation near the Tunnel

Displacement vectors around the tunnel are plotted in Figs. B.4 to B.8 for all eight cases (Appendix B). The directions of these vectors are influenced by the insitu stress state K_o and the proximity of the free surface boundary H/a. For low K_o values, radial displacements toward the openings are clearly restricted to areas above the roof, and below the floor. Near the springline, soil elements immediately adjacent to the opening exhibits inwards movements, but elements at about one radius away from the wall are not influenced much by the stress relief. For K_o close to unity, radial displacements are distributed evenly around the tunnel to a distance of about four radii from the wall. This implies that this can be approximated by the "hole-in-plate" model.

One feature of practical importance commom to Figs. 2.25 to 2.28 and B.4 to B.8 is the overall configuration of wall convergence. For K_o<1.0, initial unloading induces larger displacements at the roof and floor than at the springline. But after yielding has initiated, the plastic deformation at the springline becomes dominant and the displacements at the springline are larger than those at the roof and springline. If a liner is installed at this stage and deformed according to the configuration of wall convergence as those shown in Fig. B.4, tension will be induced at the inner face of the liner at the springline. This is in contrast to the results of conventional continuum design method, like the relative stiffness method. In these methods (Muir-Wood, 1975; Einstein and Schwartz, 1979), the liner will displace inward at the roof and floor and outward at the springline for (K_o<1.0). This causes compression instead of tension at the inner face of liner at the springline. Hence, for the determinaton of thrust and bending moments in a liner, one has to consider not only the initial external stress distribution but also the configuration at the time of liner installation.

From Figs. B.4 to B.8, it is of interest to observe that Case AP1 has a unique displacement field around the tunnel. Even at large stress relief, the magnitude of displacement is much smaller than for the other cases. The technique of simulating stress relief not only affects the extent of the yield zone but also dominates the ground displacements.

Settlement Profile above the Tunnel

Subsurface settlement profiles above the crown for various stress-relief levels are plotted in Figs. 2.29 to 2.32 for all eight cases and should be compared closely with the schematic Fig. 2.17.

For shallow tunnels in cohesionless soil (Cases ST1 and ST2), two distinct profiles can be identified. For Mode I (ST1) where localized yield zones form and the soil block above the roof does not yield, the differential settlement with depth is only due to the elastic deformations, and is small. Thus, the vertical displacement increases only slightly and gently with the depth (Fig. 2.29a). In Mode II where the opening is surrounded by a continuous yield zone, the settlement increases gently in the elastic zone and accelerates rapidly within the plastic zone (Figs. 2.29b and 2.30a). An abrupt change in settlement gradient can be observed at the elastic-plastic boundary (at

p_i=25%).

For deep tunnels (Cases DT1 and DT2) the settlement profiles are similar because the extents of the yield zone for both cases (K_o=0.5 and 0.82) are relatively small. However, at equal stress relief (say 40%) larger settlements are experienced in Case DT1 (K_o=0.5).

The behaviour is less well defined for the cohesive soils (Fig. 2.32) because the numerical model assumed that no volume change is associated with plastic deformation. However, it is interesting to observe (Fig. 2.32a) that a decrease of support stress from 50% to 40% induces a sudden, almost constant, increase in vertical displacement indicating initiation of a collapse mechanism ("plug" failure).

The relationship between surface settlement (S_s) and crown settlements (S_c) at intermediate stress-relief levels are plotted in Fig. 2.33 for all cases. Fig. 2.33 confirms the earlier discussion on the slopes of S_s/S_c for Modes I and II. It is greater for Mode I than for Mode II. Fig. 2.34 shows the relationship between the settlement ratio S_s/S_c and the stress ratio p_i/p_o. From Fig. 2.34, it can be seen that S_s/S_c is a function of p_i/p_o, especially for cohesive soil of low strength. However, for the range of support pressure typically encountered in the field, the S_s/S_c can be reasonably assumed to be constant with p_i/p_o. Atkinson and Potts (1977) observed in model tests that the S_s/S_c is independent of p_i/p_o and only a function of soil properties.

Surface Settlement

In tunnel design, one is concerned with not only the maximum surface settlement but also the differential settlement, i.e., the gradient at the inflection point and the trough width. Figs. 2.35 to 2.37 show the surface settlements profiles for all cases. At a given stress-relief level, Case ST1 is the most critical with the largest total settlement and the narrowest trough. The large settlement is due to a low K_o, i.e., low tangential arching to resist downard movement. The narrow trough can be attributed to the formation of two near vertical yield zones which restrict the downward movement of the soil block above the roof. As K_o increases, the tangential arching above the roof increases. Also, the development of localized yield zone is suppressed and Mode II takes places resulting smaller settlement above the tunnel and wider trough. For K_o=1.3 (Case ST3), the surface settlement is negligibly small because of high arching. For deep tunnels, the free surface boundary is less influenced by the tunnel, i.e., the trough is wider and gradient is gentler (Fig. 2.36).

It is of practical interest to observe the surface settlement profile of Case AP1 (Fig. 2.35), which is similar to a case of an air-pressurized tunnel. The effect of uniform pressure inhibits the propagation of the localized yield lobes to the surface and thus reduces the surface settlement significantly even at relatively low support pressure levels. This demonstrates that application of air pressure (constant p_i) is very beneficial for the two purposes of controlling the displacement distribution and the extent of the yield zone. Excellent field measurements that support these conclusions were presented by Kovari *et al.*, 1979.

Analysis No.	Soil Model	Soil Properties ϕ (deg.)	q_u (kPa)	E (MPa)	γ (kN/m3)	ν	Ko	H/a	Stress -relief
ST1	Perfectly Elastic-Plastic, Associated, Flow Rule, Mohr-Coulomb	30	0 (constant with depth)	40	20	0.4	0.5	5.0	P•
ST2	as above	30	0 (constant with depth)	40	20	0.4	0.82	5.0	P•
ST3	as above	30	0 (constant with depth)	40	20	0.4	1.3	5.0	P•
AP1	as above	30	0 (constant with depth)	40	20	0.4	0.5	5.0	U•
DT1	as above	30	0 (constant with depth)	40	20	0.4	0.5	18.0	P•
DT2	as above	30	0 (constant with depth)	40	20	0.4	0.82	18.0	P•
STC1	Perfectly Elastic-Plastic, Von Mises	0	30 (constant with depth)	40	20	0.495	1.0	5.0	P•
STC2	Perfectly Elastic-Plastic, Von Mises	0	60 (constant with depth)	40	20	0.495	1.0	5.0	P•

P - excavation simulated by unloading proportional to insitu stresses
U - excavation simulated by unloading in uniform pressure

Table 2.1 Input Data for FE Analyses (Tunnel)

Analysis No.	H/a	Ko	Initial Yielding at	Yielding Propagation	Applied Stress at last step	Type of Mode
ST1	5	0.5	Sl (81%)		35%	I-2
ST2	5	0.82	Sl (56%)		25%	II /II-1
ST3	5	1.3	Rf/(62%)		26%	III
AP1	5	0.5	Rf/Fl(80kPa)		20kPa	I-1
DT1	18	0.5	Sl (76%)		35%	I-1
DT2	18	0.82	Sl (57%)		25%	II / II-1
STC1	5	1.0	Fl (85%)		40%	II
STC2	5	1.0	Fl (66%)		0%	II

Note: Sl-springline, Fl-floor, Rf-roof
Stress-relief and collapse load expressed in % of insitu stress

Table 2.2 Summary of FE Analyses (Tunnel)

Table 2.3 Summary of p_{ys}, p_{ic}, p_{fc} (Tunnel)

Cases	Pys	Pic	Pfc
ST1 (H/a=5, Ko=0.5)	24 %	8 %	67 %
ST2 (H/a=5, Ko=0.82)	-	8 %	61 %
ST3 (H/a=5, Ko=1.3)	-	8 %	-
AP1 (H/a=5, Ko=0.5)	14kPa	8kPa	67kPa
DT1 (H/a=18, Ko=0.5)	-	3 %	67 %
DT2 (H/a=18, Ko=0.82)	-	3 %	41 %
STC1 (H/a=5, Ko=1.0, qu=30)	-	-	38 %
STC2 (H/a=5, Ko=1.0, qu=60)	-	-	-

Note: Support pressures at roof Pys, Pic and Pfc are expressed in % of overburden pressure to tunnel axis except for Case AP1

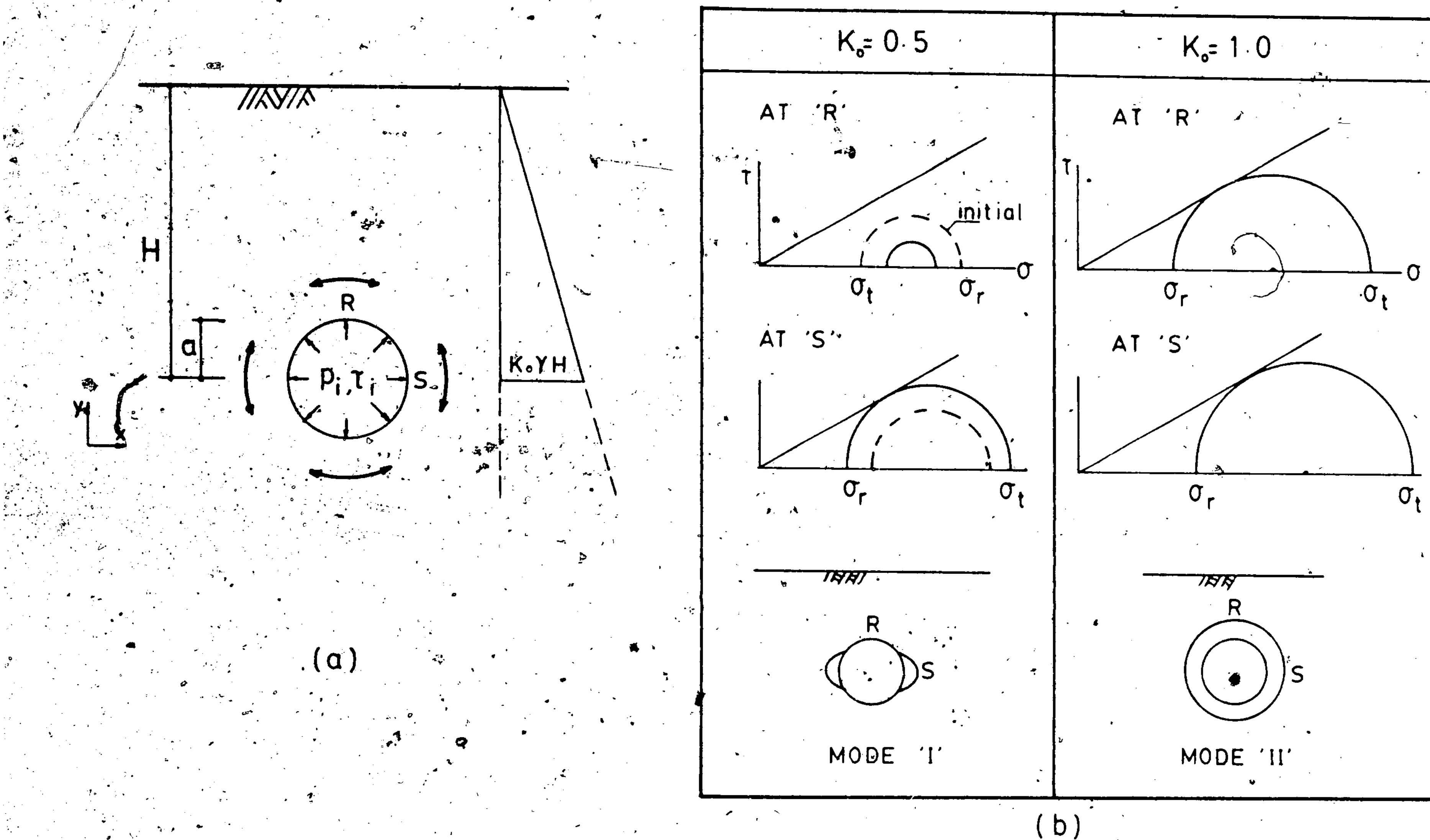

Figure 2.1 Modes of Yield Initiation

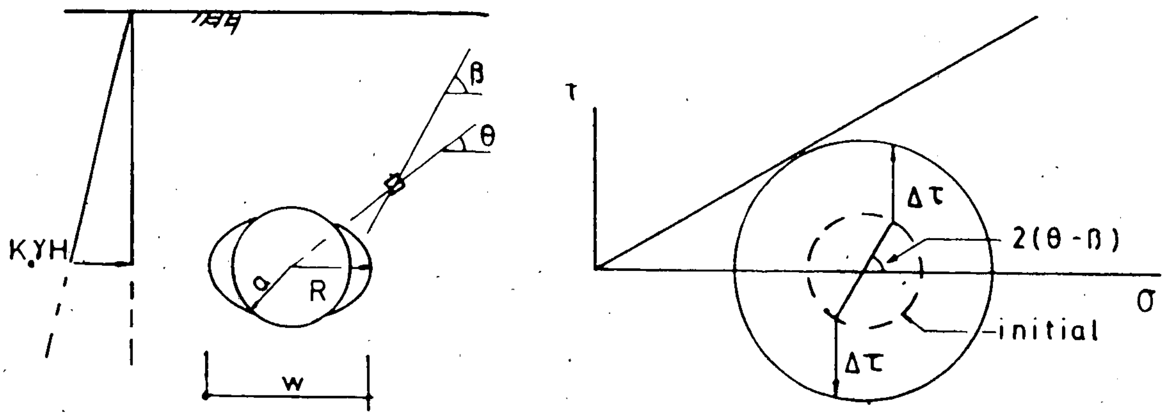

MODE 'I' (K_o=0.5)

(a)

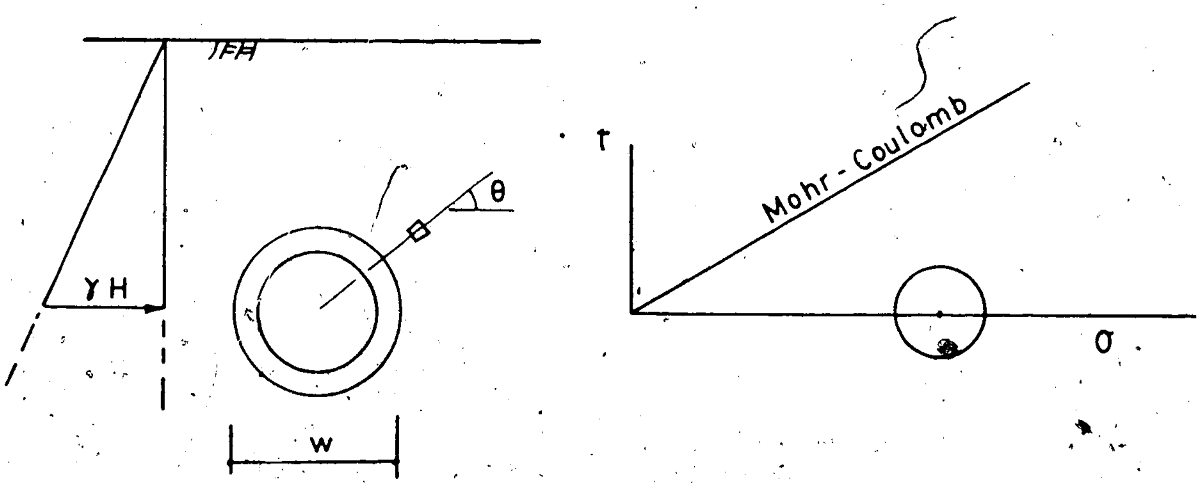

MODE 'II' (K_o =1.0)

(b)

Figure 2.2 Propagation of Yield Zone

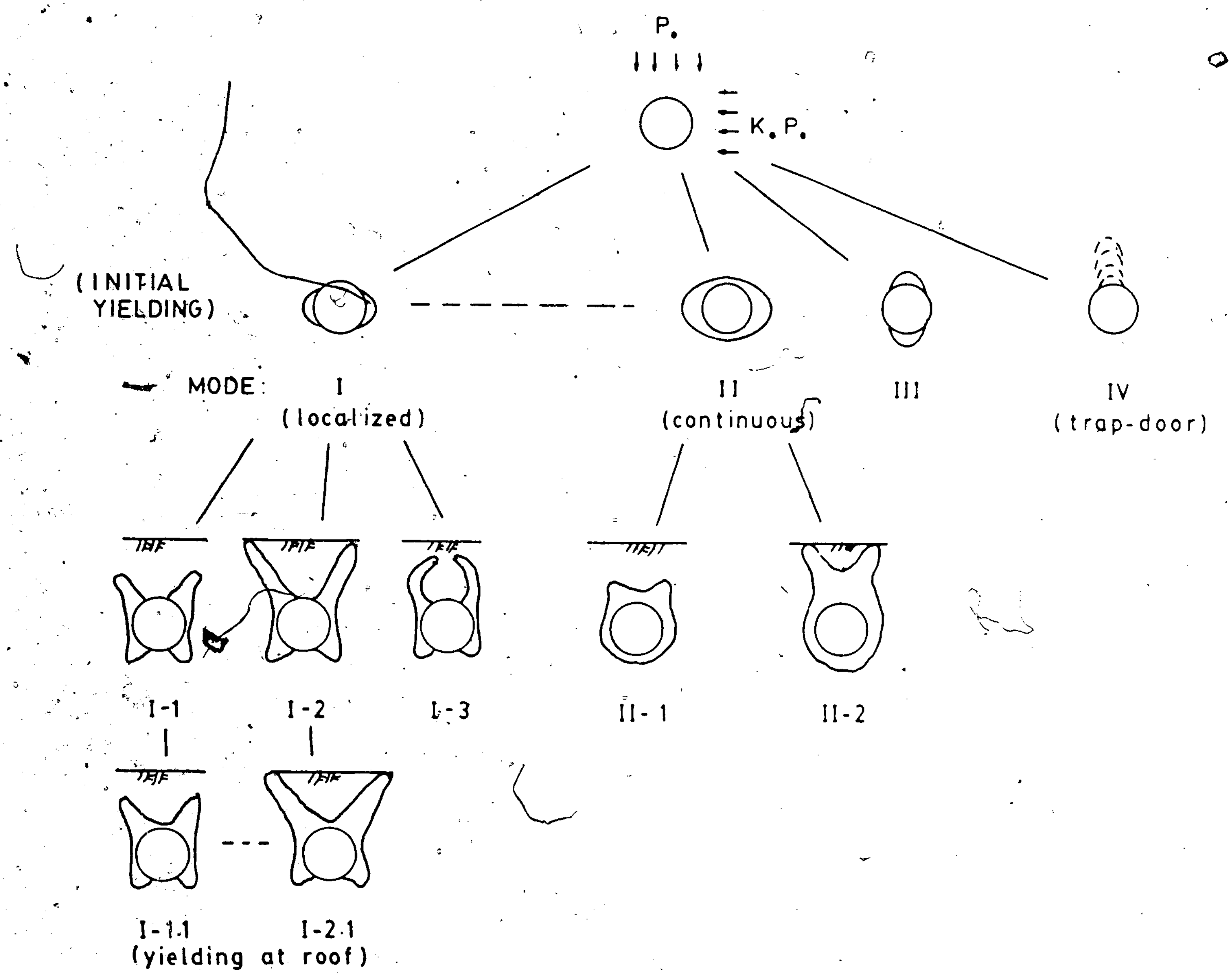

Figure 2.3 Possible Modes of Yielding near a Tunnel

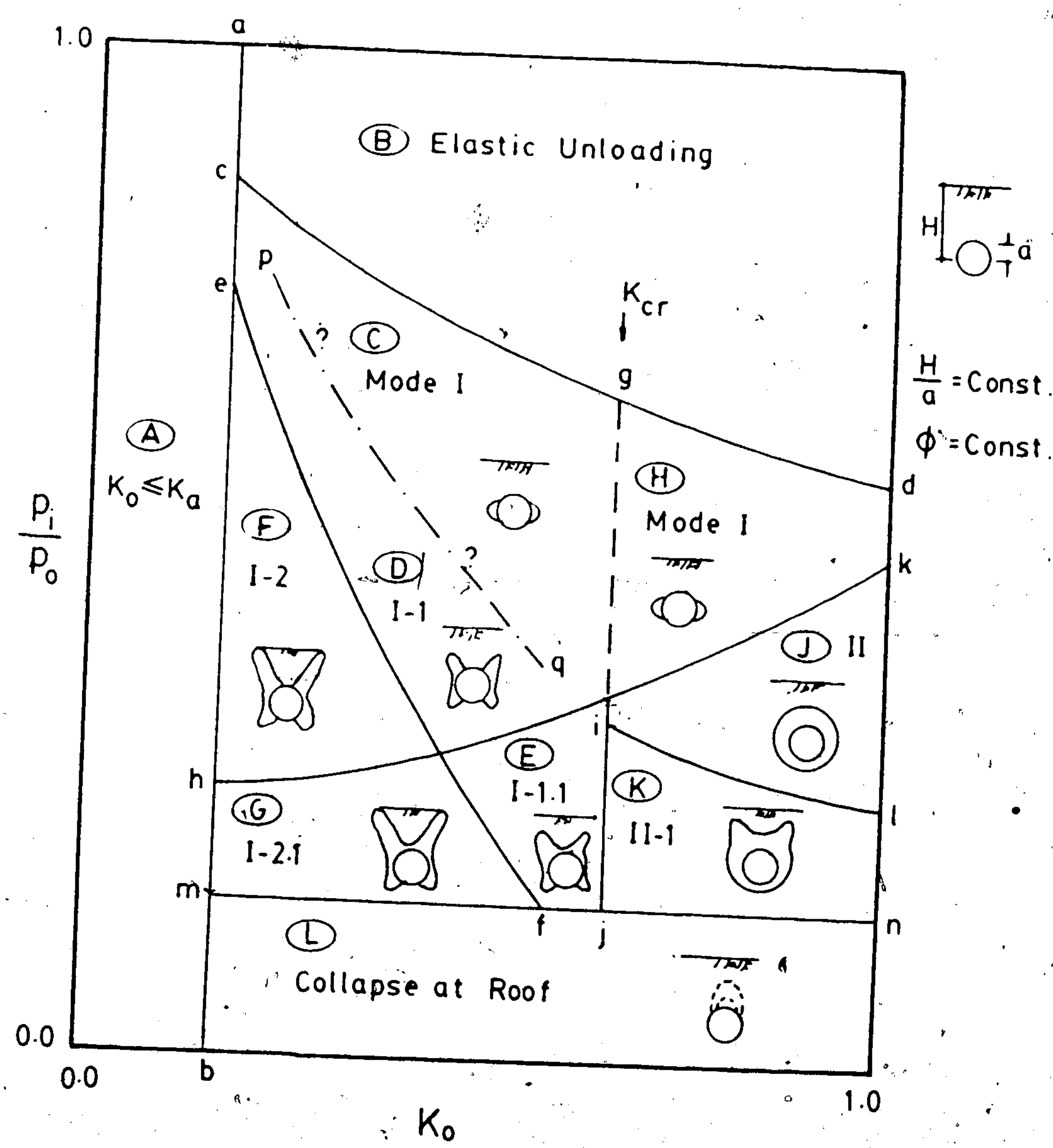

Figure 2.4 Modes of Yielding near a Tunnel

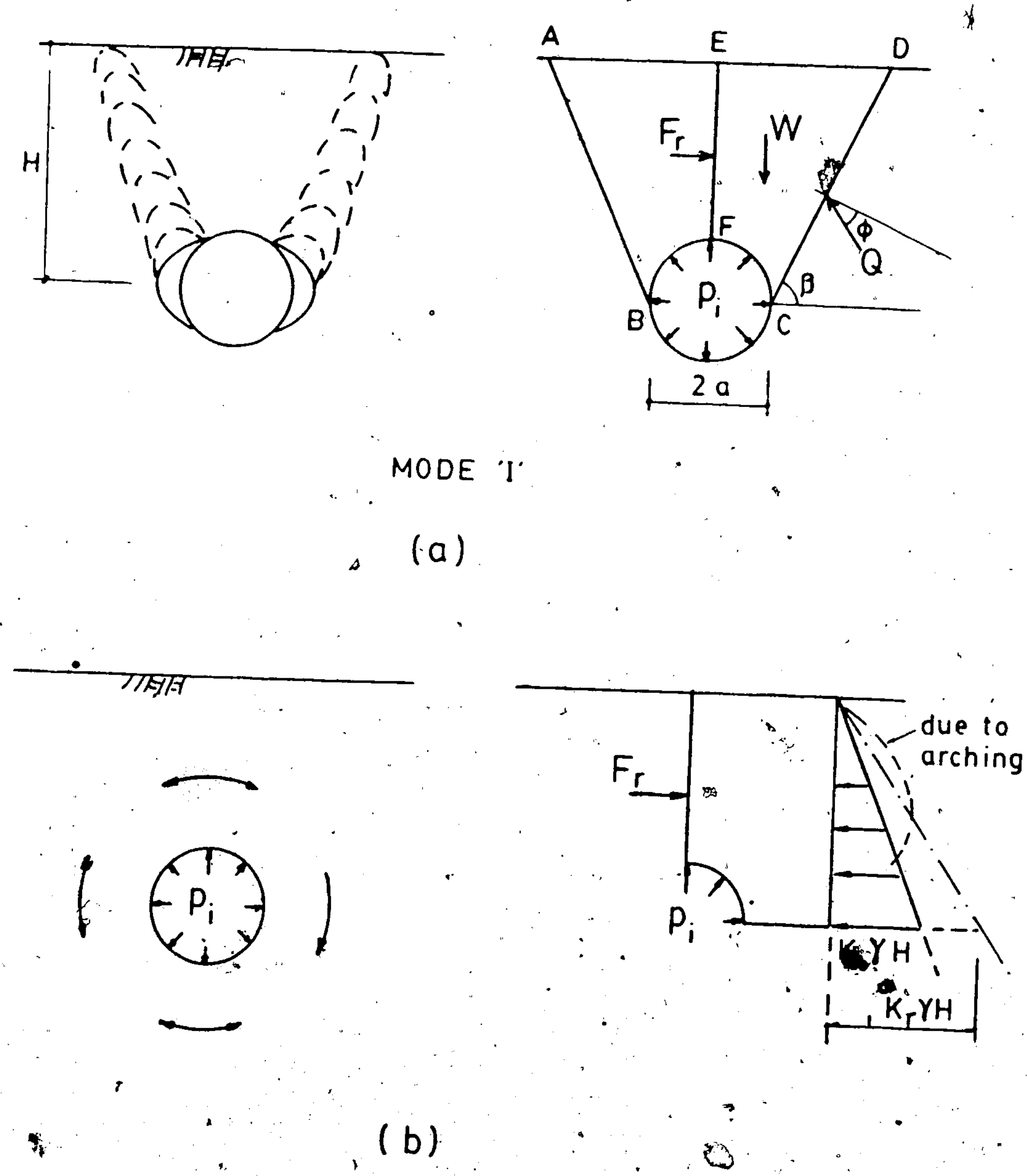

Figure 2.5 Mode I

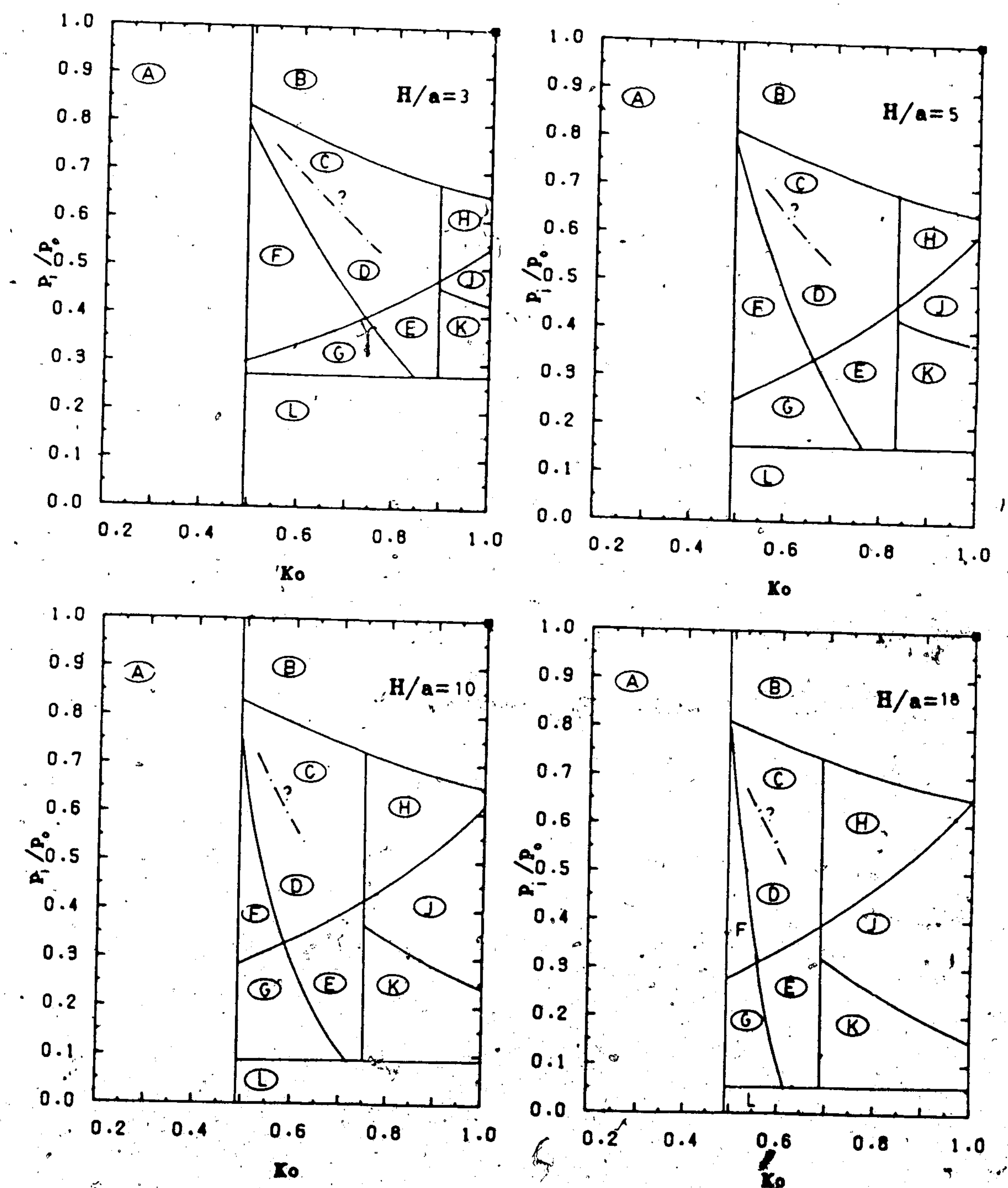

Figure 2.6 Modes of Yielding near a Tunnel ϕ=20°, c=0

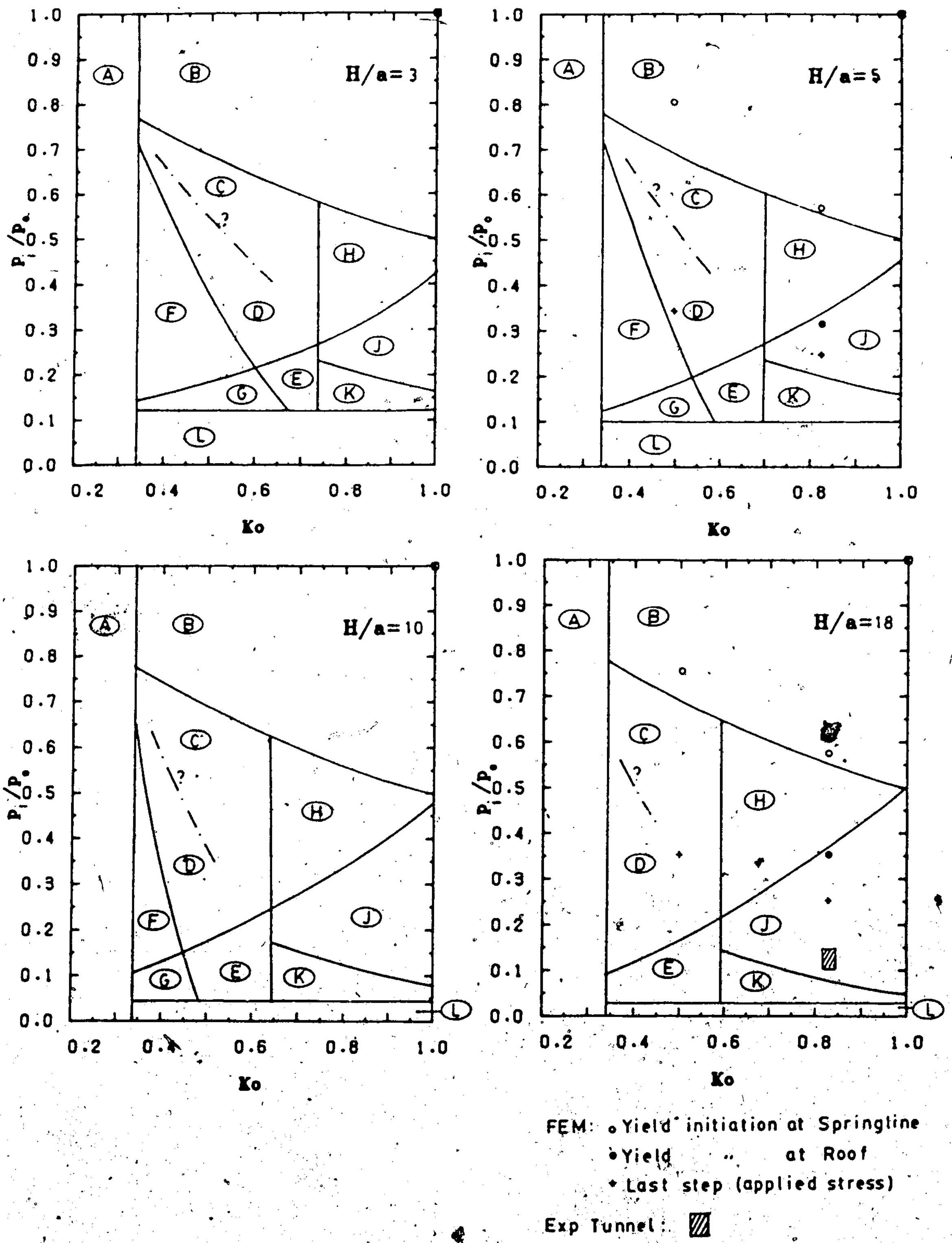

Figure 2.7 Modes of Yielding near a Tunnel ϕ=30°, c=0

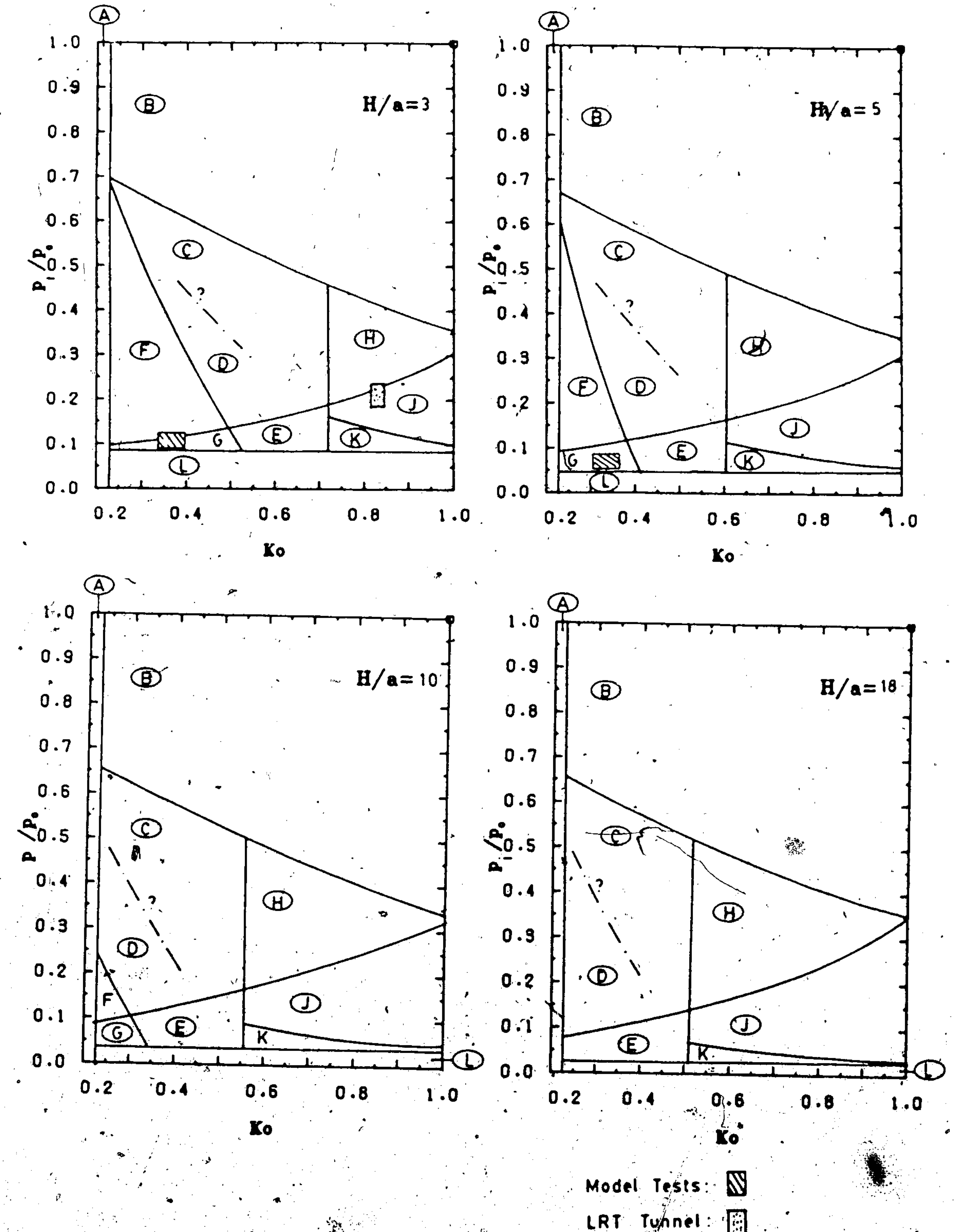

Figure 2.8 Modes of Yielding near a Tunnel $\phi=40°$, c=0

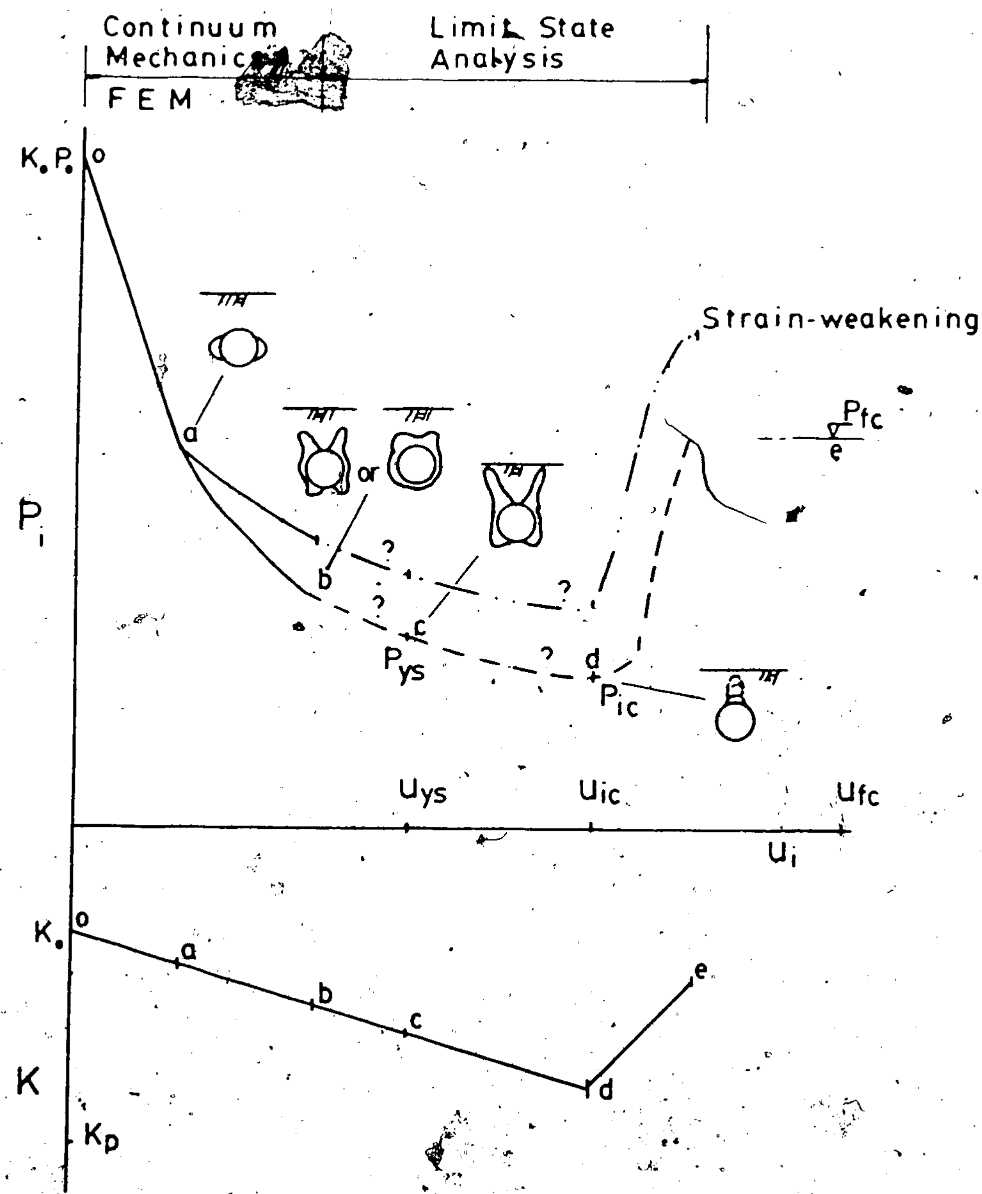

Figure 2.9 Formulation of GCC (roof) for Modes I and II

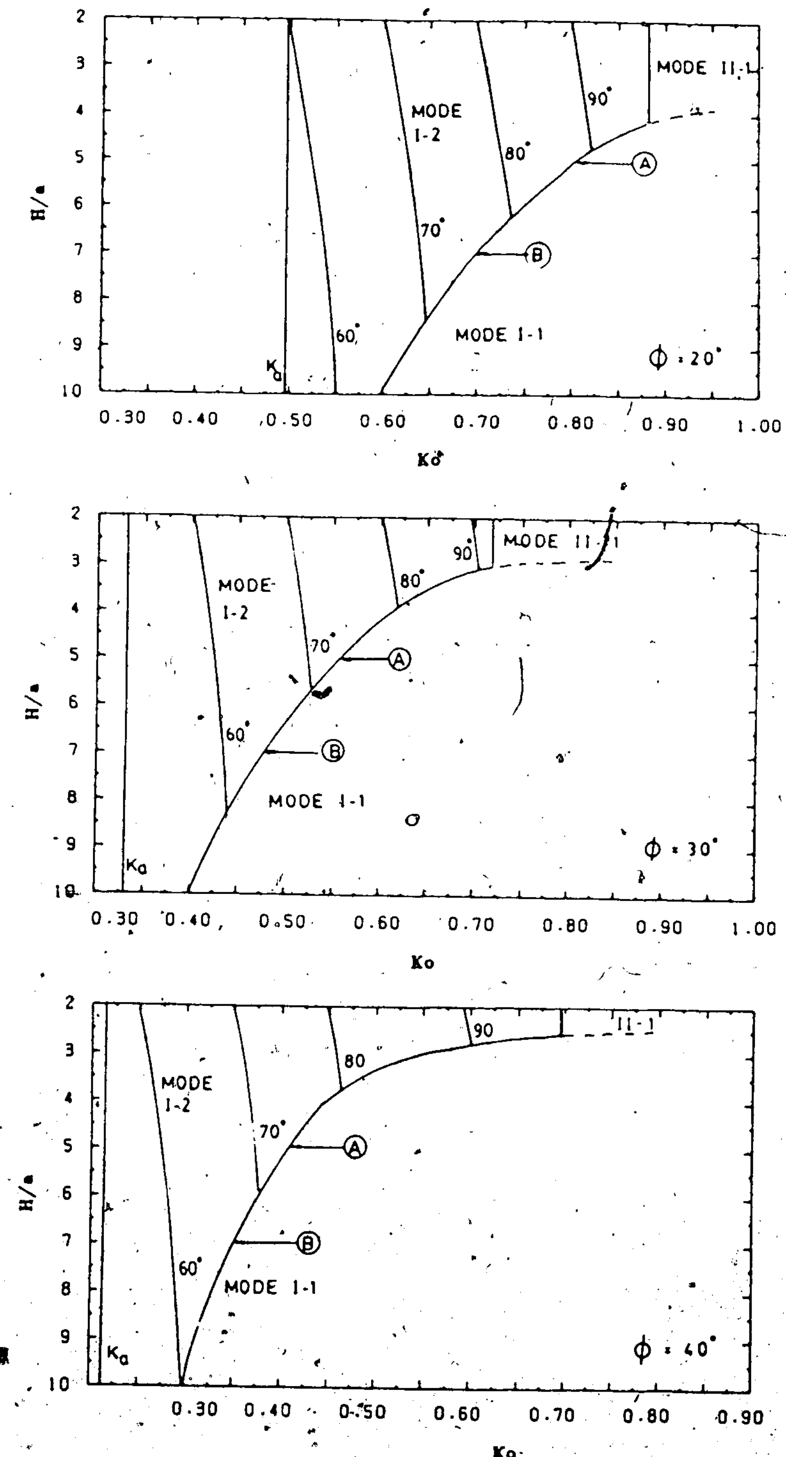

Figure 2.10 Direction of Propagation of Yield Zone (Mode I)

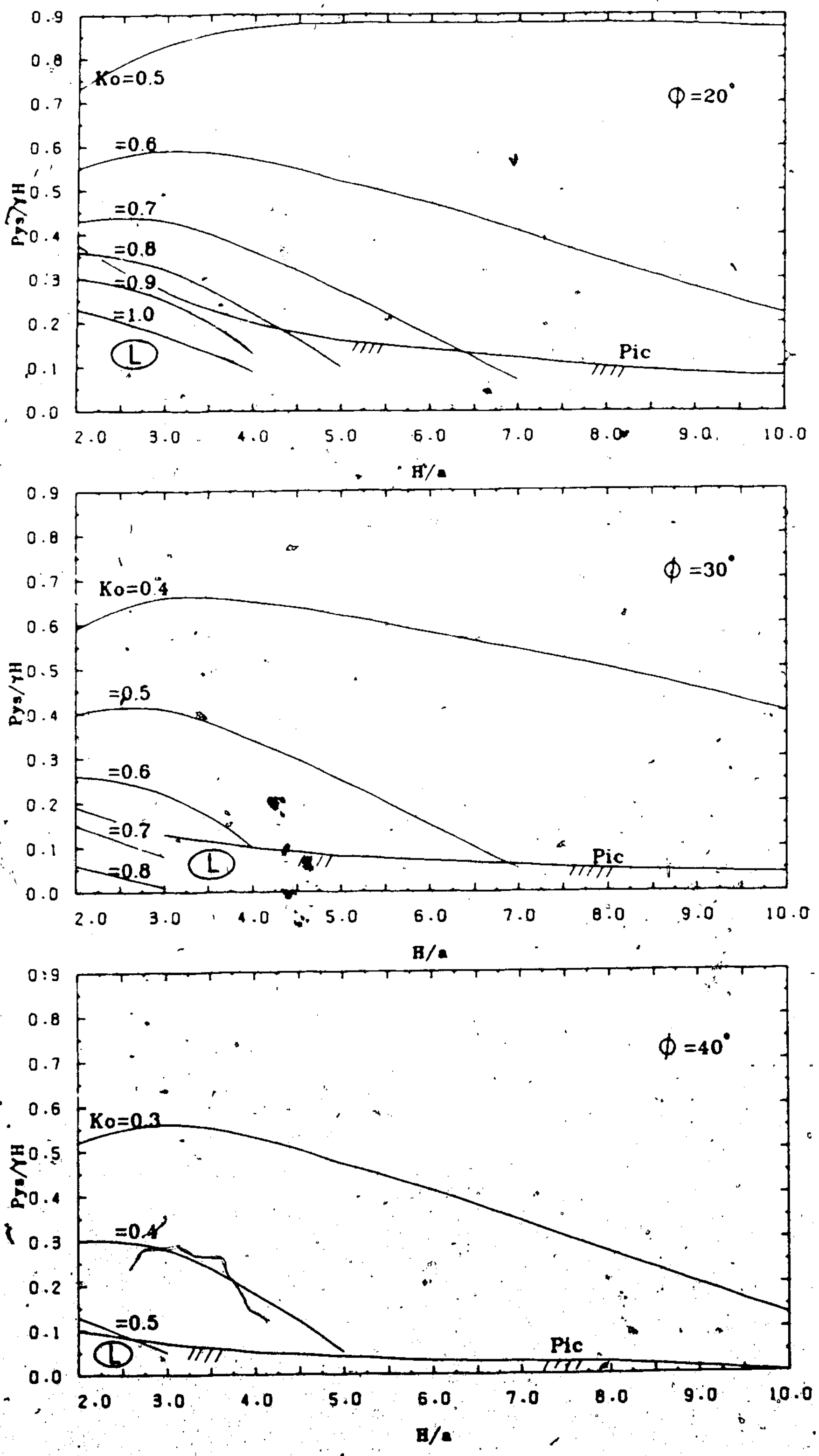

Figure 2.11 p_{ys} (and p_{ic}) as function of H/a and ϕ

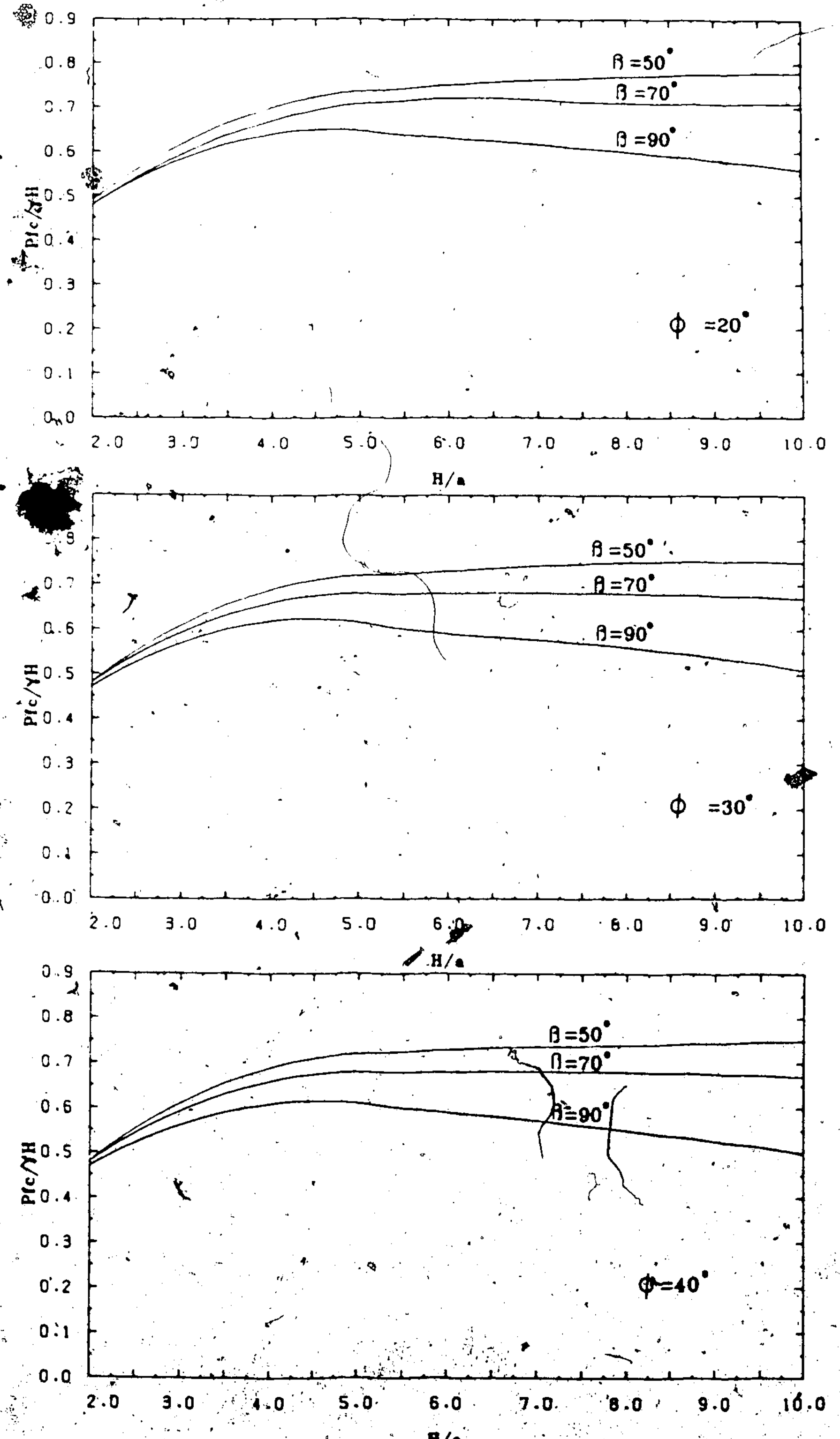

Figure 2.12 p_{fc} as function of H/a and ϕ

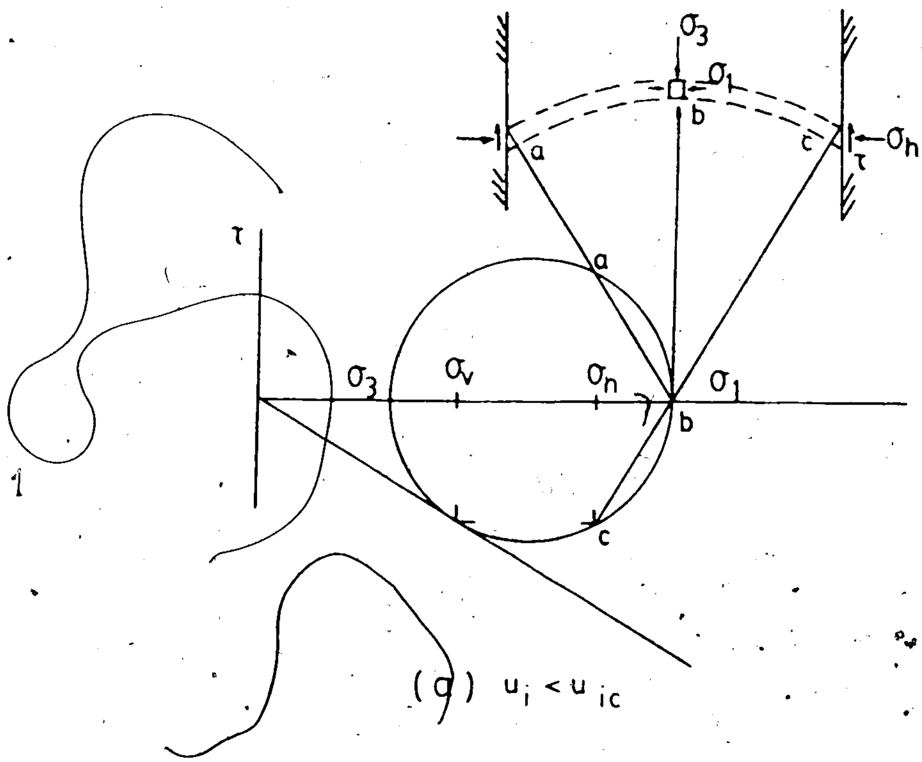

(a) $u_i < u_{ic}$

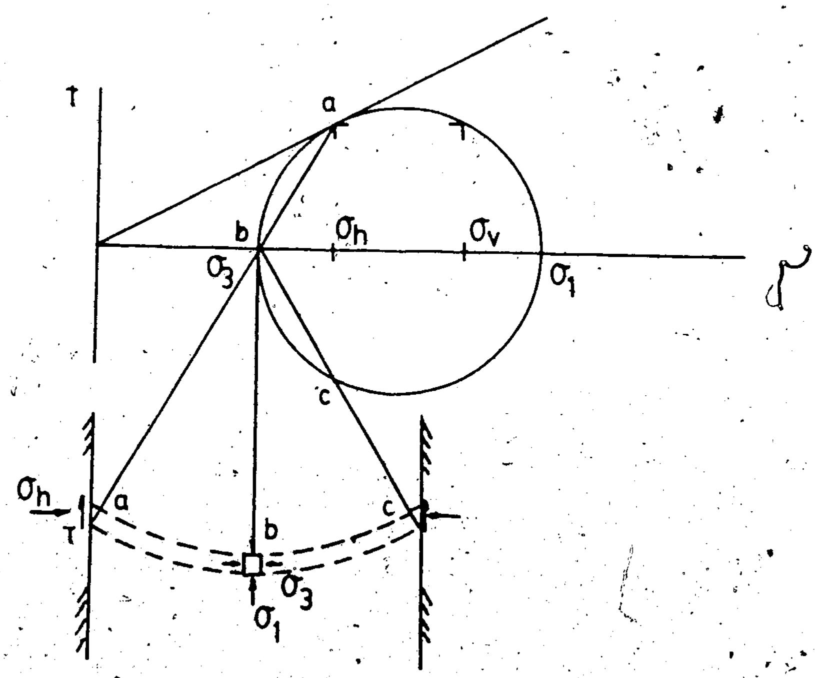

(b) $u_i > u_{ic}$

Figure 2.13 Types of Arching (a) Convex and (b) Inverted

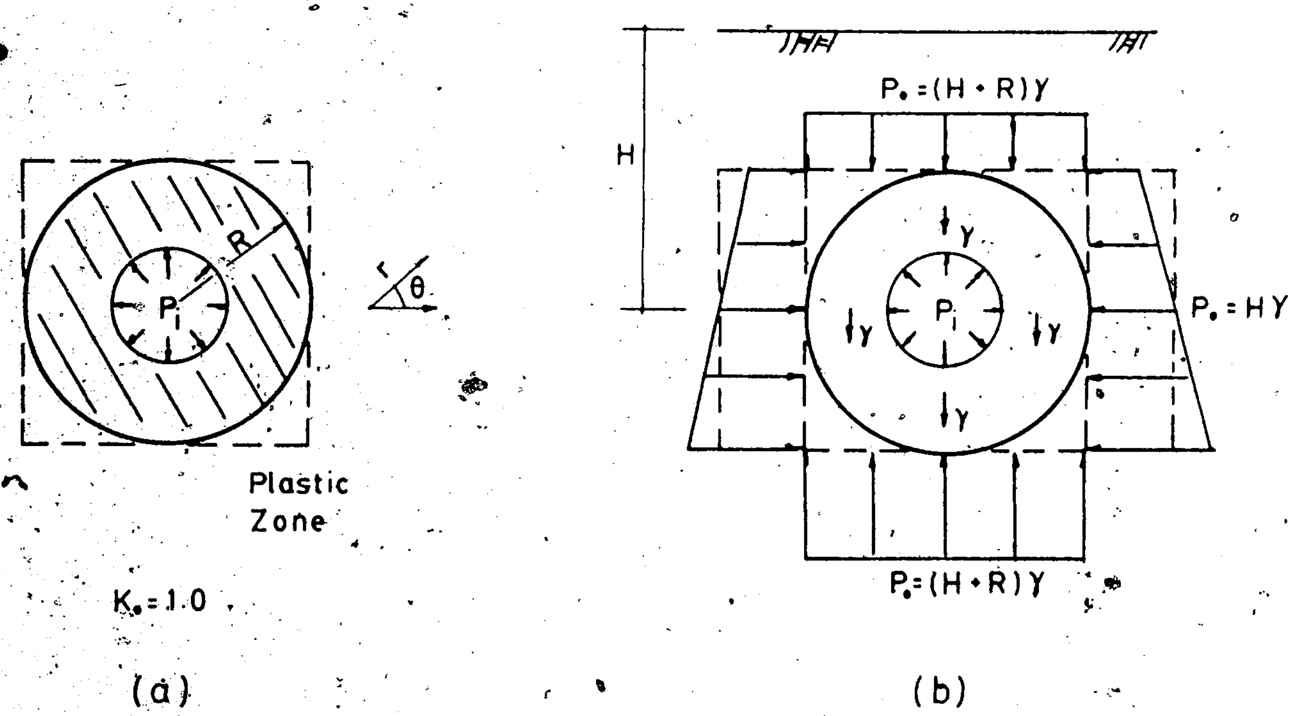

Figure 2.14 Hole-in-Plate Model for Mode II

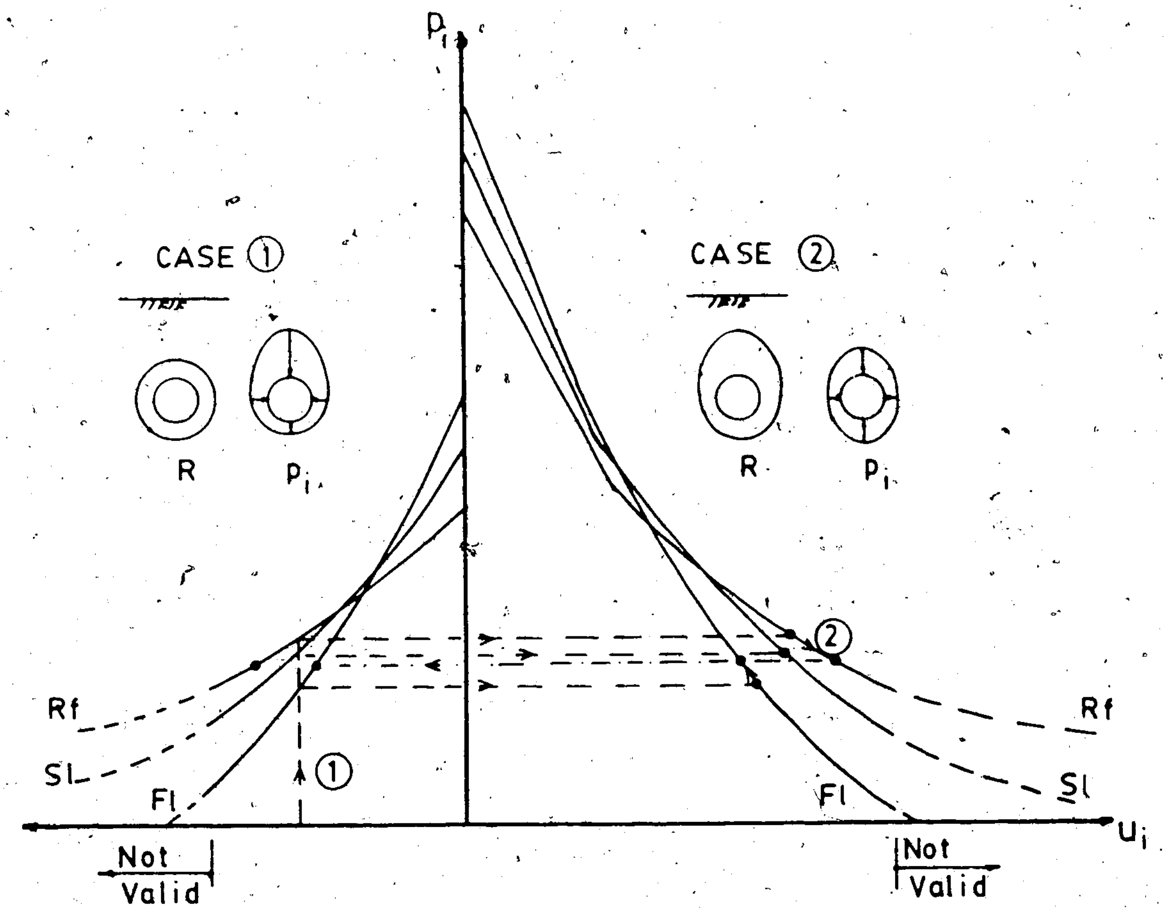

Figure 2.15 p_i-u-R Plot for Mode II

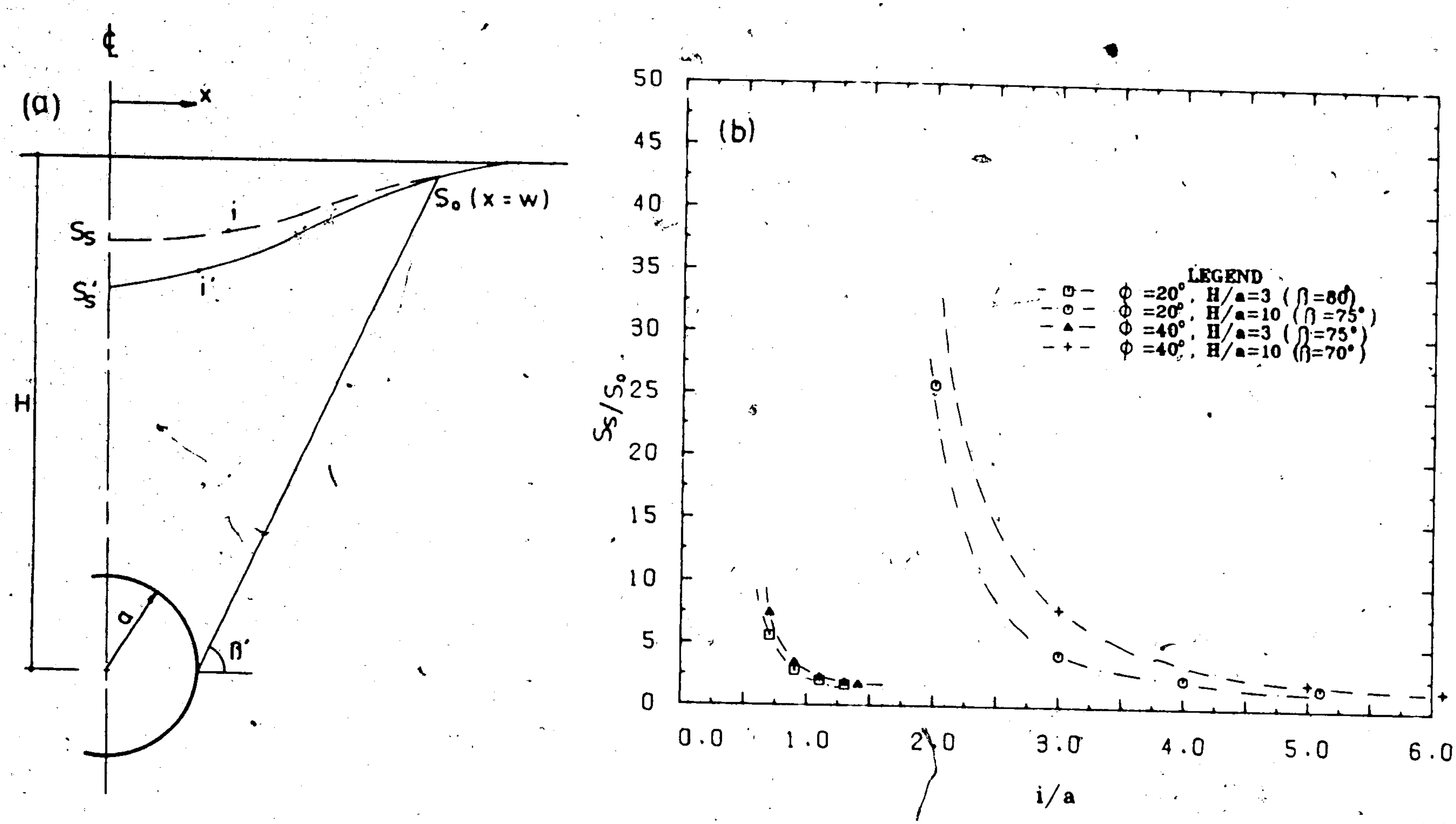

Figure 2.16 Surface Settlement Profile

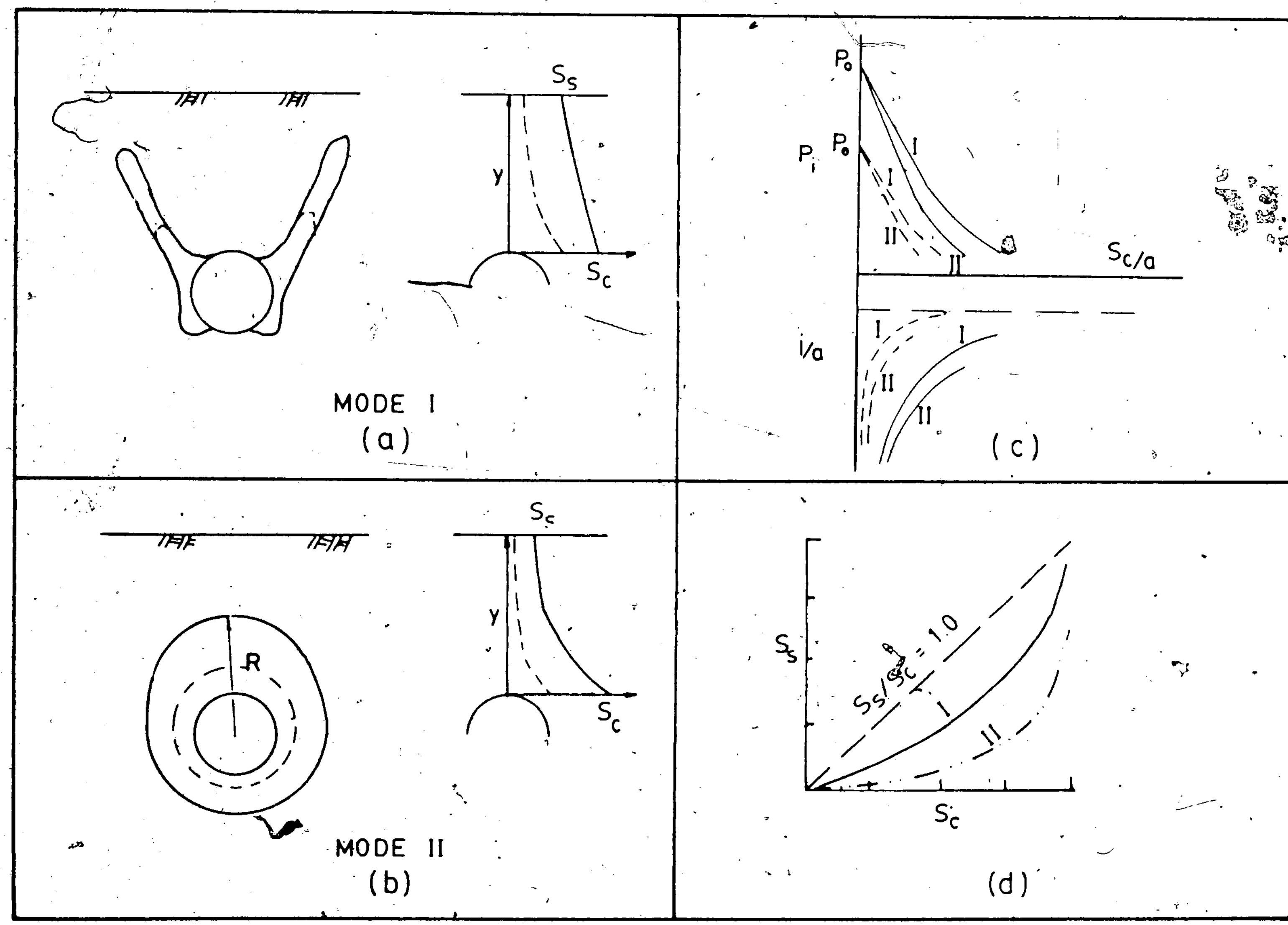

Figure 2.17 Vertical Settlement Profiles above Tunnel for Modes I and II

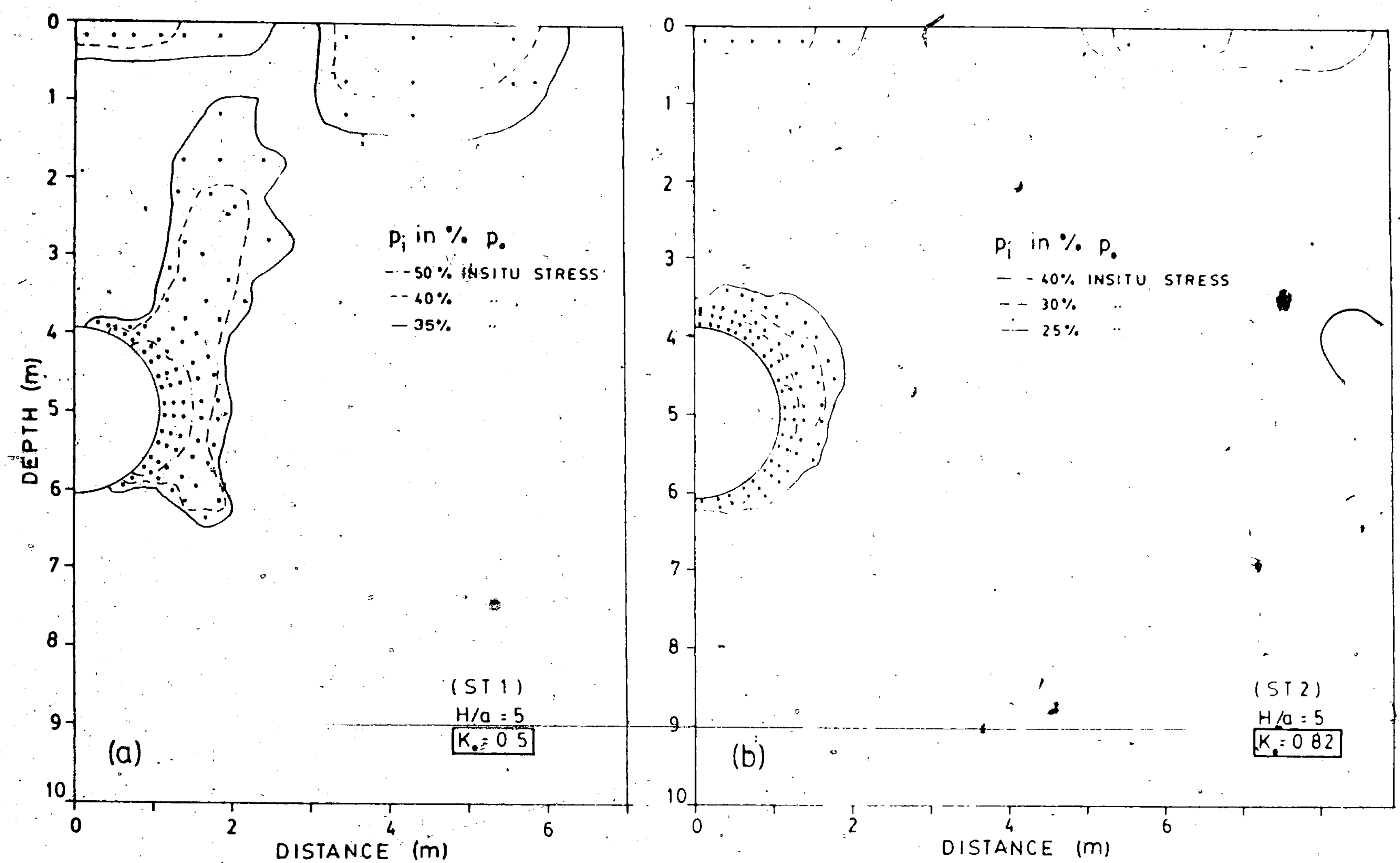

Figure 2.18 Extent of Yield Zone - Cohesionless (ST1,ST2)

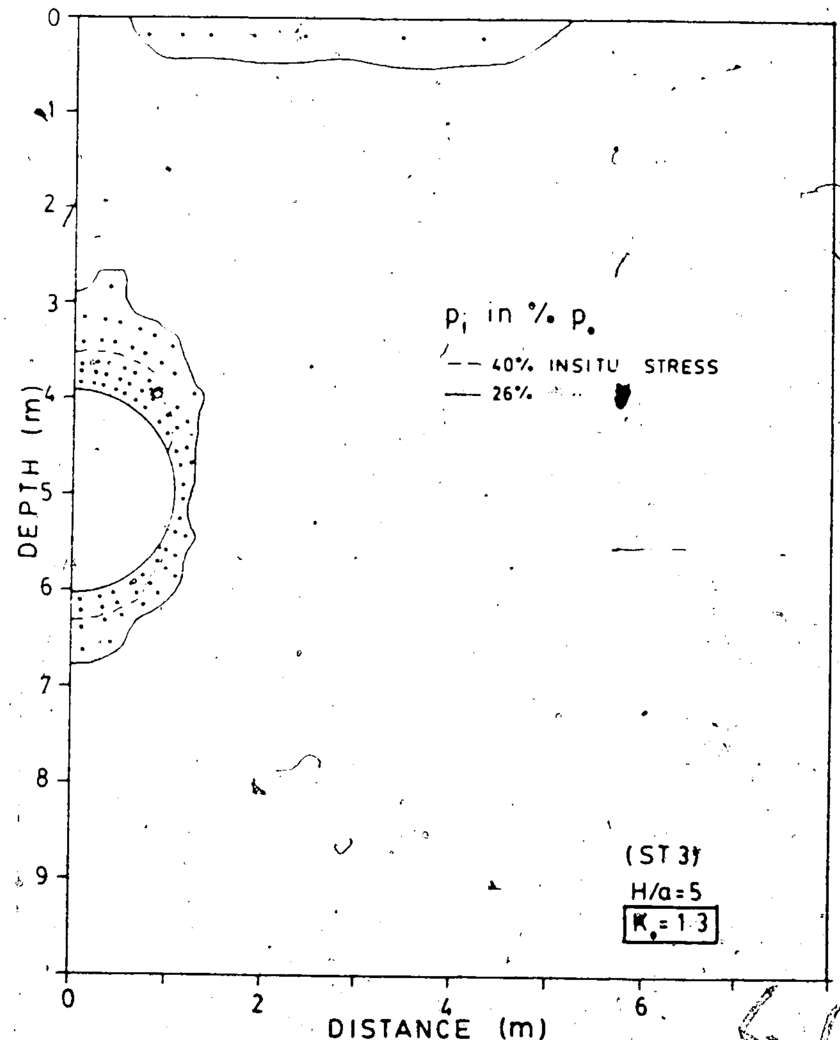

Figure 2.19 Extent of Yield Zone - Cohesionless (ST3)

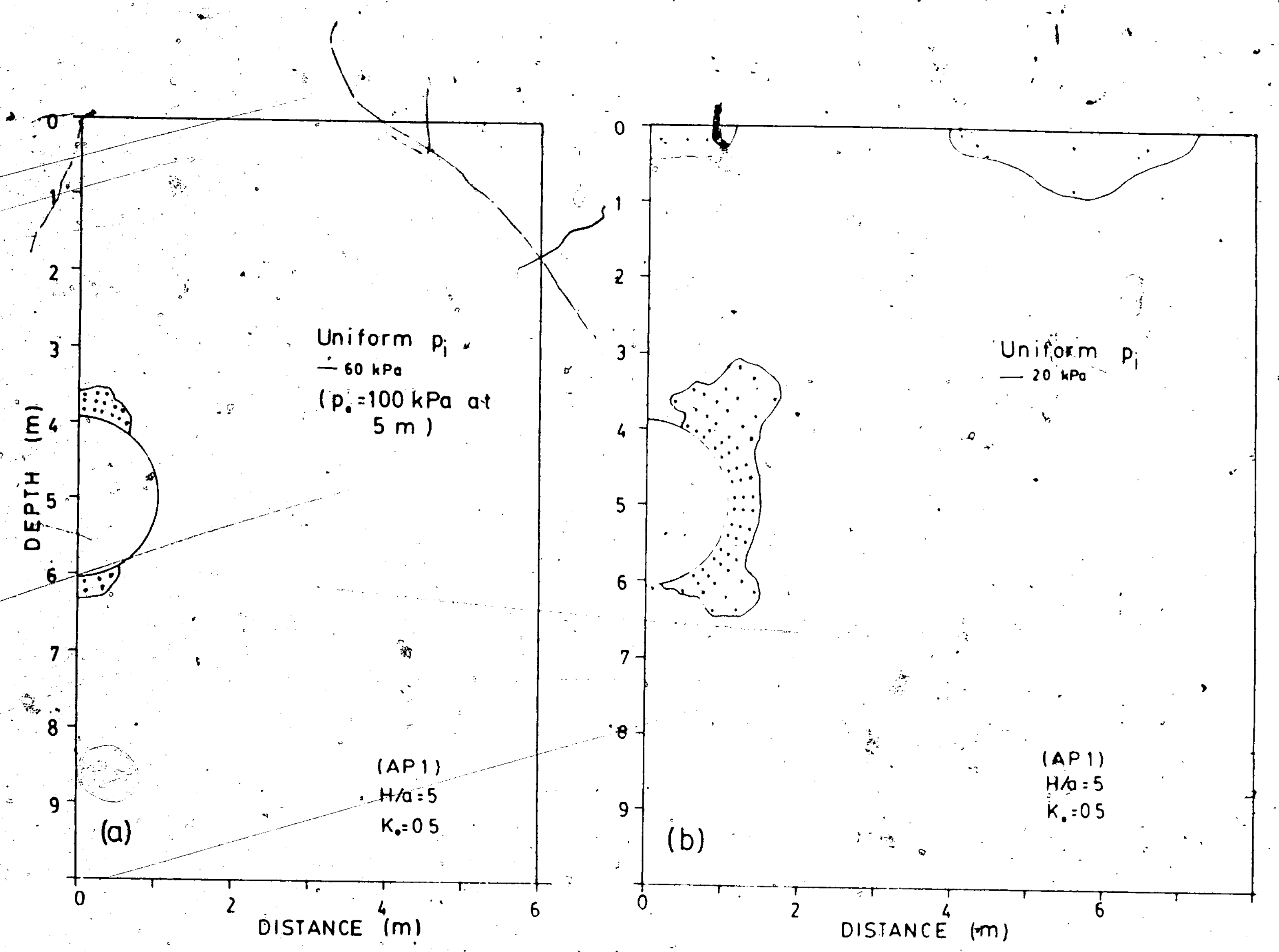

Figure 2.20 Extent of Yield Zone - Cohesionless (AP1)

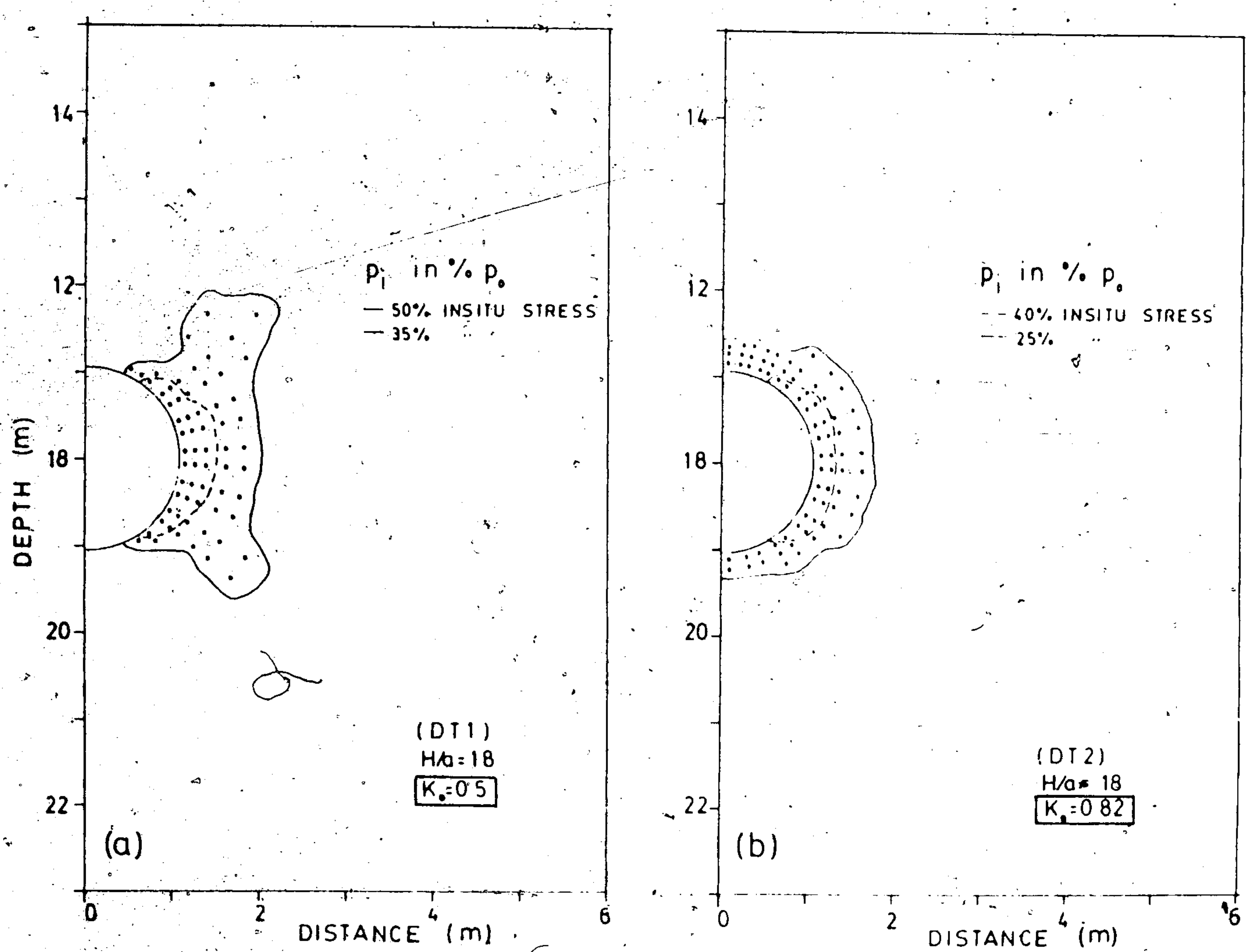

Figure 2.21 Extent of Yield Zone - Cohesionless (DT1,DT2)

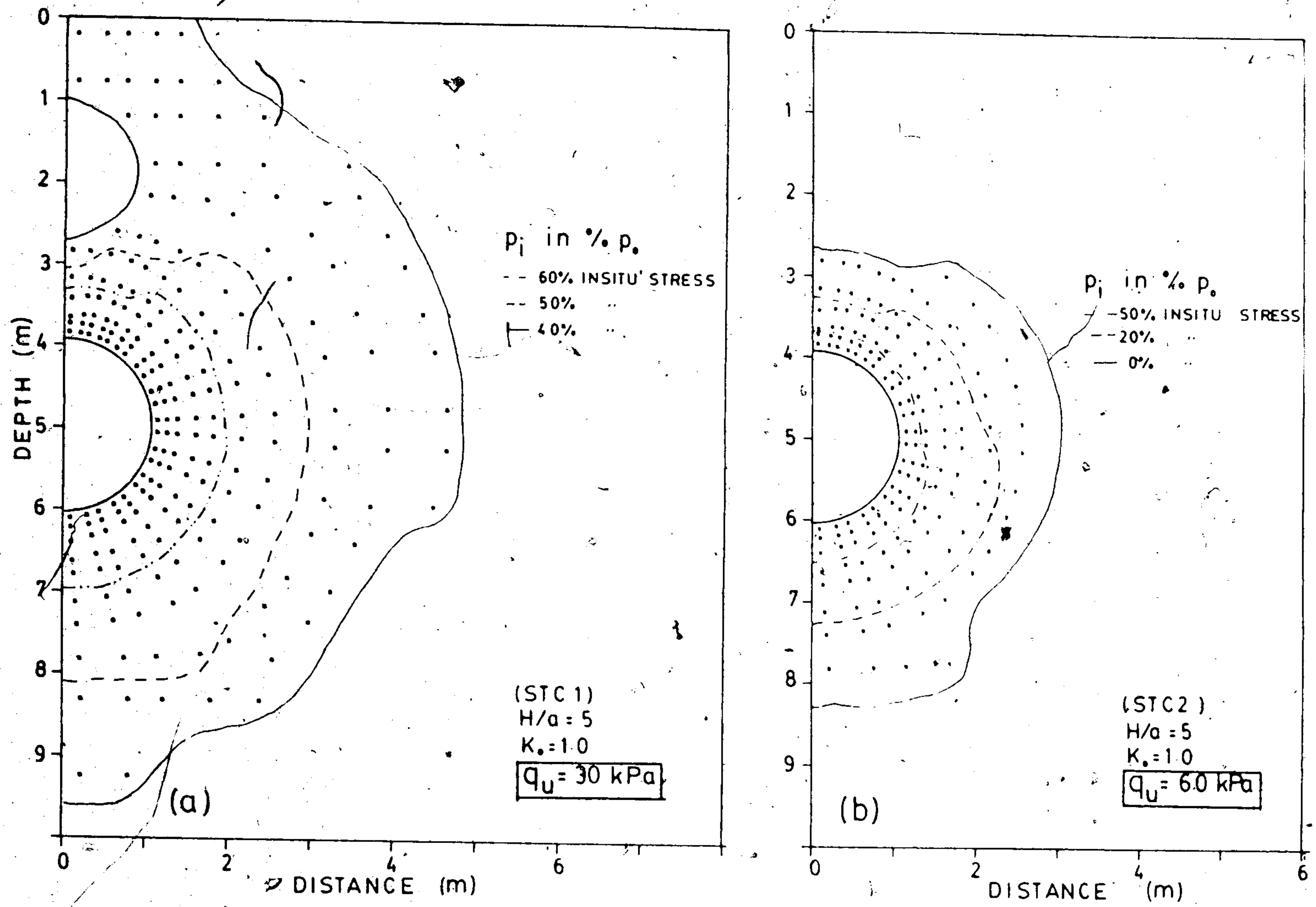

Figure 2.22 Extent of Yield Zone - Cohesive (STC1,STC2)

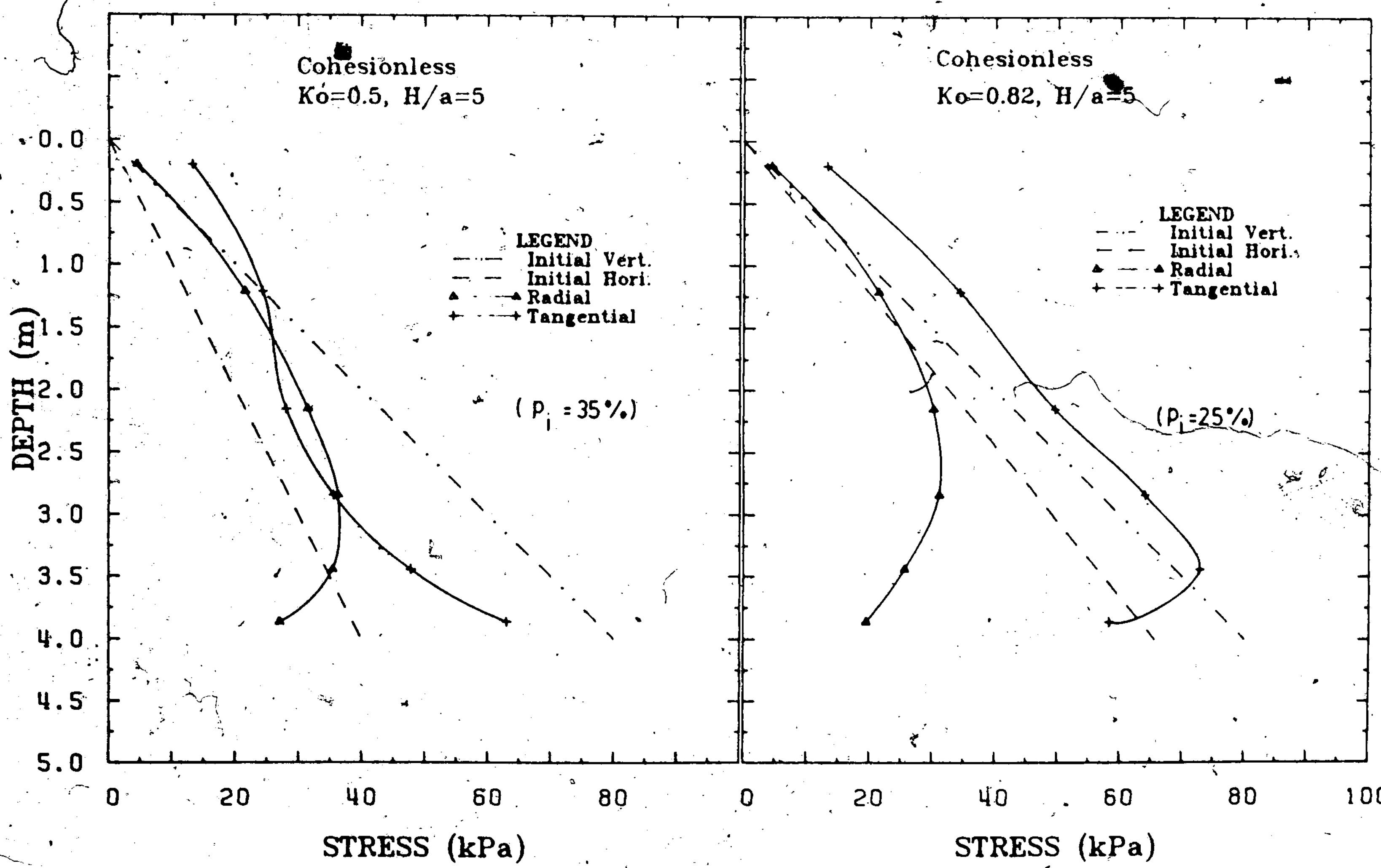

Figure 2.23 Stress Distribution above Roof - Cohesionless (ST1,ST2)

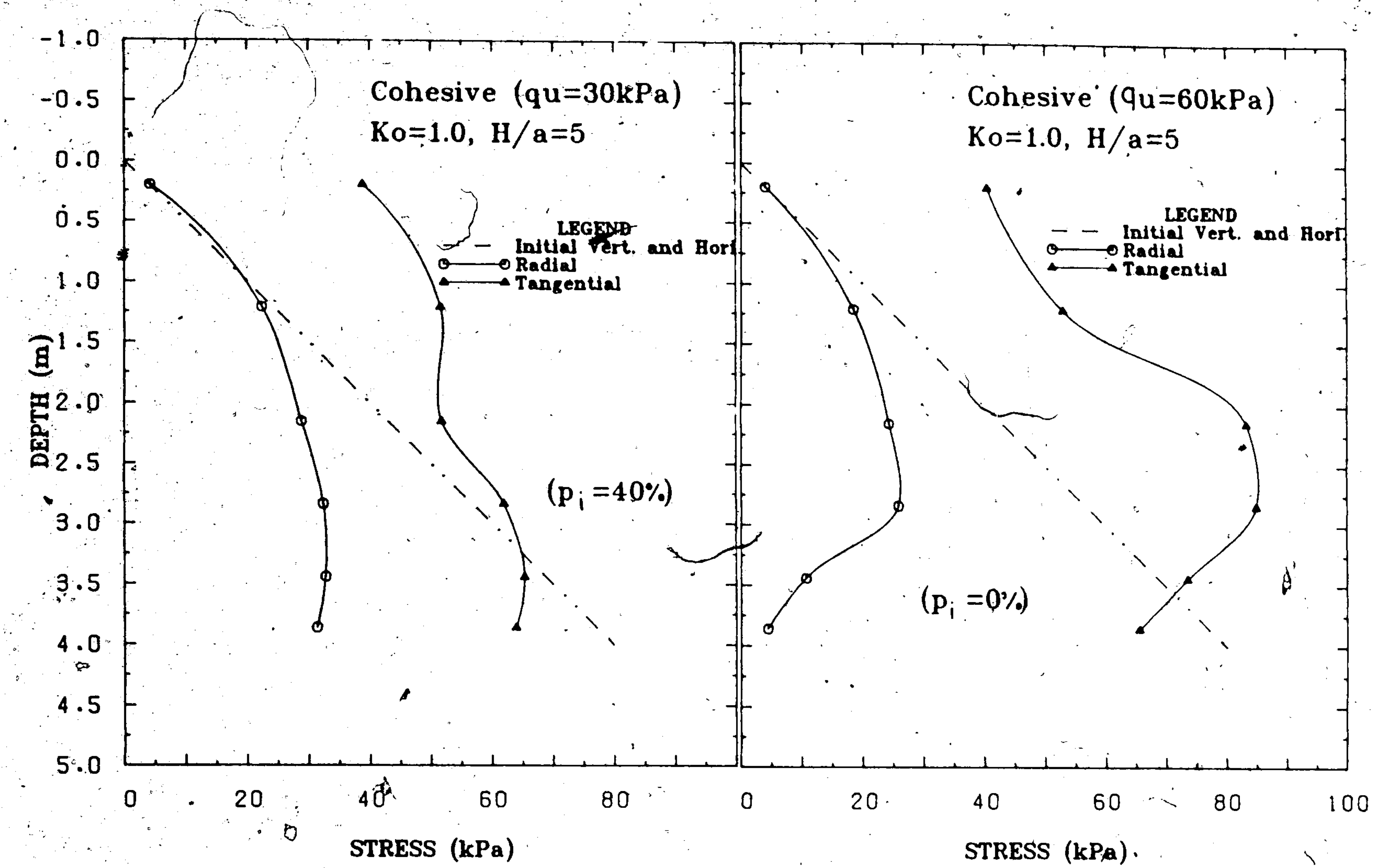

Figure 2.24 Stress Distribution above Roof - Cohesive (STC1,STC2)

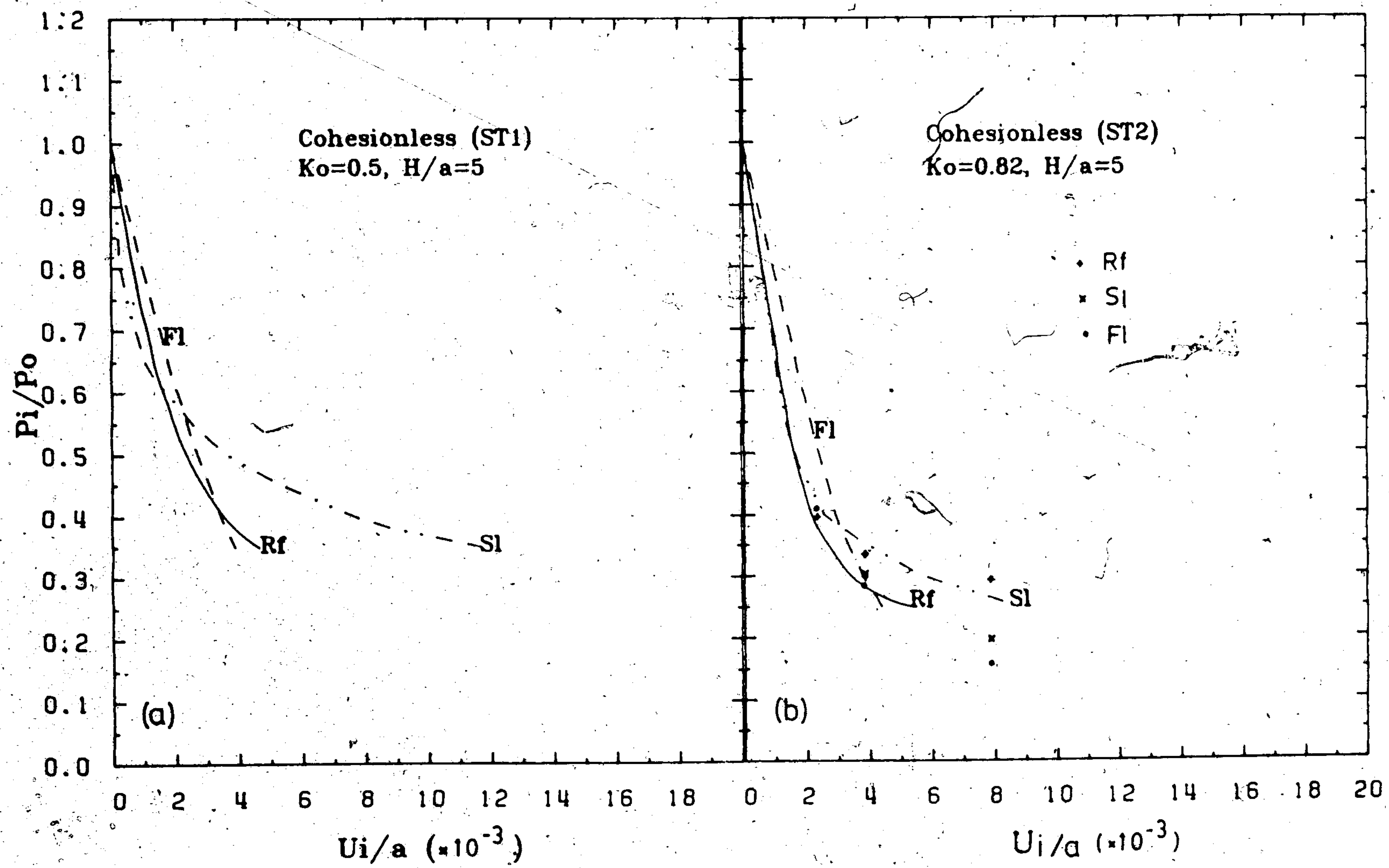

Figure 2.25 GCC - Cohesionless (ST1,ST2)

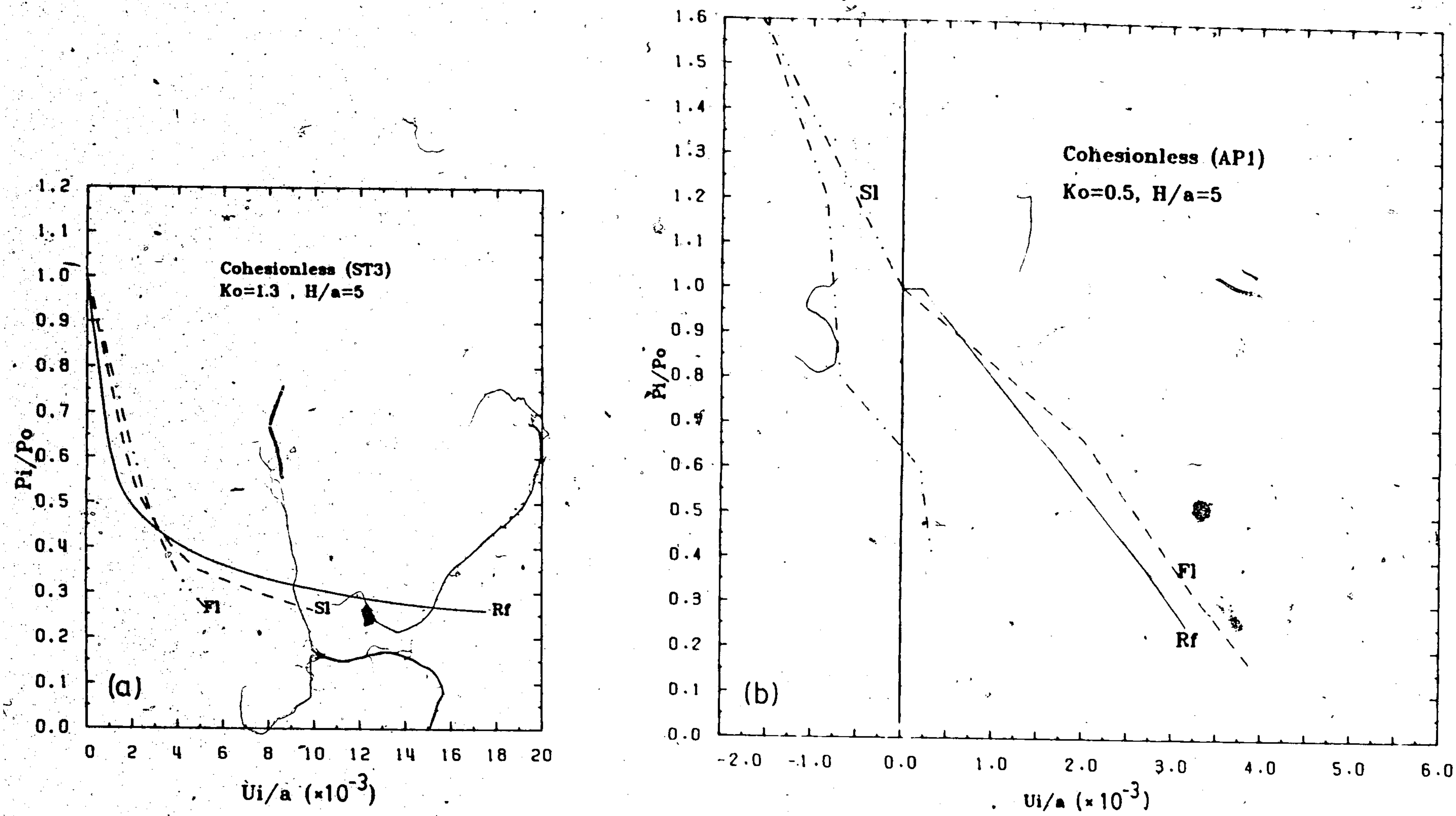

Figure 2.26 GCC - Cohesionless (ST3,AP1)

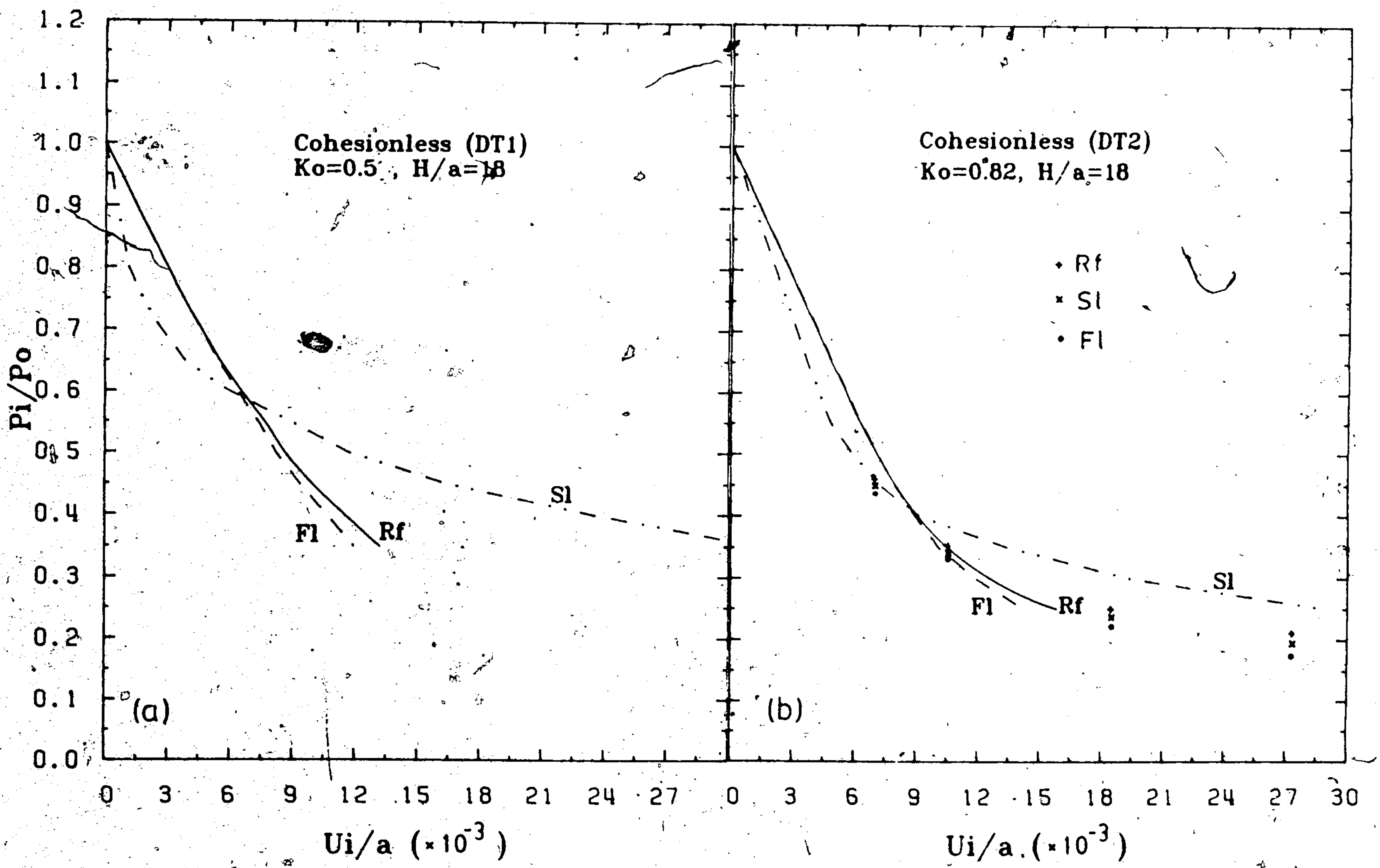

Figure 2.27 GCC - Cohesionless (DT1,DT2)

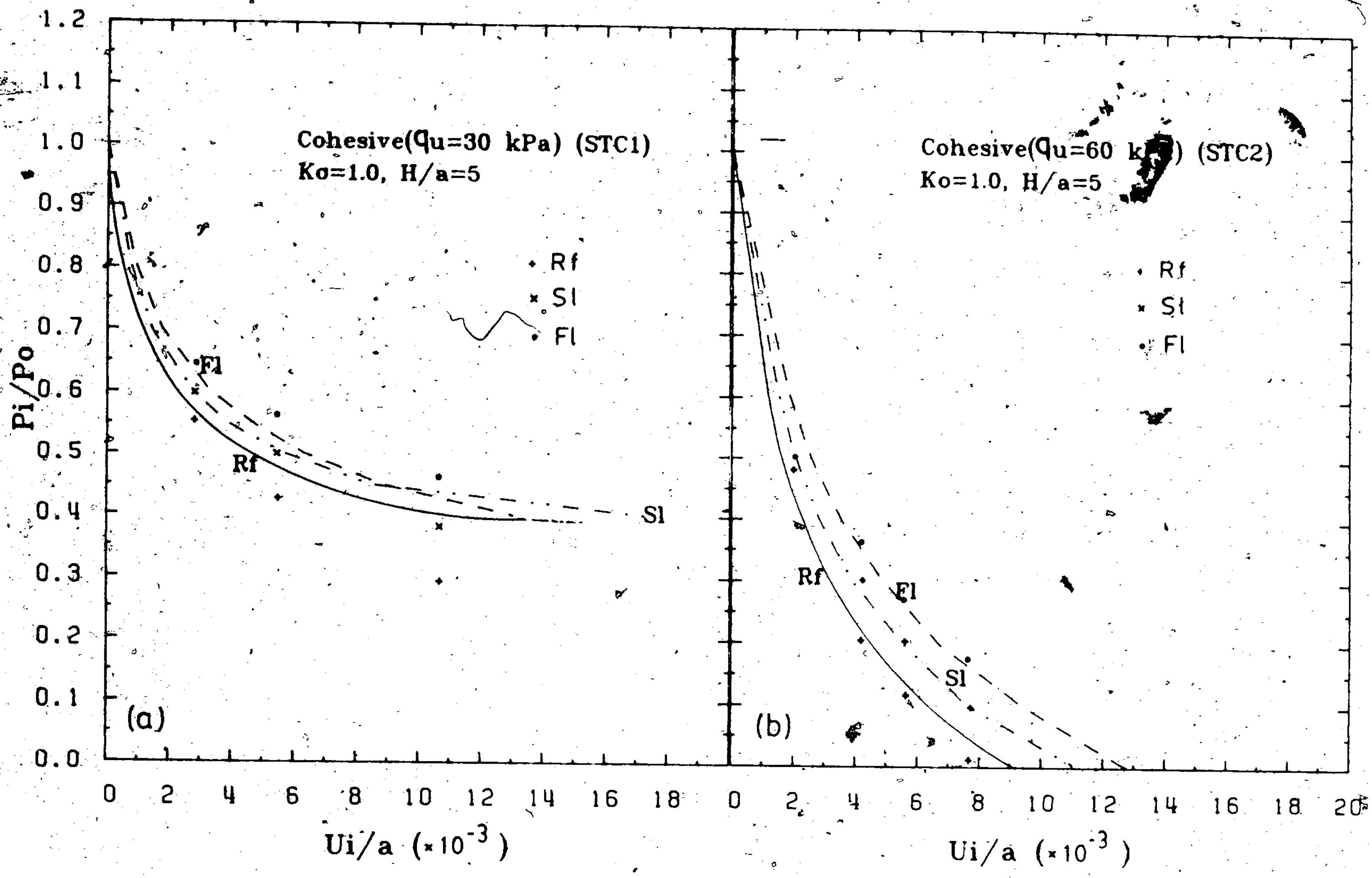

Figure 2.28 GCC - Cohesive (STC1,STC2)

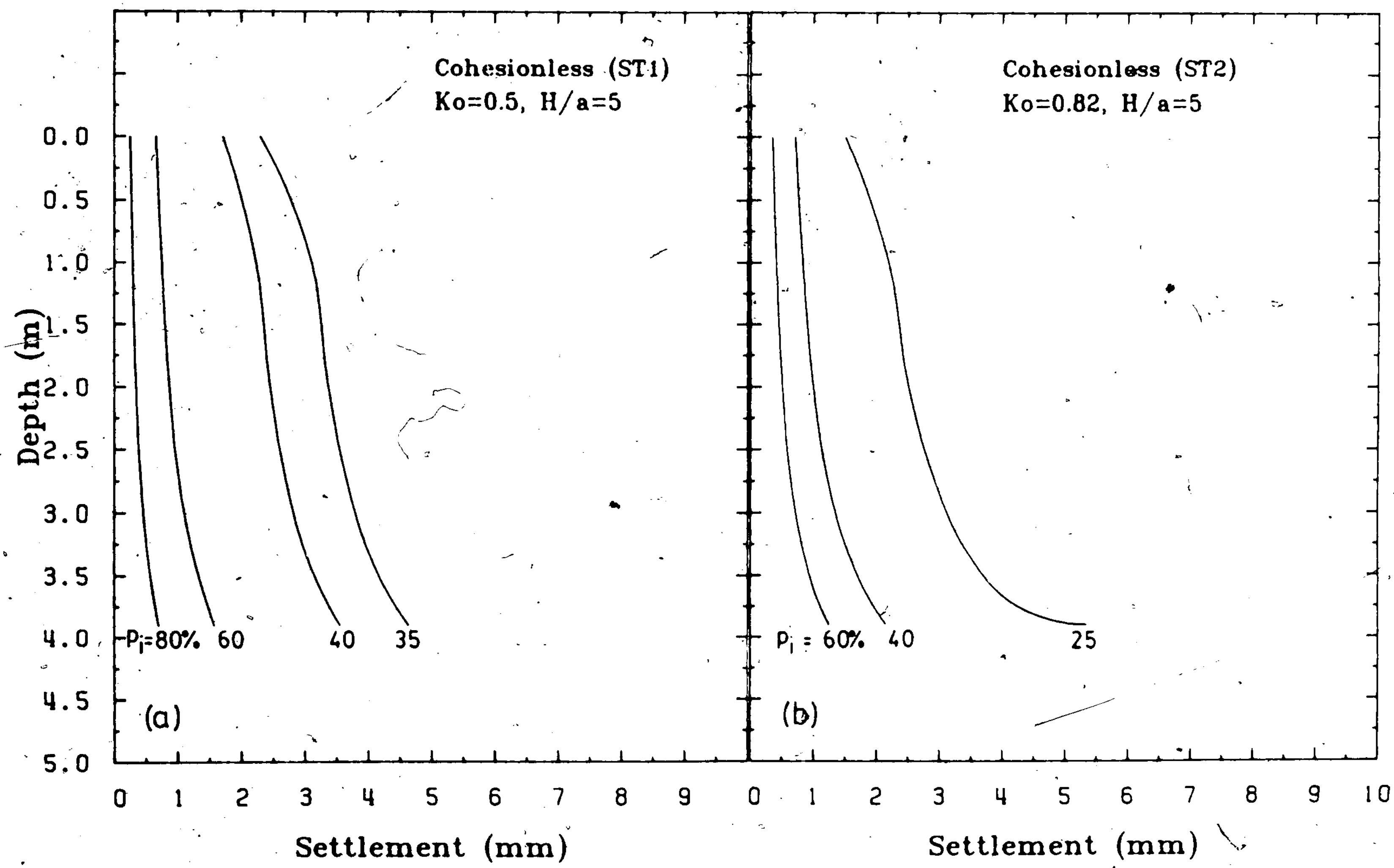

Figure 2.29 Vertical Settlement Profile above Roof - Cohesionless (ST1,ST2)

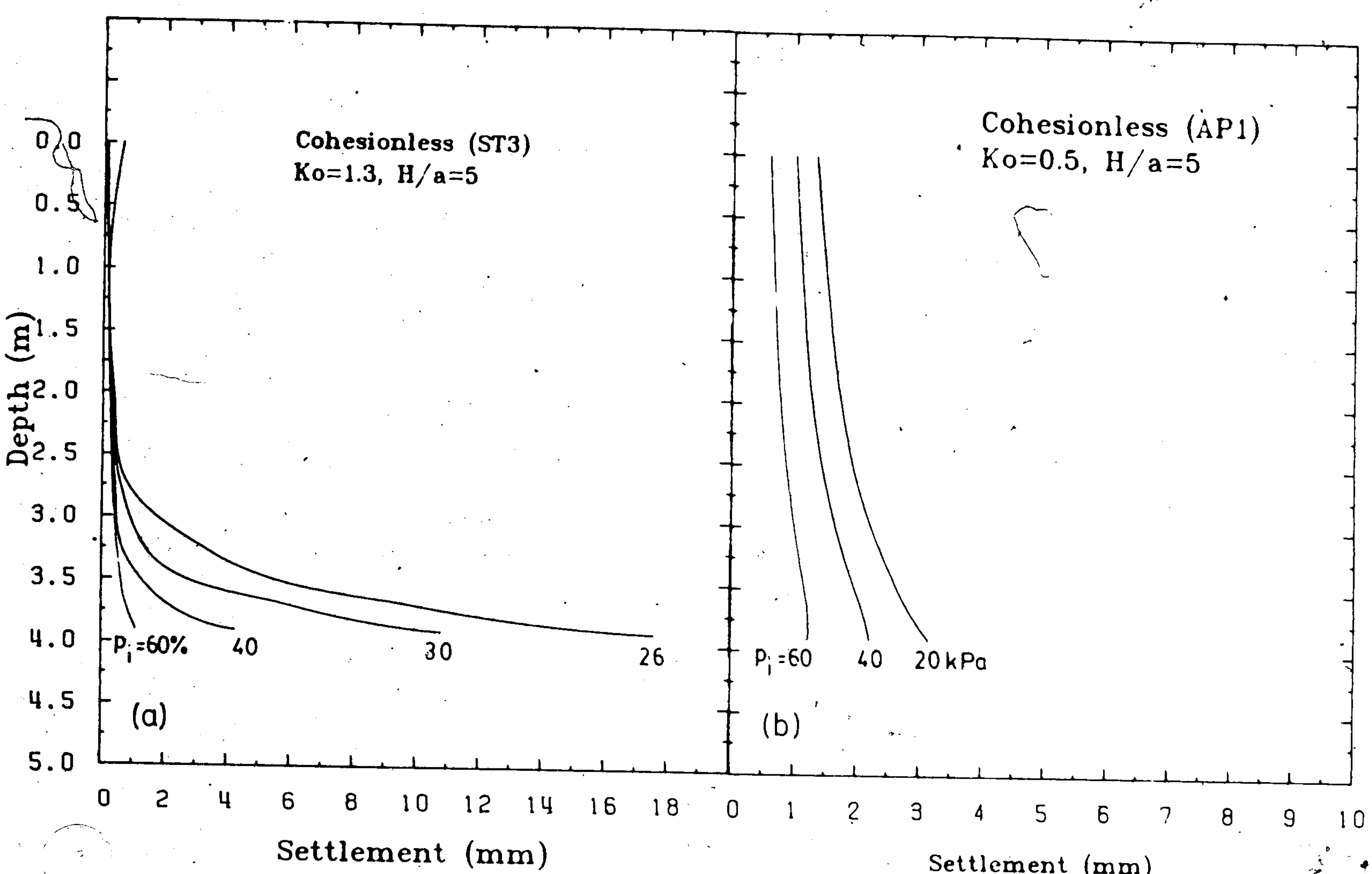

Figure 2.30 Vertical Settlement Profile above Roof - Cohesionless (ST3,AP1)

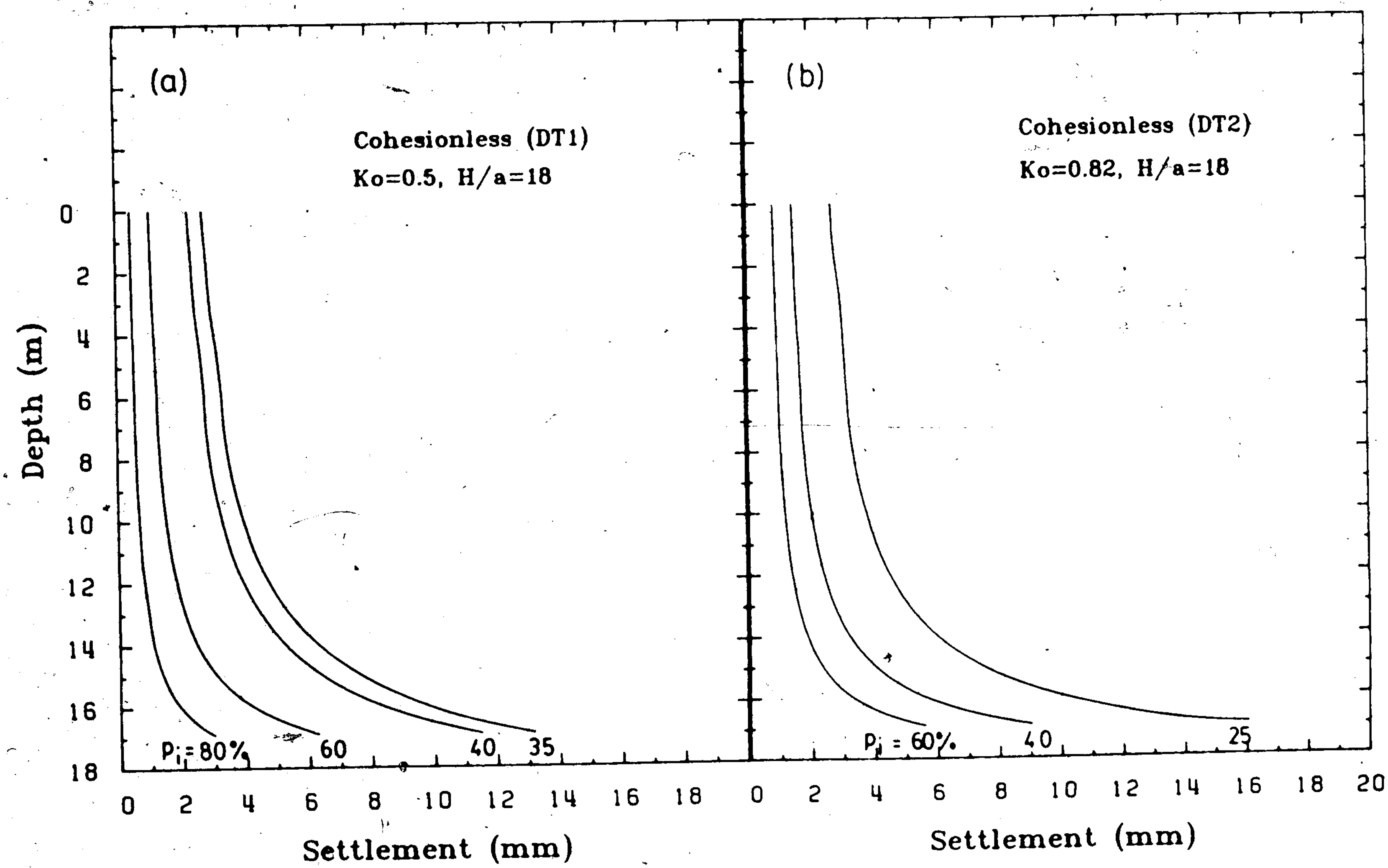

Figure 2.31 Vertical Settlement Profile above Roof - Cohesionless (DT1,DT2)

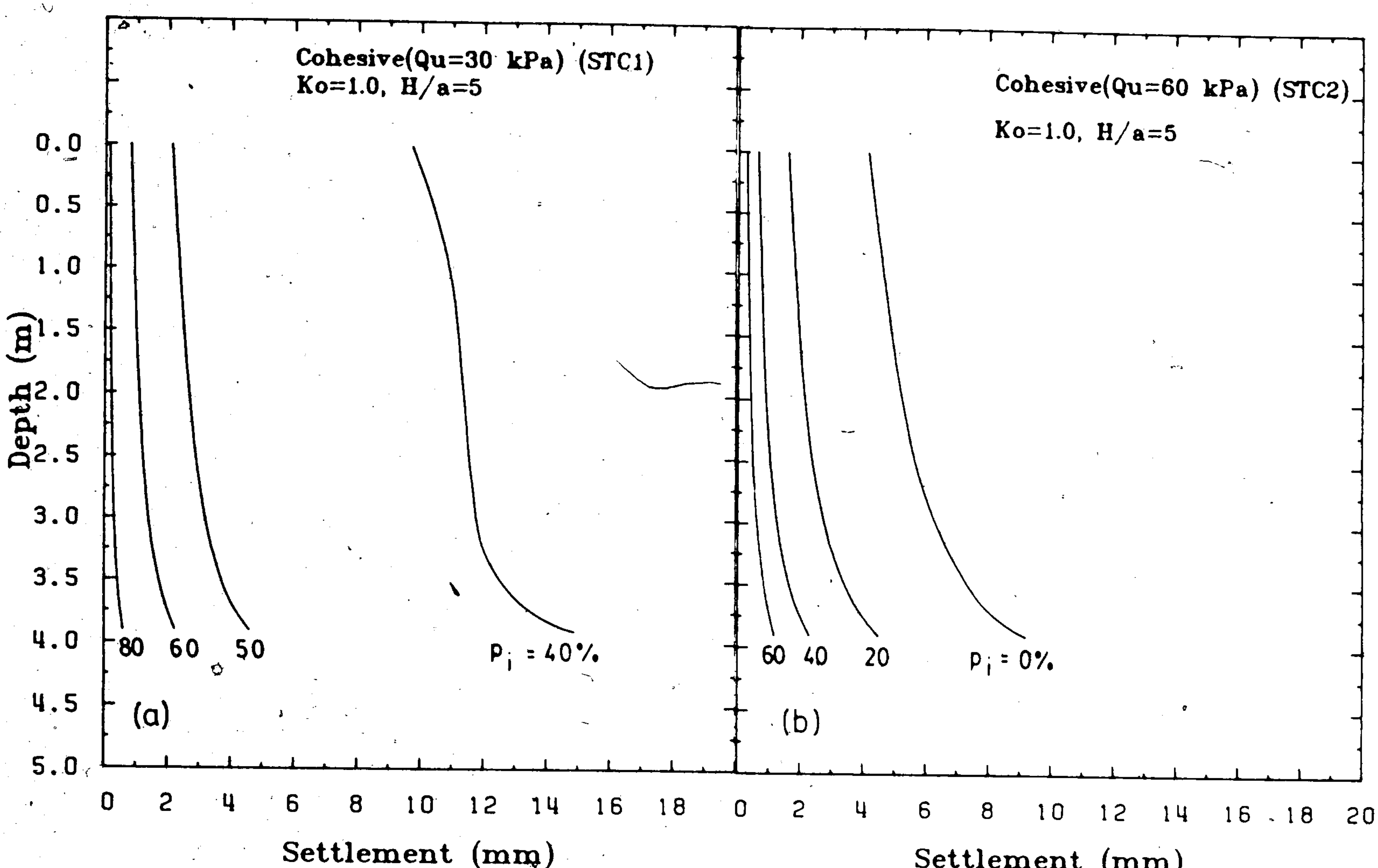

Figure 2.32 Vertical Settlement Profile above Roof - Cohesive (STC1,STC2)

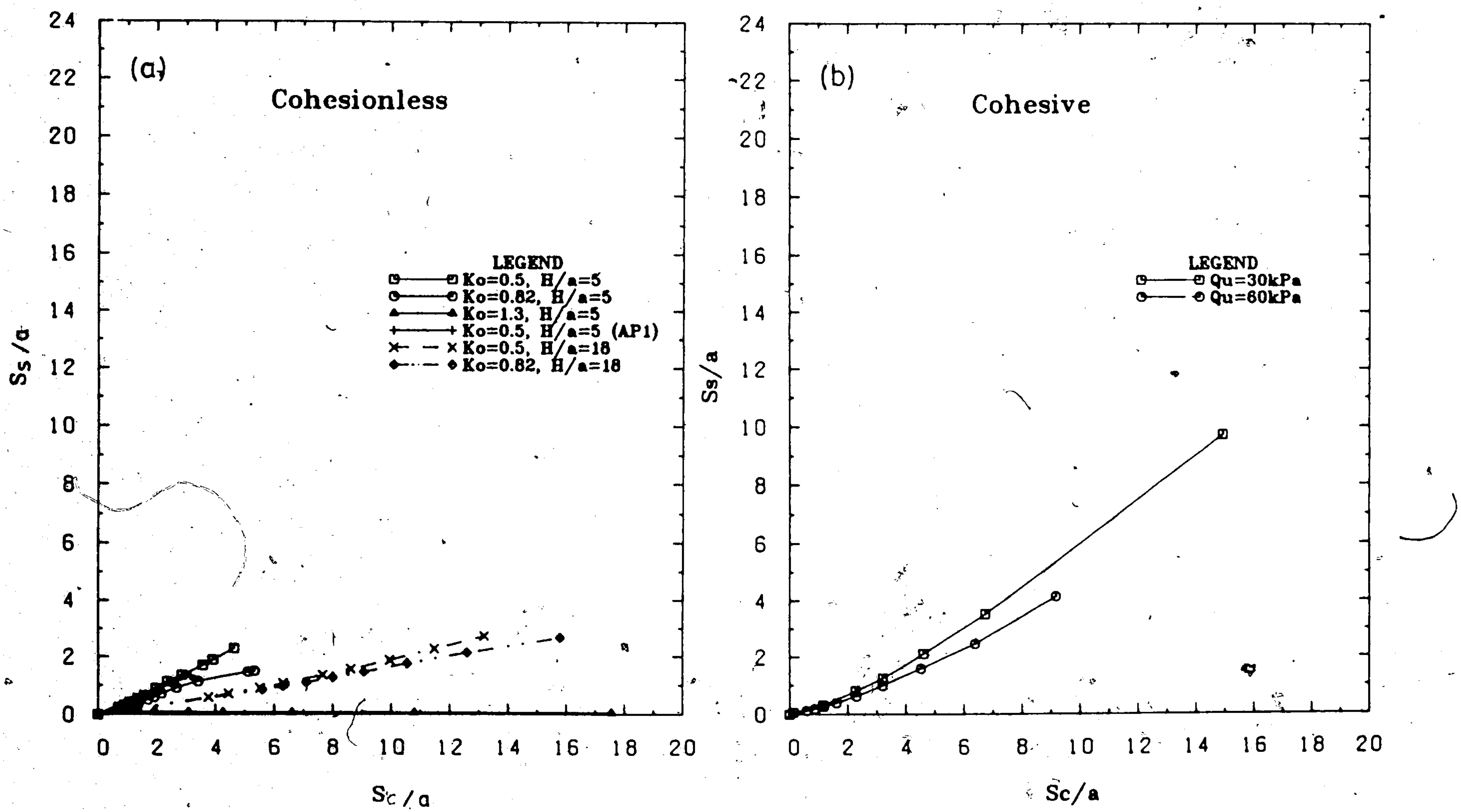

Figure 2.33 S_s/S_c Settlement Relations

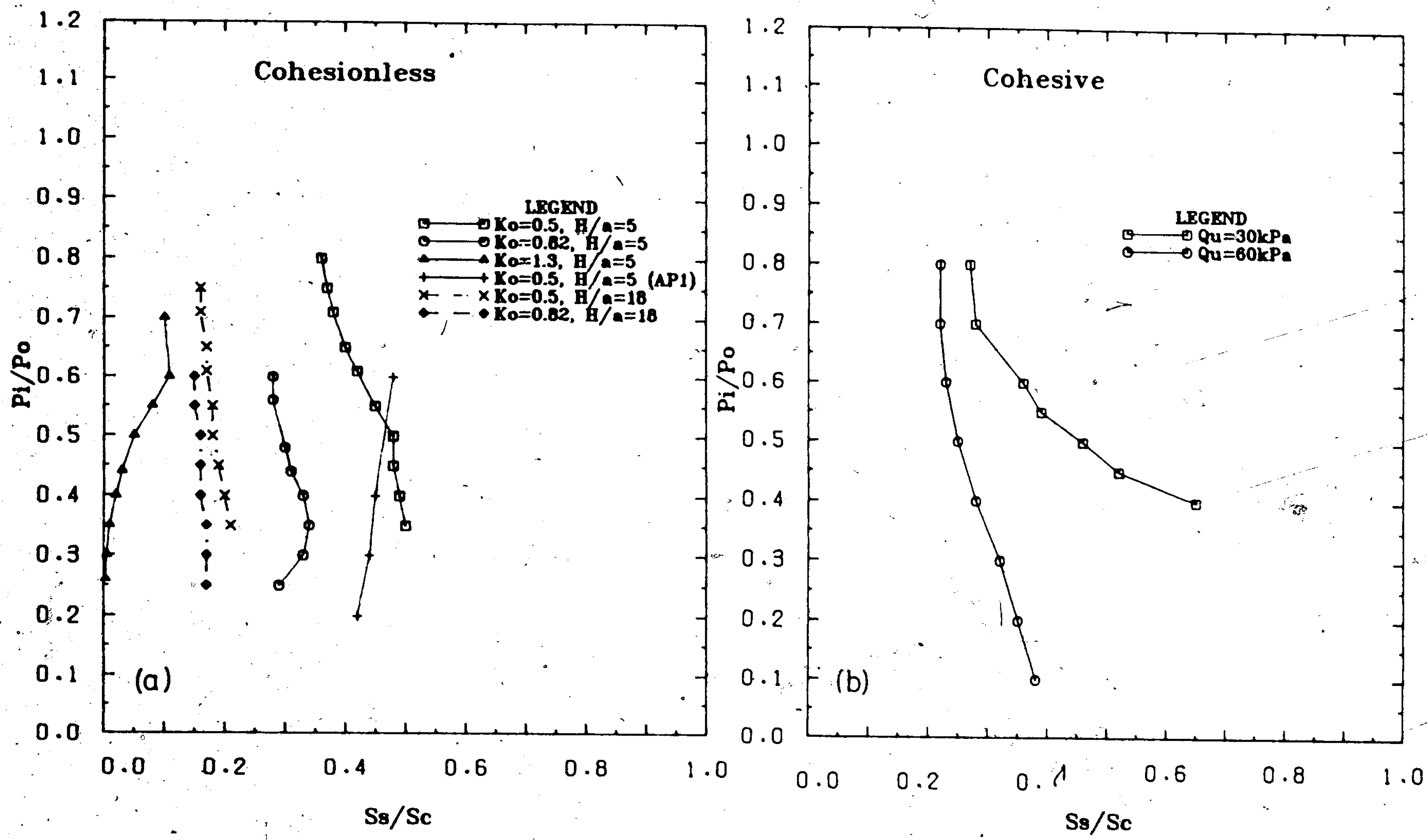

Figure 2.34 Plots of p_i/p_o versus S_s/S_c

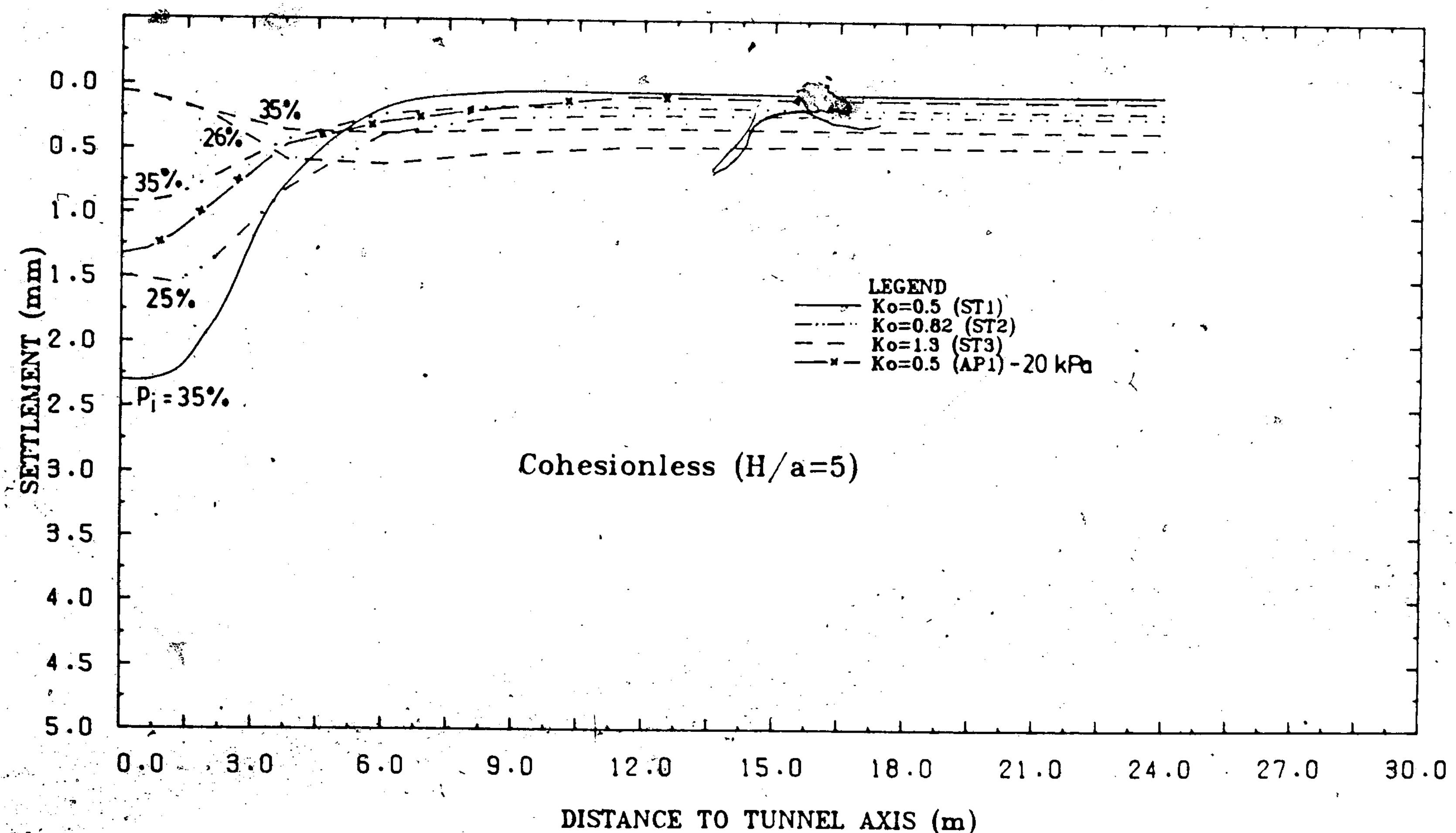

Figure 2.35 Surface Settlement-Cohesionless (ST1,ST2,AP1)

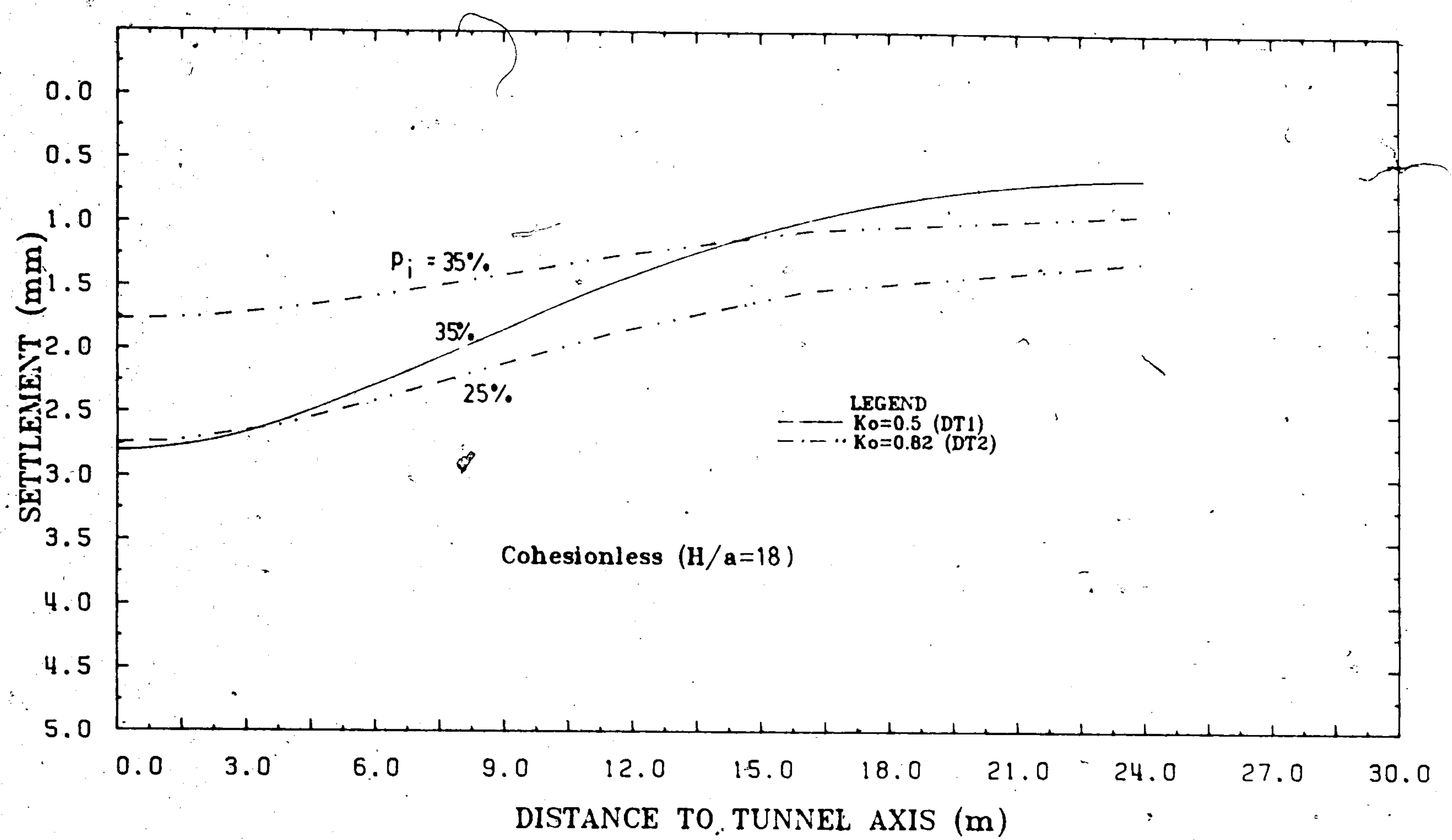

Figure 2.36 Surface Settlement-Cohesionless (DT1,DT2)

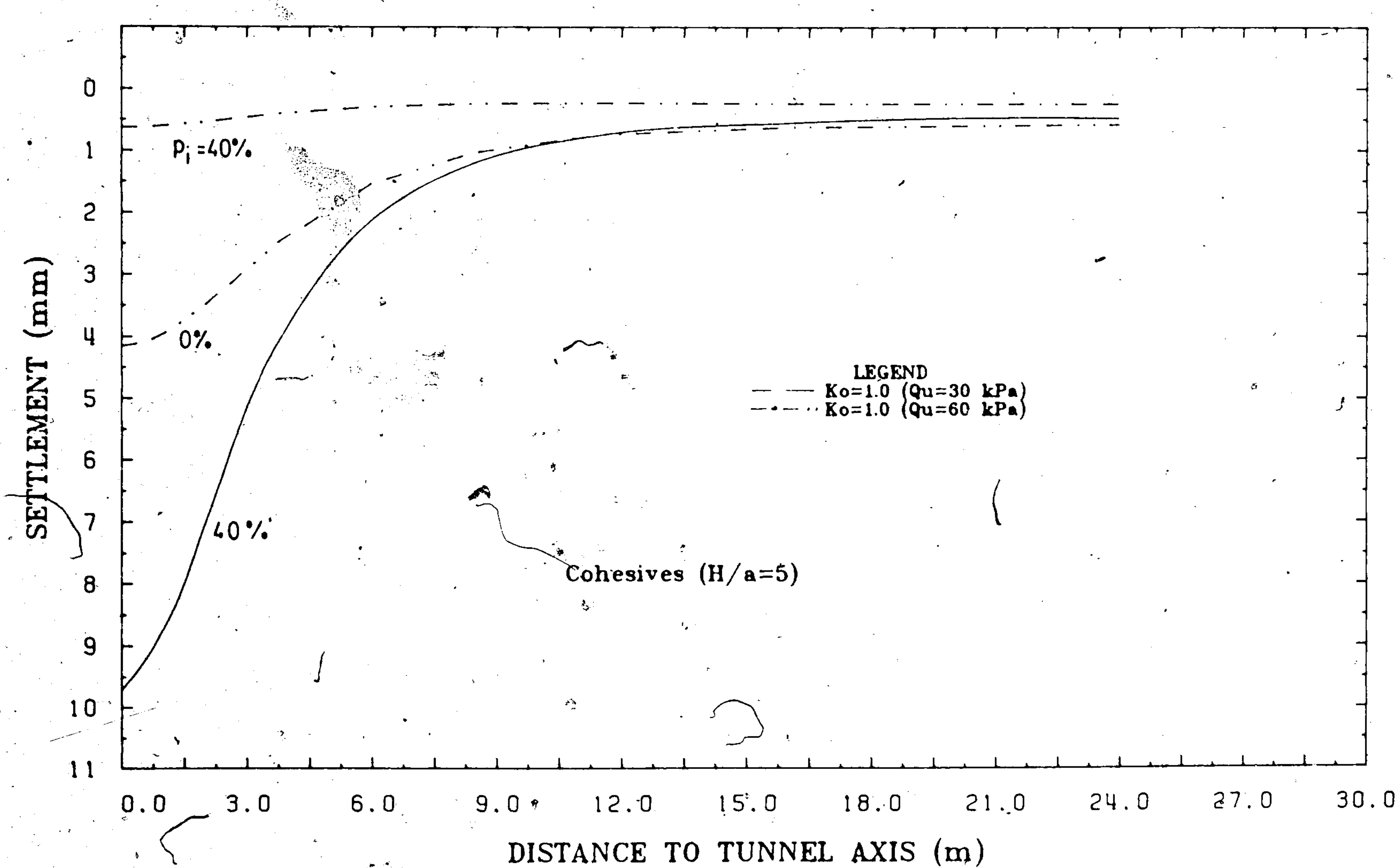

Figure 2.37 Surface Settlement-Cohesive (STC1,STC2)

3 . TUNNEL - CASE STUDIES

3.1 Introduction

The last chapter explores the mechanism of tunnel behaviour in detail and indicates that the behaviour of the ground around a tunnel is best described by the concept of ground convergence curve. This concept signifies the dependency between stress-relief and displacement of the ground. In this chapter an attempt is made to extend the application of this concept to explain results from some case histories, including model tests and field measurements.

3.2 Case Studies

3.2.1 Model Tests

The behaviour of shallow tunnels in sand and clay has been studied extensively by use of model tests at Cambridge University, England. Two types of tests were performed: (1) static tests and (2) gravity or centrifugal tests (Atkinson *et al.*, 1974; Schofield, 1977). In static tests the soil sample was subjected to an external biaxial stress field in which the K_o-value could be varied, but the self-weight of the soil became negligible and did not contribute to instability modes. In the gravity or centrifugal test the stress field was due to the gravitational force and the K_o value depended on the mobilized strength which could be approximated by the relationship ($K_o = 1 - \sin\phi$) (Brooker and Ireland, 1965 ; Lade *et al.*, 1981).

Atkinson *et al.* (1975) performed a series of model tests (Type 2 - gravity test) in dense sand to measure the support pressure and deformation at the collapse state. The tunnel was supported by a pressurized flexible rubber membrane, and collapse was produced by reducing this internal pressure. The depth-ratio (H/a) was varied from 1.9 to 5.0. As described by the authors, the soil movements were initially restricted to a wedge zone immediately above the crown. The measured support pressure at this state was close to the pressure calculated from the upper bound solution (p_{ic}, Eqn. 2.3). As the tunnel pressure was reduced further, this wedge grew upward toward the surface (Regime L in Fig. 2.4). A higher support pressure was measured to maintain the equilibrium at this final state. These observed modes correspond well with the prediction in Fig. 2.9 (Point d to Point e). The higher pressure at the final state should have corresponded to the pressure p_{fc}. Back analyses of p_{fc} are not possible because the horizontal to vertical stress coefficient (K_s) and the residual angle (ϕ_r) were indeterminate from the tests. The support pressure p_{fc} actually depends on the displacement allowed at the crown. The p_{fc} values shown in Fig. 2.13 were calculated assuming that the soil is in limit state (i.e., at lowest $K_s=K_a$). Thus the measured p_{fc} in the model tests should be and are smaller than the predicted p_{fc}.

Atkinson and Potts (1977) investigated theoretically and experimentally the stability of a circular tunnel in sand. The experimental investigation consisted of Types (1) and (2) model tests. In the gravity tests (with an assumed

$K_o = 1-\sin\phi$) the initial collapse was observed at the crown. The measured collapse pressures compare well with the pressure (p_{ic}) predicted by the theoretical upper bound theorem based on the observed collapse mode. For the static tests (where K_o conditions were not reported) the observed collapse pressures also bracketed closely the pressure range predicted using the lower bound theorem. However, their formulation (lower bound solution) assumes that a concentric yield zone develops around the opening and that the collapse state is reached when the yield zones intersect the free surface. It has been shown in Chapter 2 that this mode of yielding, i.e., Mode II is only admissible if Ko is close to unity. If the model tests were performed under $K_o = 1-\sin\phi$, the localized yield zones (Mode I) should develop, implying that the mode of yielding in the theoretical solution was not consistent with the one observed in the test.

Fig. 3.1 shows contours of volume and shear strains in sand near collapse for the gravity tests ($K_o = 1-\sin\phi$), (Atkinson and Potts, 1977). The distribution of strain around the tunnel is self-explanatory. Concentrations of shear strain with magnitude up to 20% occur between the crown and springlines, and the soil in these regions must have reached states of limiting stress. Taking shear strain as a yield criterion, the observed mode of yielding agrees well with Mode I. It is important to notice that the shear strains shown in Fig. 3.1 were observed near collapse at large displacements, probably between u_{ic} and u_{fc} in Fig. 2.9.

The shear strain at yield initiation can also be observed from the results of model tests (gravity type) performed by Cording *et al.* (1976). In their model tests a specified displacement pattern instead of uniform pressure was imposed at the tunnel perimeter. Fig. 3.2 shows shear strain from their finite element simulation of these model tests. It can be seen that fairly high shear strains are concentrated along a plane through the springline inclined approximately 65° to horizontal. Asumming ϕ=30°, the predicted β from Fig. 2.10 is about 67° which agrees with the observed one (note the boundary condition at tunnel wall are different in two situations).

All these model tests of gravity type (Atkinson and Potts, 1977, Cording *et al.*, 1976) were carried out in plane strain condition. Hence, the K_o value is presumably given by the relationship $K_o=1-\sin\phi$. With $K_o=1-\sin\phi$, the mode of yielding should be Model I-1 or I-2. The propagation of high shear strain zones is comparable to that predicted by Mode I. These results therefore support the finding that Mode I takes place for $K_o<K_{cr}$.

Potts (1976) performed a series of model tests (static test type) in sand for K_o=0.5 and 1.0. The development of shear strain around the tunnel was not reported and only the result near the collapse was recorded. Unfortunately, it is not possible to make use of these results to illustrate the occurrence of Modes I and II for K_o=0.5 and 1.0 respectively. However Mode II can be recognized very well from model tests of tunnels in over-consolidated Kaolin at K_o=1.0 (Atkinson *et al.*, 1974). The tunnel pressure was reduced from 140 kPa to zero while the surface surcharge pressure was held constant at 140kPa. Contours of shear strains at p_i=27 and 7 kPa are shown in Fig. 3.3a and b. Comparison of the contours of shear strain demonstrates a marked change in the pattern of deformation. At p_i=27kPa, the shear strain contours are approximately concentric with the tunnel axis indicating radial inward deformations (Mode II). At this stage,, contours of shear strain (say 1.0%) extend farther near the floor than the roof. This response is explained by the fact that under uniform internal pressure the deviatoric stress is higher at the floor than the roof due to the gravity stress increasing with depth. At p_i=7kPa, the shear strain contours have become non-uniform and a pair of zones of high shear strain extends upward toward the surface (Mode II to Mode II-I). The above observation verifies that Mode II develops for K_o=1.0.

The initial insitu stresses (K_o) not only govern the mode of yielding but also influence the displacement of soil around the tunnel. Potts (1976) reported surface settlement profiles for a set of model tests in sand with K_o=0.5 and 1.0 (see Fig. 3.4). The surface settlement for K_o=1.0 is much smaller than that for K_o=0.5 even at a much lower support stress. This difference is attributed to the fact that tangential arching is higher with K_o=1.0 as explained in Section 2.2.4.3. This causes an increase in resistance against the downward movement of the soil block above the crown and reduces the surface settlements. This implies that the potential for damage due to surface settlement becomes more critical for Mode I than for Mode II.

3.2.2 Field Measurements

Two cases histories of tunnelling in Edmonton till (Eisenstein *et al.*, 1981, Branco, 1981) are available where sufficient measurements of the displacement field around the tunnel and the pressure on the lining system were made. These two cases are now examined in detail by use of the ground convergence concept. Other cases documented by Attewell (1977) and O'Reilly and New (1982) will also be studied and their results along with those from model tests and FE analyses then will be synthesized.

Tunnelling in Edmonton Till

Two tunnels were built using very similar construction methods and in comparable soil conditions. The first tunnel (EXP tunnel, Eisenstein *et al.*, 1981) is a small diameter tunnel (D=2.56m) driven by a full face TBM at a depth of H=24m at the test section. The primary lining comprises segmented steel ribs and timber lagging. Fig. C.1 shows the contours of measured vertical and horizontal displacements around the tunnel. The pressure pattern on the flexible lining was found to be almost uniform with an average radial pressure of 12% of full overburden pressure. The second tunnel (LRT tunnel) is a large diameter tunnel (D=6.1m) driven at a depth of 10m at the test section. The excavation method and installation of the primary lining are similar to those used in the EXP tunnel. The measured displacement at the crown was about 16-22mm. The load on the support system ranged from 0.18 to 0.24 of full overburden pressure.

The geotechnical properties of Edmonton Till in both locations are studied by Matheson (1970), May and Thomson (1978) and El-Nahhas (1980). The ground parameters used in the ground convergence calculations are shown in Table 3.1 for each case. The K_o-value is assumed to be close to unity (K_o=0.8).

Imposing all parameters such as p_i/p_o, H/a, and K_o in the diagrams of modes of yielding (Figs. 2.7 and 2.8) shows that two tunnels lie within the Regime J of Mode II. A continuous yield zone must have developed around the tunnel. This implication permits one to use the "hole-in-plate" model (Section 2.2.4.2) to approximate the ground responses near the tunnel. The ground convergence curves for expected ranges of Young's moduli are calculated for two tunnels and plotted in Figs. 3.5 and 3.6 respectively. On these figures are also shown the relationship between the support pressure and the extent R of the yield zone. For the EXP tunnel an almost uniform radial pressure is predicted in the range of $0.18 \pm 0.05 p_o$ for the measured displacement range u/a=0.027 to 0.035. This pressure and the distribution correspond closely with the measured ($0.12 p_o$). The extent of yield zone should be slightly oval-shaped with a maximum extent at the roof (R/a=1.8±0.2). If the same procedure is applied to the LRT tunnel, the predicted pressure (p_i/p_o=0.12 to 0.15) is comparable to the measured (p_i/p_o=0.18 to 0.24). A reduced E value to 80MPa may yield better agreement. The average extent of yield zone is expected to be about R/a=1.4. However, at this stage GCC (Rf) indicates that the pressure at the roof starts to remain constant at

$0.11p_o$ for $u_i/a \geq 0.01$. Further increase in roof displacement would not compensate with decrease in ground pressure, but could accelerate the propagation of yield zones to the ground surface and thus induce large settlements.

It is of practical importance to evaluate marginal safety against the collapse state, u_{ic} for these two tunnels. The p_{ic} values calculated from Eqn. 2.3 are $0.03p_o$ and $0.09p_o$ for EXP and LRT tunnels respectively. Imposing these values on the GCCs determines the u_{ic}/a values in ranges of 0.09 to 0.13 and 0.013 to 0.018 for the two tunnels. Comparisons between u_{con}/a and u_{ic}/a clearly indicates that EXP tunnel has a higher marginal safety against the collapse state than the LRT tunnel. Because of small marginal safety (as expected for shallow tunnels), it justifies the recommendation proposed by the German Tunnelling guidelines that for shallow tunnels ground pressure of full overburden at the crown should be used in design.

Other Cases

Semi-empirical approaches for predicting the surface settlement profile (e.g., Peck, 1969) are based largely on field measurements of various case histories. In these approaches the location of point of inflection (i) is assumed to be dependent on only the depth ratio (H/a). Since some of the important factors governing the tunnel behaviour (e.g., strength-deformation properties of ground, stress-relief and boundary conditions) are not included in these approaches, a wide scatter of the observed data is expected.

The surface settlement-support stress relationship ($i\text{-}S_s/S_c\text{-}p_i/p_o$) has been introduced in Section 2.2.4.3. Case histories have been collected and presented in Tables C.1 and C.2 (Appendix C). These case histories, grouped in cohesionless and cohesive soils are used to verify the validity of the dependence between the p_i/p_o and i/a discussed eariler (Figs. 2.15 and 2.16c).

a) Cohesionless

Cohesionless soils have a smaller variation in strength-deformation properties as compared to cohesive soils. Hence it is reasonable to assume that the strength-deformation aspect does not exert significant influence on the field measurements in case histories listed in Table C.1. These results are plotted in Fig 3.7a and b, and the following aspects are observed.

1. Fig. 3.7a is a plot of H/a versus i/a similar to the one given by Peck (1969). It can be seen that a significant number of case histories (especially, H/a>5) lies outside the boundaries predicted by Peck (1969). This implies that i/a depends on H/a as well as other factors.
2. The same case histories were grouped in four depth ranges and the results are replotted in Fig. 3.7b to observe the influence of the H/a ratio. On Fig. 3.7b is also drawn boundaries for tunnels of H/a<5 and H/a>5. From comparison between Fig. 2.16b and Fig. 3.7b, similar features are identified: (i) for shallow

tunnels i decreases to a limiting value with a small increase in S_s, and (ii) for deep tunnels i also decreases with S_s but at a slower rate. The results from model tests (denoted by squares) tend to yield the lower bound of i/a values because the measurements were taken near collapse. For the depth range of H/a<5 the ratio i/a approaches its limiting value when S_s/a exceeds 1.0%. This is explained by the fact that a small displacement at the crown (S_c/a) will cause the yield zone to propagate to the ground surface and i is predetermined by β (e.g., S_c/a=0.4% for yield zone reaching the ground surface in FE analyses Case ST1). For deep tunnel the dependency between i/a and S_s/a becomes more pronounced, i.e., i will reach its limiting value through large S_s.

3. The influence of K_o cannot be properly assessed because the K_o value was seldom recorded in the case histories. However, for normally consolidated sand K_o is approximated by (1-sinϕ). Small variations of ϕ in sand limits the range of K_o. From the FE Analyses it was found that at a given p_i/p_o the i/a will be larger in high K_o than low K_o.

b) Cohesive Soils

Cohesive soils exhibit a wider variation in strength-deformation properties (E_u and c_u) than cohesionless soils. Thus in order to isolate the strength-deformation effects for better interpretation of the field measurements, the case histories are subdivided into categories of (1) c_u = 0 to 100kPa and (2) c_u >100kPa. Their results are plotted in Figs. 3.8 and 3.9 respectively. Several aspects of practical interest are dissected.

1. For c_u=0 to 100kPa (Fig. 3.8) similar observations as for cohesionless soils are found. For shallow tunnels (H/a<5) the i/a becomes independent of S_s/a when S_s/a exceeds 1.2%. Deep tunnels show strong dependency between i/a and S_s/a.
2. From Fig. 3.9 (c_u >100kPa) the surface settlement is relatively small (<1.0%) and this may be attributed to the high strength (or stiffness). There seems to be a linear relationship between H/a and i/a, i.e., i/a increasing with H/a.
3. Generally the cohesive soils have a less critical settlement trough than the cohesionless soils. This may be due to higher K_o (close to 1.0) in overconsolidated cohesive soil.

Table 3.1 Input Data for Constructions of GCC for EXP and LRT Tunnels

	EXP Tunnel (after El-Nahhas, 1980)	LRT Tunnel (after Branco, 1981)
Soil Model	Perfectly Elastic-Plastic, Cohesionless (associated flow rule)	
Angle of Internal Friction (deg.)	30	40
Young's Modulus (MPa)	40 - 80	100 - 150
Poisson's Ratio	0 4	0 4
Depth to Tunnel axis	24 m	10 m
Tunnel Radius	1 28 m	3 05 m
Depth/Radius (H/a)	18 8	3.4
Surface Settlement	7 - 12 mm	9 - 10 mm
Crown Settlement	40 - 45 mm	16 - 22 mm

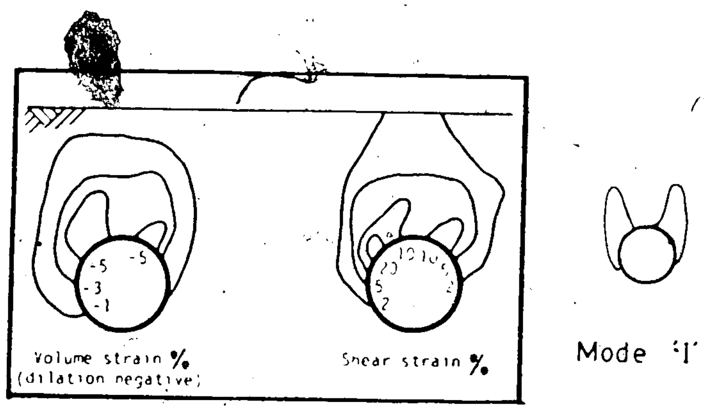

(a) Gravity test

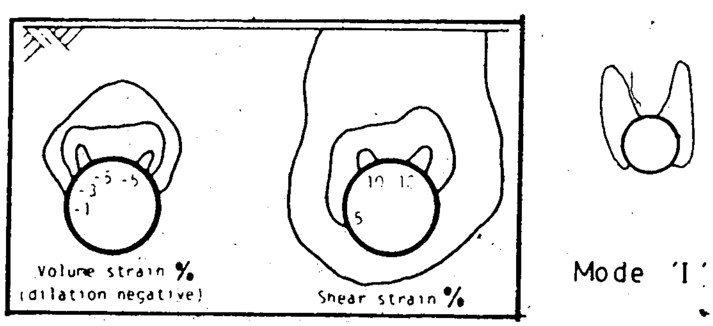

(b) Centrigual test

Figure 3.1 Contours of Volume and Shear Strains in Sand (modified from Atkinson and Potts, 1977)

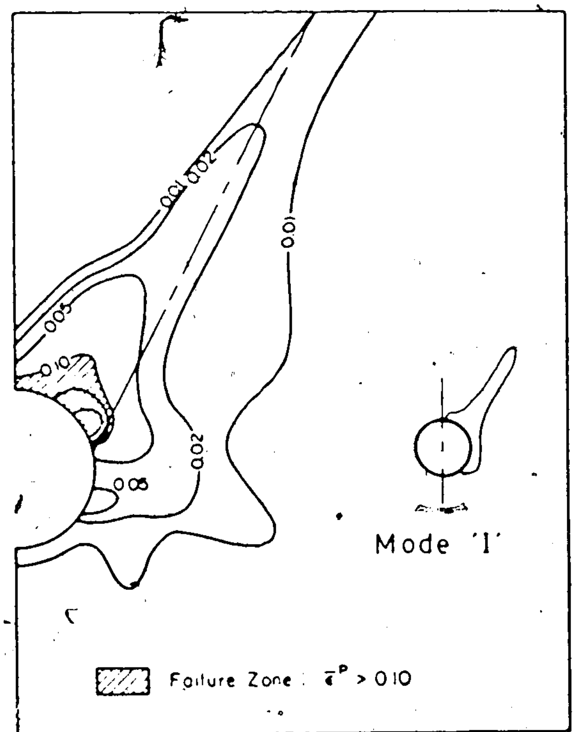

Figure 3.2 Contours of Shear Strains in Sand (modified from Cording et al. ,1976)

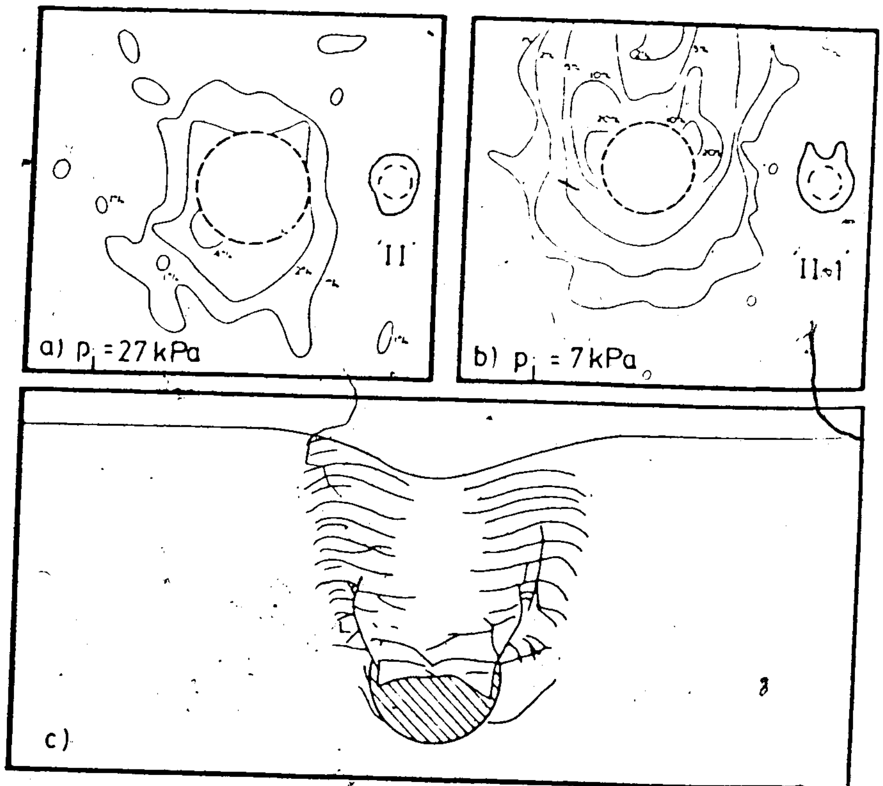

Figure 3.3 Contours of Volume and Shear Strains in Kaolin (modified from Atkinson et al., 1974)

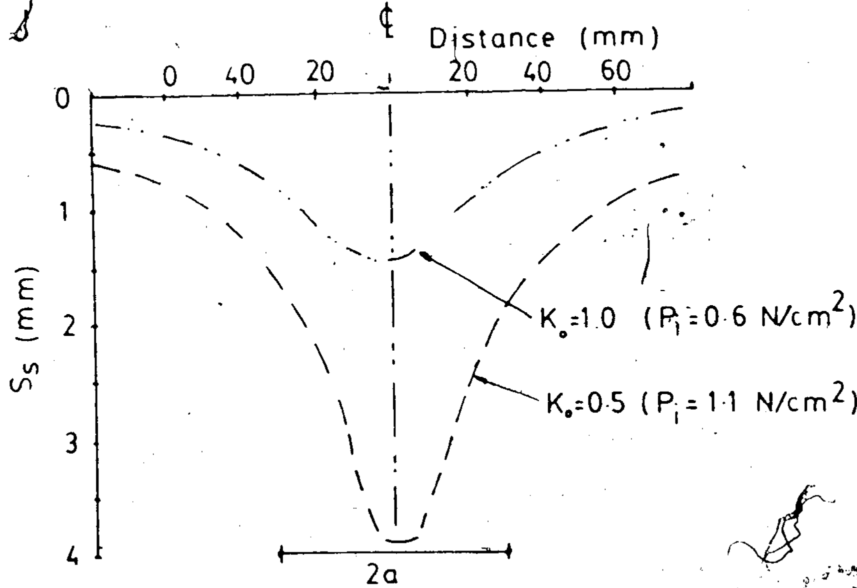

Figure 3.4 Surface Settlement Profiles in Sand (modified from Potts, 1976)

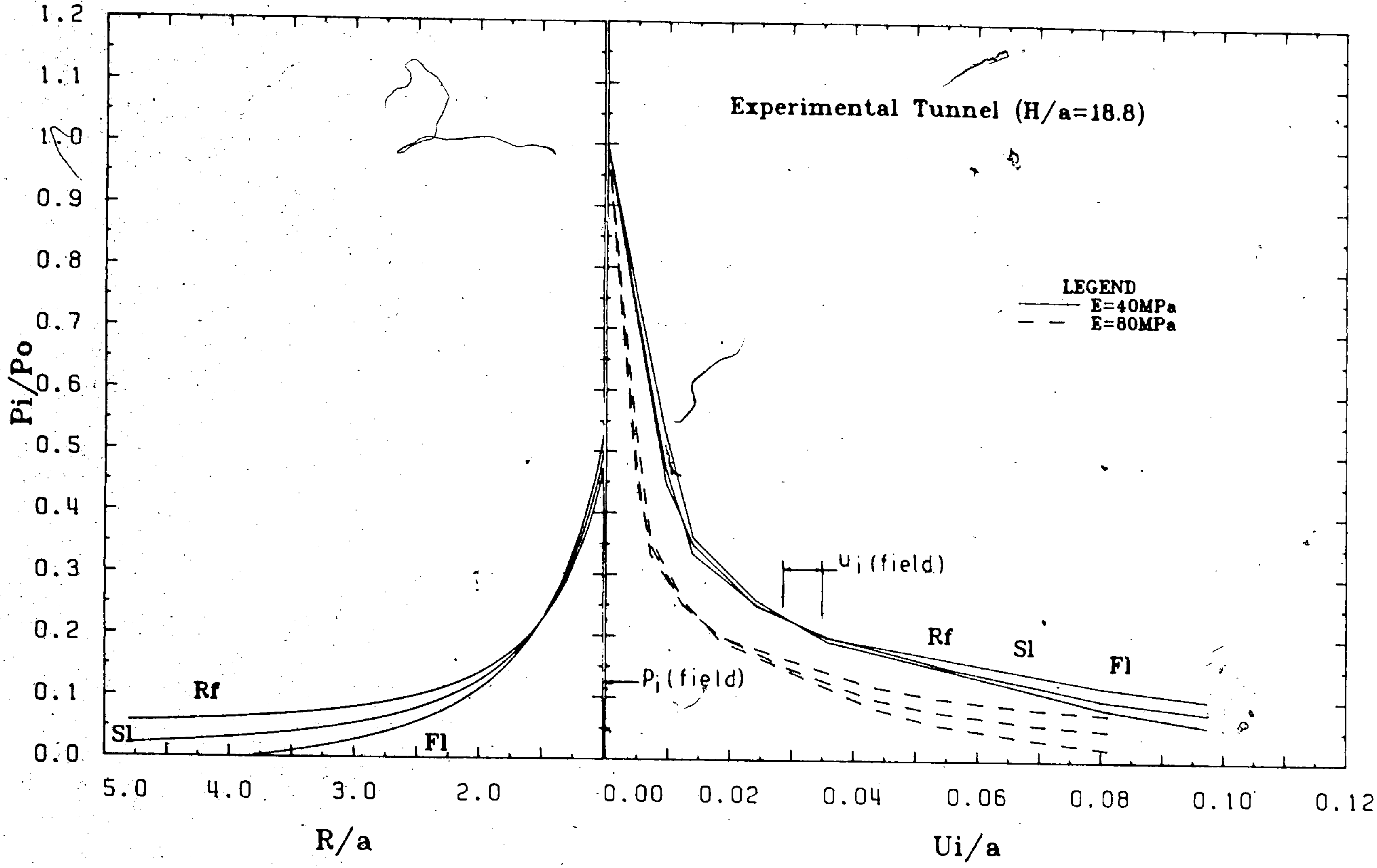

Figure 3.5 GCC and Support Pressure-Extent of Yield Zone (EXP Tunnel)

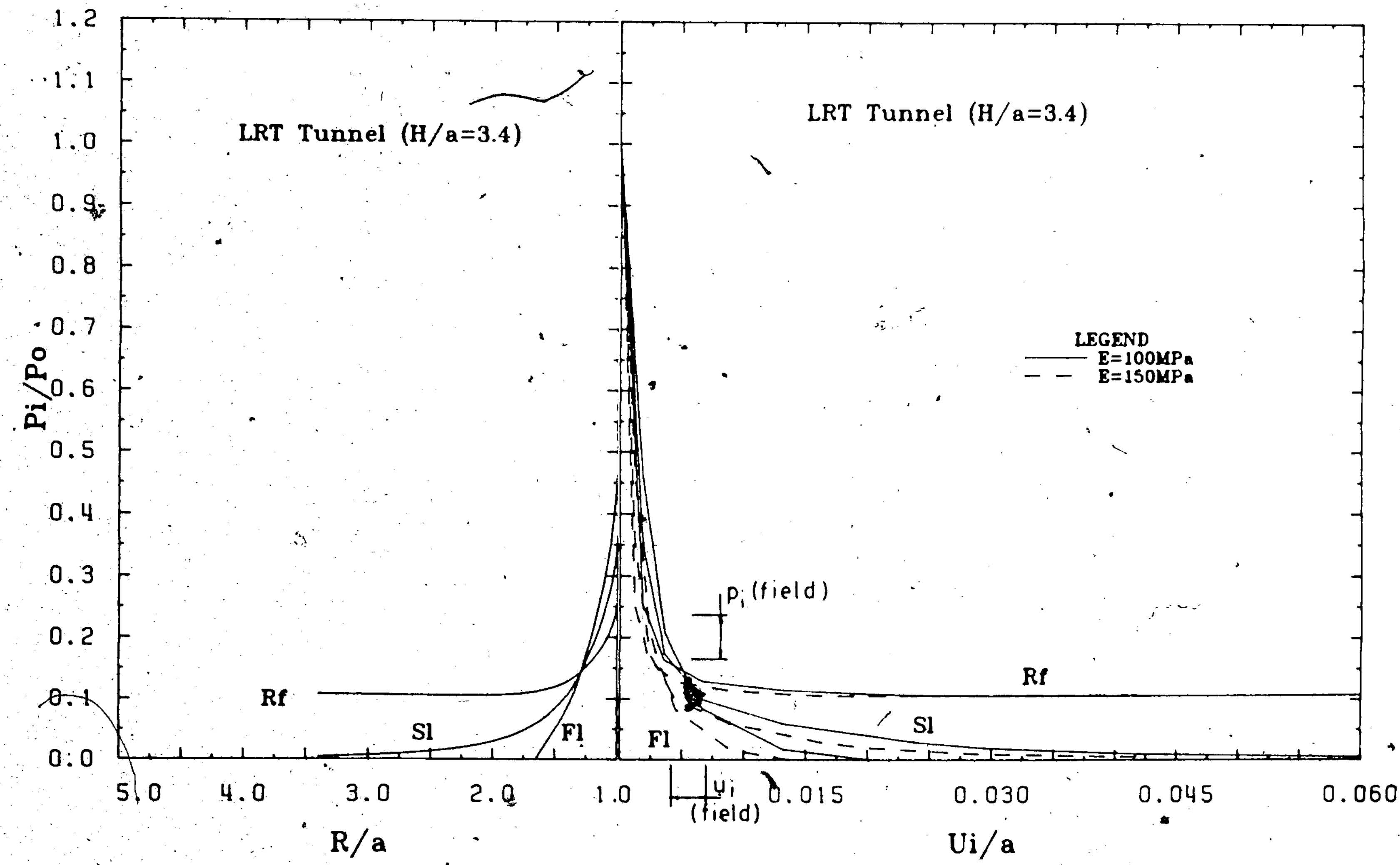

Figure 3.6 GCC and Support Pressure-Extent of Yield Zone (LRT Tunnel)

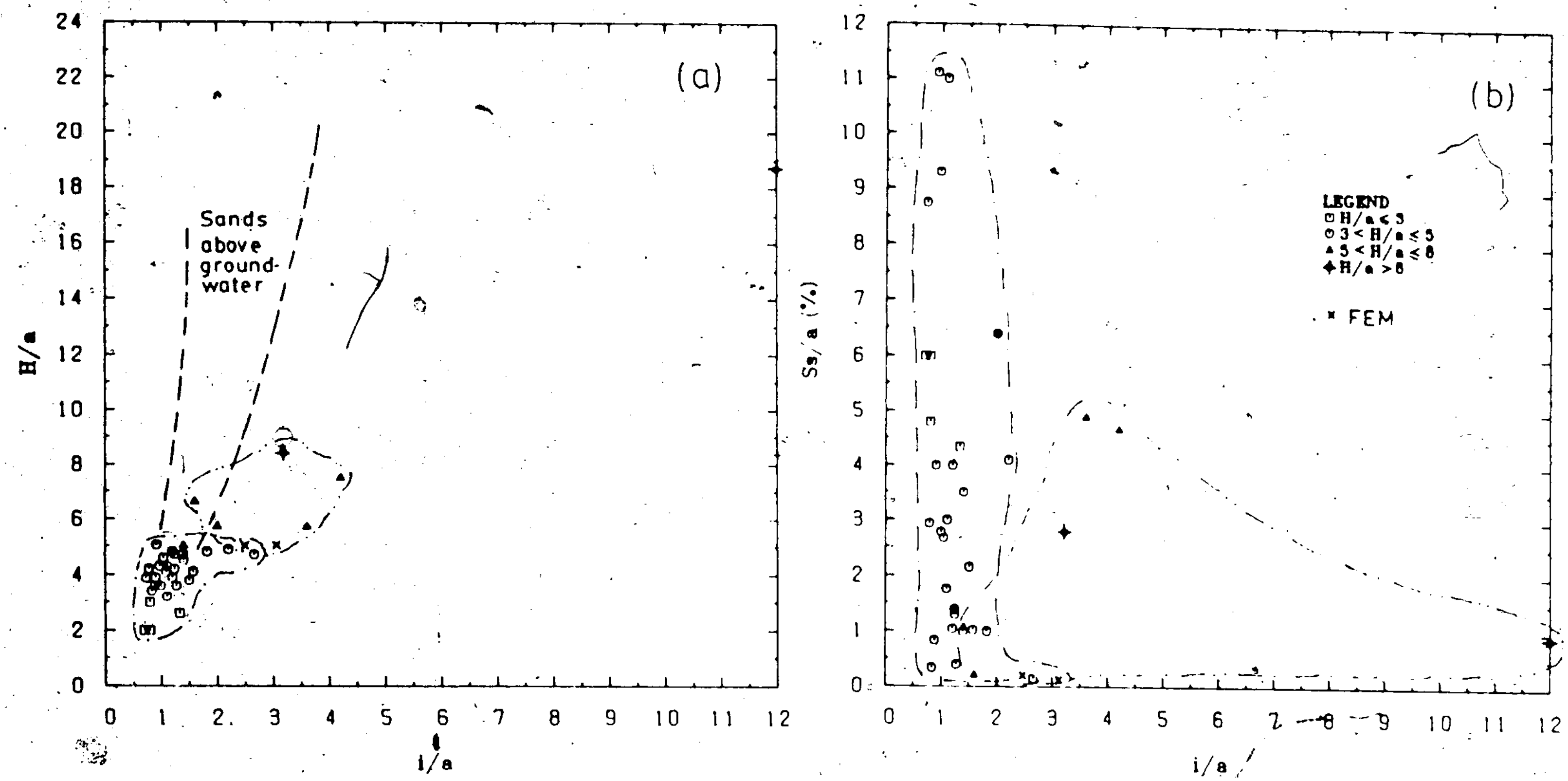

Figure 3.7 Field Measurements (Cohesionless Soils)

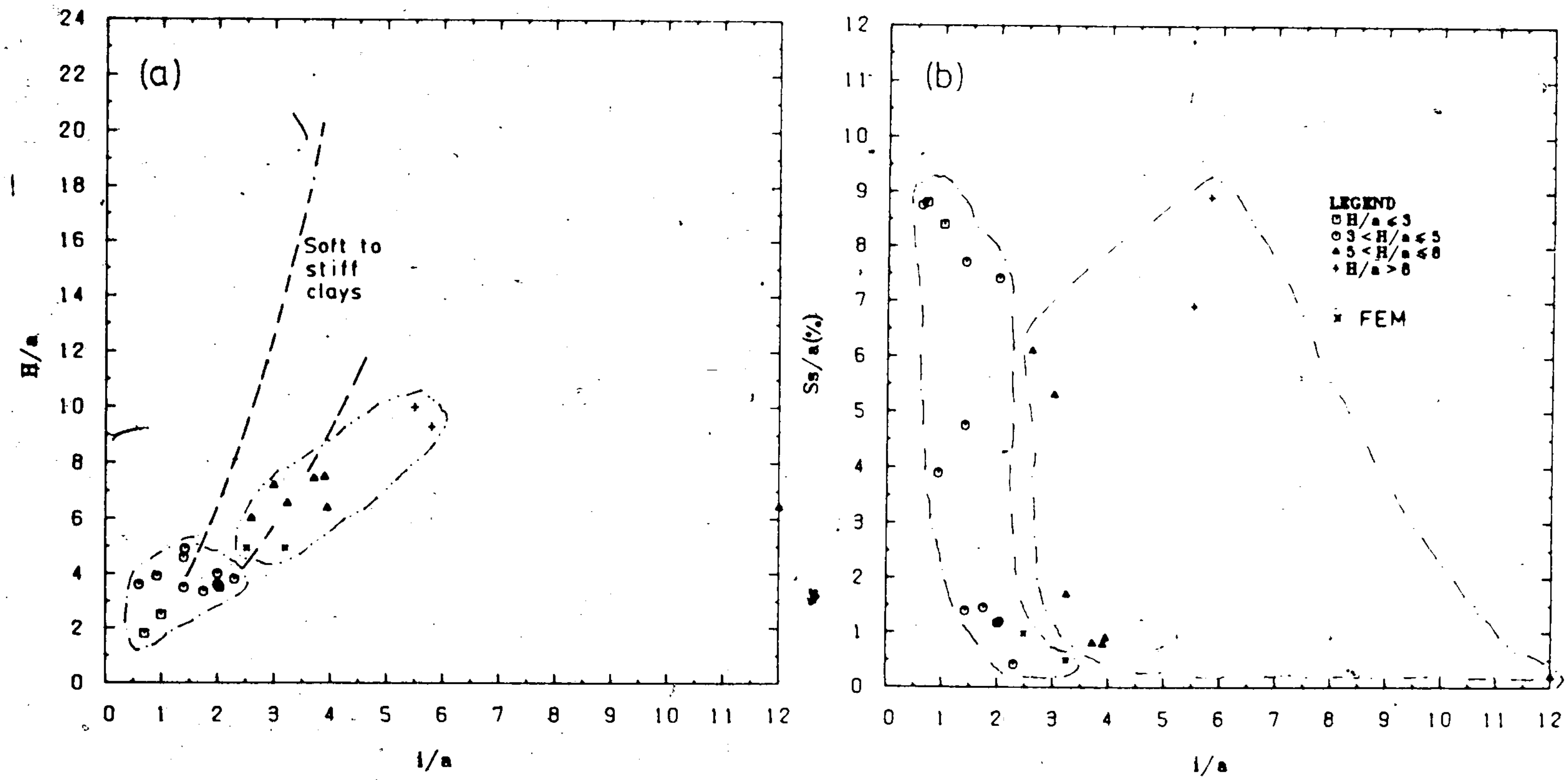

Figure 3.8 Field Measurements (Cohesive Soils, Cu= 0 to 100kPa)

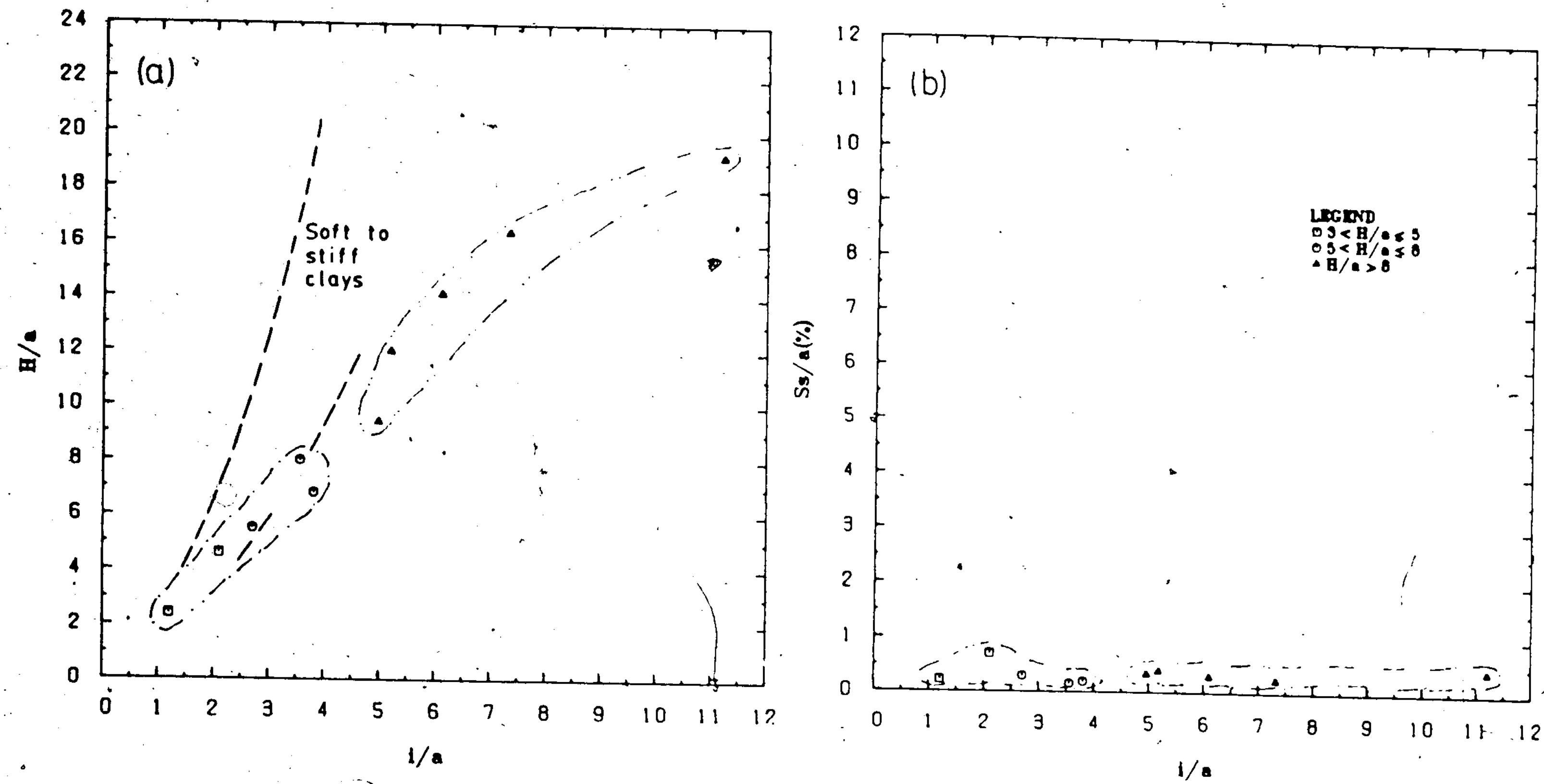

Figure 3.9 Field Measurements (Cohesive Soils, Cu>100kPa)

4 . DESIGN OF SHAFT IN SOIL

4.1 Introduction

Geotechnically, the design of a shaft in soil consists of two major steps: (1) to design the shaft lining to prevent instability of shaft wall, and (2) to estimate the soil movement associated with shaft construction. Although these two tasks are interrelated, they are usually dealt with separately.

Most of the currently available design approaches are based on limit equilibrium methods, e.g., Terzaghi (1943), Berezantzev (1958) and Prater (1977). This type of analysis considers only equilibrium of the forces acting on an assumed failure mass defined by hypothetical rupture surfaces. The formation pressures on the shaft lining are determined by satisfying force equilibrium, but these do not correspond with the actually expected pressure which depends on such factors as ground deformation, insitu stress, and ground strength-deformation properties. As the constitutive relationship of the ground is not considered explicitly, no closed-form solution is available for the determination of the displacements at the shaft wall and inside the soil mass. In these design methods, it is attempted to control and limit the displacements by choice of a suitable factor of safety. Furthermore, excessive yielding is prevented by the selection of an appropriate construction sequence. Besides for simplicity of analysis, there is no particular reason why one has to separate the determinations of the lining pressure from the ground deformation in shaft design.

The convergence confinement method provides an analytical framework to predict the formation pressure and the soil deformation simultaneously. However, this method requires additional information about the ground and support, such as insitu stress, constitutive relationship of ground, support characteristics and construction details. Also, some restrictive assumptions must be made to obtain a closed-form solution for the ground convergence curve, e.g., plane strain condition. Hence, this method has, so far, only been applied to two-dimensional circular, horizontal openings like deep tunnels.

Since the analysis of a shaft is a three-dimensional problem, the direct application of the convergence confinement method is not adequate to describe the shaft behaviour. Hence, some techniques such as force equilibrium have to be included to account for the behaviour in the third dimension. By combination of the force equilibrium technique and the convergence confinement method (CCM), it is possible to derive ground convergence curves (pressure-displacement relationships) for the shaft wall, to rationally assess the required support pressure and to evaluate the limits of applicability of conventional limit equilibrium methods for shaft design.

In the following, conventional design methods for shafts are reviewed briefly and the proposed confinement convergence method for shaft design is then presented. Typical mechanisms of shaft behaviour including yield initiation, modes of propagation of the plastic zone and gravity effects due to vertical arching are studied in detail. The second part presents examples generated by the finite element method and a comparison with results of the proposed CCM as well as the limit equilibrium methods.

The proposed technique has been applied to several case histories (Lade *et al.*, 1980; Muller-Kirchenbauer *et al.*, 1980; Britto and Kusakabe, 1984; and Kaiser and Wong, 1984) and good agreement has been achieved.

4.2 Review of Conventional Shaft Design Techniques

4.2.1 Terzaghi's Method

Based on the state of stress in the vicinity of a drill hole, Terzaghi (1943) derived the earth pressure distribution for a circular shaft located above the water table in cohesionless soil.

Near the borehole or shaft wall, the principal stresses are the vertical stress σ_v, the tangential stress σ_t and the radial stress σ_r where the radial stress is normally the minor principal stress. The orientation of the surface along which failure would occur by plastic flow is either inclined (conical) or vertical (spiral) and is determined by the maximum stress difference between $(\sigma_v-\sigma_r)$ or $(\sigma_t-\sigma_r)$. Whether σ_v or σ_t is the major principal stress depends on the insitu stress coefficient K_o. For low K_o (say ϕ=30°, K_o=0.5), failure will occur along inclined surfaces, dipping toward the shaft, i.e., governed by the stress difference $(\sigma_v-\sigma_r)$. For high K_o (say ϕ=30°, K_o=1.0), the stress concentration near the wall causes σ_t to become the major principal stress, and the stress difference

($\sigma_t - \sigma_r$) produces shear failure in vertical surfaces.

Terzaghi observed the downward and inward movements of the shaft wall, and argued that near the surface these movements of the shaft wall cause the tangential stress (intermediate stress) to increase until in the limit, the surface of plasticity becomes vertical instead of inclined (even at low K_o) (see Fig. D.1, Appendix D). This assumption permits the application of the equations describing the state of stress near the wall of a drill hole (hole-in-plate) for the shaft case. With a known state of stress and a linear Mohr-Coulomb failure criterion, the extent of the plastic zone can be determined. Terzaghi calculated the minimum support pressure to maintain the limit equilibrium state of such a plastic zone (McCreath, 1980). Terzaghi's approximation of a three-dimensional state may be viewed as a method of accounting for the necessary limit equilibrium condition of a potential failure block under the action of gravity.

4.2.2 Berezantzev's Method

Berezantzev (1958) proposed the method of earth pressure calculation on the retaining walls of circular cylindrical form, based on the solution of axisymmetrical problems of the limit equilibrium theory (Fig. D.2). He assumed the soil medium surrounding the shaft yielded along inclined surfaces dipping toward the shaft.

In Berezantzev's method, the states of stress around the shaft are given by two differential equations of equilibrium. These equations are made determinant by introducing the Mohr-Coulomb failure criterion and a simplified assumption of equalization of principal stresses. The stress conditions are determined by solving the differential equations using the numerical "step-by-step computation" technique (Sokolovsky, 1954).

4.2.3 Prater's Method

Prater (1977) computed the earth pressure on shaft linings using a limit equilibrium analysis of an assumed truncated, hollow cone failure block. He included several parameters, such as the earth pressure coefficient K_o and the tangential forces induced by the inward movement of the cone, and investigated their influence on the calculated support pressure. He found that the tangential force (T) induced by the inward movement had an outward acting wedge component (F) that increases with depth and increasing earth pressure coefficient (see Fig. D.3). Consequently, Prater's method leads to a reduction in support pressure with great depth.

The active earth pressure for a shaft wall and the earth pressures as a function of the depth factor (H/a) for typical soil parameters predicted by these three methods, are shown in Fig. 4.1 for comparison. The distribution of earth pressure predicted by Terzaghi (1943) and Berezantzev (1958) are almost identical (for ϕ=30°, c=0) and reach an asymptotic value at a depth of H/a>4. Prater predicts slightly higher pressures for this case at H/a=4 and zero pressure at H/a=9. It is intuitively obvious that the assumptions made by Prater are not valid at great depth.

There must be a minimum support pressure at great depth in yielding ground and, hence, Prater's solution cannot be valid below a critical depth unless unreasonably large movements are permitted (see also discussion on convergence confinement method).

4.2.4 Convergence Confinement Method

The convergence confinement method is an analytical approach to predict the stresses and displacements in the soil around an underground opening and in the support elements. This method describes how ground and support interact with each other. The ground behaviour is represented by a ground convergence curve (GCC) and the lining by a support confinement curve (SCC). The former describes the ground convergence in terms of the internal pressure relief while the latter relates the confining pressure acting on the lining to its deformation. The equilibrium condition for the ground-support interaction is given by the interaction of the GCC and SCC, as illustrated and described in detail earlier in Fig. 1.1.

Two basic assumptions are normally made for derivation of the GCC and the SCC: (1) two-dimensional plane strain model; and (2) plastic yielding controlled by tangential-radial stress difference ($\sigma_t - \sigma_r$). These two conditions are generally applicable to tunnelling at depth but they do not necessarily satisfy conditions near a shaft.

Brown *et al.* (1983) presented a summary of currently available GCC formulations of different material models. The characteristics of the SCC for different liner or tunnel support types were summarized by Hoek and Brown (1981) and do not need to be reviewed here. However, whether and under what conditions the shaft behaviour can be simulated by a "vertical tunnel" or by the two-dimensional, "hole-in-plate" theory needs to be investigated further.

The behaviour of a shaft is affected by gravitational forces and is a three-dimensional problem in which three stress components (σ_t, σ_v and σ_r) must be considered. The mode of yielding and its initiation and propagation, depend on the initial insitu stress state described by K_o. The shaft response to stress relief during excavation is further complicated by the influence of the free stress boundary near the ground surface resulting in a linearly varying horizontal stress field with depth. In order to apply the two-dimensional "hole-in-plate" model to determine the relationship between support pressure and shaft wall displacement, it is necessary to understand the mechanisms of shaft behaviour so that some adjustments may be made to account for these aspects in the analysis.

The excavation of a shaft can be simulated by a stress relief ($\Delta\sigma_r$ at the shaft wall causing the surrounding soil to deform both horizontally and vertically). Excessive stress relief may induce yielding near the opening and cause permanent plastic deformations. The magnitude of support pressure, wall displacement and extent of plastic zone are interrelated. The stress relief during shaft excavation causes stress redistribution near the opening, and thus induces (1) horizontal and (2) vertical archings as illustrated in Fig. 4.2. The horizontal arching is explained by the development of hoop stresses in a horizontal plane, i.e., an increase in the tangential stresses. The vertical arching arises from the formation of a plastic zone of limited extent around the shaft with a tendency to move in the vertical direction. Vertical arching develops between the shaft support and the surrounding unyielded soil mass. Collapse is prevented by these two mechanisms that need to be considered to describe mechanisms of shaft behaviour.

4.2.4.1 Simulation of Horizontal Arching

The horizontal arching is best represented by the "hole-in-plate" model. The shaft may be viewed as a stack of plates with a hole subjected to insitu stress: (Fig. 4.2b). The differential wall displacement along the shaft is assumed to cause negligible shear developed between plates. Hence, each plate can be treated individually as a two-dimensional problem. The ground convergence curve and the extent of the yield zone are characterized by the material properties, the magnitude of stress relief or wall displacement permitted, and the initial state of stress. Solutions presented by Brown *et al.* (1983) are applicable to this condition but are restricted to two-dimensional plane strain ($\sigma_t-\sigma_r$) yielding and initial uniform insitu stresses. Other modes of yielding (e.g., due to $\sigma_v-\sigma_r$) do result in different ground responses as will be discussed later.

4.2.4.2 Simulation of Vertical Arching (Gravity Effect)

Owing to the stress relief in the radial direction, the soil particles around the shaft opening will undergo vertical displacement under the effect of gravity (simply referred to as "gravity effects" in this chapter). The soil particles may remain stable and be kept in equilibrium position by the shear resistances derived from the interactions with the adjacent stationary soil mass and the shaft lining. This phenomenon is referred to as vertical arching (see Fig. 4.2a). If yielding around the shaft takes place and creates failure blocks that have a tendency to slide into the shaft opening under the gravity effect, an external support pressure may be required to prevent the instability. For example, in the case of yielding induced by the tangential-radial stress difference, the strength of the ground is reached along the vertical log-spiral surfaces only for horizontal movement. The soil will, however, still be able to resist forces due to gravity for movement in the vertical direction if the strength is not reached for movement in this direction. Hence, only part of the gravity component will create additional stresses on a shaft support (besides support stresses in horizontal arching) if yielding in vertical and horizontal directions are exceeded simultaneously.

The support stresses required in resisting the gravity effect can be determined by considering the limit force equilibrium of the yield zone. This approach has been adopted in calculating horizontal stresses on silo walls (Kendal, 1980). Handy (1984) used the same approach with some adjustment in soil-wall interaction to estimate the lateral pressures behind retaining walls, and claimed satisfactory correlation with model test observations.

Fig. 4.2(d) shows forces acting on a horizontal differential soil element within the yield zone. The vertical stresses are assumed to be uniform at each depth. Summation of vertical forces in Fig. 4.2(d) give

$$d\sigma_v = [\gamma - (2\pi\sigma_v/A)\ (K_s\mu_s\ R/\sin(a) + K_w\mu_w a)]\ dh \qquad 4.1$$

where: A - the sectional area of the plastic zone

a - the inclined angle as shown in Fig. 4.2d (This angle can be taken as 90° on the conservative assumption)

K_s - K coefficient at soil to soil interface

K_w - K coefficient at wall to soil interface

μ_s - frictional coefficient at soil to soil interface

μ_w - frictional coefficient at soil to wall interface

Integration of Eqn. 4.1 will give the vertical stress distribution along the shaft depth, and thus the horizontal stresses required to prevent instability due to the gravity effects. Detailed treatments on Eqn. 4.1 are given in Appendix D.1.

In Eqn. 4.1, the geometry of the plastic zone and the soil-lining properties govern the stress distributions. The extent of the plastic zone which was usually assumed in most past works (e.g., Handy, 1985) can be predicted with reasonable accuracy (see section on Mechanisms of Shaft Behaviour). The soil-lining properties are discussed in

Appendix D.

Several numerical examples have been generated to illustrate the role of the gravity effect in shaft design. Fig. 4.3 shows dimensions of the shaft and extent of plastic zone. Results of analyses following equations of Appendix D.1 on these numerical examples for cohesionless and cohesive soils are plotted in Figs. 4.4 and 4.5 respectively, along with the soil properties.

Fig. 4.4 indicates that for cohesionless soil, the support pressure due to gravity effect increases as the extent of yielding increases. The distribution of the support pressures also depends on the configuration of the plastic zone. The support pressure reduces to zero at great depth for cone shaped plastic zone, and to a constant value for plastic zone of constant radius which was assumed by Terzaghi (1943). Near the surface, the pressure is close to the active earth pressure (K_a case), implying that the gravity effect dominates at shallow depths.

In the cohesive soil, the support pressure to prevent any instability due to gravity effect also increases for a larger yield zone. A distinct difference in vertical arching action exists between cohesionless and cohesive soils. For cohesive soils, the support pressure applied along the whole shaft depth does not enhance the stability because the shear strength of the cohesive soil is independent of the confining pressure. The support pressure has to be applied at the bottom to inhibit the collapse mechanism (Britto and Kusakabe, 1983).

4.3 Design Based on Convergence Confinement Method (CCM)

It has been shown that the behaviour of the shaft can be described by horizontal and vertical arching around the shaft. These two arching actions can be quantified by use of the convergence confinement method and the gravity effect. Hence, it is possible to derive a relationship between the support pressure and the displacement allowed during the construction. The CCM with inclusion of gravity effect for shaft analyses can be summarized in the following steps (Fig. 4.6):

1. Identify the mode of yielding at the shaft wall. This mode, dependent on the initial in-situ stress (K_o), governs the extent of the plastic zone as well as the shape of convergence curve.
2. Calculate the ground convergence curves along with the extent of plastic zone, using appropriate two-dimensional model for various depths (h_i) (see Fig.4.6(a)).
3. For specific displacements (u_s), establish pressure versus depth and plastic zone versus depth relationships from (2) (Fig. 4.6(b)).
4. With the configuration of the plastic zone around the shaft, determine the support pressure due to the gravity effect (p_g) with depth (Fig. 4.6(c)).
5. Two pressure distributions due to horizontal and vertical archings form an envelope of design pressure (Fig. 4.6(c) is the support pressure for given displacement u_s).
6. Adjust the design pressure envelope at the bottom of

the shaft due to face effect (Panet and Guenot, 1982).

It follows from the above calculation steps that a particular displacement corresponds to a unique support pressure distribution. Hence, it is possible to evaluate the limit equilibrium method of shaft design (e.g. Berezantzev, 1958) in terms of displacement.

4.4 Mechanism of Shaft Behaviour

Prior to excavation, a soil element adjacent to the shaft wall is subjected to the initial stresses, as shown in Fig. 4.2b. The excavation of the shaft at any particular level may be simulated by progressively reducing the internal support pressure (radial stress, σ_r). For the axisymmetrical case, as long as the soil material remains in the elastic range, the stress distributions in the plane of the section are given by Eqns. 4.2 to 4.4 (Lame's equations; Terzaghi, 1943).

$$\sigma_v = \gamma h = p_o \qquad 4.2$$

$$\sigma_r = K_o p_o - [K_o p_o - p_i](a/r)^2 \qquad 4.3$$

$$\sigma_t = K_o p_o + [K_o p_o - p_i](a/r)^2 \qquad 4.4$$

It is important to realize that Eqns. 4.2 to 4.4 are derived based on the following assumptions: (i) σ_v, σ_r and σ_t are principal stresses, (ii) shear stresses along the shaft wall are small for a constant wall displacement and (iii) the bottom of the shaft is remote from the section.

As p_i is reduced, stress differences among σ_v, σ_r and σ_t are generated at the shaft wall due to the increasing σ_t and decreasing σ_r (i.e., horizontal arching). If the stress difference exceeds the strength of the soil, three possible alternatives of stress combinations may initiate yielding. Plasticity could be generated by stresses in a vertical surface by the tangential-radial stress difference $(\sigma_t - \sigma_v)$. The onset of the plasticity (the mode of yield initiation) depends on the value of K_o and strength parameters of the soil. For simplicity, the following derivations are for cohesionless material only. The formulations for cohesive material are given in Appendix D.2.

Assuming a purely frictional material with a linear Mohr failure criterion, the maximum stress ratio which may be sustained is:

$$\sigma_1/\sigma_3 = N = \tan^2(\pi/4 + \phi/2) \qquad 4.5$$

Three yielding mode criteria can be calculated from Eqns. 4.2 to 4.4, and the support pressures (p_i) corresponding to three possible modes of yield initiation are listed as follows:

$$\text{For } \sigma_t - \sigma_r: \; p_i = 2K_o p_o/(N+1) \qquad 4.6$$

$$\text{For } \sigma_v - \sigma_r: \; p_i = p_o/N \qquad 4.7$$

For

$\sigma_t - \sigma_v$: $p_i = (2K_o - N)p_o$ 4.8

The largest value of p_i will, of course, govern the mode of yield initiation, which can be expressed in terms of required K_o:

Mode A for $\sigma_t - \sigma_r$: $(N+1)/2 > K_o > (N+1)/2N$ 4.9

Mode B for $\sigma_v - \sigma_r$: $K_o < (N+1)/2N$ 4.10

Mode C for $\sigma_t - \sigma_v$: $K_o > (N+1)/2$ 4.11

Mode A is the mode commonly evaluated for tunnels in yielding ground. For example, for a typical value N of 3 (ϕ = 30°),

Mode A governs for $0.67 < K_o < 2.0$ (Fig. 4.7a);
Mode B governs for $K_o < 0.67$ (Fig. 4.7b); and
Mode C governs for $K_o > 2.0$.

Mode C, although possible, has been neglected in the following analysis because it is of less practical significance in soft ground. The boundary between the other two modes of yield initiation at the wall can be described by a critical K_o-value, K_{cr}. Mode A is observed for $K_o > K_{cr}$. For these two cases of Modes A and B, the relationships among support pressure, wall convergence and extent of plastic zone can be derived separately.

a) Mode A ($\sigma_t - \sigma_r$) at $K_o > K_{cr}$:

Fig. 4.8 shows the sequential stages for Mode A as the internal support pressure is reduced. The vertical stress always acts as an intermediate stress. Initiation of yielding and propagation of the plastic zone (R_{tr}) are controlled by the tangential-radial stress difference. The relationships between the support pressure and the radial convergence at the wall for yielding ground (i.e., ground convergence curve) have been well studied by other authors (e.g., Brown *et al.*, 1983). For simplicity, the pressure-displacement relationships are calculated herein by application of the model proposed by Ladanyi (1974) assuming associated flow rule, constant volume change and plane strain condition. Other models could be incorporated, but will not be treated in detail.

During the first stage (Fig. 4.8), the vertical stress remains constant, radial stress decreases and tangential stress increases according to Eqn. 4.2 to 4.4. Yield initiation of Mode A occurs if the condition of

$$\sigma_t/\sigma_r = N \text{ or } p_i = 2K_o p_o/(N+1) \qquad 4.12$$

is satisfied. The magnitude of wall convergence with p_i from Eqn. 4.12 is given:

$$u_i = a[(K_o p_o - p_i)(1+\nu)]/E \qquad 4.13$$

Further relaxation of the fictitious internal support pressure (p_i) causes the propagation of the plastic zone, and the tangential stress decreases to satisfy the failure criteria. The extent of the plastic zone and the radial wall convergence (Ladanyi, 1974) are given by:

$$R_{tr} = a[2K_o p_o/(N+1)p_i]^{1/(N-1)} \qquad 4.14$$

$$u_i = a\{1-[(1-e_{av})/(1+A_v)]^{1/2}\} \qquad 4.15$$

For a given p_i, the plastic radius, R_{tr} can be calculated from Eqn. 4.14, and thus the corresponding wall displacement, u_i can be determined from Eqn. 4.15. Ground convergence graphs of p_i versus u_i and p_i versus R_{tr} can be established, as schematically shown in Figs. 4.6.

As the tangential stress decreases during yielding and becomes equal to the vertical stress (Stage(2) of Fig. 4.8), p_i becomes equal to $K_a p_o$. Substitution of this p_i-value into Eqns. 4.14 and 4.15 will yield R_{tr} and u_i for this stress state, i.e., $\sigma_t = \sigma_v > \sigma_r$ and $\sigma_v = p_o$.

During Stage(3) at which the internal pressure continues to decrease, the tangential stress will decrease to satisfy the failure criteria and equilibrium state, whereas the vertical stress drops due to arching between the shaft support and the elastic ground. The value of R_{tr} and u_i at this stage can again be determined by Eqns. 4.14 and 4.15. An example is given later.

b) Mode B $(\sigma_v-\sigma_r)$ at $K_o<K_{cr}$:

Fig. 4.9 shows the stress distributions in a horizontal section through a shaft at a particular depth in sequential stages of reducing the internal support pressure, i.e., simulating the shaft excavation.

At Stage (1), the yielding initiates at the wall as the vertical-radial stress difference violates the yield criterion. The stress distributions are given by Eqns. 4.2 to 4.4. Hence, the wall displacements are elastic and can be calculated using Lame's equation assuming elastic material behaviour.

$$u_i = a[(K_o p_o - p_i)(1+\nu)]/E \text{ and } p_i = \sigma_v/N = K_a p_o$$

$$\text{or } u_i = a[(K_o - K_a)p_o(1+\nu)]/E \qquad 4.16$$

As p_i is further reduced, σ_t still increases and σ_v decreases due to vertical shear stress induced by vertical downward displacement (Stage (2) in Fig. 4.9). Yielding propagates outward from the wall and the radial and tangential stress distributions are still given by Eqns. 4.3 and 4.4. But these stresses at the wall (r=a) also satisfy the failure criterion, i.e.:

$$\sigma_t/\sigma_r = N \qquad 4.17$$

The extent of the plastic zone due to Mode B yielding at this stage is determined by equating the radial stresses at the elastic-plastic interface, i.e., the stress continuity. At the elastic-plastic boundary, the elastic radial stress is given by Eqn. 4.3, and the radial stress in the plastic zone is given by:

$$\sigma_r = \sigma_v/N \text{ and } \sigma_v = p_o \qquad 4.18$$

Equating Eqns. 4.3 and 4.18 yields

$$R_{vr} = a\sqrt{[(K_o p_o - p_i)/(K_o - K_a)p_o]} \qquad 4.19$$

Once the extent of the yield zone has been determined, it is of interest to predict the related wall displacement allowed in Stage (2). One can make use of the same model as in Mode A yielding, i.e., Eqn. 4.15.

At the end of Stage (2), the tangential stress becomes equal to the vertical stress and the support (radial) stress is given by Eqn. 4.12, or

$$p_i = 2K_o p_o/(N+1) \qquad 4.20$$

Further relief in p_i as allowed in Stage (3) causes a decrease in σ_v and σ_t in order to satisfy the failure criteria given by Eqns. 4.17 and 4.18. At this stage, the extent of the plastic zone (R_{vr} in Fig.4.9) is still governed by Mode B yielding, but the radial stress distribution will be different from that in Eqn. 4.3) because of the need to satisfy Eqn. 4.17. Hence, in order to determine the plastic zone in this stage, one needs to calculate the radial stress distribution.

Fig. 4.9(3) shows that inside the plastic zone ($r<R_{tr}$) where the states of stress are $\sigma_t=\sigma_v>\sigma_r$, the radial and tangential stress distributions are (Landanyi, 1974):

$$\sigma_r = p_i(r/a)^{N-1} \qquad 4.21$$

$$\sigma_t = Np_i(r/a)^{N-1} \qquad 4.22$$

and the plastic zone (R_{tr}) is given by:

$$R_{tr} = a[2K_o p_o/(N+1)p_i]^{1/(N+1)} \qquad 4.23$$

Between the distance ($R_{tr} < r < R_{vr}$), the radial stress distribution is governed by the stress equilibrium with tangential stress:

$$\sigma_r = K_o p_o-(K_o p_o-\sigma_r')(R_{tr}/r)^2 \qquad 4.24$$

where $\sigma_r' = K_o p_o - (N-1)/(N+1)K_o p_o$ at $r = R_{tr}$

Substituting $r = R_{tr}$ and σ_r' into Eqn. 4.24 yields the radial stress distribution in the plastic zone ($R_{tr} <r <R_{vr}$). Continuity of radial stresses at the elastic zone boundary ($\sigma_r = K_a \sigma_v$) locates the extent of the plastic zone, R_{vr} as

$$R_{vr} = a\sqrt{\{K_o[(N-1)/(N+1)][2K_o p_o/((N+1)p_i)]^{2/(N+1)}/(K_o-K_a)\}} \qquad 4.25$$

The wall displacement, u_i can thus be found in steps similar to Stage (2). The ground convergence curve without inclusion of the gravity effect can be obtained. Examples are given later.

4.4.1 Effects of Variations of E and q_u along with Depth on Shape of Plastic Zone

In previous analyses, Young's modulus (E) and shear strength (q_u) were assumed to be constant with depth. This assumption, made for purpose of simplicity, may not be valid in practice. Equations governing the extent of the plastic zone for cohesionless and cohesive materials depend on the E and q_u parameters which may be of variation with depth in reality (i.e., due to confining and consolidated overburden pressures).

Cohesionless Soils

For E constant with depth, the extent of the yield zone along the depth can be determined as s function of depth using Eqn. 4.14 and Eqns. 4.19 and 4.25 for Modes A and B, respectively. For Mode A and a constant displacement imposed at the shaft wall, yielding occurs on the vertical (spiral) surfaces and its extent decreases rapidly with the depth. For Mode B, the yielding caused by the vertical-radial stress difference occurs along inclined (conical) surfaces following the Rankine's slip lines and its configuration looks like the truncated cone assumed by Prater (1977) (Fig. D.3).

For soils with E linearly increasing with depth, the profile of the yield zone will look like those shown in Fig. 4.10. With a constant wall displacement imposed, the magnitude of stress relief with the depth is larger for this case than for E=constant. The induced stress difference in Mode A or B is larger and hence, the extent of the yield zone at depth. The geometry of the yield zone can be determined from Eqns. 4.13 to 4.25 with E=kh, where h is the depth from the surface.

Cohesive Soils

Similar reasonings as for cohesionless soils are applicable to cohesive soils. Equations governing the shape of the yield zones for Modes A ans B are given in Appendix D.2 (Eqn. D.16 and Eqns. D.21 to D.27 respectively). Fig. 4.10 illustrates possible configurations of the plastic zones for different cases. The shape may be cone-shaped or collar-shaped depending on the strength-deformation property variation with depth. That the extent of the plastic zone diminishes at the bottom of the shaft is attributed to the face effect which results in more confinement that reduces displacemnets near the base.

Britto and Kusakabe (1982, 1983) investigated the mechanism of the collapse modes of unsupported axi-symmetric excavations in soft clays theoretically and experimentally. Their findings agree well with the shapes shown in Fig. 4.10.

4.5 Comparison of Proposed Solution with FE Analysis

Numerical examples generated by the finite element method (FEM) are used to compare results with those of the newly introduced CCM. As these examples are aimed at illustrating the mechanism of the shaft behaviour and are not designed to simulate any particular case history, typical soil conditions were selected as shown in Table 4.1. Analyses of shaft behaviour in cohesionless and cohesive materials are performed to distinguish two types of response to shaft construction. The chosen numerical values of K_o result in two conditions ($K_o < K_{cr}$ and $K_o > K_{cr}$) and permit two different modes of yielding, i.e., Mode A (tangential-radial stresses) and Mode B (vertical-radial stresses).

4.5.1 FE Analysis

The finite element program SAFE, developed by Chan (1985), was used for this comparison. The soil near the shaft was discretized for the axisymmetric problem by two-dimensional elements. The configuration of the mesh is shown in Fig. D.6. Zero displacement boundaries are assumed at the three boundaries (AB, BC, and CD) for the initial step (i.e., switch on gravity). The boundary AB, representing the wall of a 2m diameter shaft, is allowed to move inward due to the shaft construction. The allowed displacement profile in the FE analyses is also shown in Fig. D.6. A constant displacement is assumed along the shaft depth except near the base.

Several problems were encountered during numerical simulations. Mohr circles of stress state for cohesionless soil have small diameters the ground surface close to zero pressure (or elements at the ground surface). Small stress relief could cause yielding at these element. For the cohesive soil, tension might be induced in the top layer at which supports were not required. Thus, to overcome this problem, a minimal surcharge equivalent to 3m and 4m depth of soil for cohesionless and cohesive materials, respectively, were applied on the ground surface. Some difficulty in obtaining convergence in equilibrium iteration was also experienced. This problem is commonly encountered in FE analysis involving non-linearity, plasticity and limit equilibrium state (Borst and Vermer, 1984; Griffiths and Koutsabeloulis, 1985). The incremental displacement in each step after formation of the plastic zone was u/a=0.01% and the number of iterations to obtain a convergence tolerance of 0.0001 varied from 4 to 10. Hence, it would be very costly to determine conditions at large displacements.

4.5.2 Results from Finite Element Analyses

Stress Distribution

The radial, tangential and vertical stress contours near the shaft after the last displacement increment are plotted in Figs. 4.11 to 4.13 for three cases. Yielding has occurred in all cases. In case SM1 (Fig. 4.11), the yielding is induced by Mode B, i.e., due to vertical-radial stress difference (the tangential stress is always the intermediate stress). In contrast, the cases SM2 and CM1 indicate that

Mode A governs the initiation of yielding and the vertical stress is always the intermediate stress. However, common stress distribution patterns exist for three cases, except at the bottom boundary. Sections at various depths indicate that horizontal arching develops around the shaft openings. The radial stress decreases toward the shaft wall because of the stress relief at the support. This stress relief in radial direction causes the stress redistribution and, results in an increase in tangential stress. This increase in tangential stress occurs in elastic regions. Within the plastic zone, the tangential stress decreases toward the shaft wall. Arching in vertical planes that develop against the elastic-plastic interfaces are observed in all cases. The plastic zone near the shaft wall tends to displace downward under the gravity effect, and is stabilised by the shear resistance derived from the adjacent elastic zone (the shaft wall being frictionless). The mechanism explains why the vertical stress decreases toward the wall within the plastic zone and experiences a small increase at the elastic-plastic boundary. The vertical arching due to the gravity effect is not very pronounced because the yielding allowed is not excessive.

The stress distributions at one horizontal section (depth h=3.789m) are plotted in Figs. 4.14 to 4.16 to compare with the results predicted by the CCM solution. This particular section is chosen because it is remote from the influence of the surface and bottom boundaries. Stress distributions at two displacement stages are plotted: first, when yielding at the wall (r=a) is initiated and second, when much yielding has occurred. A comparison of results in Figs. 4.14 to 4.16 indicates not only that the two methods agree well with repect to the mode of yield initiation at the wall, but also that stress distributions predicted by two methods are close.

Support Pressure-Displacement-Plastic Zone Radius Relationship

Figs. 4.17 to 4.19 present results of the radial pressure-wall displacement-plastic zone radius relationships obtained from the FE analyses (designated by discrete points) and the closed-form CCM (designated by full lines). On the GCC plots (p_i-u_i) are included zones corresponding to different stress stages described in Mechanisms of Shaft Behaviour (Section 4.4). For SM 1 of yield Mode B, Zone 1 represents the elastic response of the ground and Line E separates the elastic zone from the plastic. Further, displacements in excess of those given by Line E induces yielding by vertical-radial stress difference and this results in a non-linear response of the ground. Zone 2 corresponds to the stress Stage (2) of Fig. 4.9. During Stage (2), yielding (σ_v-σ_r) has occurred. Further stress relief will cause σ_t decrease and become equal to σ_v. This state is represented by Line T, and Zone 3 corresponds to Stage (3) of Fig. Fig. 4.9.

Similar reasoning can be applied for cases SM2 and CM1, except that the mode of yielding is different, i.e., induced by tangential-radial stress difference, Mode A. Lines E and T in case CM1 (cohesive) are parallel, instead of inclined as for cases SM1 and SM2 (cohesionless). This is because yielding in cohesive soil is induced by the constant stress difference given by the compressive strength, instead of stress ratio in cohesionless soil which is dependent of the confining pressure (overburden depth).

On the p_i - R plots, the plastic zone propagates outward with decreasing p_i. The result predicted by CCM agree well with those of FE analyses.

Extent of Plastic Zone with Depth

The extent of the plastic zone with the depth in vertical sections at two displacement steps obtained from two methods (FEM and CCM) are plotted in Fig. 4.20. The results of FE analyses are those of the integration points, and hence show some variations. However, both methods yield consistent results. It is interesting to note that the configurations of the plastic zone around the shaft show the distinct features discussed earlier. In general, the three cases indicate that the extent of the plastic zone increases as displacement increases. The plastic zone in the cohesionless cases not only increases in the radial direction, but also with depth.

A comparison of behaviour in cohesionless and cohesive soil demonstrate that under a constant displacement (depth (except at the shaft bottom) the radius of the plastic zone decreases with depth in cohesionless soils and forms a cone whereas it is constant with depth in cohesive soil, forming a collar (cylinder above a cone). It is also observed from Cases SM1 and SM2 that at the same displacement a larger plastic zone develop for Case SM1 (K_o=0.41) than SM2 (K_o=0.98). This implies that the pressure due to the gravity effect in Case SM1 (K_o<K_{cr}) is more dominant than in Case SM2 (K_o>K_{cr}). However, the support pressure due to horizontal arching is greater in Case SM2 because of higher insitu stress. The resultant support pressure of vertical and horizontal arching in both conditions (K_o<K_{cr}) and (K_o>K_{cr}) varies in each situation. For analysis of these three cases, the soil parameters are assumed to be constant with depth. It can be expected that the shape of the plastic zone will be different if the soil parameters vary with depth. This phenomenon has been discussed in detail earlier.

Pressure Distribution at Wall

From the GCC (Figs. 4.17 to 4.19), the required support pressures for a given displacement are determined and plotted on Figs. 4.21 to 4.23 for two displacement levels, along with results from the FE analyses. Both methods give consistent results except at the bottom boundary. These figures clearly show that the support pressure is a function of the displacement and initial insitu stress. The support pressure determined from the limit equilibrium methods proposed by Berezantzev (1958) is also included for comparison. Excessive displacement must be allowed in order to obtain these minimum pressures predicted by limit equilibrium methods.

Gravity effects due to the vertical arching within the plastic zone around the shaft are not dominant in these cases because small displacements (u/a=0.3 to 0.56%) are imposed at the shaft walls. Further movements were not simulated because it is very costly to obtain excessive displacement and also the convergence in iteration processes became very unstable. Nevertheless, the CCM provides an excellent tool to predict the ground pressure at specified displacement levels.

Analysis No.	Soil Model	Soil Properties ϕ (deg.)	c (kPa)	E (MPa)	γ (kN/m3)	ν	Ko	Kcr	Ka
SM1	Perfectly Elastic-Plastic, Associated, Flow Rule, Mohr-Coulomb	33	0	38	20	0.290	0.409	0.647	0.295
			(constant with depth)						
SM2	as above	33	0	38	20	0.400	0.980	0.647	0.295
			(constant with depth)						
CM1	Perfectly Elastic-Plastic, Von Mises	0	60	40	20	0.495	0.980	0.625-0.864	-
			(constant with depth)						

Table 4.1 Input Data for FE Analyses (Shaft)

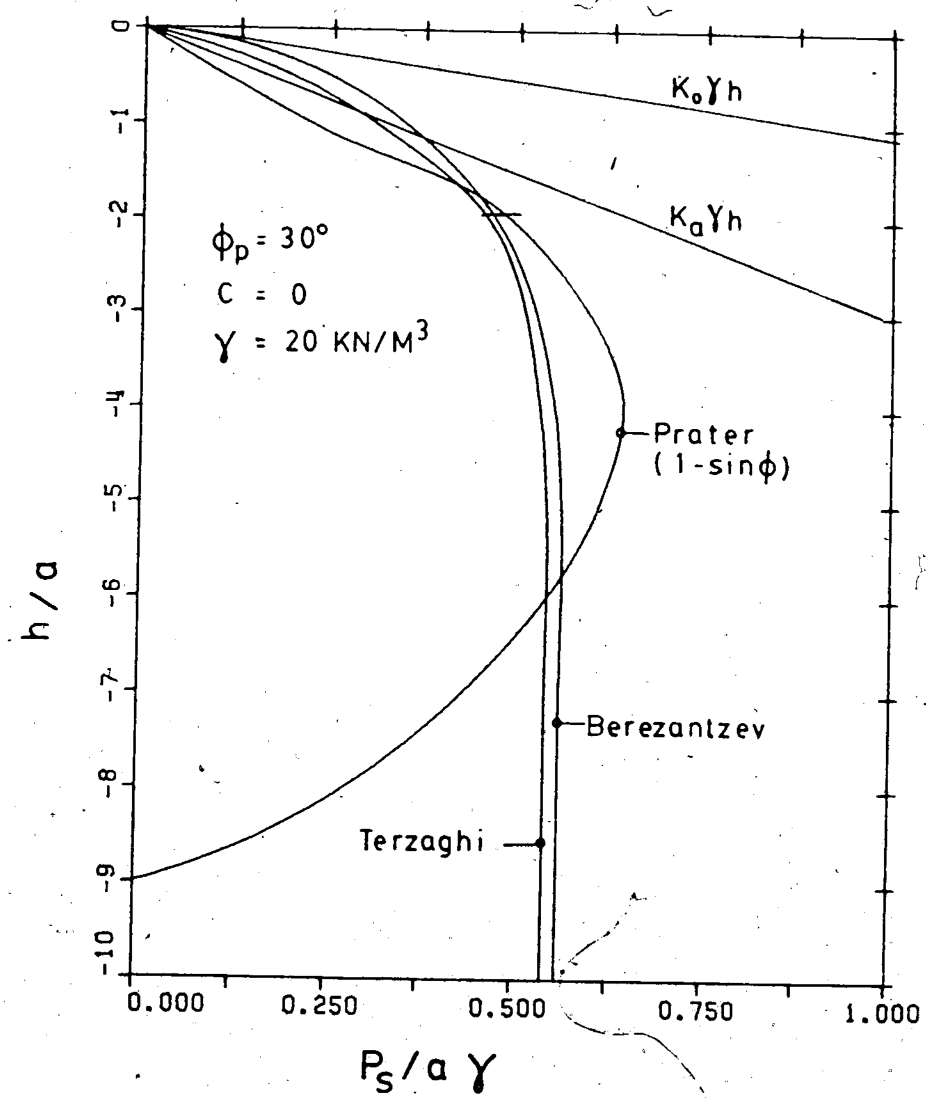

Figure 4.1 Earth Pressure as a function of Depth Ratio (H/a)

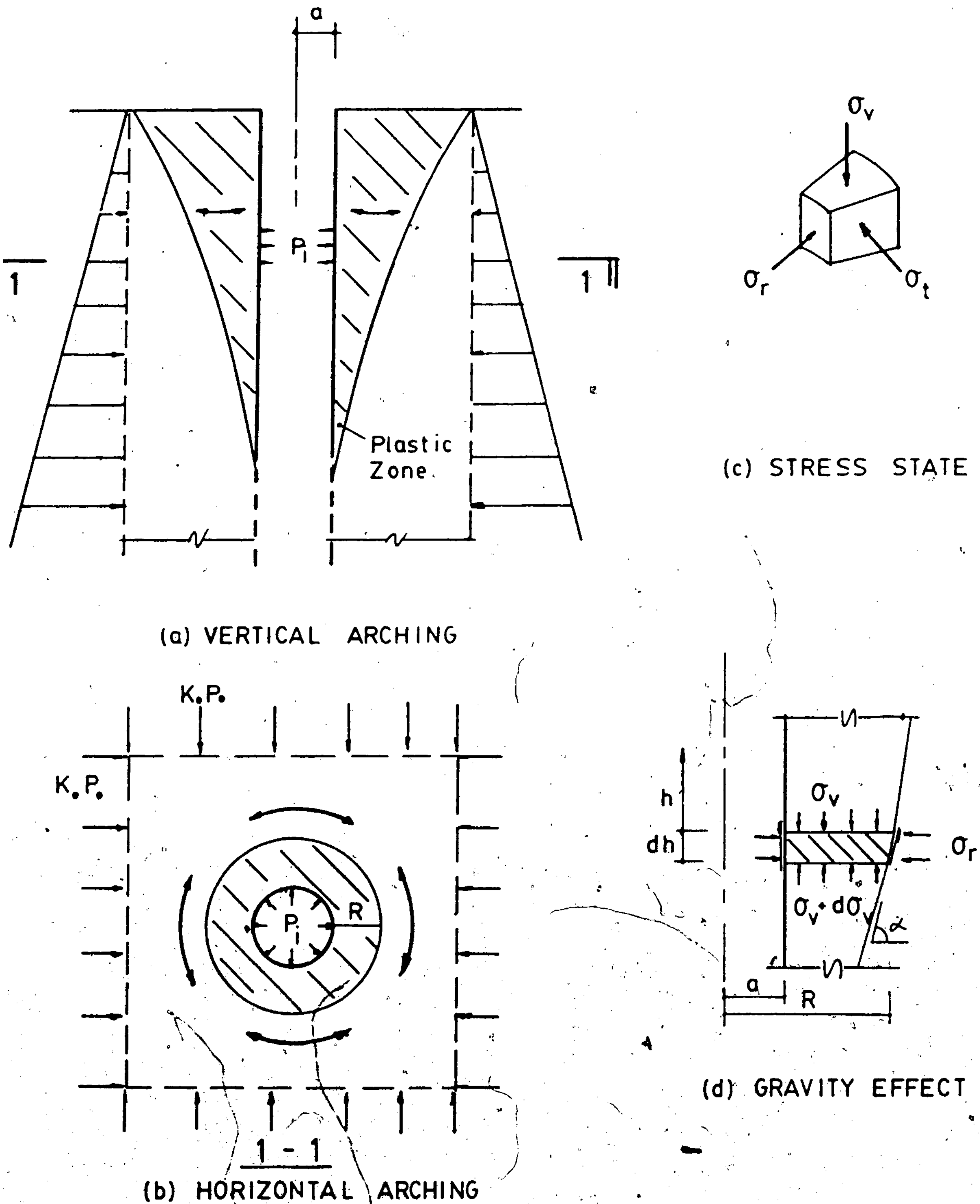

Figure 4.2 Mechanism of Shaft Behaviour

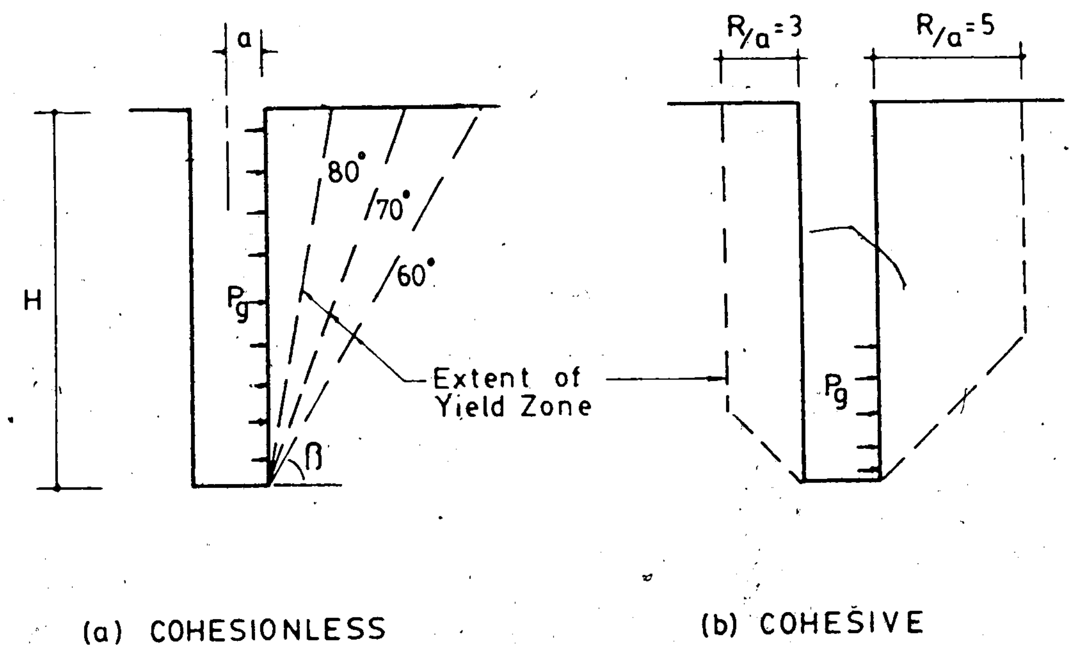

Figure 4.3 Gravity Effect due to Vertical Arching

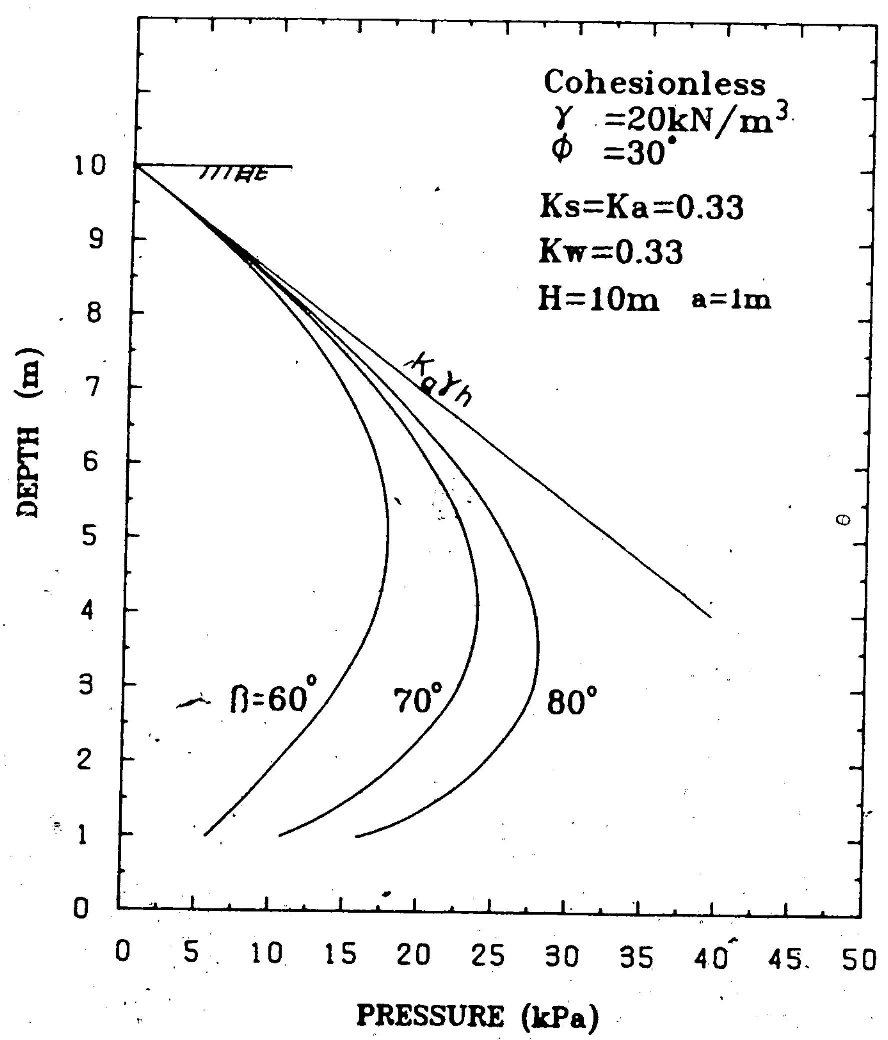

Figure 4.4 Support Pressure due to Gravity Effect (Cohesionless)

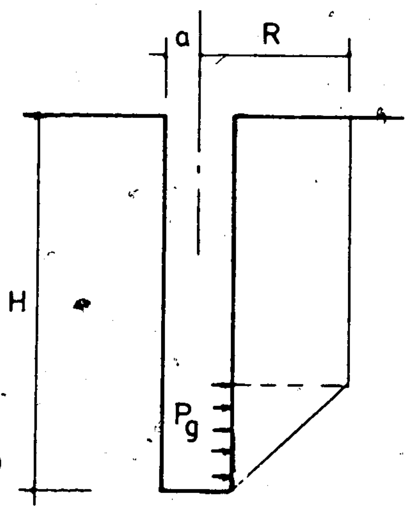

$H = 10\ m$
$a = 1\ m$
$C_u = 40\ kPa$

R (m)	P_g (kPa)
3	17
5	183

Figure 4.5 Support Pressure due to Gravity Effect (Cohesive)

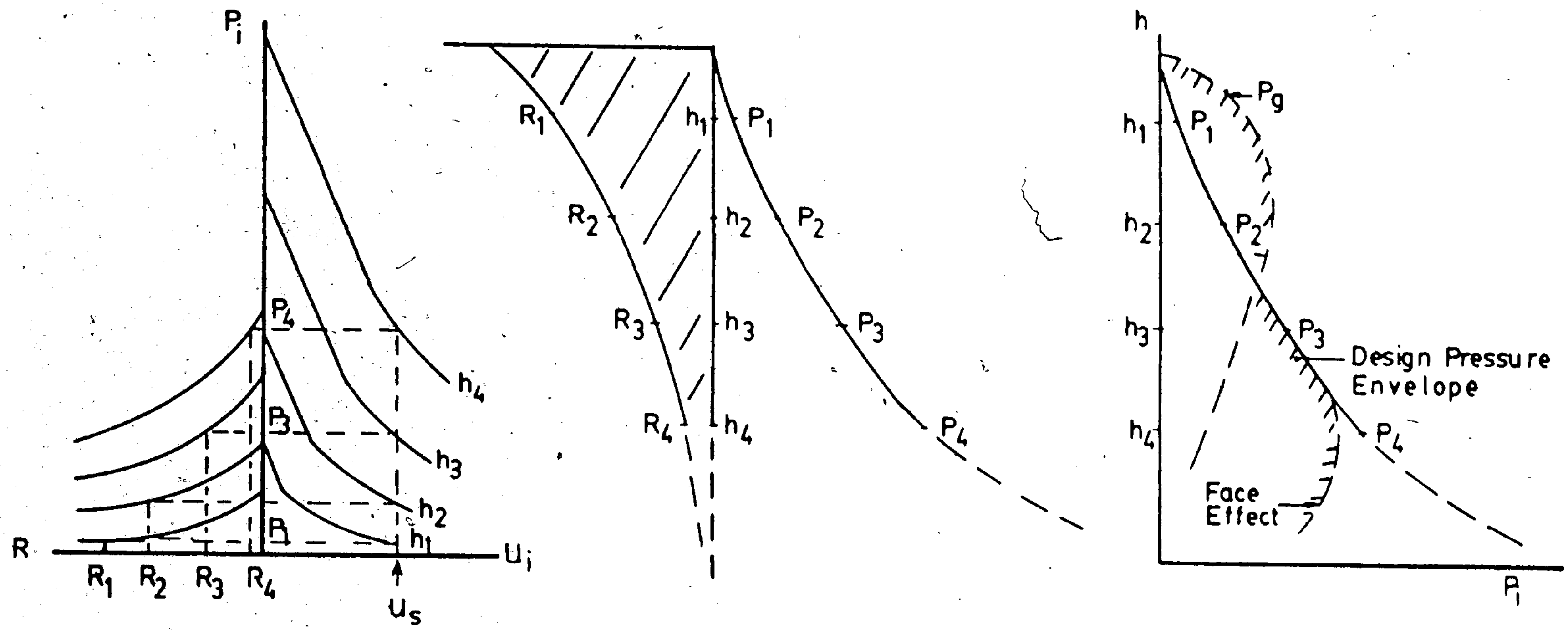

(a) GCC at different depths (no gravity effect)

(b) Plastic zone and Pressure vs Depth for Displacement, U_s

(c) Pressure diagram from CCM and Gravity

Figure 4.6 Shaft Design Approach-CCM with inclusion of Gravity Effect

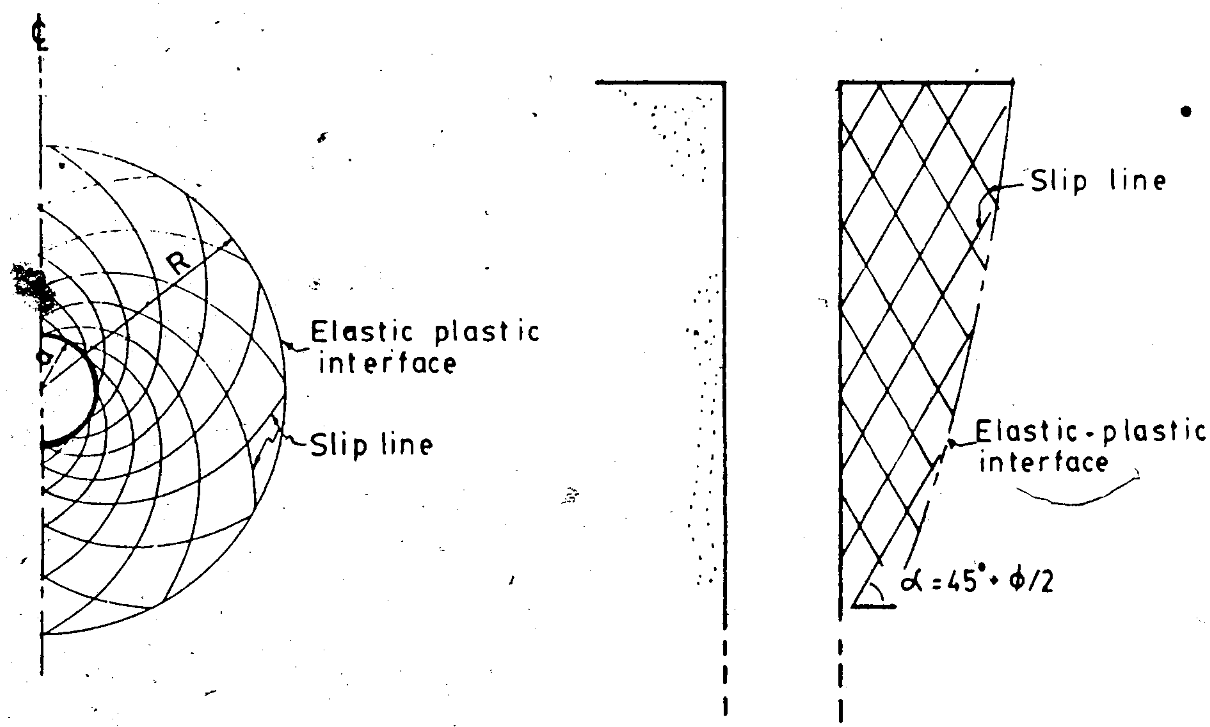

(a) MODE A
($K_o > K_{cr}$, $\sigma_t - \sigma_r$)

(b) MODE B
($K_o < K_{cr}$, $\sigma_v - \sigma_r$)

Figure 4.7 Mode A and Mode B

Stress Distribution ground opening	Stress State	Equations for		
		R	σ	U
(1) 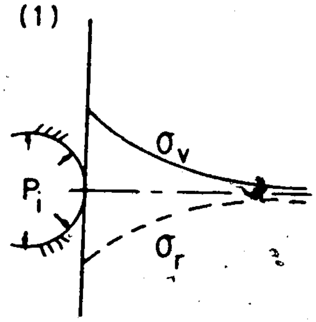	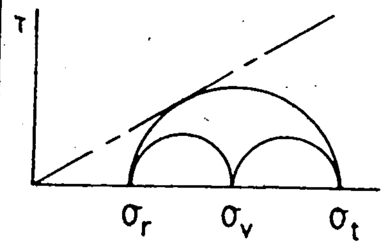	-	4.2-4.4	4.13
(2) 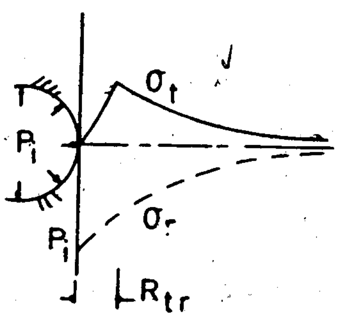	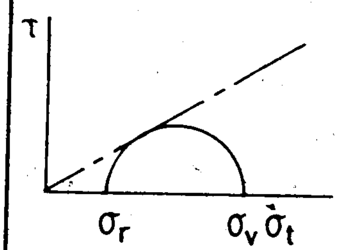	4.14	4.3-4.4 4.21-4.22	4.15
(3) 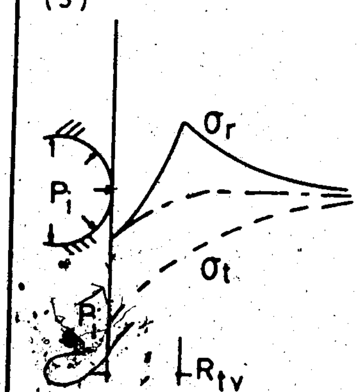	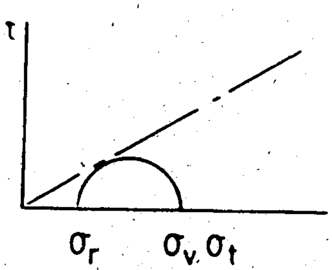	..	..	..

Figure 4.8 Stress States (Mode A)

Stress Distribution around opening	Stress State	Equations for		
		R	σ	u
(1) 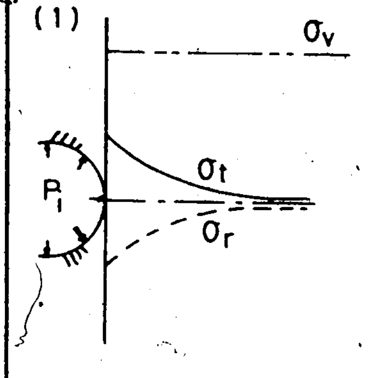	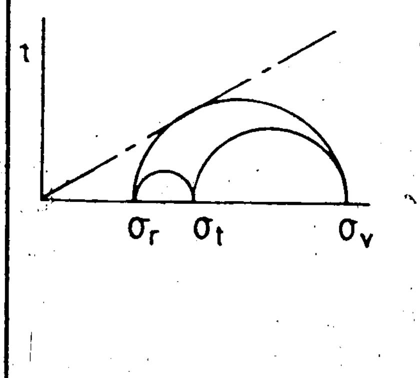	-	4.2-4.4	4.16
(2) 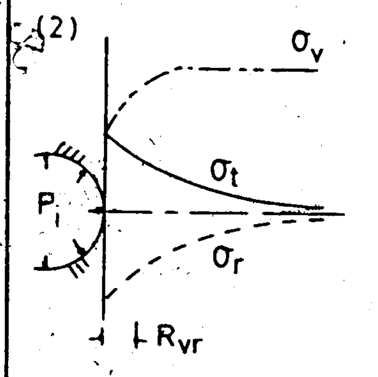	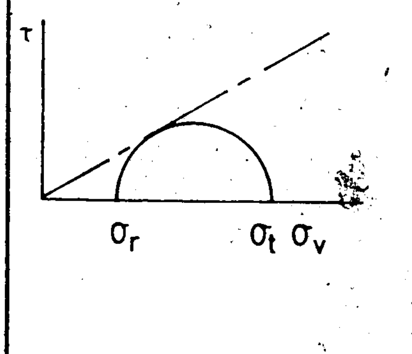	4.19	4.3 4.18 4.20	4.15
(3) 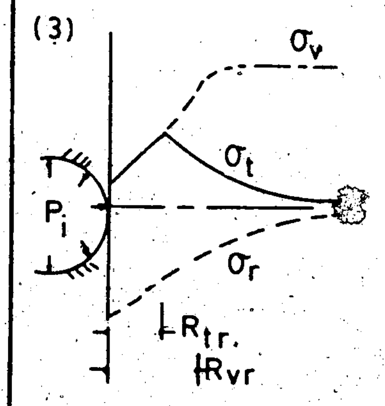	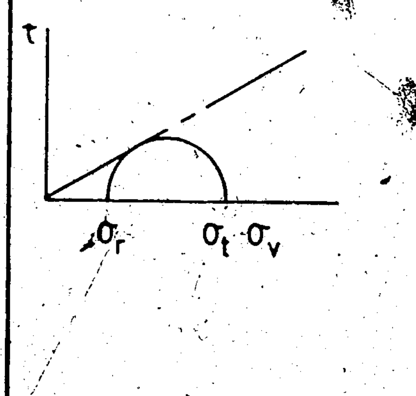	4.25	4.21 4.22 4.24	4.15

Figure 4.9 Stress States (Mode B)

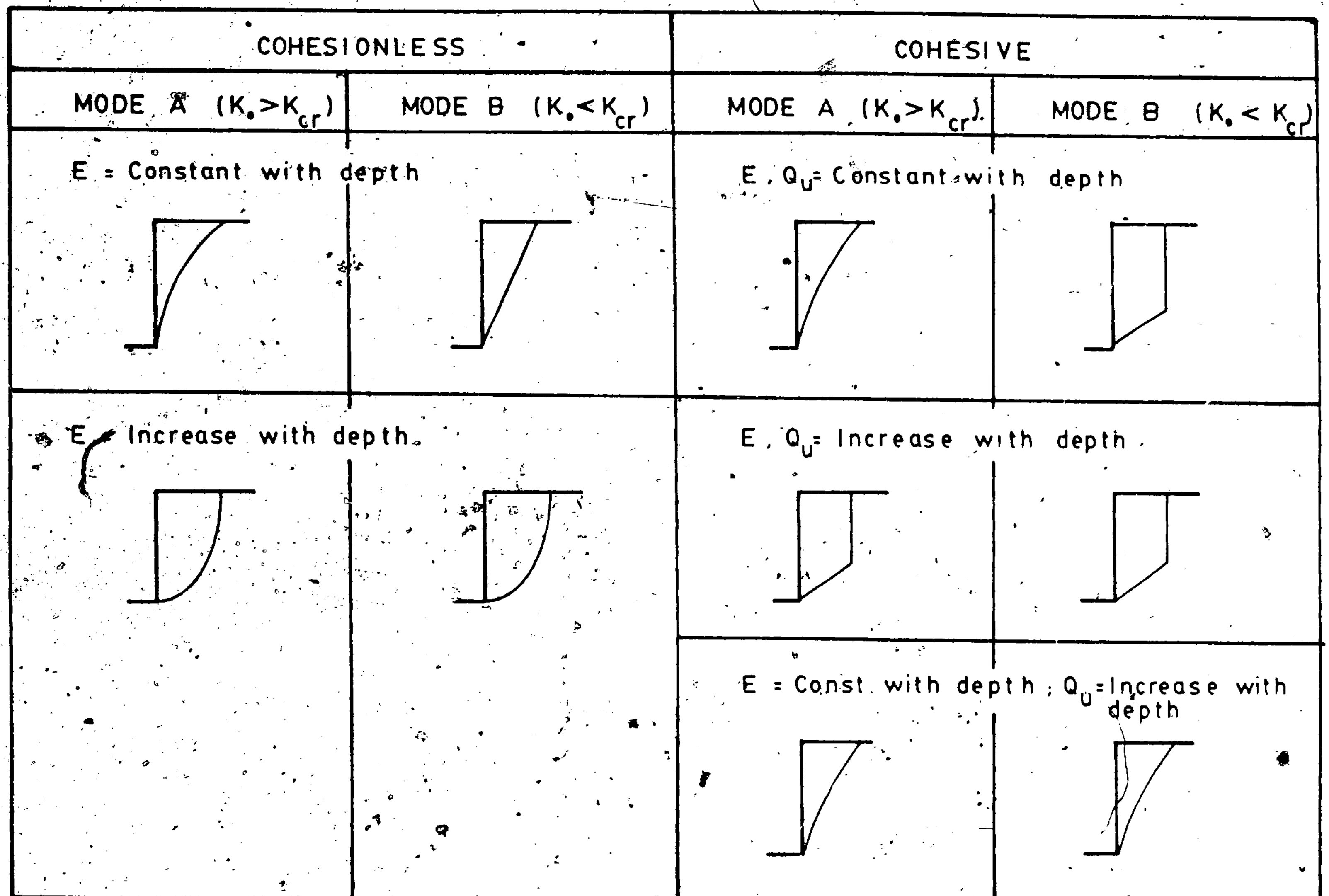

Figure 4.10 Configurations of Plastic Zones with Depth for Cohesionless and Cohesive Soils

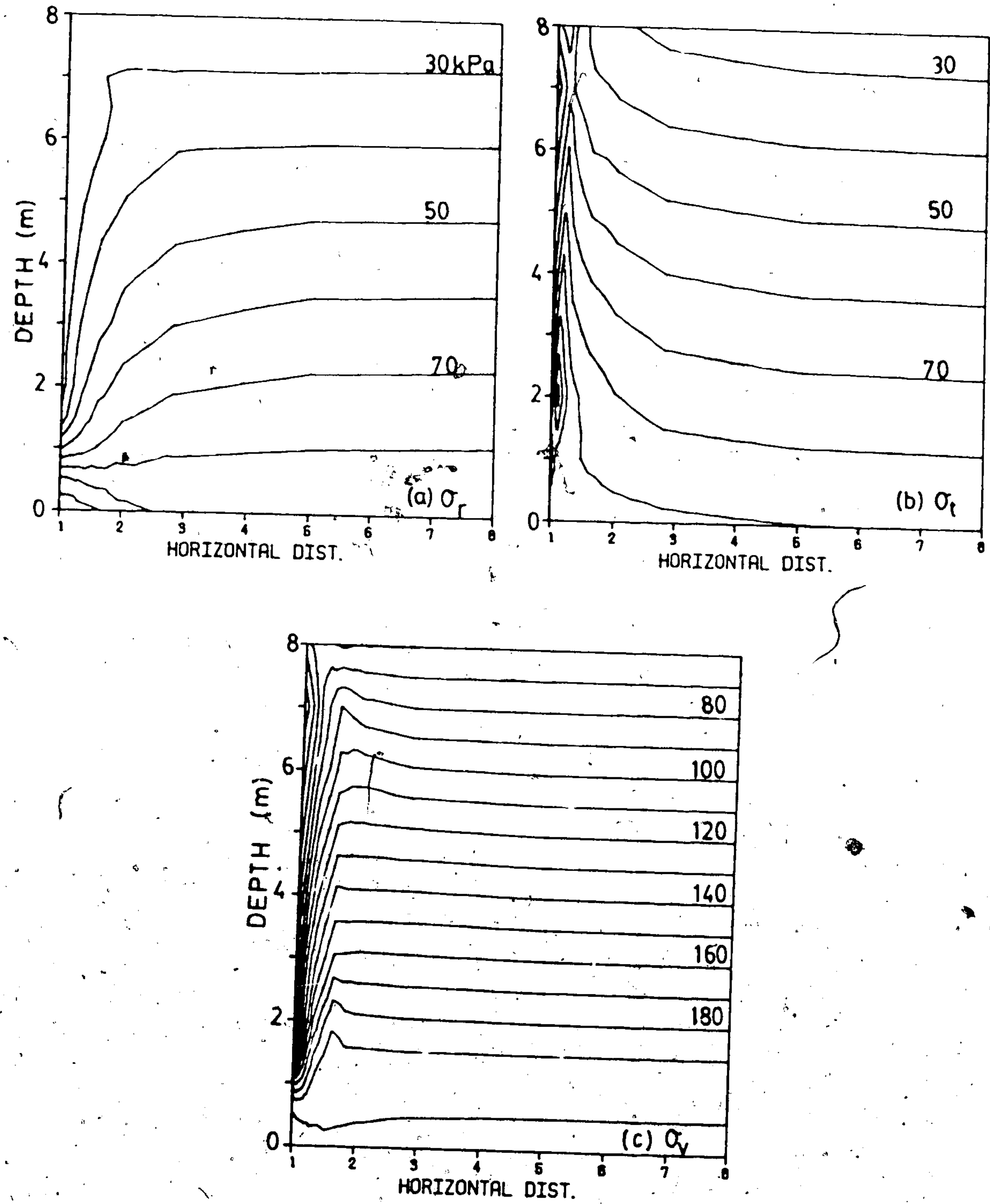

Figure 4.11 Comparison of Stress Distribution (u/a=0.3%, SM1); (a) σ_r (b) σ_t (c) σ_v

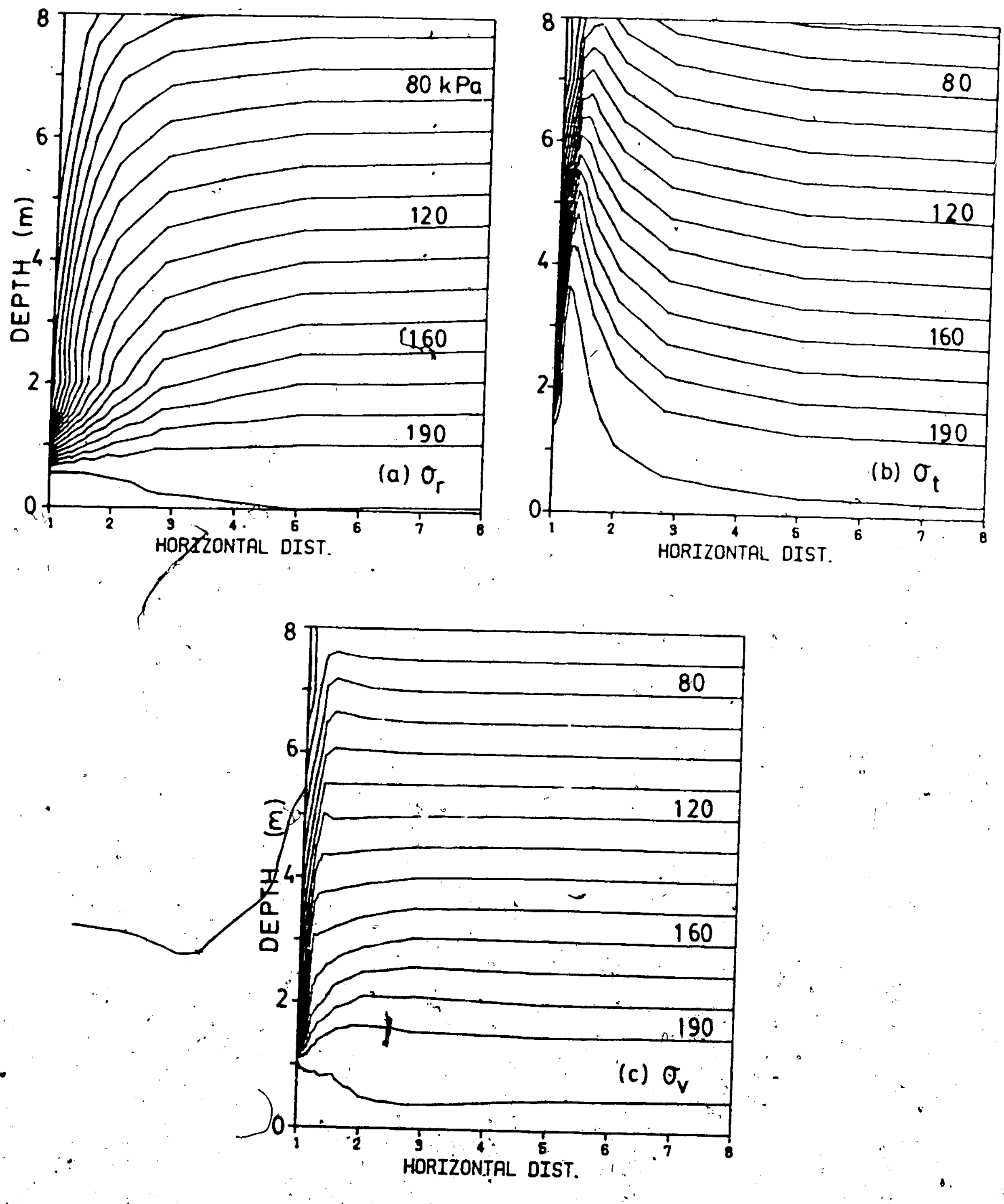

Figure 4.12 Comparison of Stress Distribution (u/a=0.5%, SM2); (a) σ_r (b) σ_t (c) σ_v

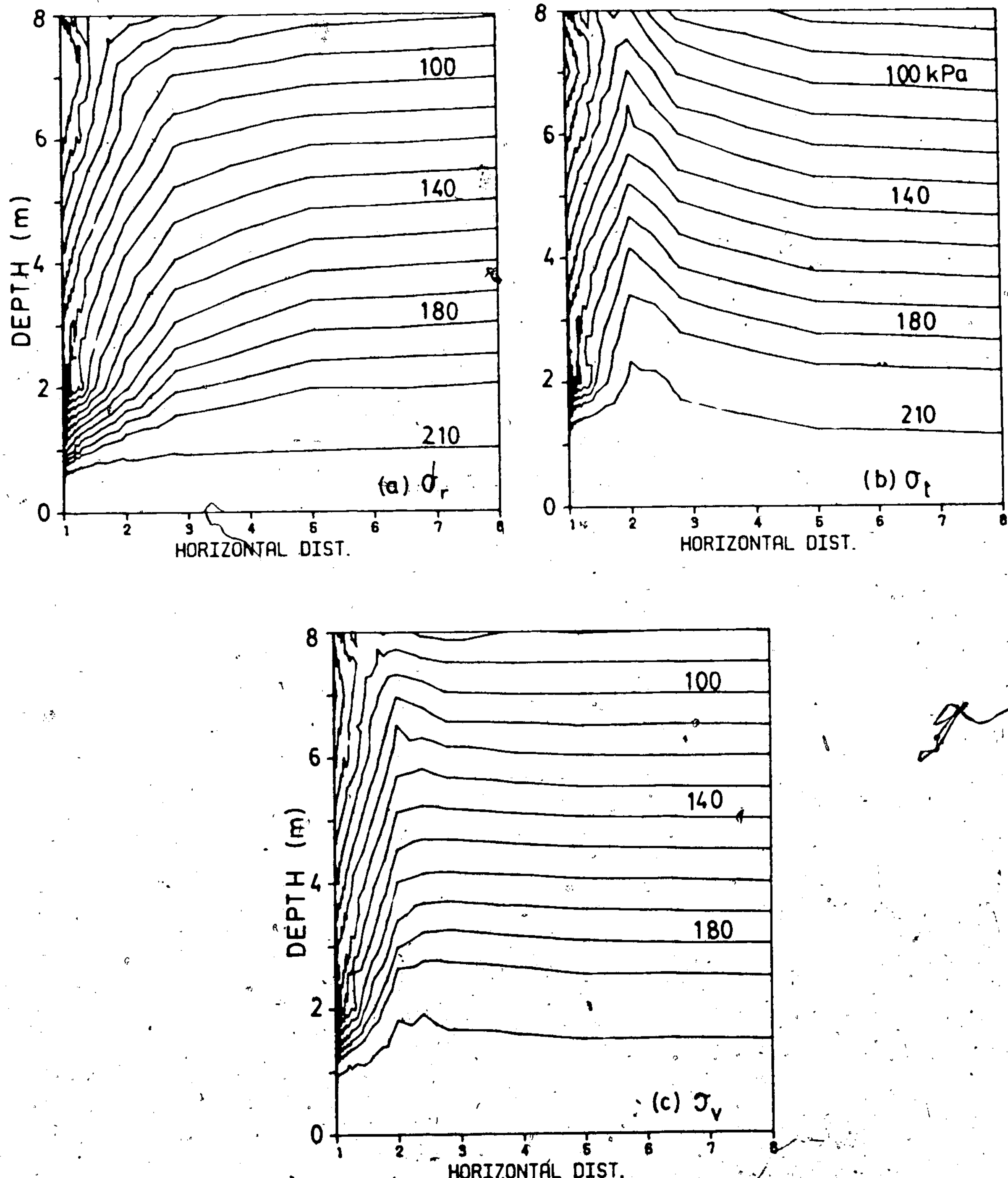

Figure 4.13 Comparison of Stress Distribution (u/a=0.56%, CM1); (a) σ_r (b) σ_t (c) σ_v.

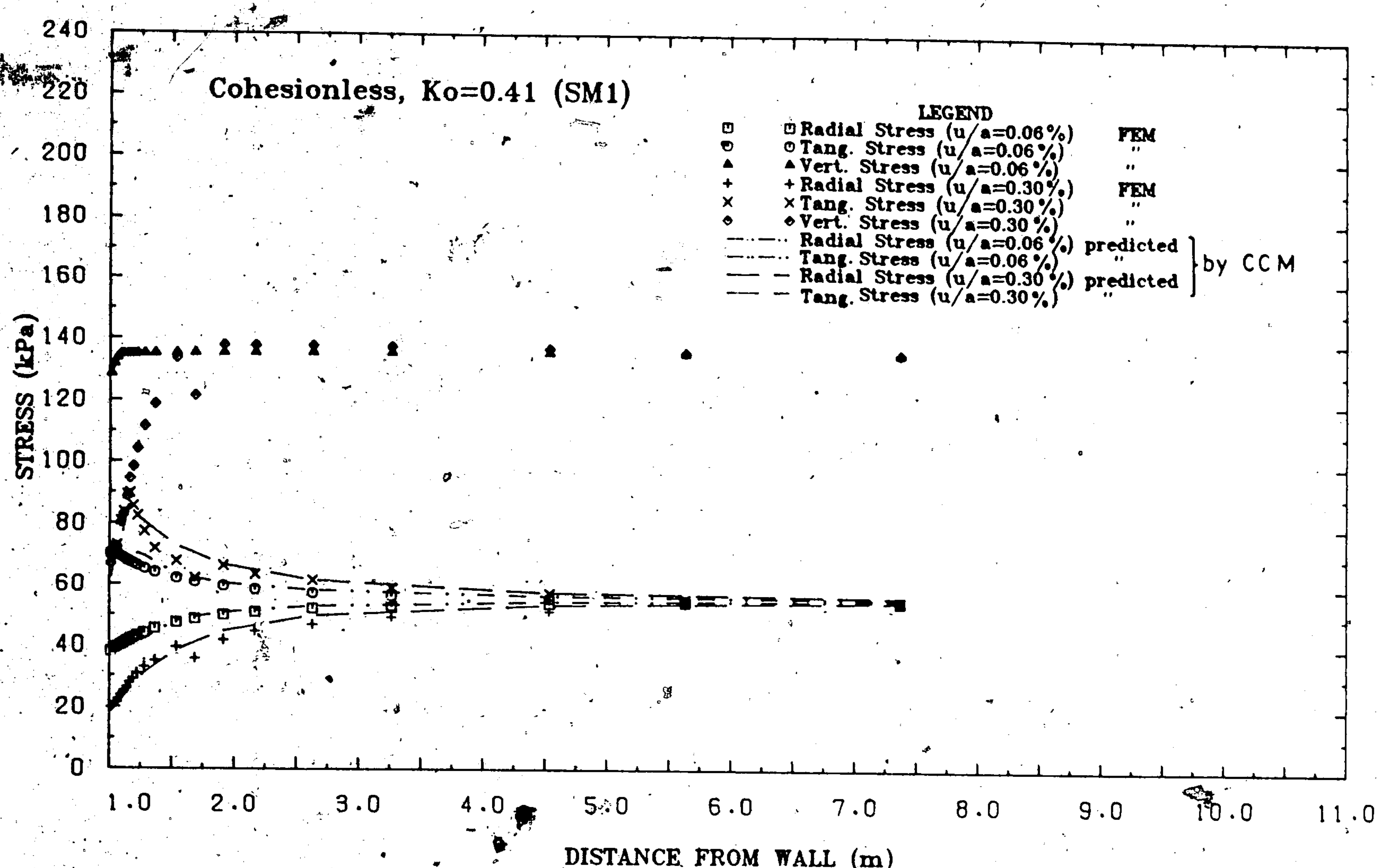

Figure 4.14 Comparison of Stress Distribution (h=3.789m, SM1)

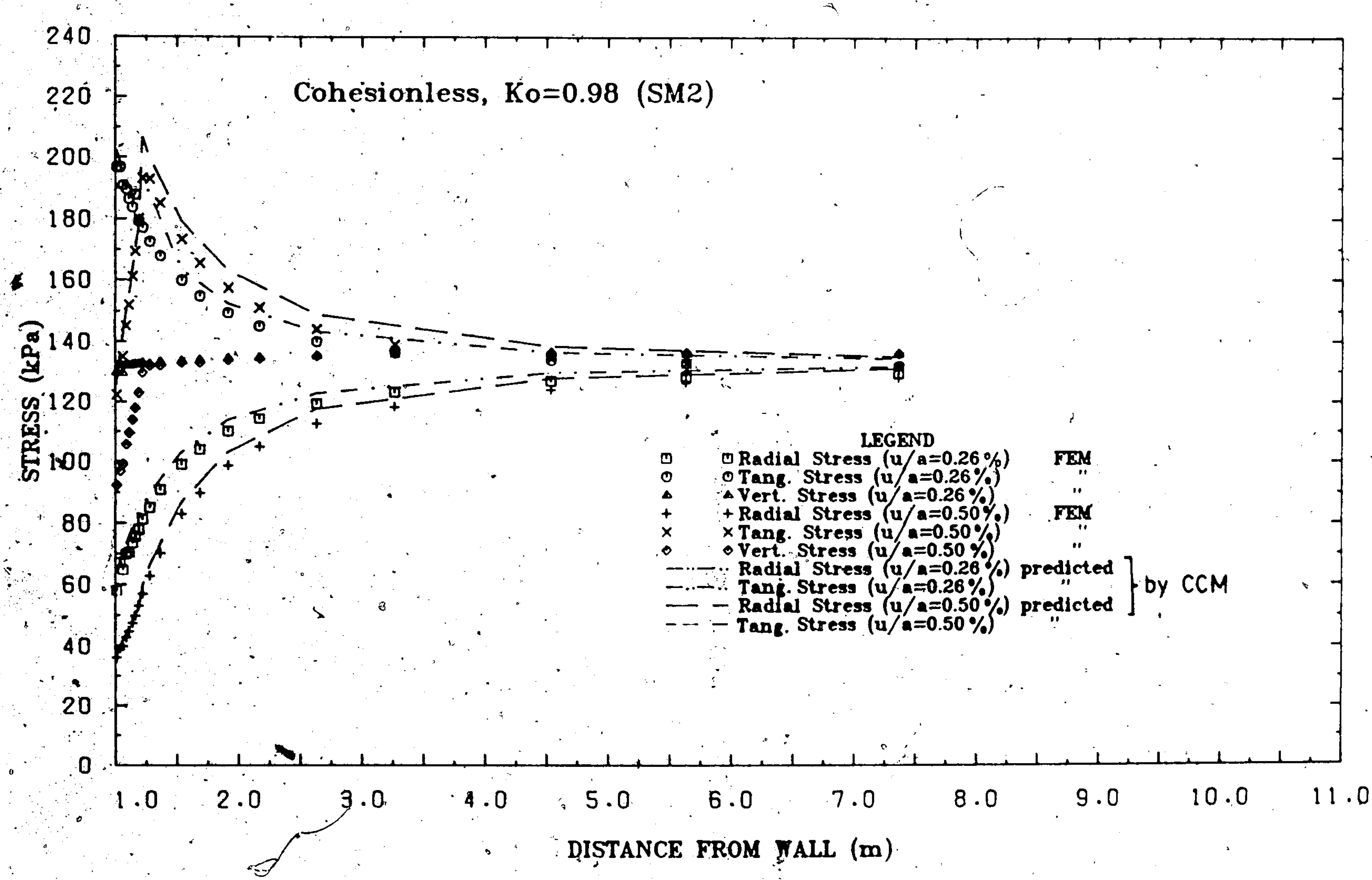

Figure 4.15 Comparison of Stress Distribution (h=3.789m, SM2)

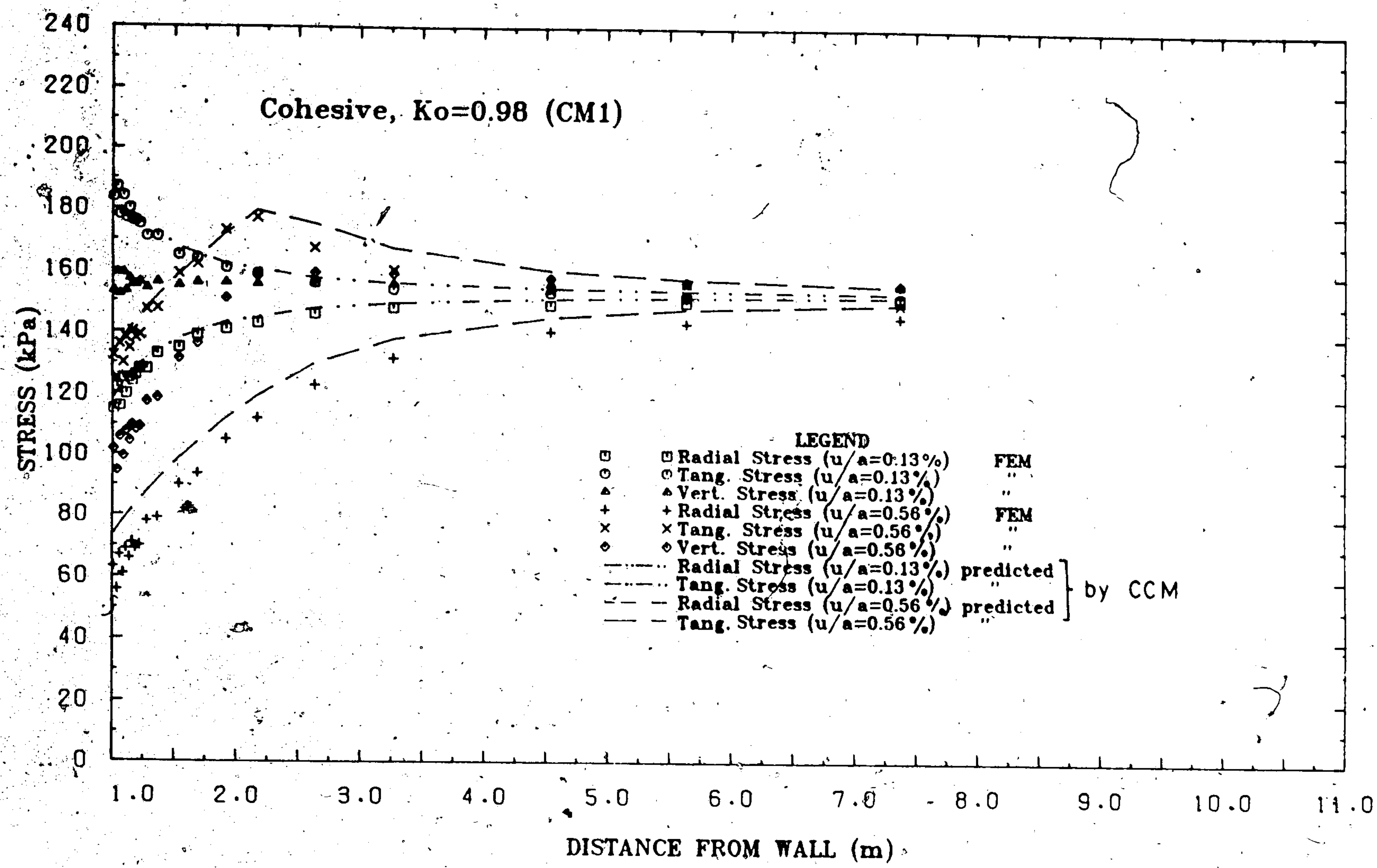

Figure 4.16 Comparison of Stress Distribution (h=3.789m, CM1)

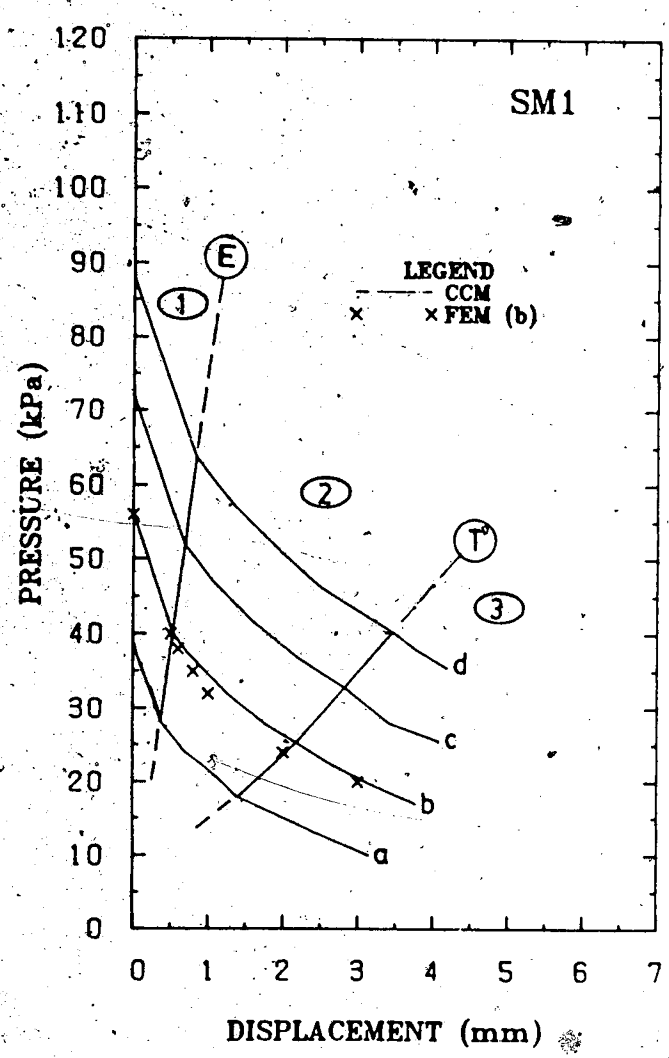

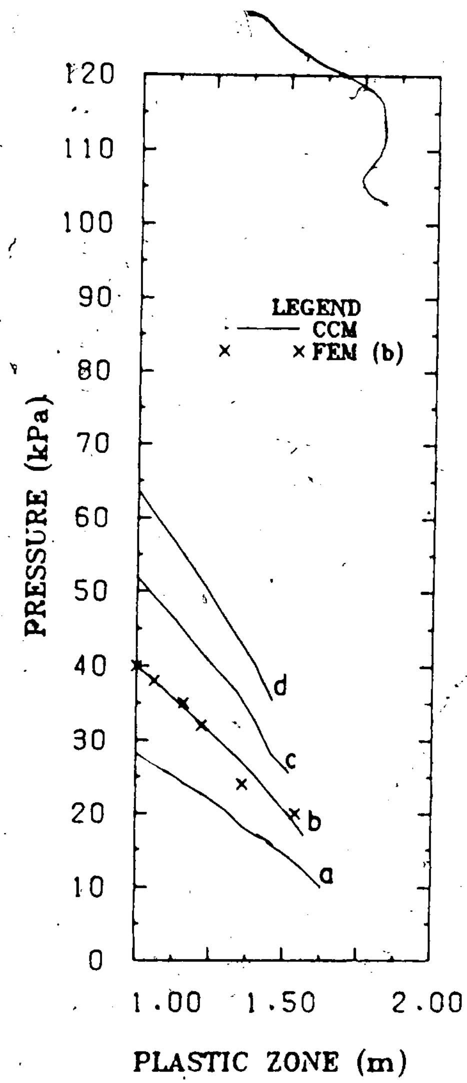

Figure 4.17 Comparison of Pressure-Displacement-Plastic Zone (SM1, Cohesionless, Ko=0.41); a) h=1.789m b) h=3.789m c) h=5.789m d) h=7.789m

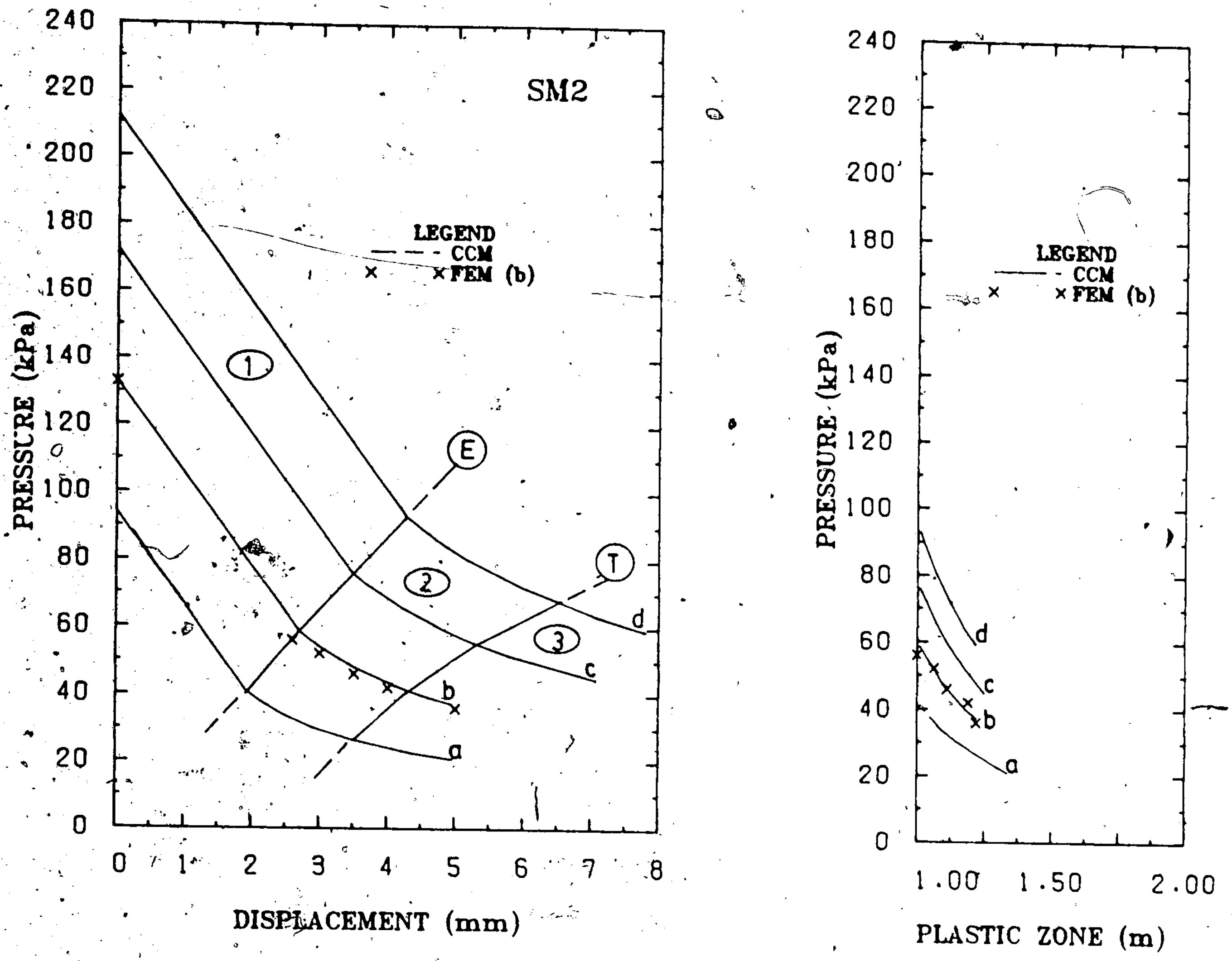

Figure 4.18 Comparison of Pressure-Displacement-Plastic Zone (SM2, Cohesionless, Ko=0.98); a) h=1.789m b) h=3.789m c) h=5.789m d) h=7.789m

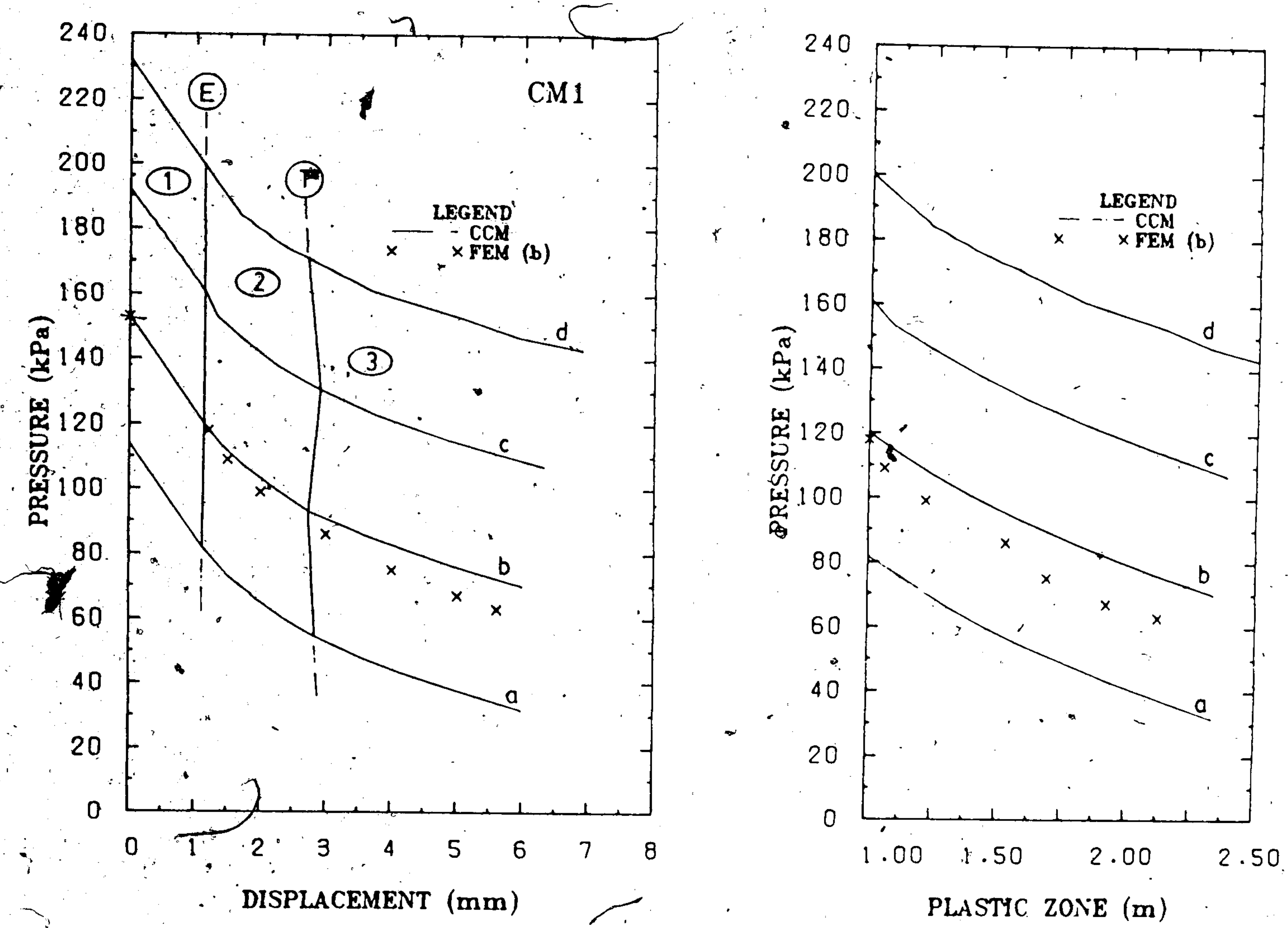

Figure 4.19 Comparison of Pressure-Displacement-Plastic Zone (CM1, Cohesive, Ko=0.98); a) h=1.789m b) h=3.789m c) h=5.789m d) h=7.789m

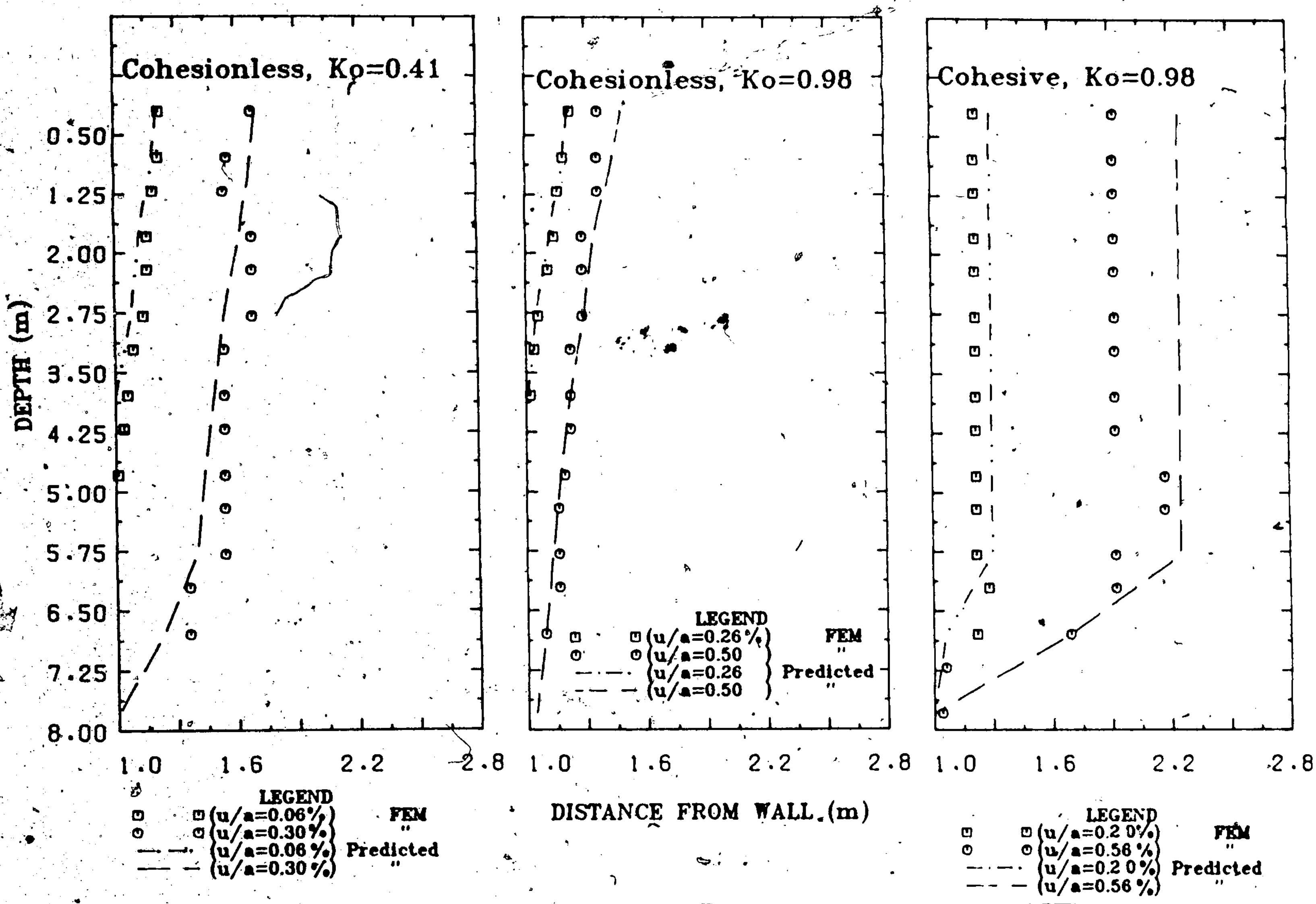

Figure 4.20 Comparison of Plastic Zone with Depth

(SM1,SM2,CM1)

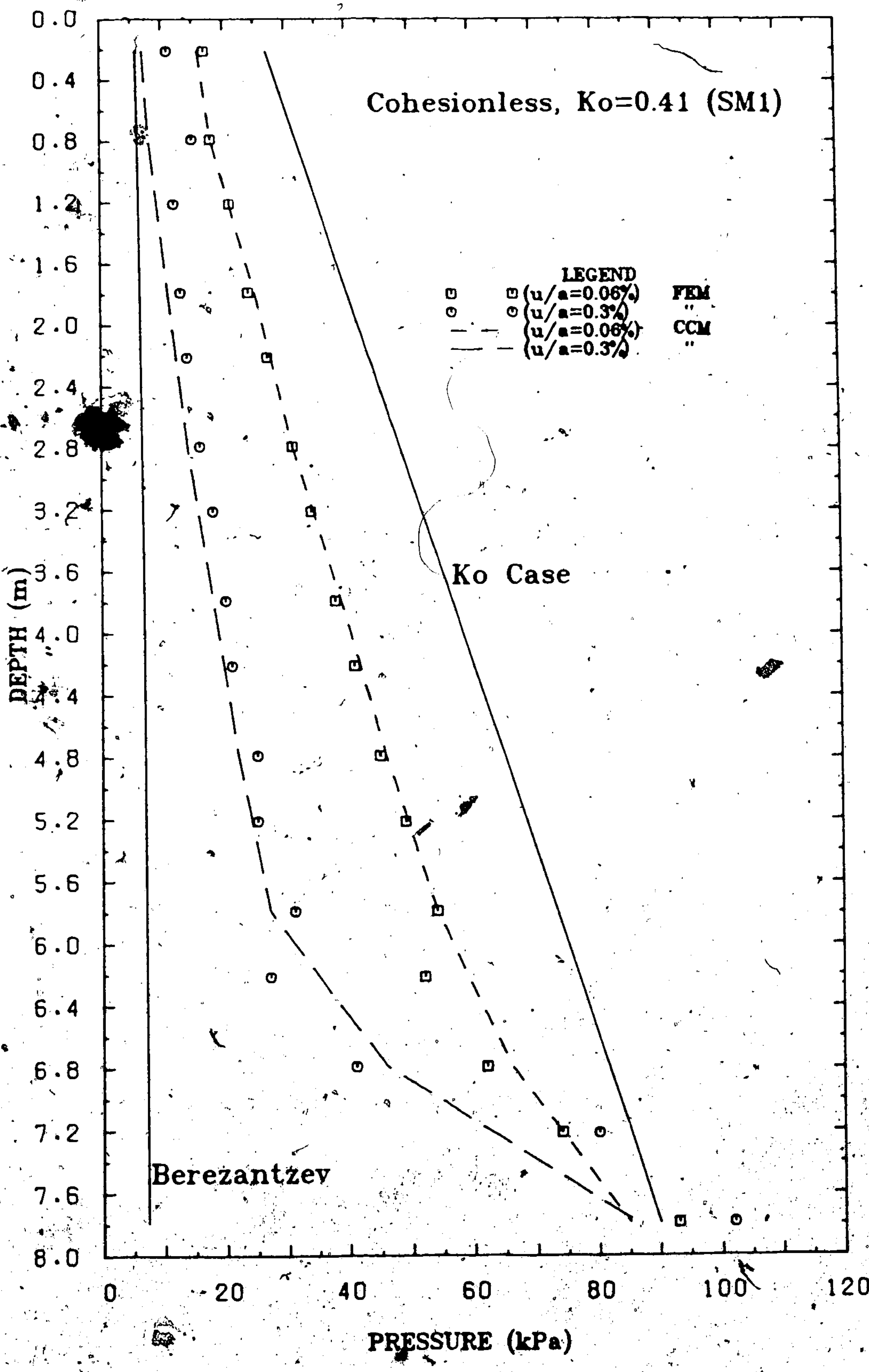

Figure 4.21 Comparison of Pressure with Depth (SM1)

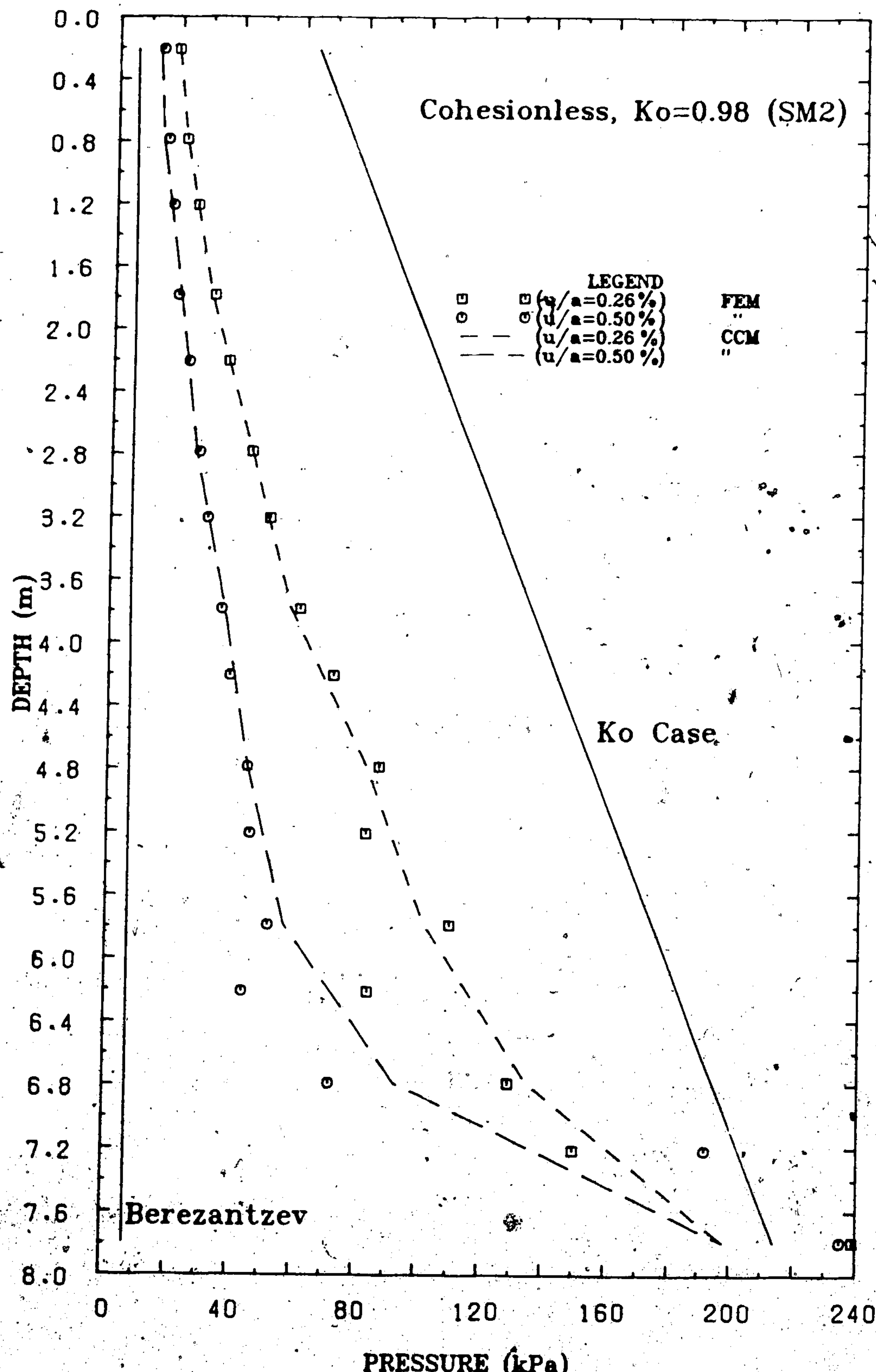

Figure 4.22 Comparison of Pressure with Depth (SM2)

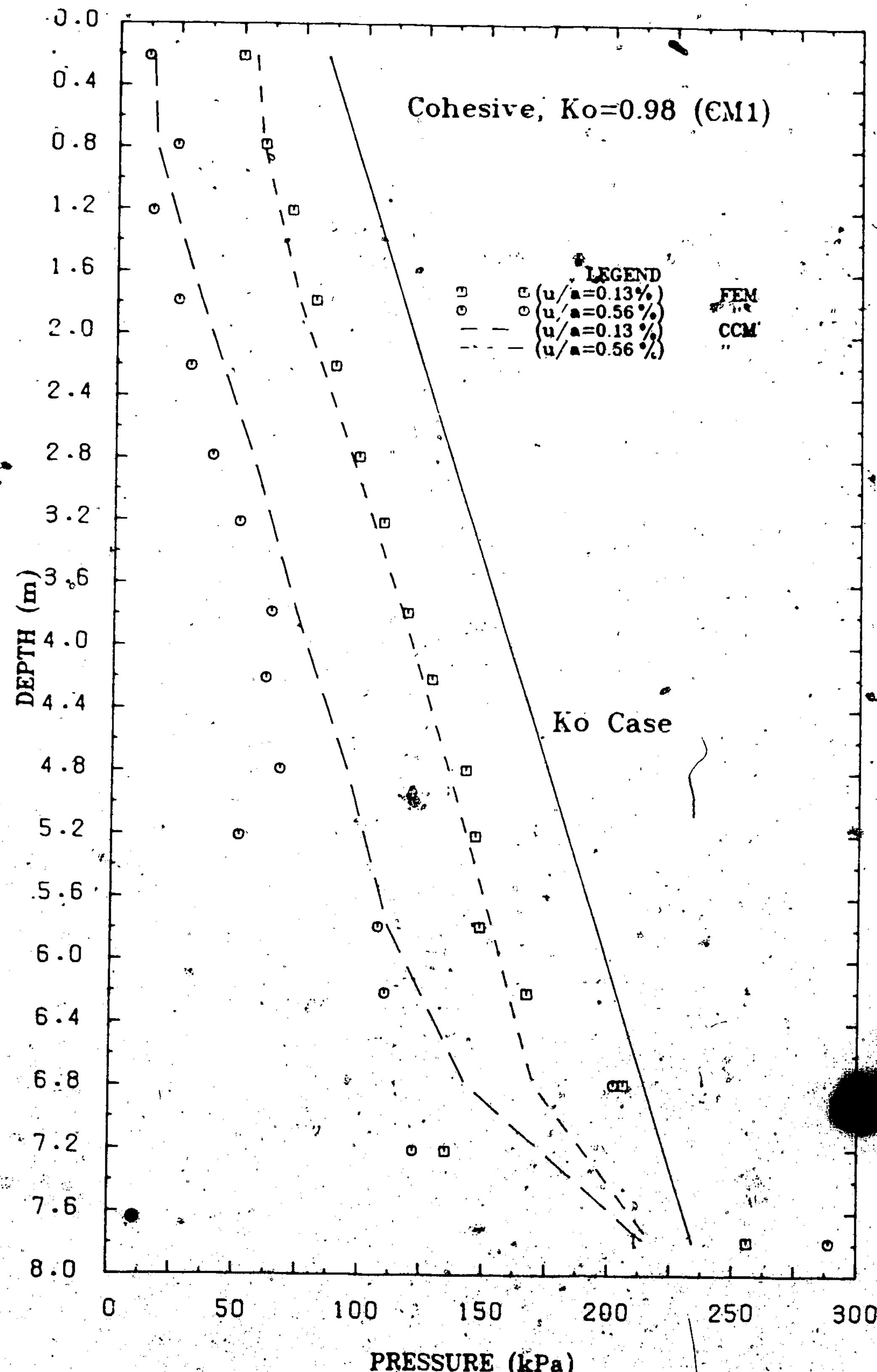

Figure 4.23 Comparison of Pressure with Depth (CM1)

5 . SHAFT - CASE STUDY (FIELD MEASUREMENTS)

5.1 E. L. Smith Plant - Terwillegar Shaft

5.1.1 Introduction

The construction of a shaft south of the E. L. Smith Plant (Terwillegar Shaft) provides an excellent opportunity to collect information for a rational evaluation of currently available design methods and the newly proposed CCM for shafts. Results of field monitoring, data interpretation and analyses of this shaft were presented in detail by Kaiser and Wong (1984). Only data and findings relevant to this thesis are highlighted herein.

The behaviour of the Terwillegar Shaft excavated in sand and Edmonton Till was studied by an approach integrating field measurement with results from finite element analyses. For this purpose, it was necessary to determine the parameters for the stress-strain model of the soil mass by laboratory testing, to observe the displacement field of the soil near the shaft, to monitor the pressure development on the temporary support and to estimate the original insitu stress. A finite element program SAFE (Chan, 1985) was used to simulate the field conditions for a comparison with field measurements.

5.1.2 Project Description

Fig. 5.1 shows the stratigraphy at the location of the Terwillegar Shaft. The lacustrine deposits (above 6m) were found to consist of a brown silty clay with streaks of grey clay intermixed. The glacial till consisted of a matrix of sand, silt and clay sizes with small pebbles and pieces of coal intermixed. Numerous sand lenses, many of which were waterbearing, were encountered in the glacial till. The bedrock consisted mainly of interbedded clay shales and sandstones. Bentonitic layers were generally present in clay shale, however no pure bentonite seams were encountered during excavtion.

The Terwillegar Shaft with a finished diameter of 2.1m was sunk using conventional shaft sinking method. The rate of excavation was about 1.6m per day. Each stage of excavation was followed by the installation of temporary lining composed of corrugated and flanged steel plates which are fully assembled from inside the shaft to form support rings. The diameter of the excavated shaft changed from 3.2m (above depth -14.5m) to 2.4m (below depth -14.5m)

5.1.3 Field Instrumentation

Fig. 5.2 shows the layout of the field instrumentation. Due to the axisymmetry of the shaft, all instruments were positioned along the diametric axes. Furthermore, all instruments were located on one side of the shaft to enable easy access for recording during construction, to prevent interruption of the construction procedure and to minimize disturbance or damages to the instruments.

Fig. 5.3 depicts a transverse section (OA) giving the instrument elevations.

Vertical displacements near the surface and at depth were measured using surface settlement points and magnetic multipoint extensometers. All readings were referred to a fixed reference point, a bench mark at about 60m from the shaft.

Two inclinometers (SI) were installed to detect the horizontal displacements due to shaft sinking.

Six pressure cells were installed on the steel liner to measure the earth pressure. These cells consisted of a flexible circular flat jack, constructed from two steel discs welded at their common periphery.

5.2 Analysis of Shaft Performance

The finite element method provides a powerful tool to analyze stress-deformation problems in geotechnical engineering where closed-form solutions are not applicable, but three pieces of information are required: (1) initial insitu stress, (2) material properties and (3) construction sequence causing a change in stress.

The finite element program SAFE used in this project provides options such as analysis for non-linear material models, excavation sequence simulation and liner installation.

The objective of the numerical simulation were:

1. To evaluate the performance and effectiveness of the stress-strain models by comparison with field measurements; and
2. To obtain numerically a realistic description of the magnititude and distribution of expected lateral pressures along the shaft lining.

Six FE analyses with different combinations of stress-strain models, support stiffnesses and construction sequences were performed. The input parameters for each analysis are listed in Table 5.1.

For the FE analysis, the soil near the shaft was discretized for the axisymmetric problem by two-dimensional elements. The configuration of the mesh is shown in Fig. 5.4. Zero displacement boundary conditions were assumed at three boundaries and zero pressure at the ground surface.

The coefficient of earth pressure at rest (K_o) is assumed to be 0.8 (Medeiros, 1979). The initial insitu stress was applied to the finite elements by 'switch-on' gravity. Thus, the horizontal stress is governed by the relationship: $\sigma_h = (\nu/(1-\nu))h\gamma$.

FE analyses based on two different types of stress-strain models were performed: linear elasticity and non-linear elasticity (Duncan and Chan, 1970). The soil parameters were obtained from laboratory tests of collected block samples (Kaiser and Wong, 1984).

Two equivalent stiffness values of 30 GPa and 3 GPa were selected for the lining. The first value was calculated from the equivalent stiffness method assuming that the liner plates are fully activated and that no voids exist behind the lining. The second, reduced value, was assumed to approximate the effect of over-excavation and imperfect interaction.

Two cases simulating the excavation sequence and lining installation procedures in the field have been performed. The first case followed exactly as those in the field and in the second case, the lining installation was delayed by one excavation step. This delay may account for any over-excavation behind the lining and simulates the delayed activation of the lining.

5.2.1 Comparison of Predicted (FEM) and Observed Performance

Surface Settlement

Surface settlements are presented in Fig. 5.5. The displacements measured are higher than those predicted by any one of the FE analyses.

The results of analyses LE2/30 and HY2/30 are closest to the measurements (needing a translation by 2 mm). The maximum displacement occurs near the shaft and the settlement decreases gradually away from the shaft. Larger surface settlements near the shaft observed along axes OB and OC are most likely due to the loss of ground in a sand lense, which only dominate the behaviour near the shaft. This lense was not properly simulated by FEM and hence, deviation is expected. It is interesting to note that analyses LE1/3, LE3/30D, HY1/3 and HY3/30D with reduced lining stiffness or delayed liner installation did not produce the greatest settlements, but tended to enlarge the zone of influence.

The results of analyses LE2/30 and HY2/30 are almost equal. This implies that non-linearity is of no significance for this problem because yielding is prohibited due to the relatively low stress levels as compared to soil strength (except in sand).

Subsurface Settlement

Fig. 5.6a and b compares subsurface settlements at distances of 2.1 and 3.1m from the centre of the shaft (0.5m and 1.5m from the shaft wall). Settlements are generally underestimated by all models. At depths above -6.0m, the analyses LE2/30 and HY2/30 yield closer prediction, and at depths below -6.0m, the analysis HY1/3 gives better correlation with field measurements. Heaving was recorded at a depth -17.5m and a radial distance of 2.1m. This response was not predicted by analysis HY1/3, but by the analyses LE2/30 and HY2/30.

Horizontal Displacement

Horizontal (radial) displacements at depths monitored by the inclinometers and predicted by the FE analyses are plotted in Fig. 5.7 for comparison.

Except the displacements in the top layer (depth -1.5m) and the displacements due to loss of ground in the sand lenses (at -6.0m), the field measurements fall near the lower bound of the ranges predicted by the FE analyses.

The maximum displacement recorded in the field is 5.0mm (at -10.5m). The calculated tangential strain is 0.24%, and this value is well within the linear portion of the stress-strain curve of Edmonton Till. Hence, it is not surprising that the linear model LE1/3 and LE2/30 (or the non-linear model HY2/30) give the best prediction.

Displacements predicted by the non-linear analyses HY1/3 and HY3/30D are much higher than those predicted by the linear analyses and those observed in the field, especially at greater depth. The delayed lining installation or the reduction in lining stiffness allows excessive soil deformation, and thus induces a decrease in deformation modulus if the soil behaves non-linear. This effect is more significant at greater depths because higher deviatoric stress causes higher deformation. However, this effect is not reflected in the linear model because it does not exhibit any reduction in stiffness with respect to stress levels.

Pressure on Lining

Results obtained from the FE analyses are presented in Fig. 5.8, together with field measurements.

Little pressure was recorded by the cells at elevations -12.7m and -16.0m. These low pressures indicate that the contact between the soil mass and the cell surface was poor. Soils pressures may have been transmitted to the lining by arching of the soil over the pressure cells. The pressure recorded by these cells are most likely not representative.

Cells at elevation -18.5m give better correlation with results predicted by the FE analyses. The large variation of pressure (two different directions) recorded by these cells may be attributed to various factors that cannot be quantified rationally.

5.3 Comparison of Measurements with Predictions from other Methods

5.3.1 Earth Pressure

The pressure as a function of depth calculated by the, methods proposed by Terzaghi (1943), Berezantzev (1958) and Prater (1977) is shown in Fig. 5.9 for a set of assumed soil parameters. These soil parameters are equal to those shown in Fig. 5.10 except the cohesion (c) is assumed to be to zero. The assumption simplifies the calculation, permits a comparison with techniques that are only applicable for cohesionless materials (e.g., Terzaghi, 1943) and should lead to an overestimation of the pressure.

The convergence curves for various depth were constructed using the CCM described in Section 4.2.4 and are shown in Fig. 5.10 together with the assumed soil parameters. Using the measured displacements (u_m), the formation pressure on the shaft was determined from Fig. 5.10 and plotted on Fig. 5.9. Futhermore, the pressures for assumed displacements of $1/3u_f$, $0.5u_f$, and $0.75u_f$ are listed in Table 5.2 and plotted in Fig. 5.9.

The pressure distribution along the shaft, analysed by the FEM model LE2/30 (see Fig. 5.8) is also plotted on Fig. 5.9.

5.3.2 Discussion

Fig. 5.9 shows the pressure disbributions predicted by five different methods. The following features are observed:

1. The five methods predict relatively consistent pressure distributions to depths of up to -6m. At greater depths, the limit equilibrium methods yield lower pressure than the CCM and FEM except if very large wall

displacements are permitted (e.g., u_i=0.75 u_f). From Fig. 5.9, it follows that displacements at depths below -6m must be in excess of 0.5 to 0.75u_f if limit equilibrium methods are adopted for design. Compared to the results of the CCM and FEM, displacements at depths of -6 to -10m are about 0.5u_f and at depths greater than -10m are well below 0.33u_f, i.e., excellent ground control.

This clearly shows a dependency between the support pressure and the wall displacement. Large pressures are exerted on the lining when displacements are limited. The support pressure calculated from the limit equilibrium methods is a minimum pressure required to maintain the stability and thus induces large wall displacements.

2. By plotting the pressure distributions predicted by the limit equilibrium methods on the convergence curves of Fig. 5.10, it is possible to estimate the ultimate wall displacement when limit equilibrium conditions are reached. This is illustrated on one example shown in Fig. 5.11 (same assumptions as for Fig. 5.10). The CCM and FEM give close correspondence with field measurements. The displacements corresponding to the methods proposed by Terzaghi (1943) and Berezantzev's (1958) are 3.5-4.0 times those measured or estimated by the GCC and FEM. Because no pressure is predicted by Prater (1977) for this depth, the displacements are excessive, i.e., about 8 times greater than those of the CCM and FEM.

However, from the above analysis it follows that the method proposed by Prater (1977) is only applicable for depth of less than 8m (h/a<5) on this project. The methods proposed by Terzaghi (1943) and Berezantzev (1958) are acceptable for this project if relative poor ground control is allowed, i.e., the displacements are in excess of about 16mm. The CCM provides fairly similar results as predicted by the limit equilibrium method for h<10 m. At h>10 m, the CCM predicts higher support pressure if displacements are restricted. The measured pressures are generally in support of these findings even though they cannot be considered adequate as proof for the proposed approach. Low pressures were recorded where large shaft wall movements were permitted and higher pressures in areas where movements were more restricted.

Analysis No.	Stress-Strain Model	Support stiff. (GPa)	Construction Sequence Case
LE1/3	A	3	No.1
LE2/30	A	30	No.1
LE3/30D	A	30	No.2
HY1/3	B	3	No.1
HY2/30	B	30	No.1
HY3/30D	B	30	No.2

*Construction sequence
No.1 - Site Conditon (Kaiser and Wong, 1984)
NO.2 - Delayed lining Installation

	Model 'A' Linear Elastic	Model 'B' Hyperbolic	Reference
Sand	E=15MPa, ν=0.3	Ei=15MPa, ν=0.3, ϕ=30° c=0, Rf=0.9 Kur=3.0	Duncan Chang (1970)
Clay	E=20MPa, ν=0.3	Ei=20MPa, ν=0.3, ϕ=25° c=10.5KPa, Rf=0.95 Kur=2.5	Thomson (1963)
Till	E=22MPa, ν=0.44, E=28MPa, E=30MPa, E=35MPa	Ei=36MPa, ν=0.44, ϕ=22.5° c=31.5KPa, Rf=0.92 Kur=2.5	KUAC Tests; Kaiser and Wong (1984)
Trans zone	E=120MPa, ν=0.44	Ei=120MPa, ν=0.44	SPT (field tests)
Clay shale	E=1GPa, ν=0.44	Ei=1GPa, ν=0.44	

Table 5.1 Input Data for FE Analyses (Terwillegar Shaft)

H/a	Depth (m)	Uf/a	Um/a	Pressure Pi (KPa)							
				Measured		0.33(Uf)		0.5(Uf)		0.75(Uf)	
				Pi/Po	Pi	Pi/Po	Pi	Pi/Po	Pi	Pi/Po	Pi
2	3.2	.0011	.0018	-	-	.52	25	.40		.22	.18
4	6.4	.0036	.0019	.33	42	.50	64	.35	45	.13	16
6	9.6	.0071	.0029	.48	93	.41	78	.23	43	.08	16
8	12.8	.0127	.0028	.44	112	.27	69	.16	41	.06	15
10	16.0	.0220	.0020	.60	192	.20	64	.10	32	.06	16
12	19.2	.0300	.0008	.93	358	.18	69	.11	42	.05	19

Table 5.2 Convergence Curve Data

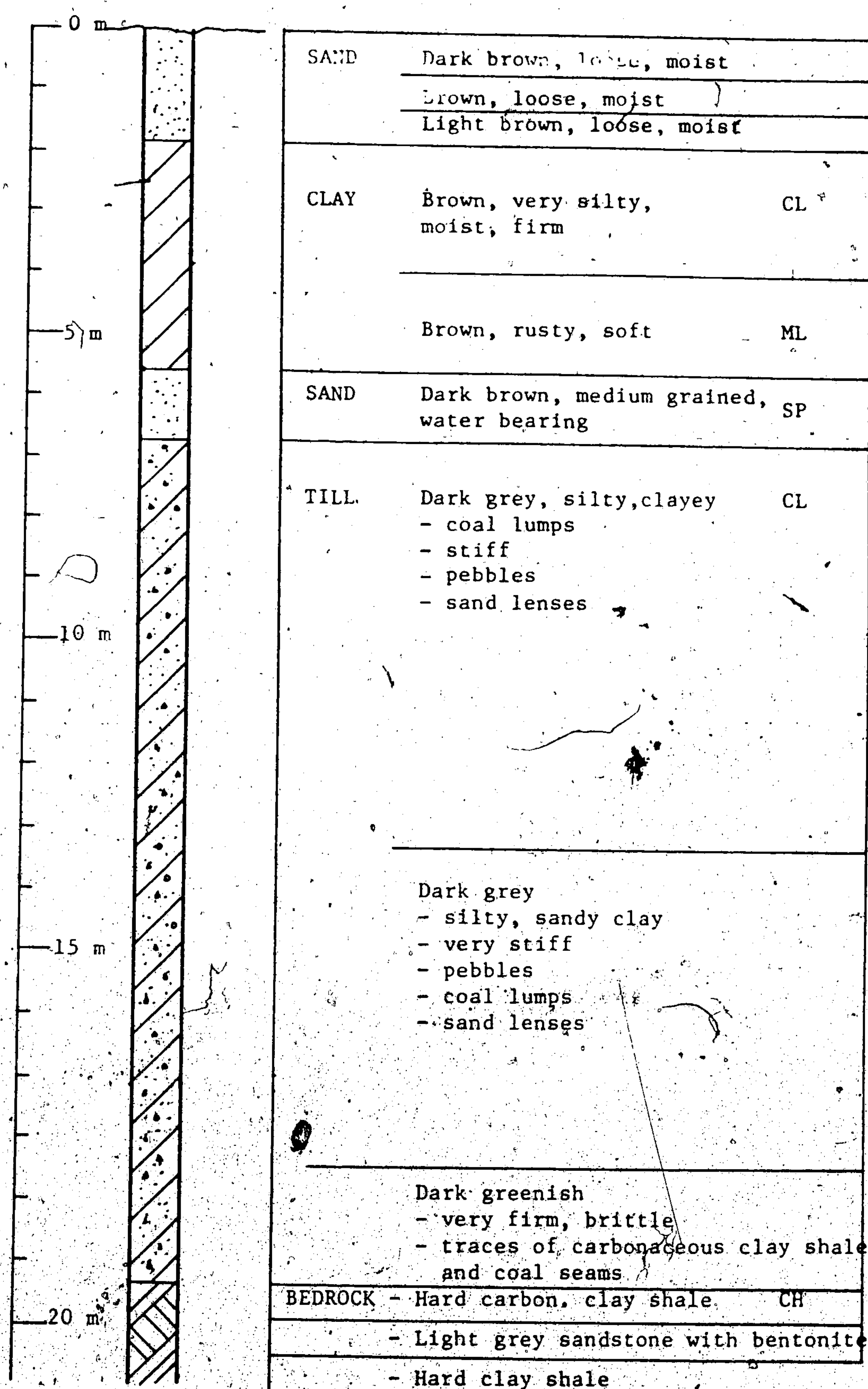

Figure 5.1 Subsurface Stratigraphy (at Terwillegar Shaft)

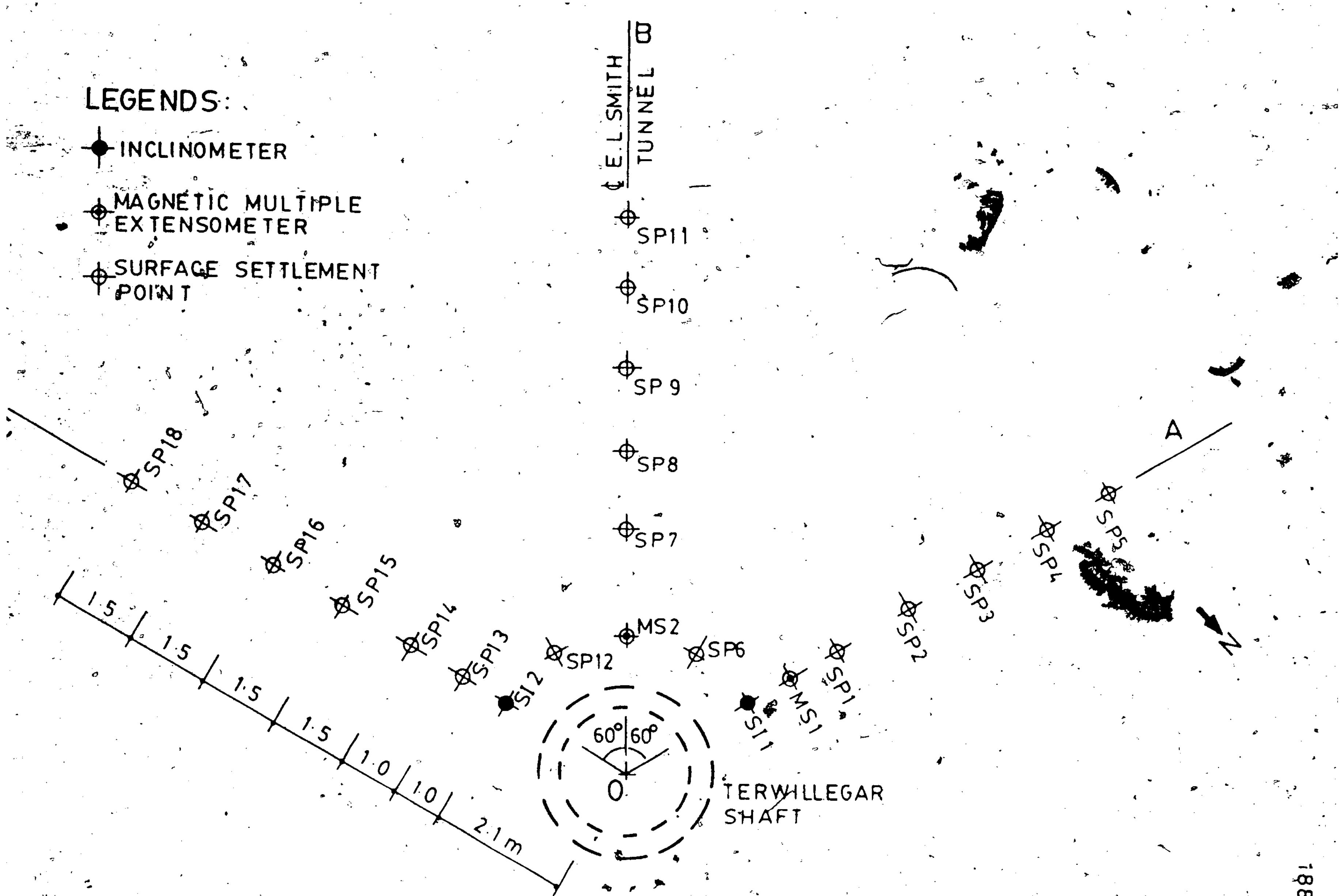

Figure 5.2 Layout of Field Instrumentation)

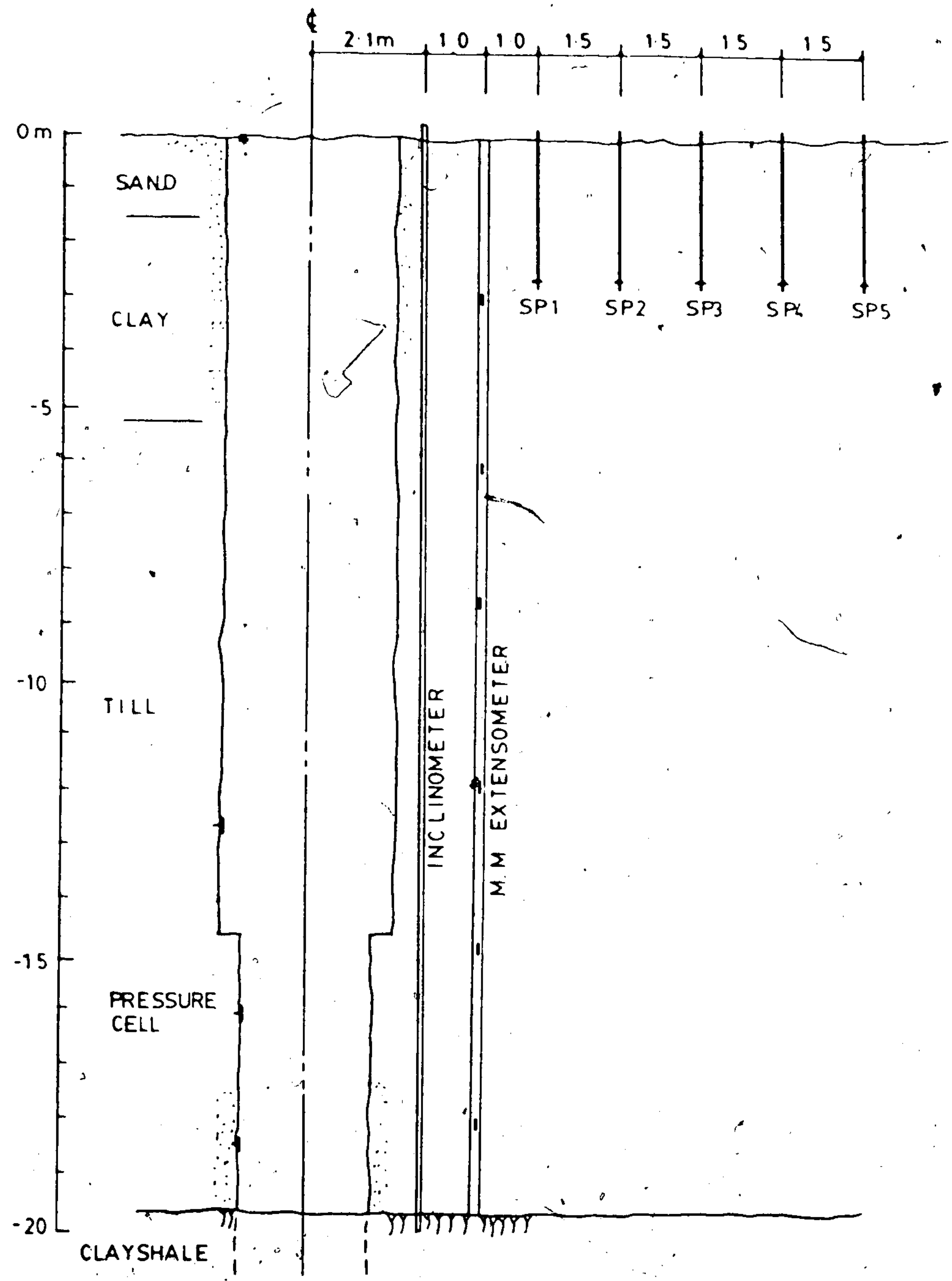

Figure 5.3 Transverse Section showing Shaft Instrumentation (along Axis OA)

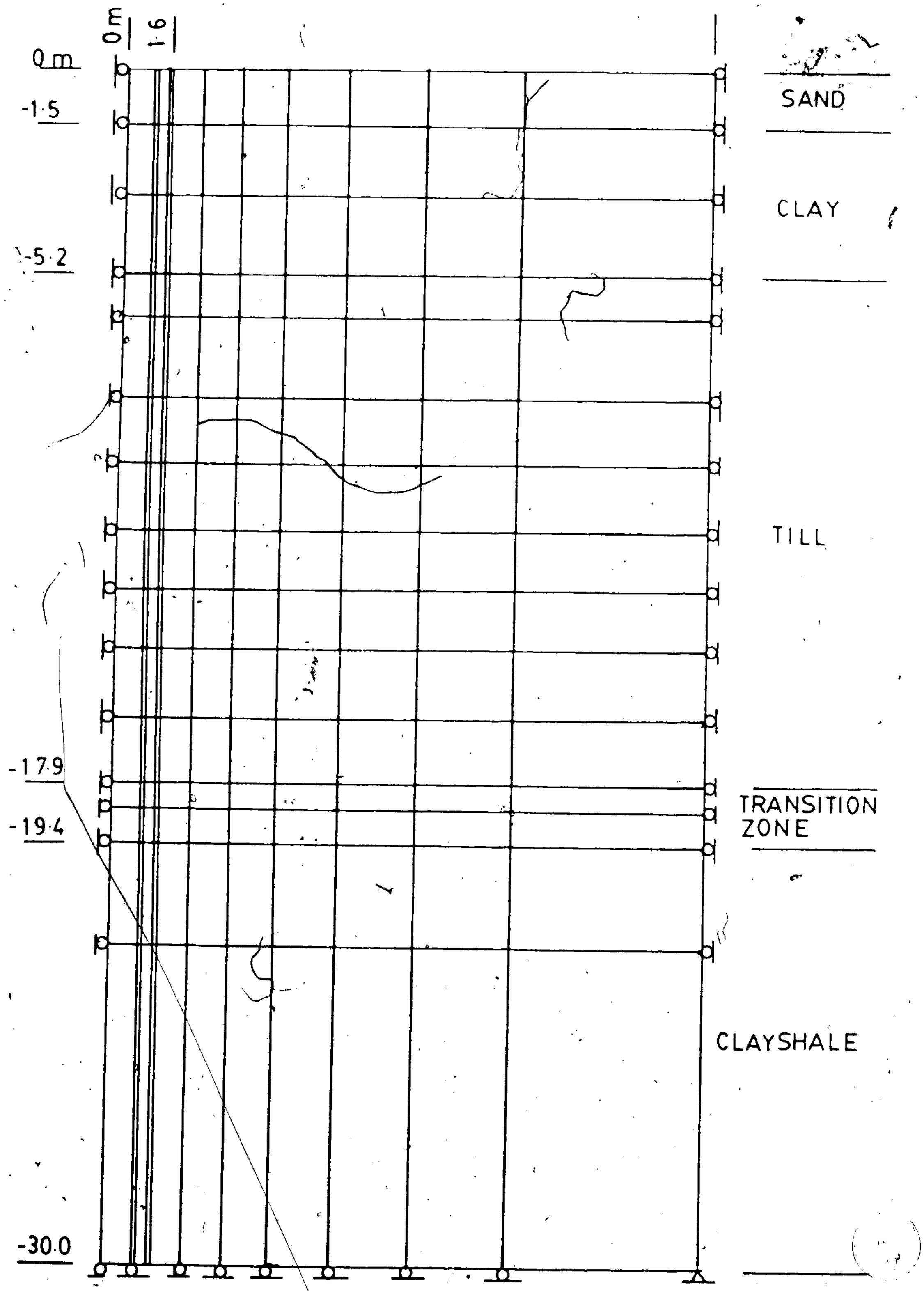

Figure 5.4 Two-Dimensional Mesh for the FE Analyses of the Terwillegar Shaft

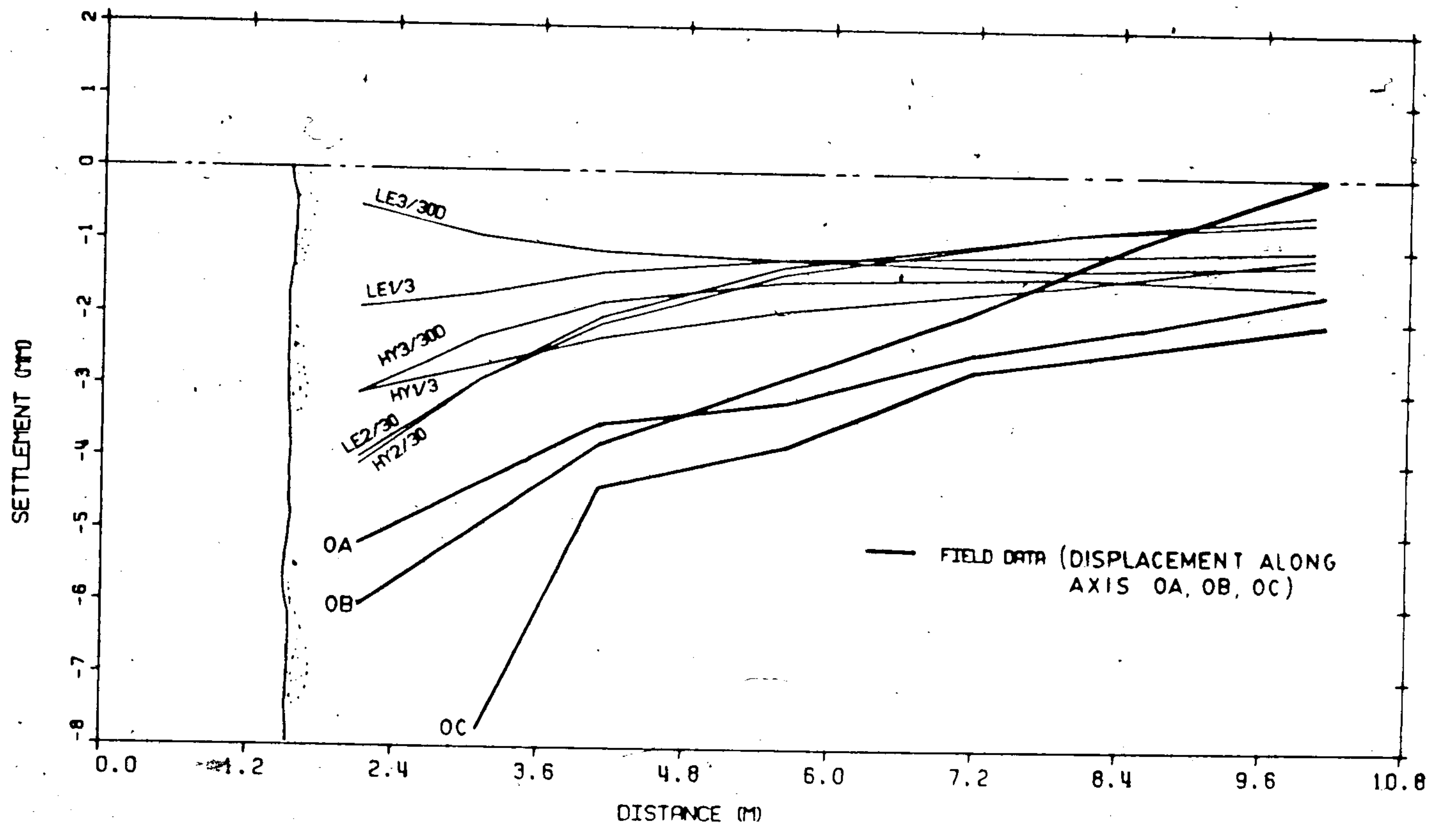

Figure 5.5 Comparison of Surface Settlements

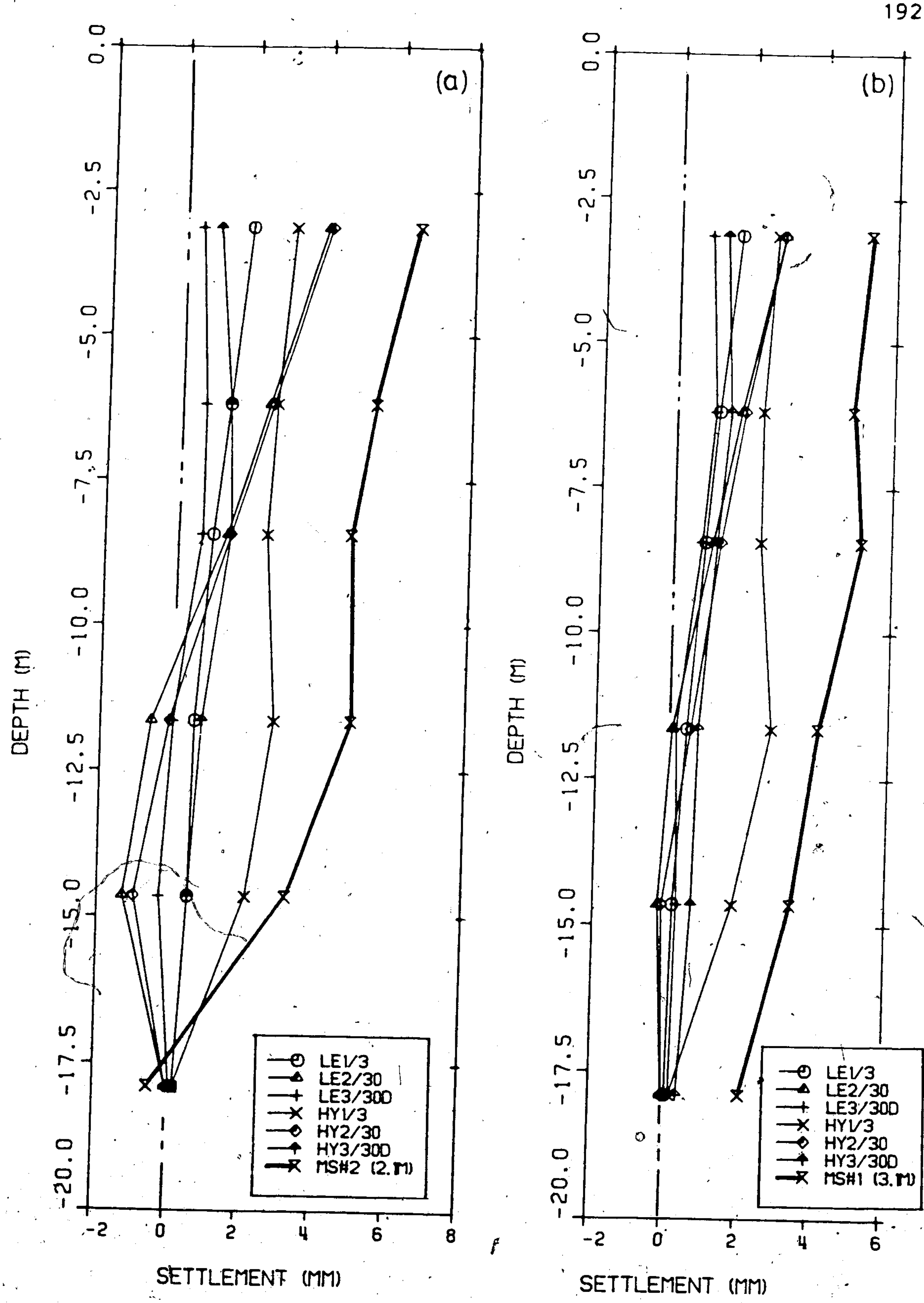

Figure 5.6 Comparison of Subsurface Settlements

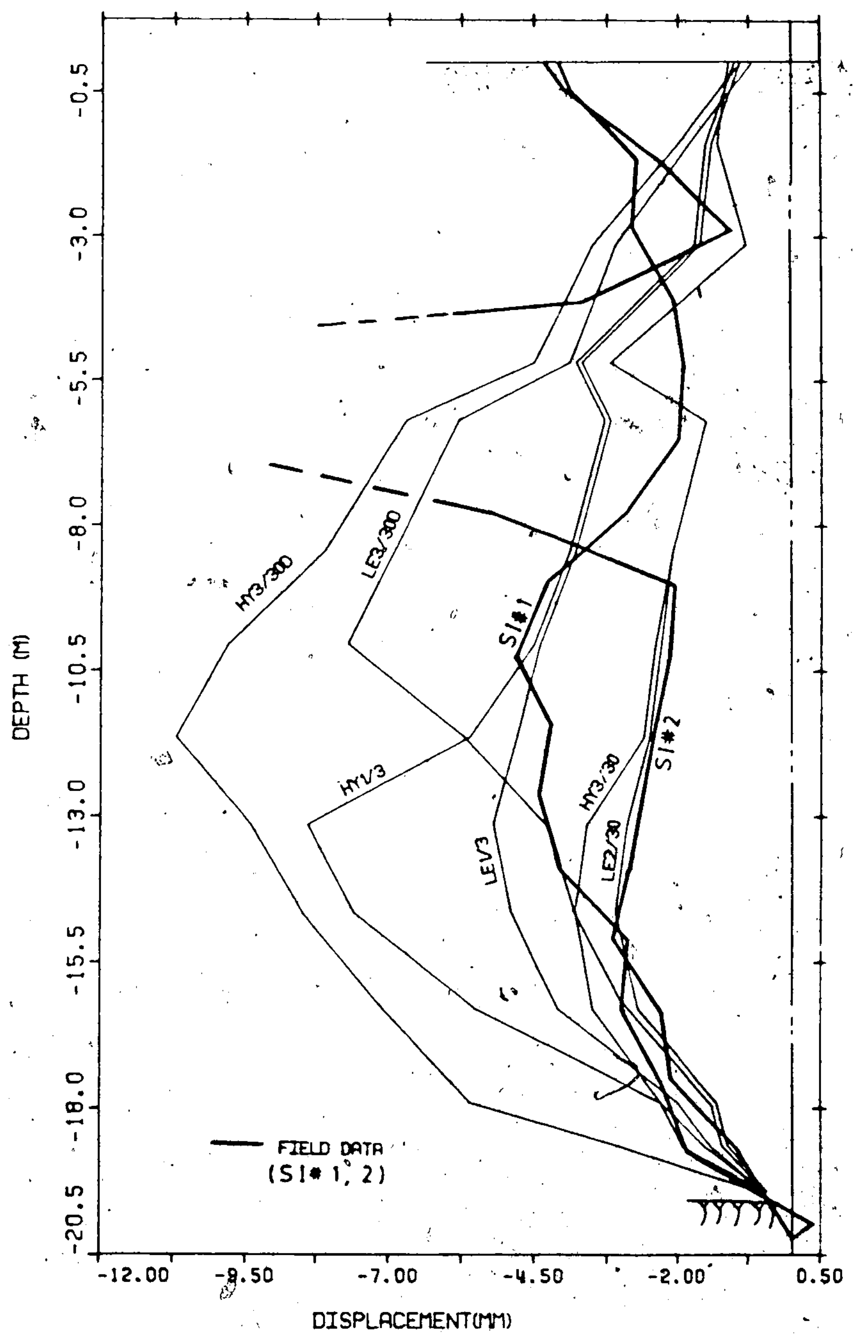

Figure 5.7 Comparison of Horizontal (Radial) Displacements

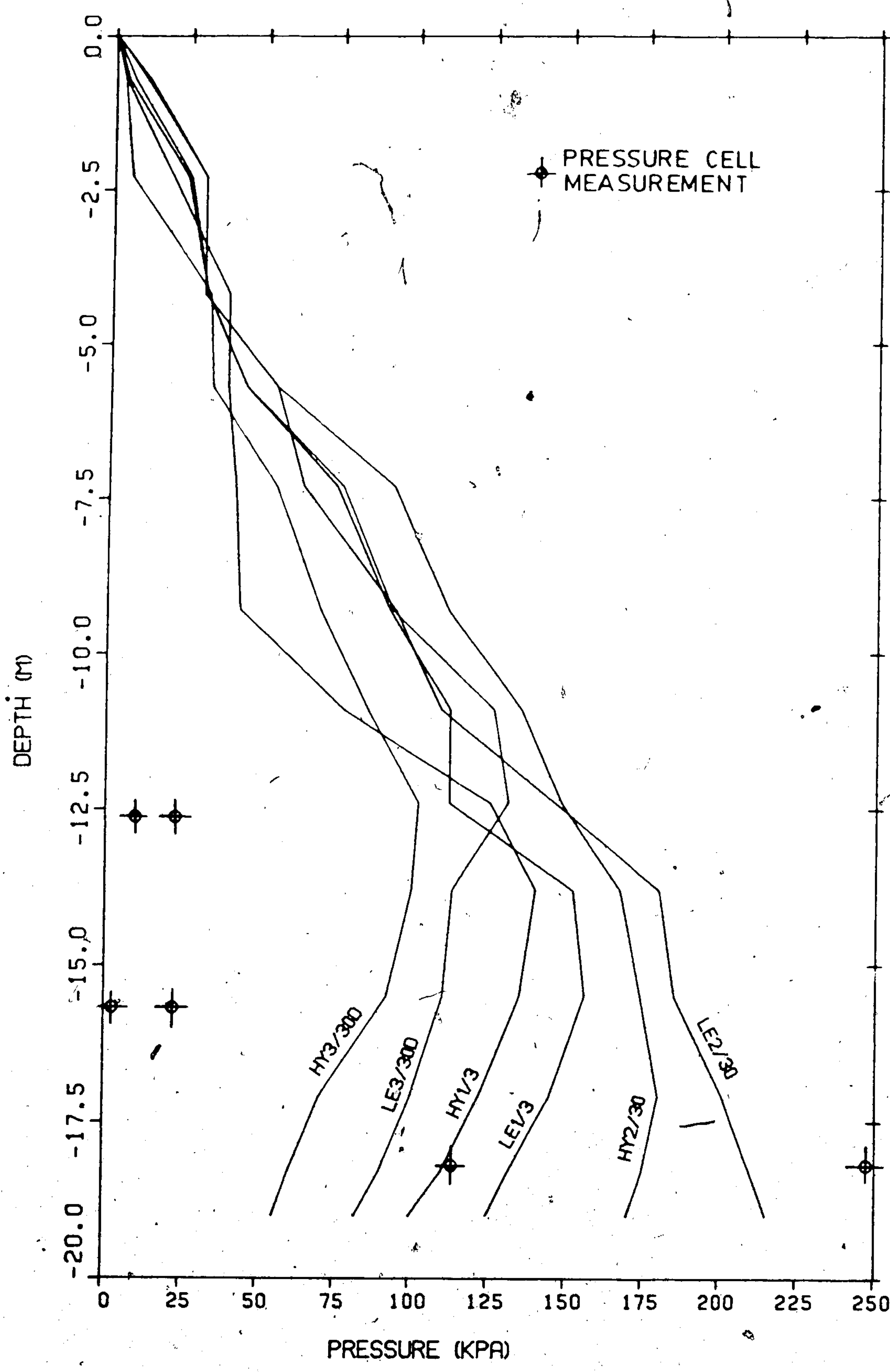

Figure 5.8 Comparison of Soil Pressures

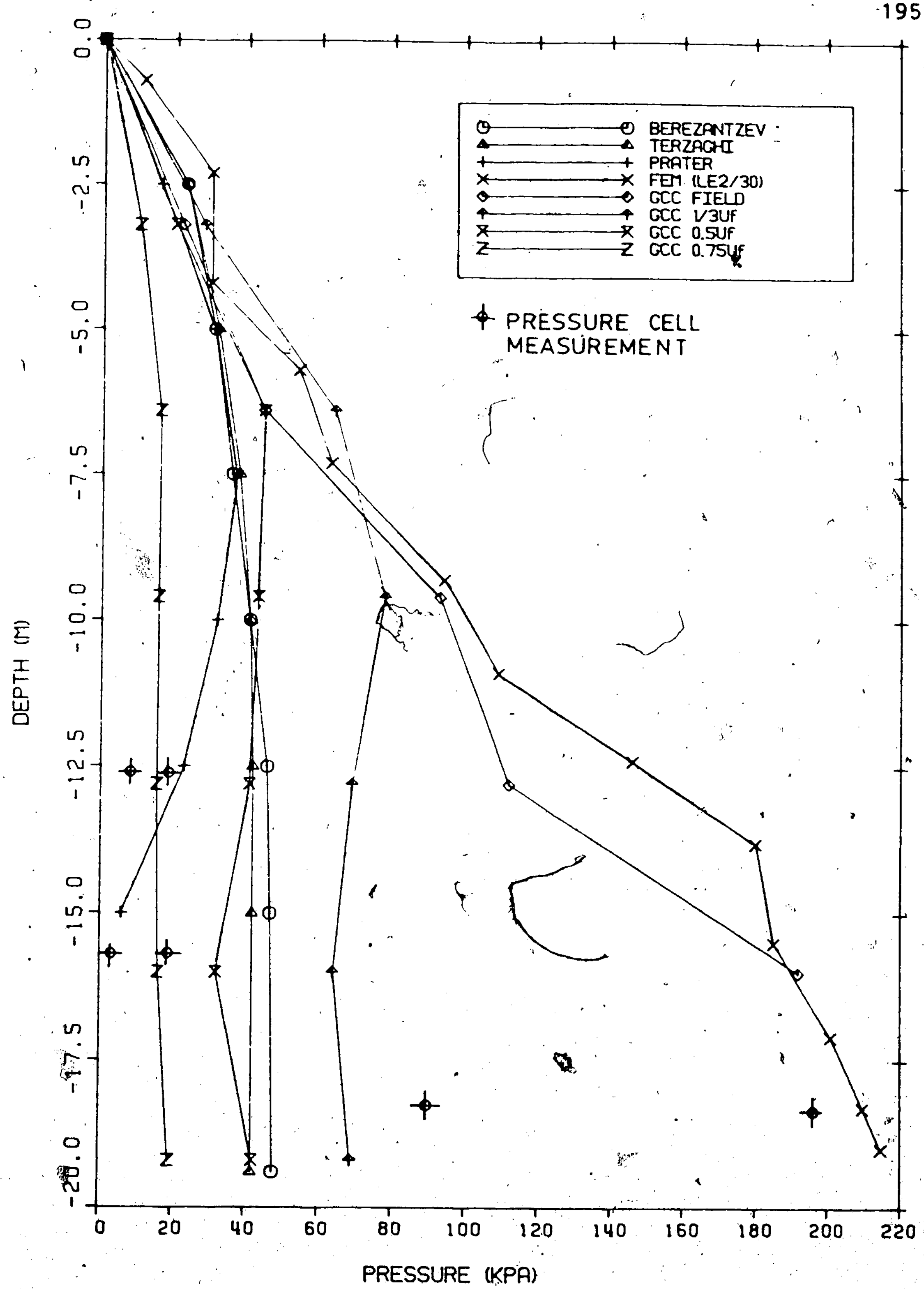

Figure 5.9 Earth Pressures versus Depth

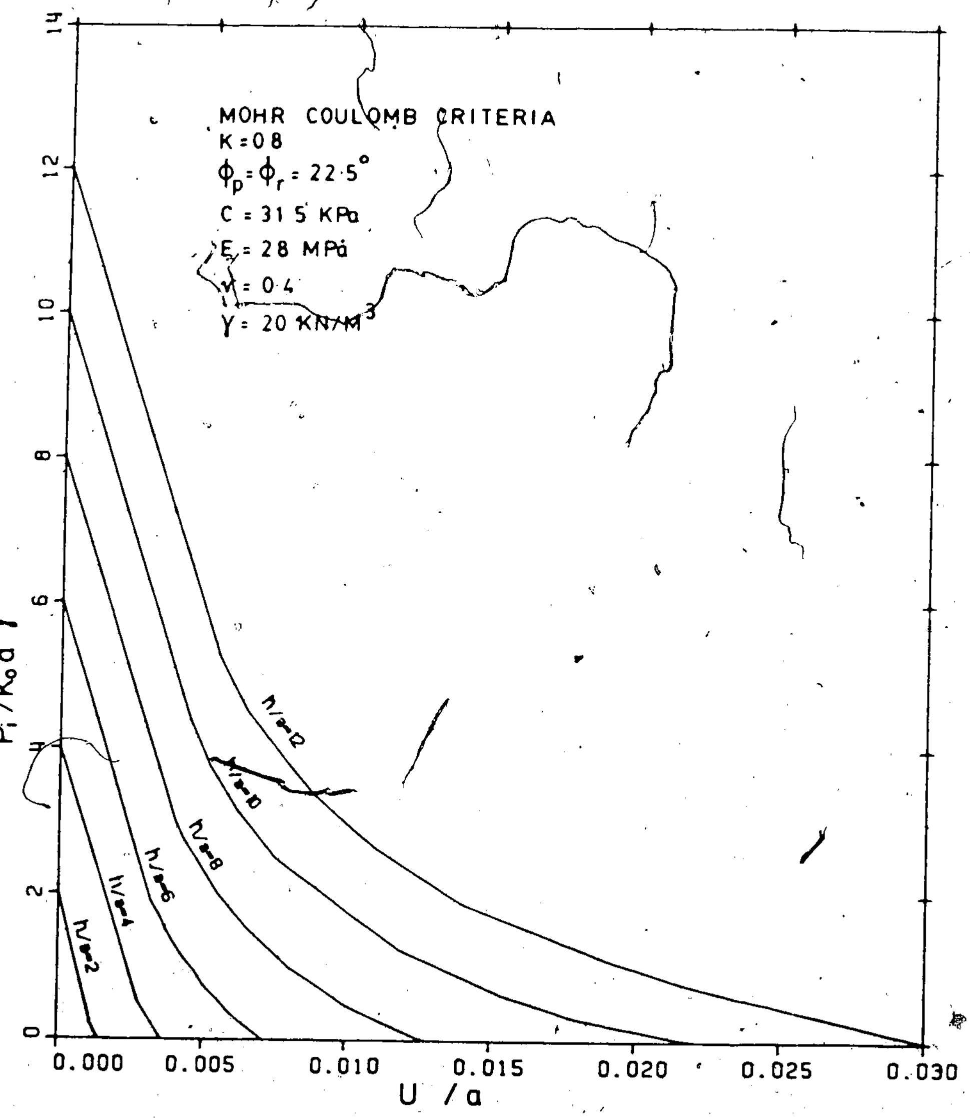

Figure 5.10 Convergence Curves

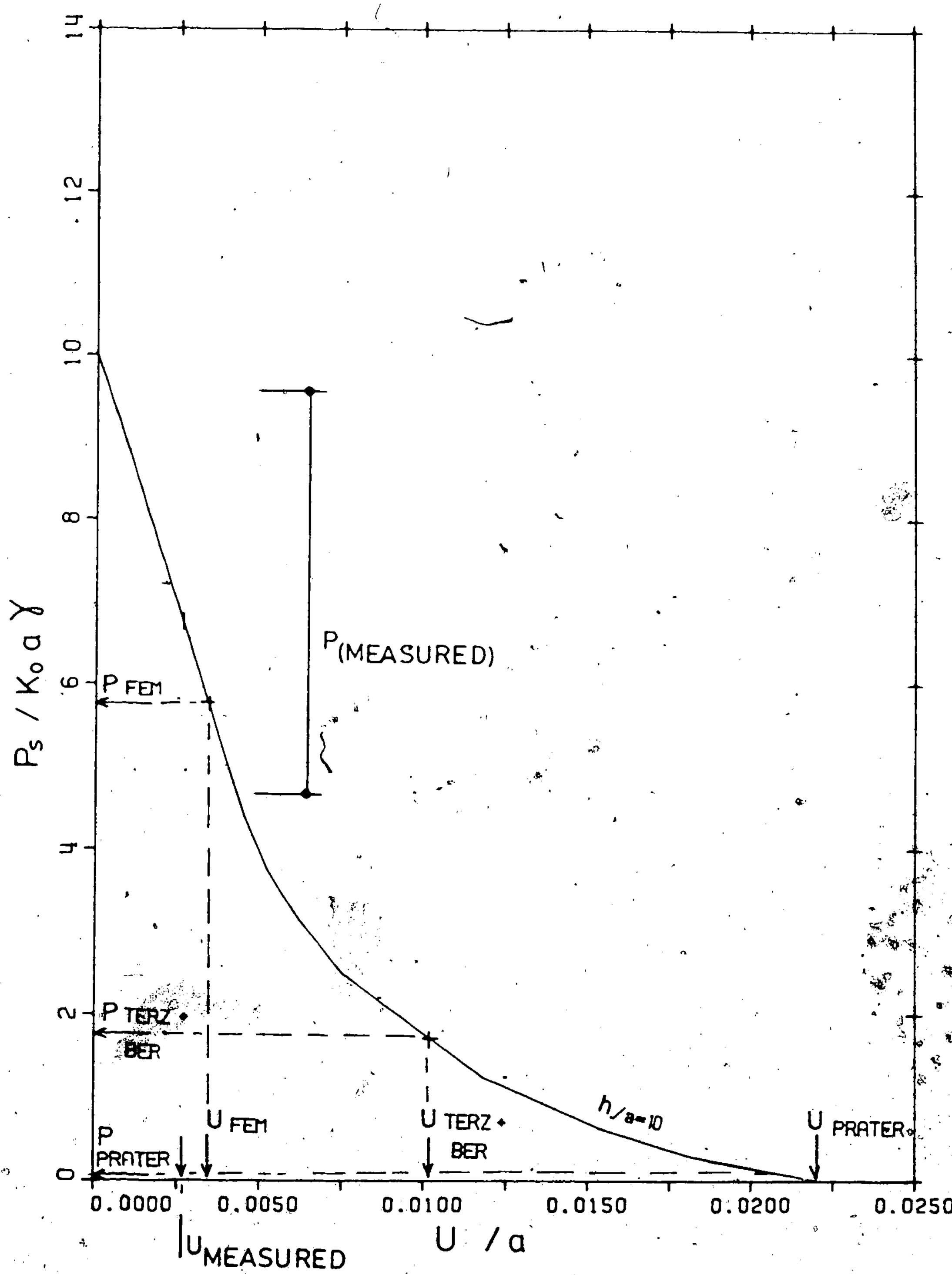

Figure 5.11 Comparison of Shaft Design Methods

6 . SHAFT - CASE STUDIES (MODEL TESTS)

6.1 Berlin Model Tests (Mode A Yielding)

6.1.1 Introduction

Muller-Kirchenbauer *et al.* (1980) carried out a series of model tests to measure the soil pressure exerted by dry sand on a cylindrical caisson (shaft lining). They observed that the pressures measured differed from those predicted by established theories (e.g., Berezantzev, 1985). Based on their results, they extended Terzaghi's method (1936) for the calculation of the active soil pressure on a plane wall to the axi-symmetrical problem by considering vertical and horizontal arching near the shaft. These two arching effects were described by two lateral pressure parameters (λ_t ,λ_s) which were obtained by fitting the measurements by polynominal functions (note: Terzaghi (1936) assumed λ_t and λ_s to be linearly distributed with depth). The active earth pressures on the shaft lining were then calculated by the force equilibrium method on horizontal slices of an assumed failure cone around the shaft.

In the following, a brief description of the testing procedures and certain test results, revelant to this thesis, are given. Their findings will be compared with predictions by the proposed convergence confinement method.

6.1.2 Testing Apparatus and Procedure

The shaft model of 100mm in diameter and 650mm in height was fabricated from steel hollow cylindrical sections. The bottom section was equipped with a sharp-edged shoe to allow easy driving. A recess of several millimeters (ranging from 0 to 5mm) was provided behind the shoe. This recess corresponds to the soil displacement allowed during the excavation. The dimensions of the shaft model are shown in Fig. E.1.

The model was sunk into a test container filled with sands (D=0.2 to 1.0 mm, n_{max}=44%, n_{min}=32.5%) of constant density index. The soil was excavated from inside the shaft. The forces on the shaft lining were measured at different depths. Two types of models (Model I and II) were employed to monitor the pressure. In Model I (Fig. E.2(a)), the axial forces along the shaft height (i.e., frictional forces on the shaft wall) were measured, and the active pressures on the rings were calculated indirectly by assuming a constant wall friction. In Model II (Fig. E.2(b)), three sets of calibrated strain gauges oriented at 120° are installed in each steel segment to monitor the pressure directly.

Model shafts with different recesses (s=0, 1.0, 1.5, 3.0, 3.5, 5.0mm) were excavated in sand with various density indices (I_D=20%, 55%, 80%, 90% and 95%) corresponding to unit weights of 16.2, 16.8, 17.6 and 18.2 kN/m³ were measured. No laboratory test results were presented on the strength-deformation properties of the sand.

Earth pressure cells were placed in the soil to measure the radial stresses outside the shaft before and during excavation. The vertical settlement profiles at the surface were also monitored.

6.1.3 Test Results

An example of the active earth pressures (I_D=80%) on the shaft lining using Model I is plotted against the depth of the shaft in Fig. 6.1. The larger pressure distribution corresponds to the model test with recess (s=0mm). The pattern of the pressure diagram indicates that some difficulties in measuring pressures existed. Fig. 6.2 shows the effect of recess (s) on the total active force acting around the circumference of the shaft at different depth ratios (h/a) for four density indices. The active force decreases significantly with small increase in recess (s) and reaches a minimum. After a critical recess that depends the density index the active force starts to increase slightly.

Results of one test using Model II are given in Fig. 6.3. The sand sample had a density index of 80% and the recess was 1.5mm. The active pressures plotted were obtained by averaging readings from three sensors. A further discussion of this figure will follow later.

Fig. 6.4 shows some typical radial stresses measured in the sand outside the shaft before and after excavation. It can be seen that even before excavation, the initial radial stress varied significantly within the sand mass. Assuming the initial vertical stress is equal to the overburden pressure, the calculated K_o value varies from 1.27 to 1.45. The radial stress decreases due to stress-relief in shaft excavation. Typical settlement profiles near the shaft for I_D=55% and 95% and different reccesses are plotted in Fig. 6.5. For

I_D=55% the magnitude of the settlements in general increases with increasing s and the maximum settlement occurs near the shaft wall. For I_D=90% surface heaving instead of settlement is observed for small s=0.5mm. This response is due to the dilation of dense sand at small straining.

6.1.4 Interpretation of Model Test Results by CCM

Two systems (Models I and II) were employed to measure the active earth pressures on the shaft lining using different approaches. The authors reported that tests on Model II gave better and more representative results than those on Model I. For this reason, the results of Model I are treated qualitatively and those of Model II quantitatively.

Model I

The sinking of the shaft consists of pushing the shoe into the soil and removing the soil inside the shaft. The recess provided a gap between the shaft lining and the vertical excavated face. Hence, the soil can displace inward by a variable amount (s) until it interacts with the lining. For the soil lining interaction, the recess can be viewed as the displacement component allowed during sinking in addition to the displacement ahead of the face (assumed to be negligible). Since the active pressure on the shaft lining depends on this displacement, it should be related to the selected recess. Larger recess will cause smaller active pressures. This phenomenon is confirmed by the results shown in Fig. 6.1 where the pressures for s=0mm are about 2.5 to 3 times larger than for s=5 mm. It is interesting to note that the pressures for zero wall displacement is significantly lower than the pressure at rest. This implies that some stress-relief and displacement u_o took place ahead of the bottom of the shaft.

The pressure-displacement relationship in underground opening is best described by the ground convergence curve. As long as the ground does not yield (elastic), the relationship between displacement and pressure is linear as shown in the inset of Fig. 6.2. Non-linear response will take place due to general plasticity or localized yielding. The shapes of the curves shown in Fig. 6.2 can be compared with those shown in the inset. These curves actually represent the ground convergence curve for a wall displacement in excess of the displacement u_o (ahead of the face). The curves of Fig. 6.2 are reproduced from Muller-Kirchenbauer *et al.* (1980) and are plotted in terms of total force instead of pressure. These curves are not accurate because they are obtained by joining discrete measurements and the initial slope may actually be steeper. The true ground convergence curve can be obtained by shifting the measured data horizontally with u_o. It can be seen that taking displacement as s (neglecting u_o) will not induce significant error in pressure prediction when s is large (s >1.0mm) because the slope of the convergence curve is gentler in this stage than the initial slope.

It is most important to note that the total force increases in most cases for large recesses. This can be explained by the gravity effect (see later) due to vertical arching after a failure mechanism has been established at a critical amount of wall movement (between s=1 and 3 mm). This gravity effect may become dominant as excessive displacements are allowed.

The negative slopes of the initial portion of these curves (Fig. 6.2) increases as the density index decreases. This response is expected because sand of higher density index has a higher Young's modulus. Thus, an equal amount of displacement imposed on sand of high density index will cause relatively more stress-relief than for sand of low density index. Furthermore, the compaction to achieve a dense sand will produce higher initial stress, i.e., the GCC will originate at a high initial stress as can generally be observed from Fig. 6.2.

Model II

The model test with 80% density index and 1.5mm recess was chosen for a quantitative interpretation and comparison with predictions from the CCM because this test gave typical and representative features of the pressure distribution of all model tests. The measurements were presented earlier in Fig. 6.3 and show: two maxima at H/a= 3 and 10.

In order to calculate the pressure using the CCM and to compare them with the measured results, some necessary parameters had to be assumed. These include the insitu stress state, the stress-strain law and the strength of the soil. No measurements of insitu stresses were reported by Muller-Kirchenbauer *et al.* (1980) for this model test, but some results from model tests of

I_D=90% were given as shown in Fig. 6.4. The initial insitu stress coefficient obtained from these measurements were found to vary between 1.27 and 1.45. It is reasonable to assume that the model test (I_D=80%) has a K_o close to or in excess of 1.0. (The test results with I_D=90% was not used here because the pressure distribution was not presented by Muller-Kirchenbauer *et al.* (1980)). Furthermore, no test results were available to study the stress-strain relationship of the sand. However, the stress-strain curves should be hyperbolic with an initial almost linear portion. From the settlement measurements shown in Fig. 6.5 the sand of high density index (I_D=95%) exhibited heave at small straining and must have dilated. This complicates the strain calculation. For this and other reasons the model test with high density index was discarded for data interpretation. Because of the limited information available, the following simplified assumptions were made to obtain a closed-form solution for the calculation of the GCC. The sand is assumed to behave as an elastic perfectly plastic, frictional material that obeys the associated flow rule during plastic straining. The angle of friction of the sand and Poisson's ratio were assumed to be 37° (also used by Muller-Kirchenbauer *et al.*, 1980) and 0.4, respectively and the Young's modulus was asumed to be 44MPa.

The mode of yielding at the shaft wall is due to the tangential-radial stress difference because K_o is greater than K_{cr} (=0.62). Hence, horizontal arching can be described quantitatively by the GCC of a 2-D plane strain hole-in-plate. The GCC at various depth levels were calculated, and the pressures were determined by imposing a wall displacement of 1.5mm (or u/a=3.0%) and plotted in Fig. 6.3. The extent of the plastic zone (Fig. 6.6) was also obtained for each elevation and used to calculate the component due to gravity or vertical arching. Assuming a wall friction angle of 2/3ϕ (downward shear) as suggested by Muller-Kirchenbauer *et al.* (1980). Two sets of coefficients on soil to soil and soil to lining wall interaction (K_s and K_w) were used and the resulting pressure distributions are shown in Fig. 6.3. These distributions reduced to zero at about h/a=12.5. The pressures exerted on the lining are greater for K_s=0.6 and K_w=0.5. It was shown in Appendix D that for Mode A yielding (tangential-radial) K_s and K_w should be closer to K_o than K_a because the vertical stress always remains the intermediate stress. Hence, the pressures due to the gravity effect given by the larger values seem to be more appropriate in this model test. Combination of the pressure envelopes given by the vertical arching (gravity effect) and the horizontal arching yields the pressure distribution on the shaft lining for u/a=3.0%. The resultant envelope compares well with the measured one, except at the bottom of the shaft where the shoe provided a shielding effect attracting the pressure from surrounding soil and reduced the pressure on the lining just above (h/a=13).

From the above analysis, it becomes obvious why the pressure distribution on the shaft lining has two maxima. The upper maximum is caused by the gravity effects which dominate only near the surface due to the shape of the plastic zone and the relatively large wall displacements.

The lower maximum is induced by the steadily increasing pressure with depth and the elevated pressure due to restraint of movement by the shoe (s=0mm). This reduction is only temporary and larger pressures would develop as the shaft advances further.

6.2 Cambridge Centrifuge Model Tests (Mode B Yielding

6.2.1 Introduction

A series of centrifuge tests was performed in the Cambridge University Geotechnical Centrifuge to study the behaviour of deep, vertical shafts in dry sand with particular emphasis on the horizontal pressures acting on the shaft lining. A detailed description and the results of a series of these small scale shaft tests in Leighton Buzzard sand are given by Lade *et al.* (1981). Schofield (1980) presented a detailed description of the Cambridge University Geotechnical Centrifuge and some of the projects performed with it. Here, we shall give a brief description of the testing procedure and results of certain tests which will be needed for comparison with predictions of the CCM.

6.2.2 Testing Apparatus and Procedures

A sketch of the model package along with the dimensions and locations of instruments is given in Fig. E.3. The shaft, its lining made of polyetheylene Melinex, was installed within the sand before excavation to simulate artifical ground freezing techniques in construction of deep shafts (physical properties of shaft lining listed in Table

E.1).

Strain gauges bonded to the surface of the shaft tube were employed to measure the radial strain in the tube. Pressure cells were placed in the soil to monitor the vertical, radial, and tangential stresses as shown in Fig. E.1. The vertical settlements across the tub and the vertical movement of the bottom of the shaft were recorded by LVDTs.

Since it was not possible to actually excavate soil in the centrifuge test during flight, the soil in the shaft was substituted with a fluid which could be removed in stages to model the excavation process of the shaft. The $ZnCl_2$-solution of density 1.55 g/cm³ and a parafin oil with a density of 0.765g/cm³ were used to model the vertical stresses at the shaft bottom and the horizontal stresses inside the shaft, respectively.

6.2.3 Test Results

The centrifuge tests were performed using dry fine Leighton Buzzard Sand 120/200, whose properties are given in Table E.2. Fig. E.4 shows the stress-strain relations obtained from triaxial compression tests over the appropriate range of confining pressures.

Results of three successful tests PL2, PL5 and PL6 will be summarized and discussed. The details of each of the three tests are listed in Table 6.1.

Fig. 6.7 shows a comparison of the radial strains measured in the shaft liner for each test plotted versus non-dimensional depth h/a. The vertical axis on this figure indicates zero strain corresponding to the unstressed Melinex liner without earth and fluid pressure. Ideally, the shaft lining should not expand during centrifuge acceleration but even when paraffin oil with much lower density than soil was used did some expansion occur as observed in Fig. 6.7. However, for the three tests discussed here, the initial horizontal earth pressure near the shaft were only slightly higher than the at rest pressure (i.e., $K_o = 1-\sin\phi$)

Fig. 6.7 indicates that as excavation of the shafts proceeds, the flexible lining moves inward and the formation pressures on the shaft lining increase to the bottom level as shown in Fig. 6.8, a plot of normalized earth pressures versus normalized depth. In all cases do the earth pressure increase near the bottom of the shaft. The earth pressures calculated from Berezantzev's formula are shown for comparison. It appears from this comparison that the earth pressures measured in a flexible shaft are higher than those predicted.

The radial and tangential earth pressures measured with earth pressure cells at level 3 after excavation for Test PL5 are shown in Fig. 6.9. It is clear from the measured pressure distribution that arching develops around the shaft causing the radial stresses to decrease in response to the small radial movement of the shaft wall during excavation.

6.2.4 Prediction of Model Test Behaviour by the CCM

One of the essential input parameters for the CCM analysis is the stress-strain relationship of the soil. The triaxial compression tests on Leighton Buzzard Sand (Fig. E.4) indicate that the stress-strain relations are hyperbolic and dependent on the confining pressure levels. The sand is slightly dilatant at small strains and contractant at large strains.

To simplify the formulation of the ground convergence curve, it is necessary to make the following assumptions on the stress-strain law of sand:

1. The hyperbolic stress-strain relations are approximated by the elastic perfectly plastic models. Because of the non-linearity of the stress-strain curve the Young's moduli E are obtained by averaging the slope on the portion of the curve of the expected strain range. The displacements measured in the model tests were about 0.2%, hence, it seems reasonable to use E at 0.2%. However, it is also realized that there exists an initial strain (0.2 to 0.4%) if the stress difference in K_o condition is imposed in the isotropic compression triaxial tests (Kaiser and Wong, 1984). To account for this aspect, the E values at 0.5% strain are the appropriate parameters for the elastic perfectly plastic models.

   The E-values also depend on the confining pressure or the depth. The confining pressures are isotropic in the triaxial tests whereas they are anisotropic in the model tests. To account for this difference, the first stress variance is used (i.e., $I=(\sigma_1+2\sigma_3)/3$) for the triaxial tests and $I=(1+2K_o)\sigma_1/3$ in the model tests).
2. The stress path involved in the triaxial tests

(isotropic consolidated passive compression) is different from that (anisotropic consolidated active compression) involved in the model tests. To make use of the results from the triaxial test it is required to assume that the stress path did not exert great influence on the stress-strain relations.

With the above assumptions the E-values as a function of the confining pressures for 0.2% and 0.5% strains are calculated and plotted in Fig.6.10. The modulus increases with the confining pressure or overburden depth, which can be approximated by linear equations as shown.

Mode of Initial Yielding and Extent of Yielding Zone

For ϕ=38.3°, K_o (=0.38) is less than K_{cr} (=0.62) and initial yielding should be induced by the vertical-radial stress difference or Mode B.

The displacement u_y to determine how much radial displacement can be tolerated before yielding around the shaft wall takes place is:

$$u_i = a[(K_o - K_a)p_o(1+\nu)]/E \qquad 6.1$$

Table 6.2 lists the calculated displacement u_y for test no. PL2, PL5 and PL6, along with intermediate steps involved in calculations. A comparison of the normalized displacement (u_y/a) with the measured radial strains in the model test (Fig. 6.7) reveals that the soil in the upper zones (PL2, PL5: h/a<1/2, and PL6: h/a<1) is in the elastic state and the soil below has been strained beyond the yield point.

With the measured strain of 0.2% relationships between the extent of the plastic zone and the shaft depth for the model tests are calculated using Eqn. 4.23 or 4.25 and are plotted in Fig. 6.11. The shapes and extent of the predicted plastic zone are cylindrical with depth, which are comparable to the one shown in Fig. 4.10.

Soil Pressure Distribution along the Shaft Depth

The soil pressures acting on the shaft lining are calculated using Eqns. 4.15 with the assumed strain of 0.2% for the tests, and plotted in Fig. 6.8, along with the measured results for comparison. The observed pressures correspond well with the predicted values. The pressures near the surface lie within the envelopes given K_o and K_a whereas below a depth (h/a=1.0) the pressures are much lower than the given by K_a, i.e., yielding and related stress redistribution take place. The soil pressures on the shaft linings are, however, higher that those predicted from Berezantzev's formula because Berezantzev's method only provides minimum support pressures for conditions of large or excessive deformation.

Higher pressures developed near the shaft bottom. As the vertical confining pressure exerted by the soil above (fluid in model tests) is removed during excavation, the soil beneath the excavation bottom yields. The horizontal pressures are redistributed and attracted to the shaft lining of high stiffness. This result in high pressure at the bottom of the shaft. If the material at the face is strong enough to prevent yielding, the face effect would reduce, instead of increase the pressures.

Stress Distribution

From the reduced tangential stress near the shaft wall (Fig. 6.9), it is evident that arching develops in horizontal planes around the shaft.

Lade *et al.* (1981) calculated the stress distribution in the horizontal plane and compared it with the measured pressures. They found that the general pattern of the stress distribution predicted by the model proposed by Klein and Gerthold (1979) agreed reasonably well with the measured stress distribution but that the extent of the plastic zone was underestimated. This underestimation is due to the fact that Lade *et al.* (1981) assumed Mode A yielding (tangential-vertial stress). The actual mode is, however, Mode B which is governed by stress difference (vertical-radial) as discussed earlier. The extent of the plastic zone induced by Mode B yielding is given by Eqn. 4.23 or 4.25.

Using the measured pressure on the Melinex tube, one can calculate R_{vr}. The calculated R_{vr} of 1.69a or 97mm and the related tangential stress distribution agree better (Fig. 6.9) with the measured and confirms that the CCM with the appropriate mode of yielding is capable of predicting the ground behaviour with sufficient accuracy.

Gravity Effect due to vertical arching inside the yield cone (Fig. 6.9) are not dominant in these model tests because of the relatively small straining.

Table 6.1 Centrifuge Model Test Data

Test No.	Model Dimensions d (cm)	H (cm)	N	Prototype d (m)	H (m)	H/a	Soil Density (kN/m3)	Fluid used
PL2	8.3	24.0	39.6	3.3	9.5	5.76	15.50	ZnCl2
PL5	11.5	45.0	111.8	12.9	50.3	7.80	15.31	ZnCl2
PL6	7.8	54.0	112.9	8.8	61.0	13.86	15.43	Paraffin Oil

a - radius of shaft
d - diameter of shaft
H - depth of shaft
N - gravity ratio in centrifuge

Table 6.2 Calculation of Displacement u_y

TEST NO.	h/a	h (m)	Po (kPa)	I (kPa)	E (MPa)	u/a (%)
PL2	1	1.65	25.1	15.2	19.0	0.032
(H=9.5m,	2	3.30	50.2	30.4	23.4	0.053
a=1.65m)	3	4.95	75.3	45.6	27.7	0.067
	4	6.60	100.4	60.9	32.1	0.077
	5	8.25	125.4	76.0	36.5	0.084
PL5	1	6.45	97.4	59.0	31.6	0.076
(H=50.3m,	2	12.90	194.8	118.1	48.6	0.098
a=6.45m)	3	19.35	292.2	177.1	65.6	0.109
	4	25.80	389.6	236.1	82.6	0.116
	5	32.25	487.0	285.2	99.6	0.120
	6	38.70	584.4	354.2	116.6	0.123
	7	45.15	681.8	413.2	133.6	0.125
PL6	1	4.40	66.4	40.2	26.2	0.062
(H=61.0m,	3	13.2	199.3	120.8	49.4	0.099
a=4.4m)	5	22.0	332.2	201.3	72.6	0.112
	7	30.8	465.1	281.9	95.8	0.119
	9	39.6	598.0	362.4	119.2	0.123
	11	48.4	730.8	442.9	142.2	0.126
	13	57.2	863.7	523.5	165.6	0.128

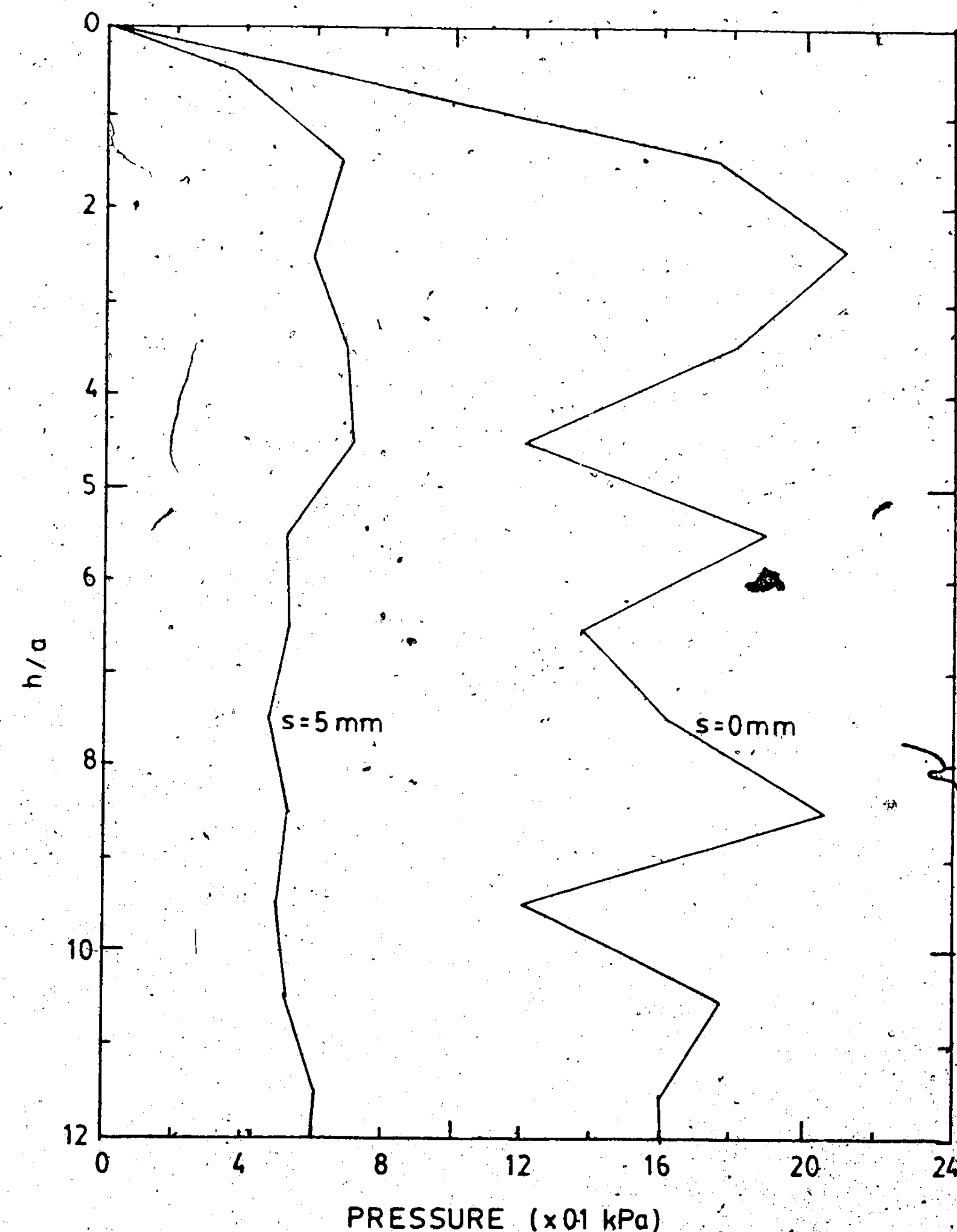

Figure 6.1 Pressure versus Depth - Model I (modified from Muller-Kirchenbauer et al., 1980)

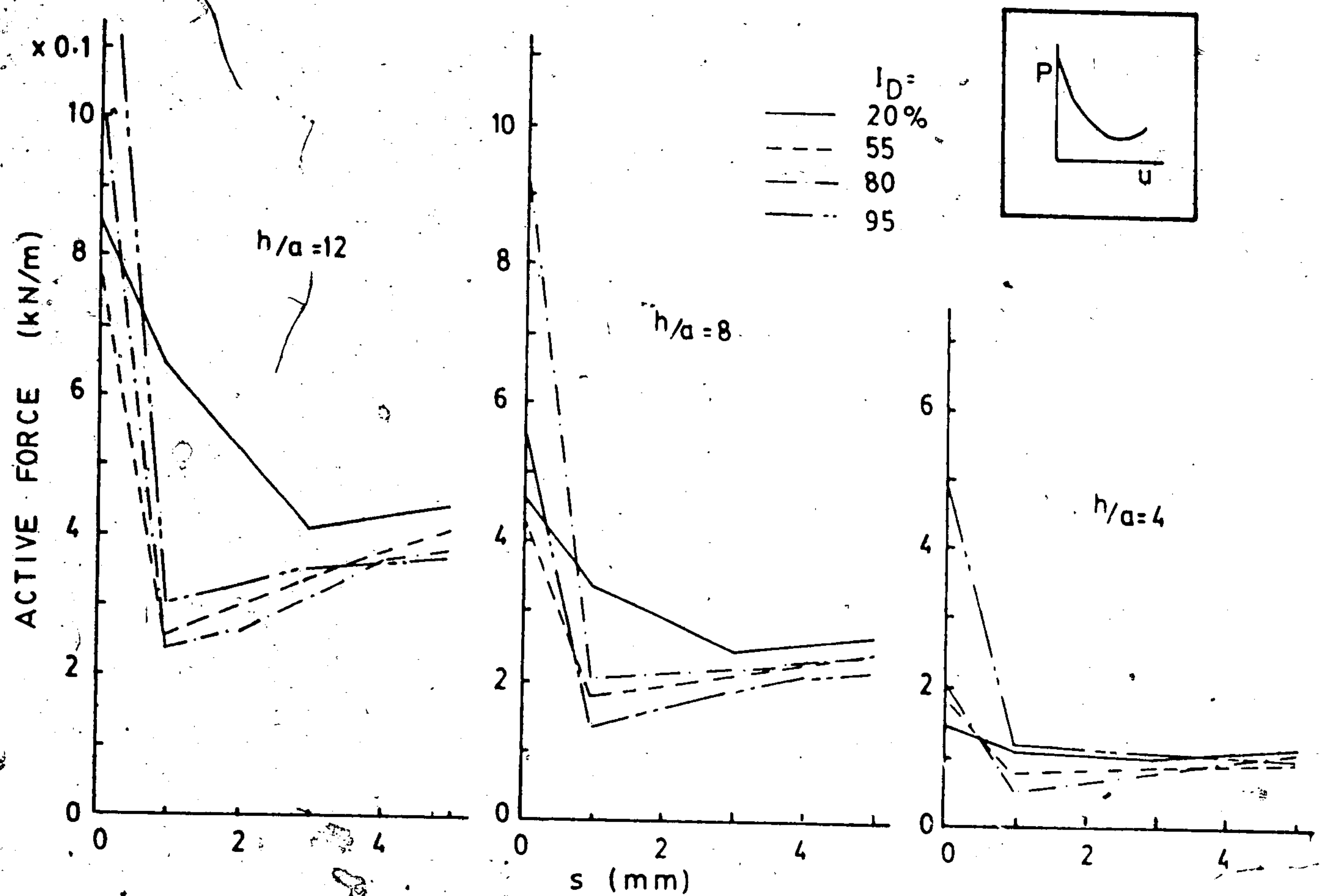

Figure 6.2 Active Force versus Recess Parameter - Model I
(modified from Muller-Kirchenbauer et al., 1980)

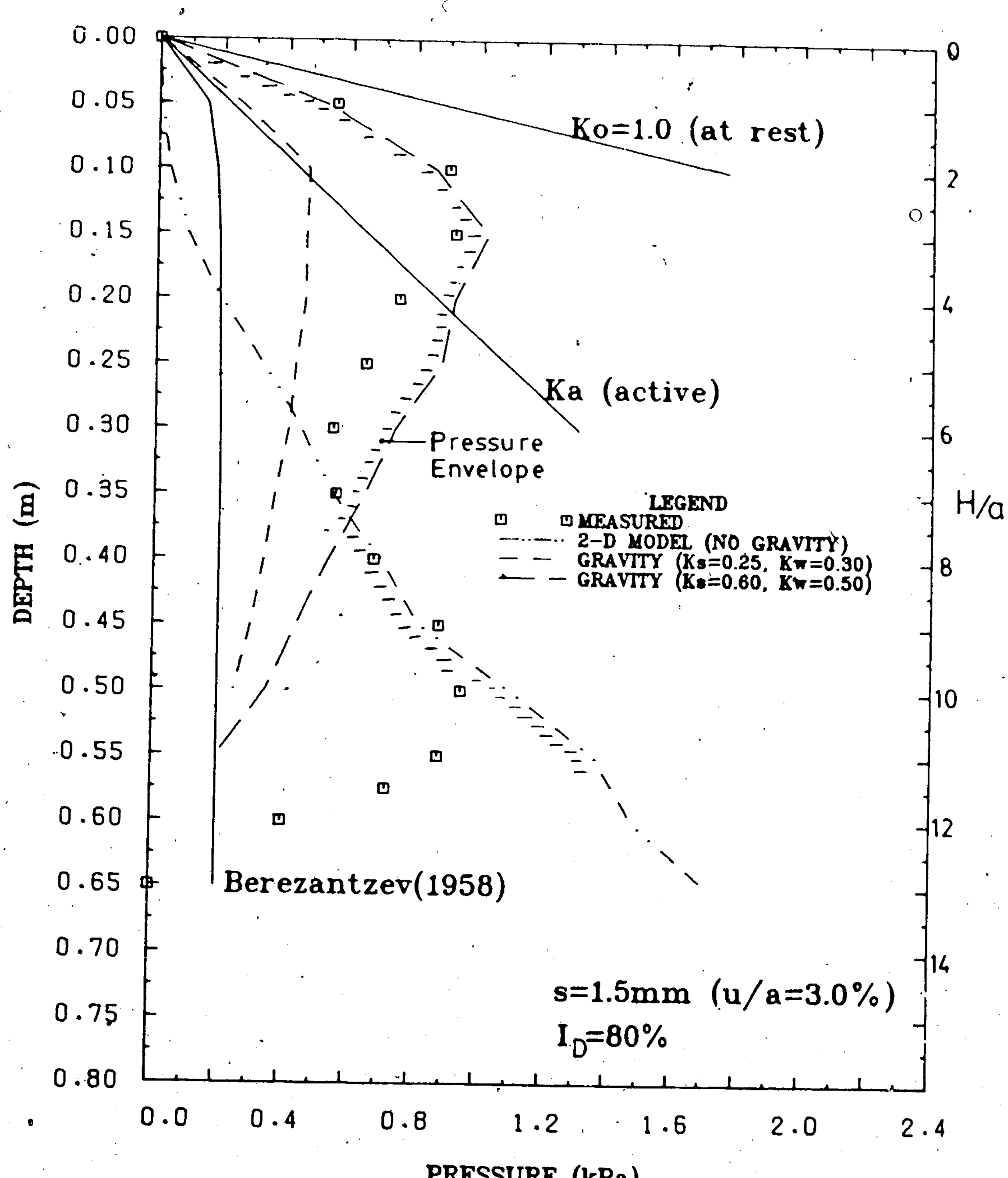

Figure 6.3 Comparison of Active Pressures - Model II

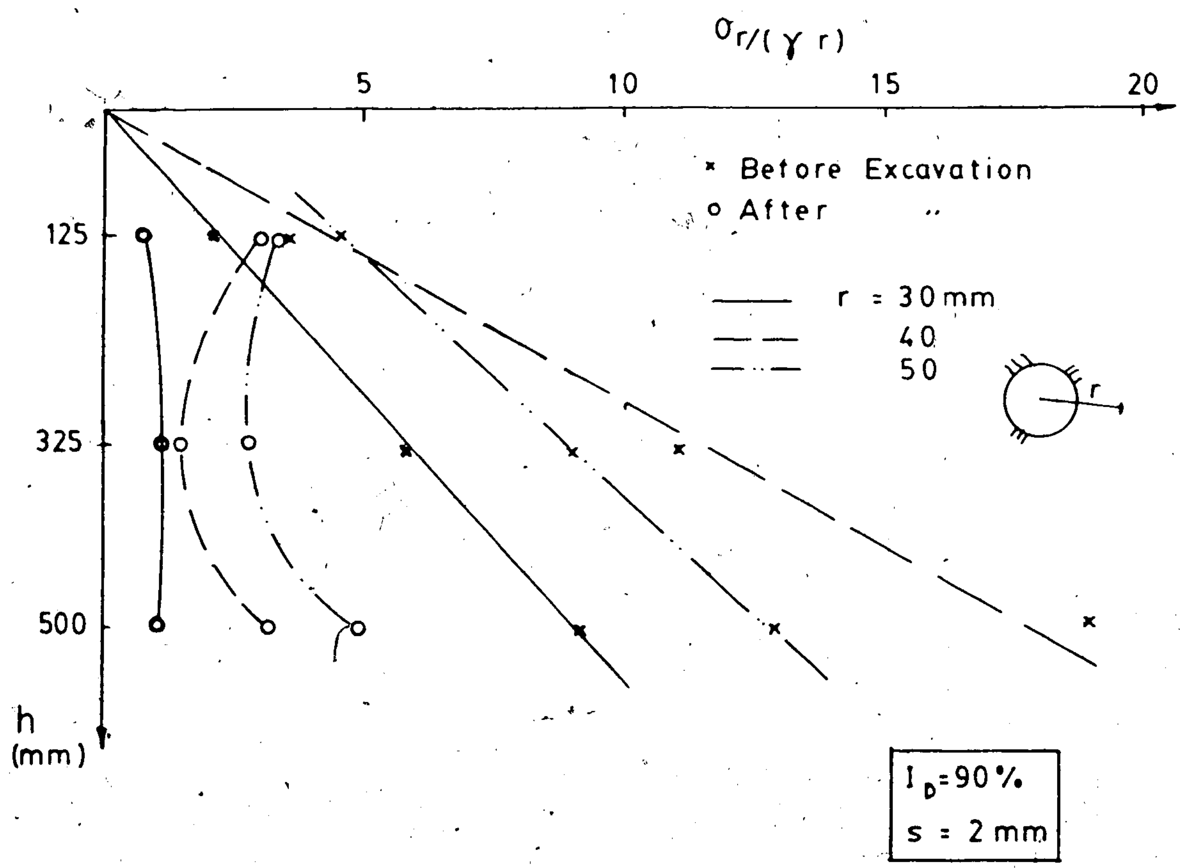

Figure 6.4 Measurement of Stresses Before and After Excavation (modified from Muller-Kirchenbauer et al., 1980)

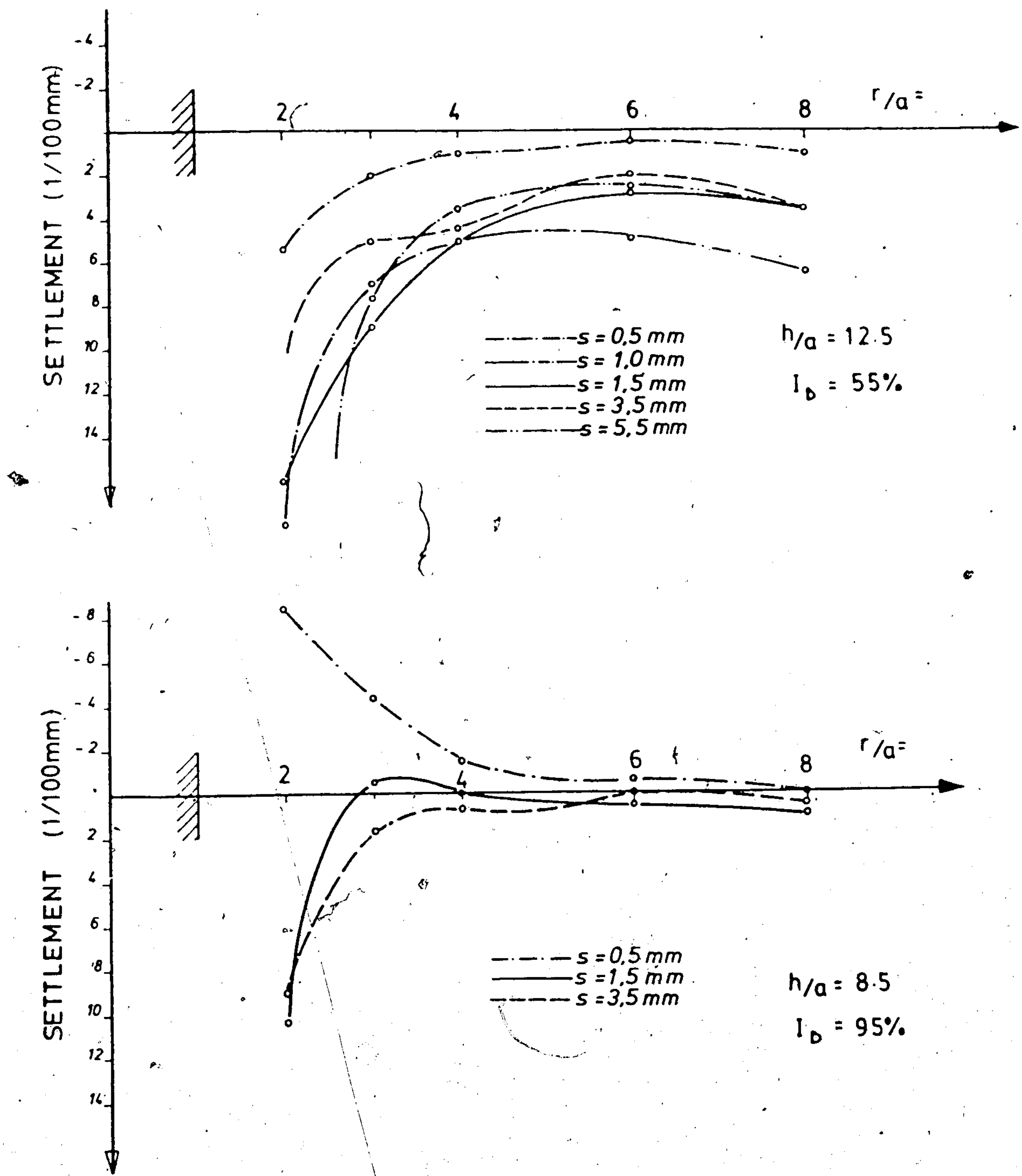

Figure 6.5 Measurement of Surface Settlement (modified from Muller-Kirchenbauer et al., 1980)

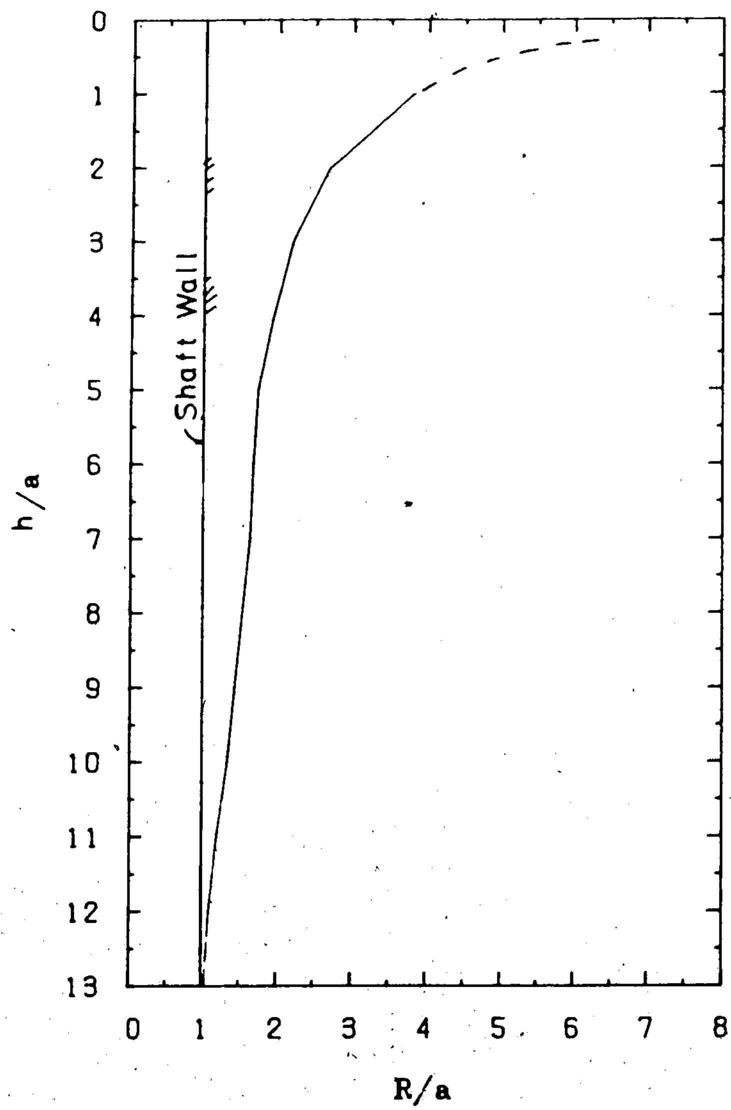

Figure 6.6 Predicted Plastic Zone with Depth

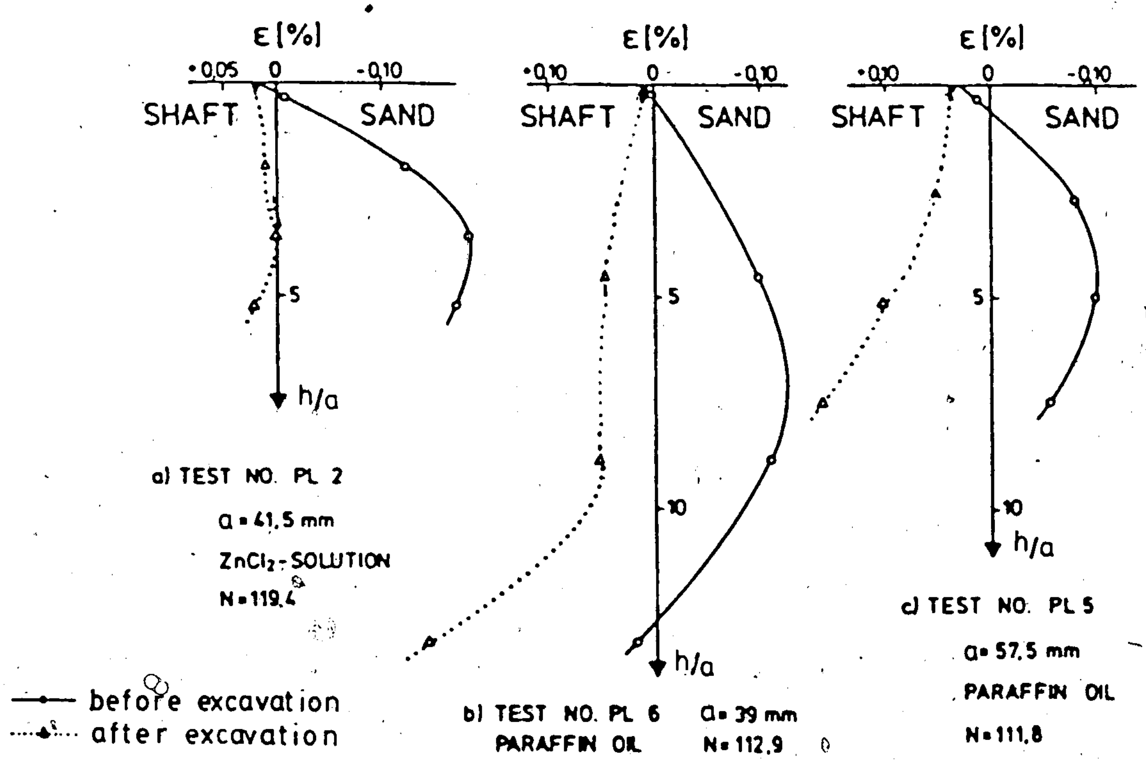

Figure 6.7 Radial Strains in Melinex Shafts versus Depth (modified from Lade et al., 1981)

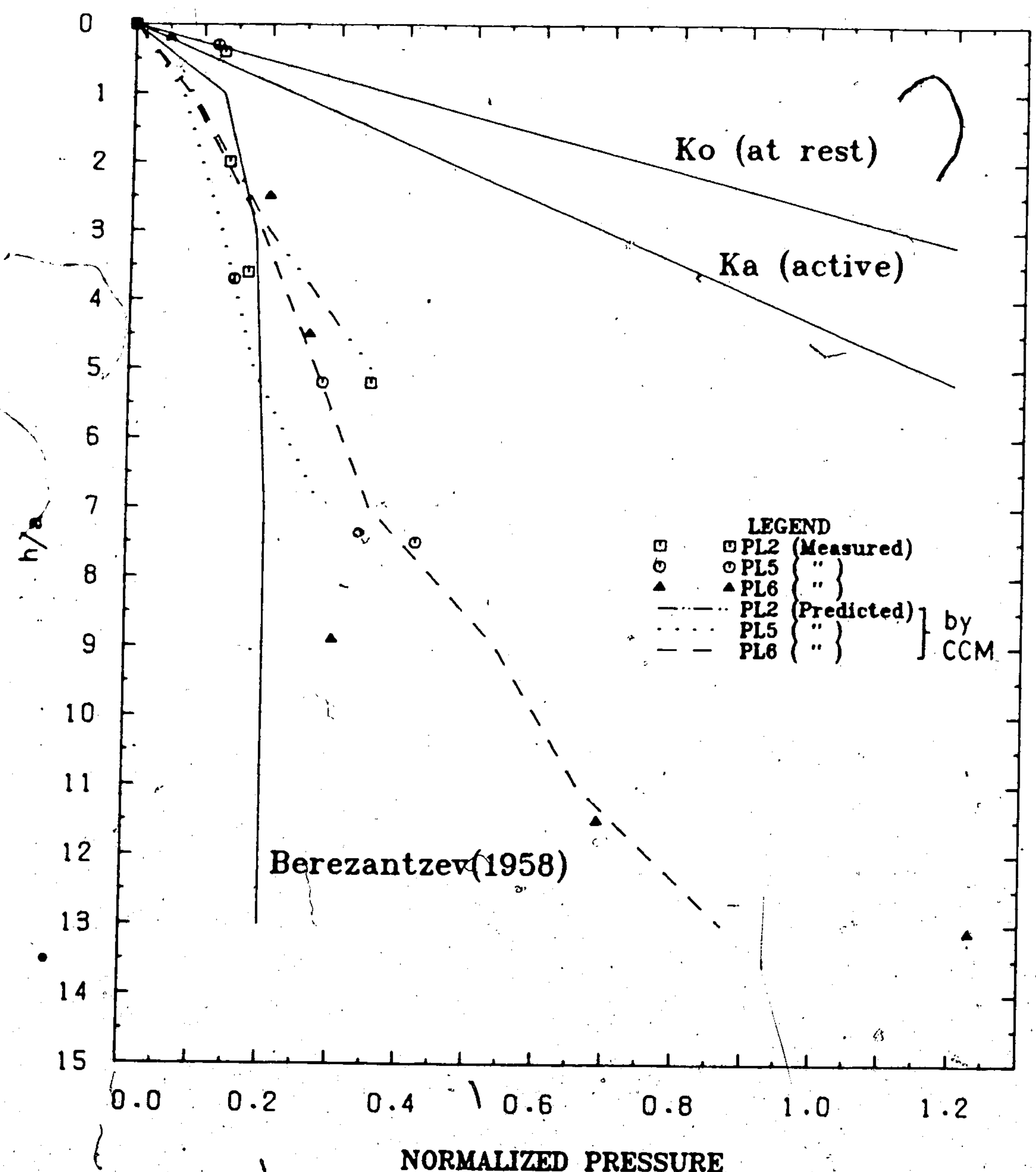

Figure 6.8 Comparison of Pressures with Depth

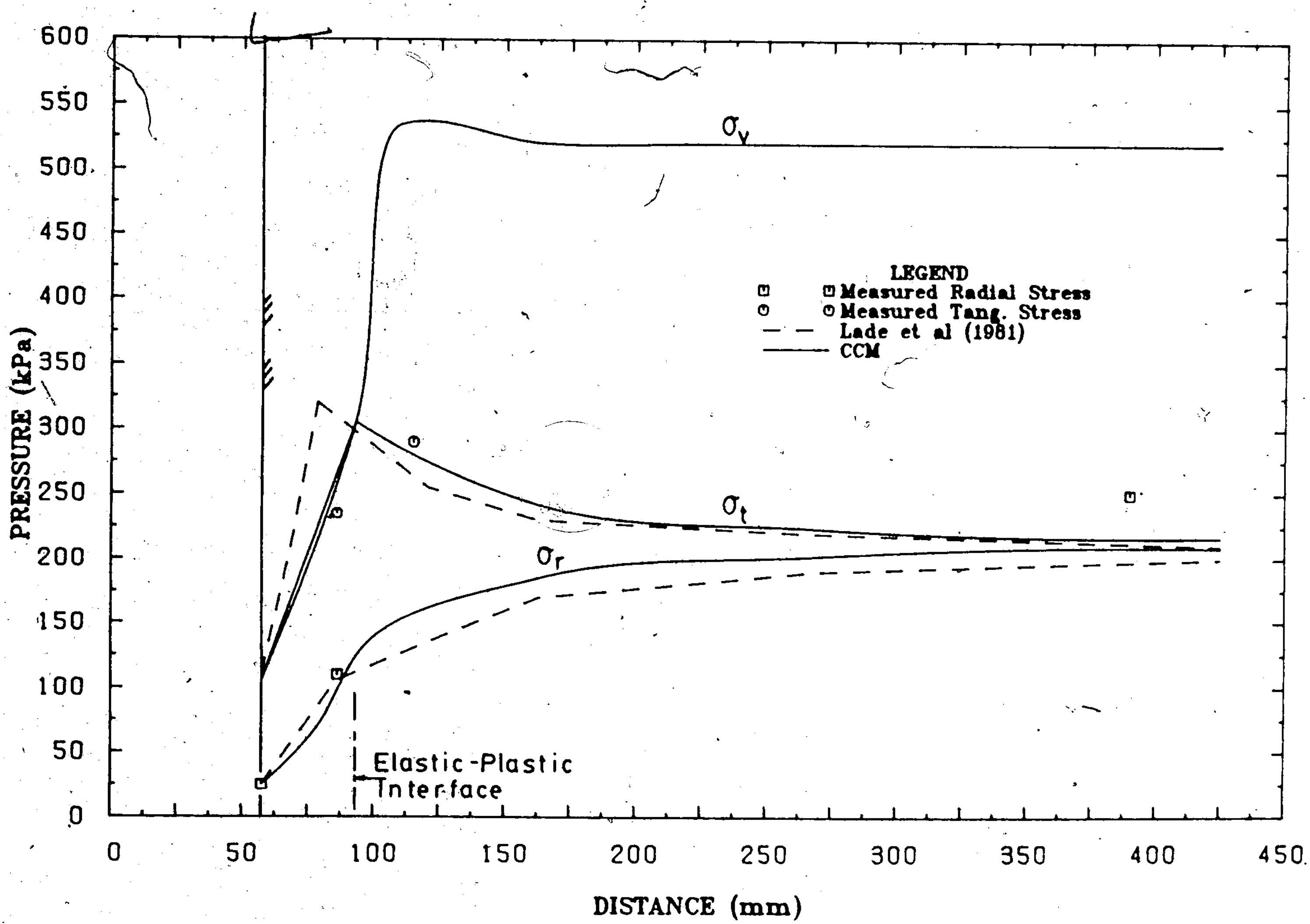

Figure 6.9 Comparison of Stress Distribution

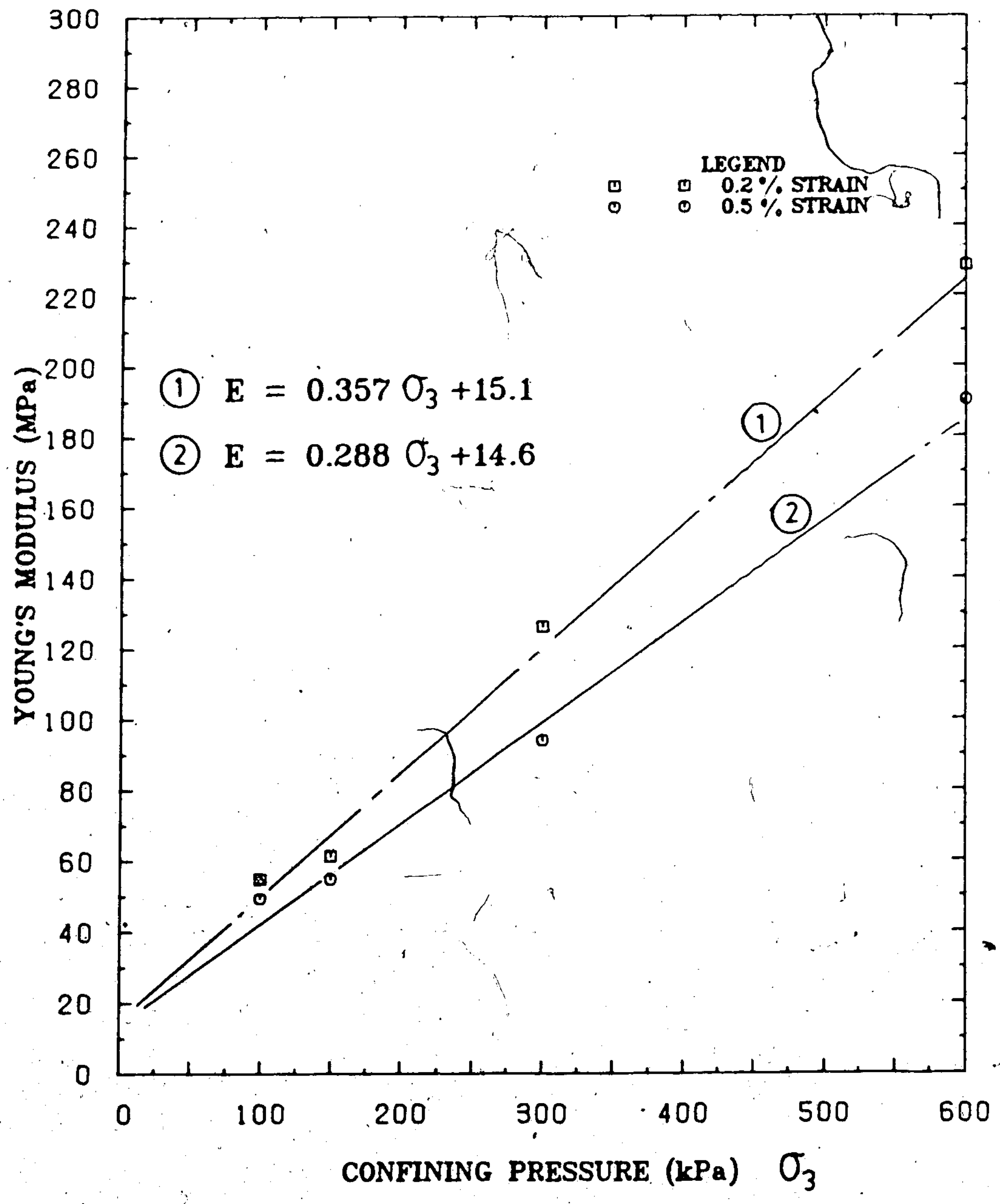

Figure 6.10 Young's Modulus versus Confining Pressure

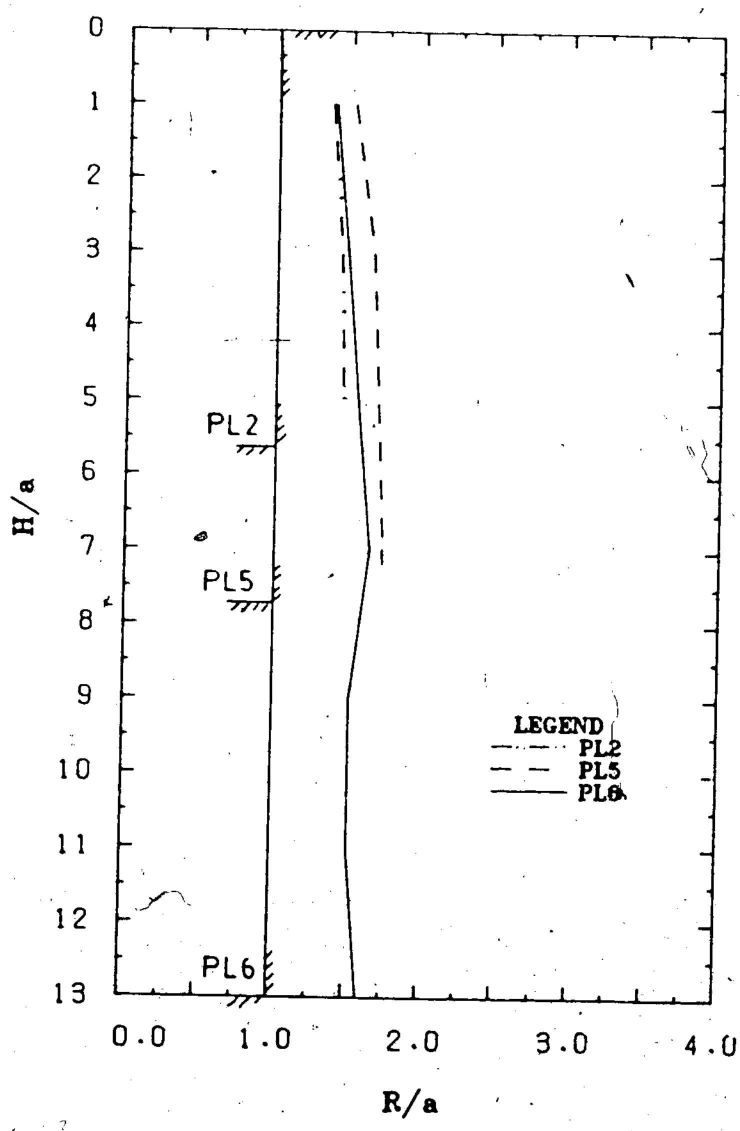

Figure 6.11 Predicted Plastic Zone

7 . SUMMARY AND CONCLUSIONS

7.1 Introduction

This thesis examines the behaviour of tunnels and shafts in soils including elastic response, yield and collapse states. These ground responses can be interpreted by the use of the ground convergence curve and analytical techniques are proposed to predict the ground behaviour. These techniques are evaluated by comparison of the predicted with the observed behaviour in model tests and field measurements or by comparison with results from numerical simulations.

The following sections of this chapter summarize the conclusions, practical implications and recommendations for further studies.

7.2 Conclusions on Tunnel

7.2.1 Tunnel Behaviour

The objectives of this study are (i) to investigate the mechanisms of ground behaviour near shallow and deep tunnels, (ii) to develop an approach to assess behavioral modes of both shallow and deep tunnels, and (iii) to verify this approach by comparison with results of behavioral mode, support pressure and ground displacement from finite element analyses, field measurements and model tests.

The tunnel is viewed as a two-dimensional plane strain "hole-in-plate" model and the excavation process can be simulated by progressively proportional unloading of the initial insitu stress at the tunnel periphery. All ground behavioral stages from elastic unloading to collapse due to stress relief are studied by use of continuum mechanics, finite element method and limit state theory. It was found that the mode of behaviour of tunnel and surrounding ground is dictated by the mode of initiation and propagation of yield zone. Four different modes (Modes I to IV) are identified and they are governed by the following parameters: (1) the depth ratio (H/a) relating the free surface boundary, overburden and geometry of the opening, (2) the external boundary stress (K_o), (3) the internal boundary stress (p_i, τ_i) and (4) the ground strength properties. Mode I with localized yield zone propagation from the shoulders of the tunnel to the free surface and Mode II with continuous yield zone propagation near the opening are only considered in detail in this thesis because they are commonly encountered in soft ground tunnelling at $K_o<1.0$.

For a given tunnel configuration a critical K_o value (K_{cr}) exists that separates Mode I from Mode II. Mode I will occur for $K_o < K_{cr}$ and Mode II for $K_o > K_{cr}$ (e.g., $K_{cr}=0.7$ for a tunnel with H/a=5, $\phi=30°$ and c=0). The magnitude of K_{cr} decreases with increasing H/a and ϕ. The existences of Modes I and II have been confirmed by the finite element analyses and model tests (Atkinson *et al.*, 1974; Atkinson and Potts, 1977; Cording *et al.*, 1976). The signifance of identifying these modes of yielding is two-fold. Firstly, it can verify the mode of yielding assumed in any available numerical models predicting the pressure-deformation around the opening. The mode of yielding in a proposed model must be consistent with that observed for satisfactory prediction. Secondly, a proper understanding of the mode of yielding provides excellent insight into the tunnel behaviour with aspects of displacement fields including surface settlement profile.

The ground responses of different stages in Modes I and II can be identified in sequence of progressive stress-relief as follows:

1. elastic unloading
2. yield initiation
3. yield zone propagation (yield zone may or may not intersect the free surface)
4. kinematic collapse at the roof
5. propagation of roof collapse to the free surface (with states of stress at the roof disturbed)

From Stage (1) to Stage (4) the support pressure (at roof) decreases at the expense of increased displacements. This support pressure reduces to an optimum value and then may increase beyond Stage (4). At Stage (5) a kinematic collapse mechanism occurs at the roof. The soil block above the tunnel will undergo a sudden collapse and the related settlement will in general be excessive and unacceptable in practice. Hence, one of the practical implications in locating Stage (4) by the use of the ground convergence curve is that the tunnel design engineer can estimate the marginal safety against the collapse state (Stage (4)) by comparing the displacement permitted during construction with the displacement initiating the occurrence of Stage

(4).

For Mode I the ground responses from Stages (1) to (3) can be determined by the use of the finite element method until severe problems are confronted during the numerical iteration process. The ground responses of Mode II may be approximated by the "hole-in-plate" model under isotropic stress field with the effect of the surface boundary (supported by studies on two case histories of field measurements) provided that all governing parameters satisfy conditions of Mode II. The responses in the remaining stages (i.e., 4 and 5) are determined using limit state theory. This method only provides the ultimate support pressures but the related displacements are currently unresolved. However, extrapolation of the ground convergence curve from Stage (2) or (3) to (4) or (5) can permit one to obtain an approximate support pressure-displacement relationship beyond Stages (4).

The surface settlement profile, defined by the maximum surface settlement (S_s) and the point of inflection (i) is a function of the support pressure (p_i) or crown displacement (S_c), depth ratio (H/a) and soil properties. In general, the distance from the centreline to the point of inflection decreases with increasing S_c at a faster rate for shallow tunnels than for deep tunnels. Modes I and II display several distinctly different and unique features in their settlement profiles because they represent different modes of yielding. If the crown settlement S_c is small, the extent of the yield zone is small. The vertical settlement profiles of Modes I and II are initially very similar, but the magnitude of settlement is larger in Mode I than in Mode II. Small displacement occurs at the elastic zone and large plastic straining within the yield zone. For excessive S_c (i.e., the yield zone reaches the surface), Modes I and II exhibit distinct differences in vertical settlement profile above the crown. In Mode I, two localized shear planes develop and the soil block displaces toward the opening as a rigid body. It remains elastic so that the differential displacement between the crown and the surface is small. Hence, the ratio of the surface to crown displacement (S_s/S_c) tends to be close to unity. In Mode II, a plastic zone surrounded by the elastic ground develops around the opening. The elastic displacement is relatively small and most of the straining will occur inside the plastic zone. Thus the settlement ratio S_s/S_c must be much less than unity. At an equal support stress, the surface settlement in Mode II (K_o=1.0) is much smaller than that in Mode I (K_o=0.5). This difference is attributed to the fact that tangential arching near the opening is higher for K_o=1.0 and the resistance against the downward movement of the soil block above the crown is larger. This results in smaller ground settlements.

7.2.2 Practical Implications

Based on all of the results presented herein, several observations of practical importance can be made:

1. From the ground convergence concept, the support pressure decreases with increased displacements. This

support pressure reduces to an optimum value (specified by displacement u_{ic}) and increases thereafter. Reduction of lining pressure can be ensured if the displacement permitted during construction (u_{con}) is smaller than u_{ic}. This displacement u_{ic} not only corresponds to the optimum support pressure, but also denotes the point of initiation of roof collapse and a state of change in arching action above the crown (from convex upward to inverted downward). This transition in arching signifies an abrupt increase in settlement above the roof. Hence, a comparison between u_{con} and u_{ic} provides information on the marginal safety against the development of the roof collapse. For good ground control u_{con} must be much less that u_{ic}.

2. The initial insitu stress (K_o) not only governs the mode of yielding but also influences the displacements of soil around the tunnel. There exists a critical K_o value (K_{cr}) to differentiate between Mode I ($K_o < K_{cr}$) and Mode II ($K_o > K_{cr}$) of yielding. The surface settlement in Mode II is much smaller than that in Mode I at an equal support pressure. In addition, Mode I has a narrower settlement trough than Mode II. It implies that the potential for damage due to surface settlement becomes more critical for Mode I than for Mode II. For normally consolidated soils where $K_o = 1 - \sin\phi$, the mode of yielding is generally Mode I. Tunnelling in low K_o is much more risky as intuitively expected.

3. Boundary stresses along the periphery of a tunnel opening exert great influence on the tunnel behaviour

in terms of yield zone development and displacement field. Studies demonstrate that the application of uniform pressure tends to inhibit the propagation of localized yield zones to the ground surface and reduces the surface settlement. This explains why tunnel construction methods such as air-pressurized tunnelling and earth pressure balance shields, provide better ground control. However, this also shows clearly that the approach of applying a constant fictitious support pressure at the tunnel circumference to simulate excavation process does not provide a reasonable solution of ground responses. Ground convergence curves predicted by constant pressure relief are inaccurate. The effects of K_o and H/a must be evaluated by a correct simulation procedure.

4. The German Tunnelling guidelines (Duddeck, 1980 and 1982) for 'shallow' (H/a<5) and 'deep' (H/a>7) tunnels are generally justified both in terms of ground pressure and structural models. These guidelines are reasonably conservative for normally consolidated soils provided that u_{con} is always less than u_{ic}.

5. Terzaghi (1943) derived a solution for the roof loading above a tunnel in cohesionless soil. It is shown that Terzaghi's case is only valid for one special case of tunnel behaviour (for a specific crown displacement the horizontal stress to vertical stress coefficient K of soil above the crown is equal to unity). The support pressure may not be on the safe side if u_{con} is greater than (or much less than)

u_{ic}.

7.3 Recommendations for Further Studies (Tunnel)

Although the tunnel behaviour has been quite extensively studied in this thesis, there are still many unresolved areas. For example, the boundary between Mode I-2 and Mode I-3 is not well defined. Also, the relationship between the surface and crown settlements was not quantitatively treated and further studies are required to arrive at the exact solution.

Finite element method has proven to be an effective tool in understanding the tunnel behaviour. Techniques in predicting the responses near collapse are definite assets to understand the tunnel behaviour at the limit. Improved techniques in soil behaviour modelling are also necessary for predicting the real and actual tunnel behaviour.

7.4 Conclusions on Shaft

7.4.1 Shaft Behaviour

The behaviour of a shaft is a three-dimensional problem in which three stress components (σ_v, σ_t and σ_r) must be considered. The excavation process simulated by relief in radial stress component causes both horizontal and vertical archings around the shaft.

Horizontal arching develops due to hoop stresses in a horizontal plane (an increase in tangental stress), and can be quantified in terms of stress-relief (or support pressure) and wall displacement by the use of the convergence confinement method. This support pressure-wall displacement relationship is dependent on the insitu stress and soil strength-deformation properties.

Vertical arching arises from the formation of a plastic zone of limited extent around the shaft with a tendency to move in vertical direction under the effect of gravity. The support pressure due to vertical arching (or gravity effect) can be determined using the theory of arching. The magnitude and distribution of this support pressure (due to the gravity effect) depends on the extent of the plastic zone, the soil and interface properties. The extent of the plastic zone is governed by the mode of yield initiation (which is dictated by K_o), the soil strength parameters and wall displacement permitted during construction. An envelope of support pressures resulting from horizontal and vertical archings yields the formation pressure around the shaft for a given wall displacement. In other words, the convergence confinement method with consideration of the gravity effect, which may be viewed as a technique of accounting for the three-dimensional conditions near a shaft, can be used as an analytical approach to predict the true support pressure and the wall displacement around the vertical opening.

From studies on mechanisms of shaft behaviour, it was confirmed that three modes of yield initiation (Modes A, B and C) are possible, and that they are primarily governed by K_o. Mode A (σ_t-σ_r) and Mode B (σ_v-σ_r) are commonly encountered in the field. A critical value K_{cr} may be used to differentiate between these two modes. The support pressure-wall displacement relationships have been derived for Modes A and B. They are completely different in terms of yield initiation, yield zone propagation, distribution and magnitude of support pressure, and wall displacement.

Variation of strength-deformation parameters (e.g., q_u, E) with depth also exerts a significant influence on the shape and extent of the plastic zone and, thus, on the distribution and magnitude of the support pressure. Furthermore, it was also confirmed that the shaft exhibits distinctly different behavioral modes in cohesionless and cohesive soils.

Numerical examples generated by the finite element method (FEM) were used to compare results obtained from the FEM and the newly introduced CCM. These examples included analyses of shaft behaviour of Modes A and B yielding, and responses in purely cohesionless and cohesive materials. Good agreement in terms of mode of yield initiation, extent of yield zone, stress distribution and support stress-wall displacement relationship was found for the two techniques. This suggests that the proposed confinement convergence method provides a valid analytical approach to predict the behaviour of shafts.

The results of three case histories (including one field study and two model tests) have been described and analyzed. The field measurement (Terwillegar Shaft, Edmonton) and the Berlin model tests (Muller-Kirchenbauer *et al.*, 1980) provided cases histories for Mode A yielding whereas the Cambridge Centrifugal model tests (Lade *et al.*, 1981) simulated Mode B of yielding. It was shown that the mode of yielding dominates the behaviour of shaft with respect to the extent of the yield zone, wall displacement and formation pressure around the shaft. The CCM, which includes important governing factors such as mode of yield initiation, insitu stress state, strength-deformation properties of soils and wall displacement permitted during construction (i.e., effect of construction method), provides a much improved framework of interpretation for the three case histories than conventional techniques.

7.4.2 Practical Implications

Based on the studies of shaft behaviour presented herein, the following implications of practical importance can be summarized:

1. With the formation pressure-wall displacement relationship calculated from the CCM, it is possible not only to rationally assess the required support pressure for a given shaft, but also to evaluate the limit of applicability of the conventional limit equilibrium methods for shaft design. The studies of three case histories showed that the support pressures determined from the limit equilibrium methods proposed by Terzaghi (1943), Berezantzev (1958), and Prater (1977) are much lower than those actually observed in the field or model tests. These conventional methods do not distinguish properly among the various yield mechanisms, and neglect the significance of the shape of the yield zone. They are based on limit equilibrium analyses of one specific assumed failure mode. No strength-deformation relationships are included in

their formulation and full strength mobilization is assumed. Hence, these methods only provide lower limits of support pressure or the pressure required to prevent collapse. These limits are only reached after large ground movements have occurred either due to poor ground control during construction or in cases where large movements have accumulated for other reasons.

2. It was shown that the mode of initiation and propagation of yield zone governs the ground response near an opening. Hence, for the prediction of shaft behaviour it is essential to verify the mode of yielding assumed in a numerical model and to ensure that it is consistent with the actual mode observed in the field or model test. The convergence confinement method is the only effective technique to evaluate field observations. Well positioned radial extensometers should be employed to determine the extent of yield zone. Unfortunately, in most field monitoring projects and model tests displacements or stresses are only measured at few locations. Kaiser *et al.* (1985) demonstrated that data interpretation based on one-directional convergence measurements may lead to misinterpretation because many displacement fields and internal stress redistribution mechanisms could cause the same wall movements. Case histories such as Terwillegar shaft and Berlin model test (modified from Muller-Kirchenbauer et al., 1980) have the same limitations. Cambridge model tests (Lade et al., 1981) provides better data on stress distribution but still

insufficient data on displacement field near the shaft opening.

7.5 Recommendations for Further Studies (Shaft)

The convergence confinement method has been shown to be a practical analytical method to predict actually expected support pressures and wall displacements. The results determined from the CCM compare well with field measurements in the experimental shaft study and the results obtained from finite element analyses. However, one limitation of the CCM is the assumption of the two-dimensional plane strain condition. This condition prevails at depth, but not near the ground surface where vertical displacements dominate. Hence, some studies on how the two-dimensional plane strain condition affects the results should be encouraged. Further studies should concentrate on effects of boundary conditions, water table and construction sequence on the shape of the convergence curves.

The ground control involved in the case histories studied were relatively good, and little yielding did occur. In future projects, it might be valuable to allow large ground deformations to observe the collapse mode of a poorly supported or unsupported shaft.

References

Atkinson, J.H. and Cairncross, A.M. 1973. Collapse of a Shallow Tunnel in a Mohr-Coulomb Material. Proceedings of the Symp. on the role of Plasticity in Soil Mechanics, Cambridge, pp.202-206.

Atkinson, J.H., Cairncross, A.M. and James, R.G. 1974. Model Tests on Shallow Tunnel in Sand and Clay. Tunnels and Tunnelling, July, pp.28-32.

Atkinson, J.H., Brown, E.T. and Potts, D.M. 1975. Collapse of Shallow Unlined Circular Tunnels in Dense Sand. Tunnels and Tunnelling, January, pp.81-87.

Atkinson, J.H. and Potts, D.M. 1977. Subsidence above Shallow Tunnels in Soft Ground. Journal of Geotechnical Engineering, GT4, pp.307-325.

Atkinson, J.H., Brown, E.T. and Potts, D.M. 1977. Ground Movement near Shallow Model Tunnels in Sand. In Proceedings Conference of Large Ground Movement and Structures. Cardiff, United Kingdom, pp.372-387.

Attewell, P.B. 1977. Ground Movements caused by Tunnelling in Soil. In Proceedings Conference of Large Ground Movement and Structures. Cardiff, United Kingdom, pp.812-948.

Berezantzev, V.G. 1958. Earth Pressure on the cylindrical retaining walls. Brussels Conference 58 on Earth Pressure Problems, Vol.II, pp.21-24.

Bishop, A.W. and Wesley, L.D. 1975. A Hydraulic Triaxial Apparatus for controlled stress path testing. Geotechnique, Vol.25, No.4, pp.657-670.

Booker, J.R. and Davis, E.H. 1977. Stability Analysis by Plasticity Theory. Numerical Methods in Geotechnical Engineering edited by Desai, C.S. and Christian, J.T. 748pp.

Branco, P. 1981. The Behavior of Shallow Tunnels in Edmonton Till. M.Sc. Thesis. Dept. of Civil Engineering, University of Alberta, Edmonton, Alberta, 331pp.

Britto, A.M. and Kusakabe, O. 1982. Stability of Axisymmetric Excavations. Geotechnique, 32, No.3, pp.261-270.

Britto, A.M. and Kusakabe, O. 1983. Stability of

Axisymmetric Excavations in Clays. Journal of Geotechnical Engineering, ASCE, Vol.109, No.5, pp.666-681.

Britto, A.M. and Kusakabe, O. 1984. On the Stability of supported Excavations. Can. Geotech. Journal, 21, pp.338-348.

Brooker, E.W. and Ireland, H.O. 1965. Earth Pressure at Rest Related to Stress History. Canadian Geotechnical Journal, Vol.2, No.1, pp.1-15.

Brown, E.T., Bray, J.W., Ladanyi, B. and Hoek, E. 1983. Ground-Response Curves for Rock Tunnels. Journal of Geotechnical Engineering, 109(1), pp.12-23.

Chan, D. 1985. Finite Element Analysis of Strain-softening Materials. Ph.D. Thesis. Dept. of Civil Enginnering, University of Alberta, Edmonton, Alberta. 355pp.

Corbett, I. 1984. Load and Displacement Variation along a Tunnel. M.Sc. Thesis. Dept. of Civil Engineering, University of Alberta, Edmonton, Alberta, 246pp.

Cording, E.J., Hansmire, W.H., MacPherson, H.H. Lenzini, P.H., and Vonderohe, A.P. 1976. Displacement around Tunnels in Soils. Report prepared for Dept. of Transportation, Washington, Civil Engineering Department, University of Illinois.

Curtis, D.J. 1976. The circular tunnel in an elastic ground. Discussion. Geotechnique, Vol.26, pp.231-237.

Daemen, J.J. 1975. Tunnel Support Loading by Rock Failure. Ph. D. Thesis. Dept. of Civil and Mineral Engineering, University of Minnesota, Minnesota.

Davis, E.H., Gunn, M.J., Mair, R.J. and Seneviratne, H.N. 1980. The Stability of Shallow Tunnels and Underground Openings in Cohesive Material. Geotechnique 30, No.4, pp.397-416.

De Borst, R. and Vermeer. 1984. Possibility and Limitations of Finite Element for Limit Analysis. Geotechnique 34, No.2, pp.199-210.

Detournay, E. 1983. Two-Dimensional Elastic-plastic Analysis of a Deep Cylindrical Tunnel Under Non-hydrostatic Loading. Ph. D. Thesis. Dept. of Civil and Mineral Engineering, University of Minnesota, Minnesota, 133pp.

Duddeck, H. 1980. On the basic requirements for applying the Convergence Cofinement Method. Underground Space, Vol.4, No.4, pp.241-247.

Duddeck, H. and Erdmann, J. 1982. Structural Design Models for Tunnel. Tunnelling'82, pp.83-91.

Duddeck, H. 1980 and 1982. Empfehlungen zur Berechnung von Tunneln im Lockergestein (1980) Deutsche Gesellschaft fur Erd- und Grundbau. Bautechnik, 349-56; also in Taschenbuch fur den Tunnelbau 1982, 115-44.

Duncan, J. and Chang, C.Y. 1970. Non-linear Analysis of stress and strain in soils. ASCE, Vol.96, SM5, pp.1629-1643.

Egger, P. 1975. Erfahrungen beim Bau eines seichtliegenden Tunnels in tertiaren Mergeln. Rock Mechanics (Springer, Vienna), Suppl. 4, pp.41-54.

Einstein, H.H. and Schwartz, C.W. 1979. Simplified Analysis for Tunnel Supports. Journal of Geotechnical Engineering, GT4, pp.499-517.

Eisenstein, Z. 1982. The contribution of numerical analysis to design of shallow tunnels. Proceedings to International Symposium on Numerical Models in Geomechanics, Zurich.

Eisenstein, Z. Heinz, H. and Negro, A. 1984. On Three-Dimensional Ground Response to Tunnelling. Proc. of ASCE-Geotech. '84, Atlanta, pp.107-127.

Eisenstein, Z. and Negro, A. 1985. Comprehensive Design Method for Shallow Tunnels. ITA/AITES, International Conf. Underground Structures in Urban Area, Prague, Czechoslavakia.

Eisenstein, Z. and Thomson, S. 1978. Geotechnical Performance of a tunnel in till. Can. Geot. Journal, Vol.15, pp.332-345.

El-Nahhas, F. 1980. The behavior of tunnels in stiff soils. Ph. D. Thesis, Dept. of Civil Engineering, University of Alberta, Edmonton, Alberta, 305pp.

Fenner, R. 1939. Untersuchungen zur Erkenntnis des Gebirgsdruckes. Gluckauf, Ann. 74:32,33.

Griffiths, D.V. and Koutsabeloulis, N. 1985. Discussion on 'Possibility and Limitations of Finite Element for Limit Analysis', Geotechnique, 35, No.1, pp.90-94.

Handy, R.L. 1985. The Arch in Soil Arching. Journal of Geotechnical Engineering, ASCE, Vol.111, No.3, pp.302-319.

Hansen, B. 1958. Line Rupture regarded as Narrow Rupture Zones: basic equations based on kinematic consideration. Pro. Conf. Earth Pressure Problems, Brussels, 1, pp.39-48.

Heinz, H. 1985. Applications of the New Austrian Tunnelling Method in Urban Areas. M. Sc. Thesis. Dept. of Civil Engineering, University of Alberta, Edmonton, 320pp.

Hill, R. 1962. Acceleration Waves in Solids. J. Mech. Phys. Solids, 10, pp.1-16.

Hill, R. and Hutchinson, T.W. 1975. Bifurcation Phenomenon in Plane Tension. J. Mech. Phys. Solid, 22, pp61-71.

Hoek, E. and Brown, E.T. 1980. Underground Excavation in Rock. Institution of Mining and Metallurgy, London, U.K., 527pp.

Kaiser, P.K. and Hutchinson, D.E. 1982. Effects of Construction Procedures on Tunnel Performance. 4th International Conference on Numerical Methods in Geomechanics, 2, pp.516-569.

Kaiser, P.K., Guenot, A. and Morgenstern, N.R. 1985. Deformation of Small Tunnel-IV Behaviour during Failure. Int. J. Rock. Mech. Mining Science and Geomechanics.

Kaiser, P.K., Mackay, C. and Morgenstern, N.R. 1982. Performance of a shaft in weak rock (Bearpaw Shale). ISRM Symposium on Caverns and Pressure Shafts, Aachen, Vol.2, pp.613-622.

Kaiser, P. K. and Wong, R.C.K. 1984. Interpretation of Measurement on Tunnel in Clay Shale and Shaft in Edmonton Till. Report submitted to Department of Water and Sanitation, City of Edmonton, and the AOSTRA, 277pp.

Kendal, N.O. 1980. The Practical Design of Silo and Bunkers with reference to the Codes of Practice. International Conference on design of Silos for strength and flow.

Klein, J. and Gerthold, A. 1979. Die Fließbedingungen von Drucker/Prager im Vergleich zu anderen Bruchkriterien bei der Bemessung von Gefrierschachten, Die Bautechnik 11, S. 368-375.

Kovari, K., Amstad, C.H., Koppel, J. 1979. New Developments in the Instrumentation of Underground Openings. Proc. 4th Rapid Excavation and Tunnelling Conference, Atlanta, Ga., USA.

Korpach, D.R. 1983. Stresses near the Tunnel Face. M. Sc Thesis. Dept. of Civil Engineering, University of Alberta, Edmonton, Alberta. 248pp.

Kusakabe, O. and Schofield, A. N. 1982. Rectangular Open Pit Excavations modelled in the Geotechnical Centrifuge. Paper presented at the 61st Annual Meeting of the U.S. Transportation Research Board in Washington, D.C.

Ladanyi, B. 1974. Use of the Long-Term Strength Concept in the Determination of Ground Pressure on Tunnel Linings. Advances in Rock Mechanics, Proceedings of the Third Congress of the International Society for Rock Mechanics, Vol.2, Part.B, National Academy of Science, Washington, D.C., pp.1150-1156.

Ladanyi, B. 1980. Direct Determination of Ground Pressures on Tunnel Lining in non-linear viscoelastic Rock. 13th Canadian Rock Mechanics Symposium Cim Special Volume 22, Canadian Institute of Mining and Metallury, pp.126-132.

Lade, P.V., Jessberger, H.L., Makowski, E. and Jorden, P. 1981. Modelling of Deep Shaft in Centrifuge Tests. Proceeding 10th International Conference on Soil Mechanics and Foundation Engineering, Vol.1, pp.683-642.

Lo, K.Y., Ng, M.C. and Rowe, R.K. 1984. Predicting Settlement due to Tunnelling in Clay. Tunnelling '84, pp.46-75.

Lombardi, G. 1973. Dimensioning of Tunnel Linings with regards to Construction Procedure. Tunnels and Tunnelling, Vol.5, pp.340-351.

Matheson, D.S. 1970. A Tunnel Roof Failure in Till. Can. Geot. Journal, Vol.7, pp.313-317.

May, R.W. and Thomson, S. 1978. The Geology and Geotechnical Properties of till and related deposits in Edmonton, ALberta. Can. Geot. Journal, Vol.15, pp.362-370.

Mayne, P.W. and Kulhawy, F.H. 1982. Ko-OCR Relationships in Soil. Journal of Geotechnical Engineering, ASCE, Vol.108, No.6, pp.851-872.

McCreath, D.R. 1980. Analysis of Formation Pressure on Tunnel and Shaft Linings. M.Eng. Report, Civil Engineering Dept., University of Alberta, Edmonton, Alberta, 73pp.

Medeiros, L. 1979. Deep Excavations in stiff soils. Ph.D. Thesis, Dept. of Civil Engineering, University of

Alberta, Edmonton, Alberta, 310pp.

Molenkamp, F. 1985. Comparisons of Frictional Material Models with respect to Shear Band Initiation. Geotechnique, 35, No.2, pp.127-195.

Muir-Wood, A.M. 1975. The Circular Tunnel in Elastic Ground. Geotechnique, 25, No.1, pp.115-127.

Muller-Kirchenbauer, H., Walz, and Klapperich, H. 1980. Experimentelle und Theoretische Untersuchungen Zum Erddruckproblem auf Radial Symmetrische Senkkaasten und Schachte, Berlin, 113pp.

Needleman, A. 1979. Non-normality and Bifurcation in Plane Strain Tension and Compression. J. Mech. Phys. Solids. 27, pp.231-254.

Oda, E. and Yamagami, T. 1979. On the Distribution of Stress around a Circular Tunnel under Internal Pressure in Gravitating Plastic Ground with Frictional Resistance. Numerical Methods in Geomechanics, Vol.2, pp.847-859.

O'Reilly, M.P. and New, B. 1982. Settlements above Tunnels in the U.K.-their Magnitude and Prediction. Tunnelling '82, pp.173-181.

Pacher, F. 1964. Measurements of deformations in a test gallery as a means of investigating the behaviour of the rock mass and specifying lining requirements. Rock Mechanics and Engineering Geology, Supplement I, pp.149-161.

Palmer, A.C. and Rice, J.R. 1973. The Growth of Slip Surfaces in the Progressive Failure of Over-consolidated Clay. Proc. Royal. Doc. London, A332, pp.527-548.

Panet, M. and Guenot, A. 1982. Analysis of Convergence behind the face of a tunnel. Tunnelling 1982, the Institution of Mining and Metallurgy, pp.197-204.

Peck, R.B. 1969. Deep Excavations and Tunnelling in Soft Ground. Proc. 7th International Conference on Soil Mechanics and Foundation Engineering, State of the Art Volume, Mexico City, Mexico, pp.225-290.

Peck, R.B., Hendron, A.J. and Mohraz, B. 1972. State of the art of soft ground tunneling. Proc. 1st Rapid Excavation Tunnel Conference, Chicago, Vol. 1., pp.259-286.

Pender, M.J. 1980. Simplified Analysis for Tunnel. Discussions. ASCE, GT7, p.833-835.

Potts, D.M. 1976. Behaviours of Lined and Unlined Tunnels in Sands. Ph. D. Thesis. Cambridge University, England.

Prater, E.G. 1977. An examination of some theories of earth pressure on shaft linings. Can. Geot. Journal, Vol.14, No.1, pp.91-107.

Rabcewicz, L.V. and Golser, J. 1973. Principles of Dimensioning the Supporting System for the New Austrian Tunnelling Method. Water Power (March):88.

Reyes, S.F. and Deere, D.U. 1966. Elastic-plastic Analysis of Underground openings by the Finite Element Method. Proc. 1st International Conference on Rock Mechanics, Lisbon, Vol.2, pp.477-483.

Rudnicki, J.W. and Rice, J.R. 1975. Conditions for the Localization of the Deformation in Pressure-Sensitive Dilatant Materials. J. M .Phys. Soilds, 23, pp.371-374.

Schofield, A.N. 1977. Centrifugal Model Tests on Shallow Tunnels in Dense Sand. Tunnel and Tunnelling, January, pp.59-62.

Schofield, A.N. 1980. Cambridge Geotechnical Centrifuge Operations. Geotechnique, Vol.30, No.3, pp.227-268.

Schmidt, H. 1926. Statishe probleme des Tunnel and Druckstollenbauses und ihre gegenseitgei Beziehungen. Verlag Von Julius Springer, Berlin 16/26

Smith, I.M. 1973. Numerical Analysis of Plasticity in Soils. Proceedings of the Symp. on the role of Plasticity in Soil Mechanics, Cambridge, pp.279-289.

Sokolovsky, V.V. 1954. Statics of Earthy Medium.

Terzaghi, K. 1936. Distribution of the Lateral Pressure of Sand on the Timbering of Cuts. Journal of the Boston Society of Civil Engineering, Vol.23, pp.211-215.

Terzaghi, K. 1943. Theoretical Soil Mechanics. John Wiley and Sons. 502pp.

Thomson, S. and El-Nahhas, F. 1980. Field Measurements in two tunnels in Edmonton. Can. Geot. Journal, Vol.17, No.1, pp.20-33.

Vardoulakis, I., Goldscheider, M. and Gedehus, G. 1978. Formation of Shear Bands in Sand Bodies as a Bifurcation Problem. Int. J. Numerical Analysis Methods in Geomechanics, 2, pp.99-128.

Vardoulakis, I. 1979. Bifurcation Analysis of the Triaxial Test an Sand samples. ACTA Mechanica, 32, pp.35-54.

Vardoulakis, I. 1981. Bifurcation Analysis of the Plane Rectilinear Deformation on Dry Sand Samples. Int. J. of Solids and Structures, 17, pp.1085-1101.

Vardoulakis, I. 1985. Stability and Bifurcation in Soil Mechanics. Proceedings of Symposium on Constitutive Relations for Soils.(in press)

Young, N.J.B. 1976. Bifurcation Phenomena in the Plane Compression Tests. J. Mech. Phys. Solids, 24, pp77-91.

APPENDIX A

Notations

Symbols

The following symbols are used in this thesis:

a = radius of tunnel or shaft

H = depth of tunnel or shaft

h = depth measured from ground surface

y = elevation measured from bottom of shaft

A = area of cross section

R = radius of plastic zone

R_{tr} = radius of plastic zone induced by tangential-radial stress difference (Mode A)

R_{vr} = radius of plastic zone induced by vertical-radial stress difference (Mode B)

r = radial distance

dh = differential soil element thickness

u_i = radial displacement (convergence) at wall (r=a)

u_{con} = radial displacement allowed during construction

u_{ic} = radial displacement at support pressure p_{ic}

u_{ys} = radial displacement at support pressure p_{ys}

u_{fc} = radial displacement at support pressure p_{fc}

σ_r = radial stress

σ_v = vertical stress

σ_t = tangential stress

σ_1, σ_3 = major and minor principal stress

σ_x = normal stress in x-direction

σ_y = normal stress in y-direction

τ_i = shear stress along the periphery of the opening

τ_{xy} = shear stress in xy-plane

σ_h = horizontal stress

p_i = internal support pressure (radial stress) at wall

p_o = vertical initial insitu stress

p_g = stress due to gravity effect

p_{ic} = support stress for initiation of roof collape

p_{ys} = support stress for yield zones propagating to the surface

p_{fc} = support stress at the final limit equilibrium state

p_{ro} = support stress at the time of installation

$d\sigma_v$ = differential (incremental) vertical stress

γ = soil unit weight

I_D = density index (relative density) of sand

ν = Poisson's ratio

E = Young's modulus

e_{av} = average plastic dilation

A_v = parameter calculating plastic deformation

ϕ = angle of internal friction of soil

N = $\tan^2(45° + \phi/2)$

q_u = unconfined compression strength of cohesive soil

c_u = shear strength of cohesive soil

μ_w = wall friction coefficient

μ_s = soil friction coefficient

K = ratio of horizontal to vertical stress

K_s = K at soil-soil boundary

K_w = K at soil-wall boundary

K_o = K at rest

K_a = K at active state (= $\tan^2(45°-\phi/2)$)

K_{cr} = critical K-value to distinguish Mode I (or A) from Mode II (or B) yielding

K_r = coefficient of tangential arching above the roof of the tunnel

S_o = a surface settlement constant

S_s = maximum surface settlement

S_c = vertical displacement at the crown

i = point of inflection at the surface settlement trough

APPENDIX B

Tunnel Analyses

B.1 Schmidt's Equations of Stress Distribution around a Tunnel

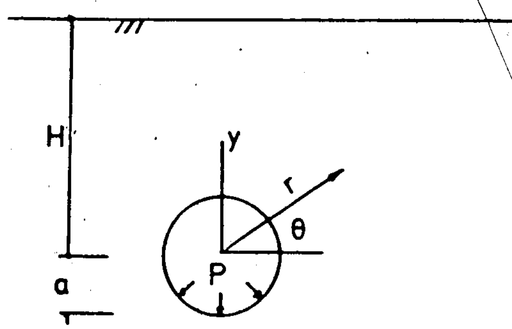

Radial Stress:

$$\sigma_r = -pq - AH(1-q) + (1-q)(A+B/2-(m\gamma + B/2)q)r\sin\theta + BH(1-q)(1-3q)\cos 2\theta - B/2(1-q)(1+q-4q^2)r\sin 3\theta \qquad B.1$$

Tangential Stress:

$$\sigma_t = pq - AH(1+q) + (A-B/2-m\gamma q-(m\gamma+B/2)q^2)r\sin\theta - BH(1+3q^2)\cos 2\theta + B/2(1-q^2+4q^3)r\sin 3\theta \qquad B.2$$

where: $q = (a/r)^2$

$A = (1+1/(u-1))\gamma/2$

$B = (1-1/(u-1))\gamma/2$

$u = 1/\nu$, ν is Poison's ratio

$u_1 = (u+1)(u-1)/u$

$u_2 = (u+1)(u-2)/u$

$m = -u_2/4u_1$

(the negative normal stress is compressive)

Computer programs (TUN1 and TUN2, Appendix F) are written for the above calculations.

B.2 Formulation of Mode II

For the bifurcation Mode II, i.e., continuous domain (Fig. B.1a), the stresses within the plastic zone must satisfy the equilibrium equations (it is assumed that the unit weight of soil γ and the direction of gravity is in direction at an angle θ to x-axis):

$$d\sigma_x/dx + d\tau_{xy}/dy = \gamma\cos\theta \qquad \text{B.3}$$

$$d\tau_{xy}/dx + d\sigma_y/dy = -\gamma\sin\theta \qquad \text{B.4}$$

and the Mohr-Coulomb failure criterion (for cohesionless soil)

$$(\sigma_x-\sigma_y)^2+4\tau_{xy} = (\sigma_x+\sigma_y)\sin^2\phi \qquad \text{B.5}$$

Substitution of the failure criterion (Eqn. B.5) into the equilibrium equations yields a pair of quasilinear hyperbolic equations (Booker and Davis ,1977). Associated with a set of hyperbolic equations are two families of lines known as α- and β- characteristics. The equations of these characteristics (Fig. B.1b) are:

$$\alpha \text{ lines: } dy/dx=\tan(\theta-\mu) \qquad \text{B.6}$$

$$\beta \text{ lines: } dy/dx=\tan(\theta+\mu) \qquad \text{B.7}$$

where: $\mu = \pi/4 - \phi/2$ (Fig.B.2)

Integration of stress equations along the α- and β-lines with known boundary stress at the periphery of the tunnel can yield the stress distribution within the plastic zone. Booker and Davis (1977) described methods of numerical integration for these hyperbolic stress equations for three classes of problem. The tunnel problem (Fig. B.1a) belongs to the initial value , or Cauchy problem. The boundary stresses along the periphery of the tunnel opening are known, i.e., P_{11}, P_{22}, and etc. The values at successive points, e.g., P_{12} are initially estimated from those at P_{11} and P_{22} and solved iteratively by expressing the derivatives in hyperbolic and characteristic equations in the finite differences. The solution is assumed to converge when the sum of the absolute difference among the values in each iteration does not exceed a specified tolerance. Non-convergence may be encountered, implying that the hyperbolic and characteristic equations are not satisfied at that point. Similar procedures can be applied to find values at Points P_{13}, P_{23} and etc. A computer program (TUN3, Appendix F) entailing all numerical integration processes described above is given herewith (Appendix F).

Within the plastic zone R (Fig. B.1a) where the hyperbolic and characteristic equations are satisfied, the solution will converge. Outside the plastic zone divergenece exists. Thus, using this criterion one can determine under what parameters (H/a, ϕ, p_i and K_o) Mode II becomes dominant in a tunnel. Limitations of using the convergence criterion to locate Line i-1 are recognized. The postulate that Mode II develops into Mode II-1 is made based on observed results of model tests, and needs further confirmation. Also, Line i-1 separating Mode II from Mode II-1 is obtained from trial cases. The exact solution of this boundary which must satisfy all necessary conditions such as equilibrium, stress continuity across elastic-plastic interface, and boundary conditions (e.g., Detournay; 1983) is not available in this stage.

B.3 Calculation of Coefficient K_r

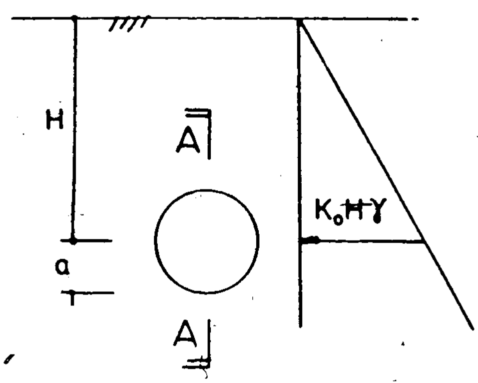

Along A-A, the resultant of horizontal forces are:

initially: $K_o\gamma H(2a)$

at η% support pressure: $\eta\gamma H(2a)$

Assuming even stress redistribution at the roof and floor, the total horizontal force at the roof is given by:

$$1/2K_o\gamma(H-a)^2 + (1-\eta)\gamma Ha$$

which can be expressed in terms of

$$1/2(K_o+\Delta K_r)\gamma(H-a)^2$$

Therefore

$$\Delta K_r = [2K_o(H/a)(1-\eta)]/(H/a-1)^2 \quad \text{B.8a}$$

$$K_r = K_o + \Delta K_r \quad \text{B.8b}$$

For results see Fig. B.2.

B.4 Calculation of Tunnel Support Pressure p_{fc}

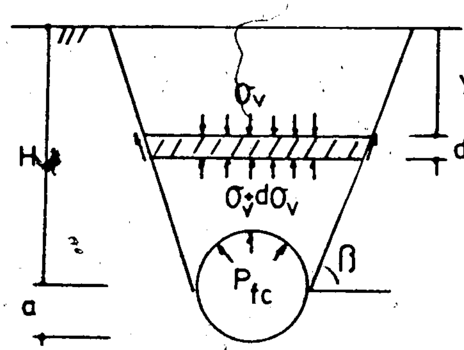

Summation of vertical forces for the slice yields

$$-d\sigma_v = (1/A_r)[\gamma dy(A_r) - F_s] \qquad B.9$$

where: $A_r = 2a + 2(H-y)/\tan\beta$

$F_s = K_s \sigma_v \tan\phi (dy)$

Integration of Eqn. B.9 yields the vertical stress distributions above the roof, i.e., p_{fc}. A computer program (TUN4, Appendix F) is written for this purpose.

B.5 Analysis of 2-D Plane Strain Hole-in-Plate Problem (Ladanyi, 1974)

Material Characteristics (Linear Coulomb):

Peak (Elastic):

$s_p = c_p/\tan(\phi_p)$

$N_p = \tan^2(45°+\phi_p/2)$

$M_c = (1+(N_p-1)K_o p_o/\sigma_c)/(N_p+1)$

Residual (Plastic):

$s_r = c_r/\tan(\phi_r)$

$N_r = \tan^2(45°+\phi_r/2)$

Extent of Plastic Zone:

$$R = a[(K_o p_o + s_r - M_c \sigma_c)/(p_i + s_r)]^{1/N_p - 1} \qquad \text{B.10}$$

Radial Displacement at Wall:

$$u_i = a\{1-[(1-e_{av})/(1+A_v)]^{1/2}\} \qquad \text{B.11}$$

where: $A_v = (2(u_e/R) - e_{av})(R/a)^2$

$e_{av} = [2(u_e/R)(R/a)^2]/[((R/a)^2-1)(1-1/B)]$

$B = 2D[\ln(R/a)]$ if $R/a < 1.732$

$1.1D$ if $R/a > 1.732$

$D = -\sin\phi_p$

Convergence Curves:

Combining Eqns. B.10 and B.11, p_i can be expressed in terms of u_i. A computer program (SFT1, Appendix F) is written to calculate this relationship.

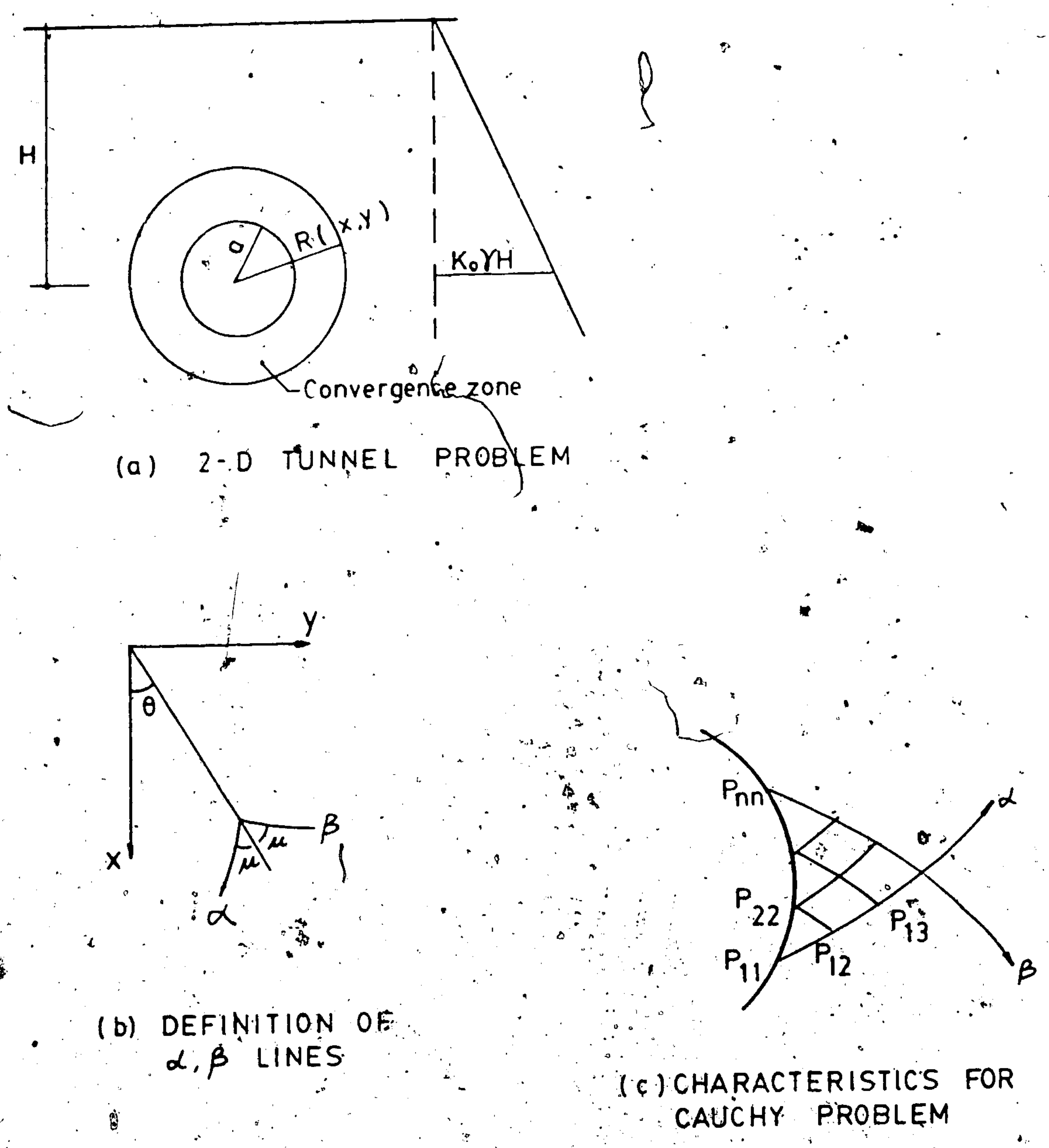

Figure B.1 Cauchy Problem

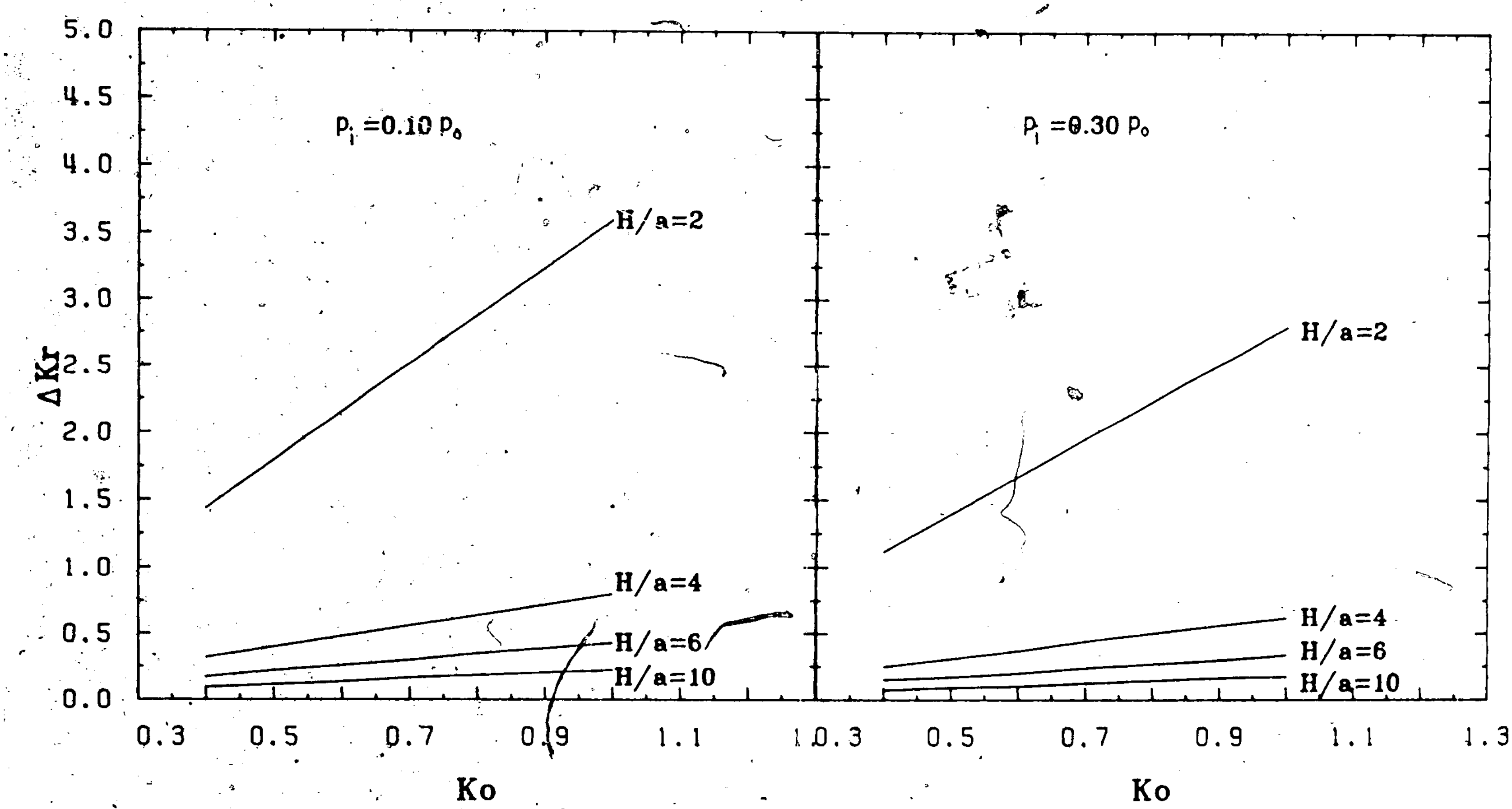

Figure B.2 K_r-values

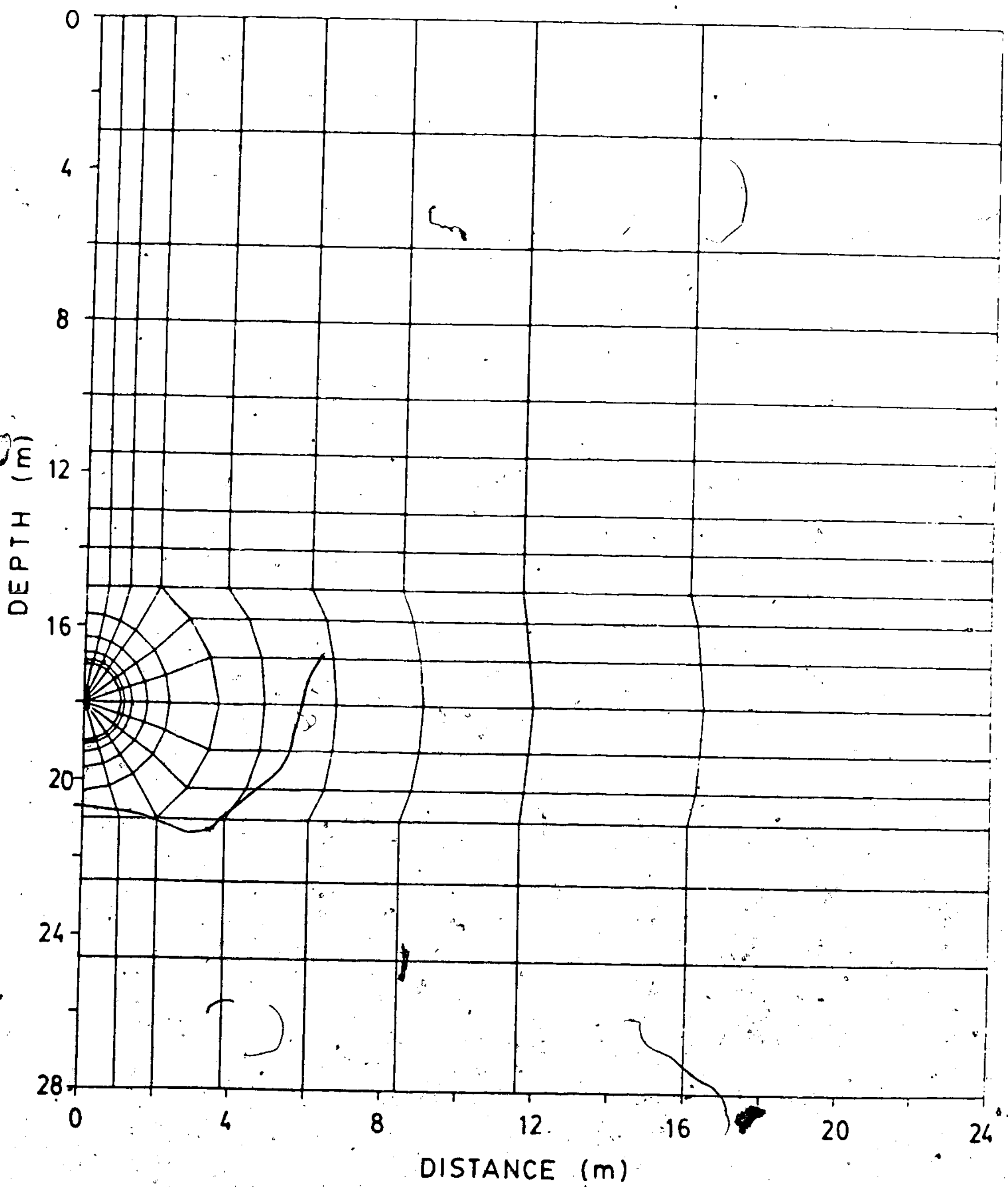

Figure B.3 Finite Element Mesh for Tunnel Analysis

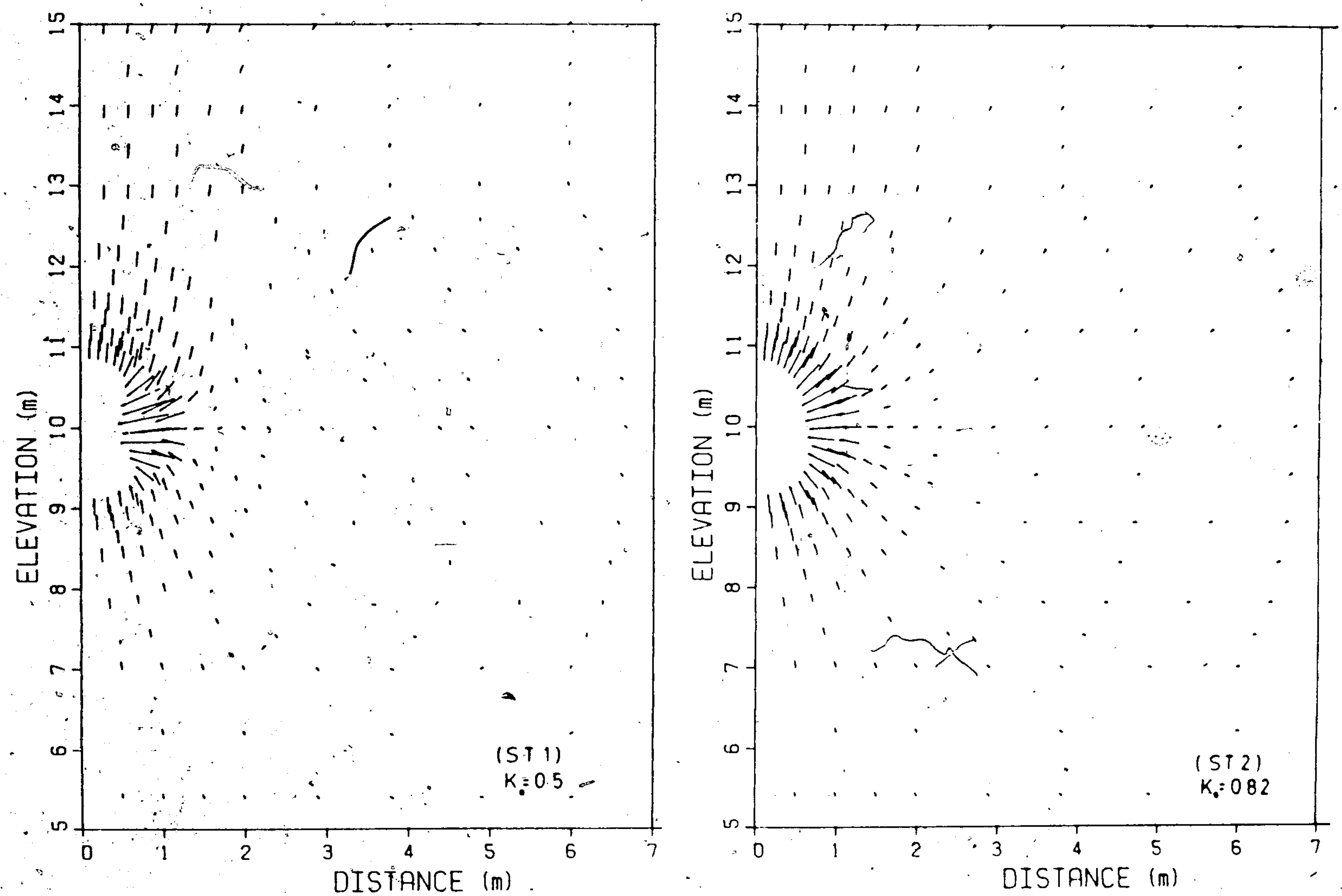

Figure B.4 Displacement Vectors (ST1 and ST2)

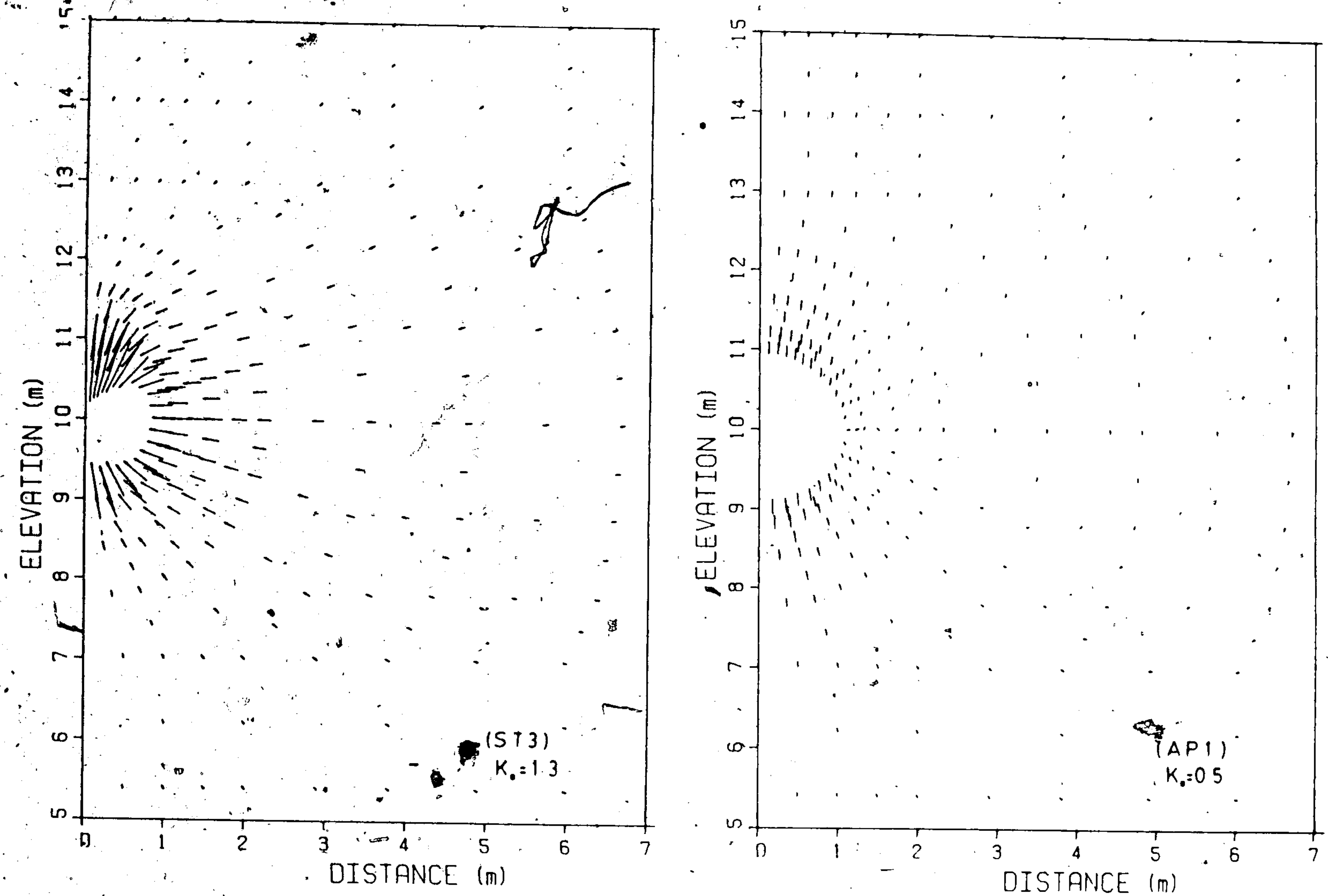

Figure B.5 Displacement Vectors (ST3 and AP1)

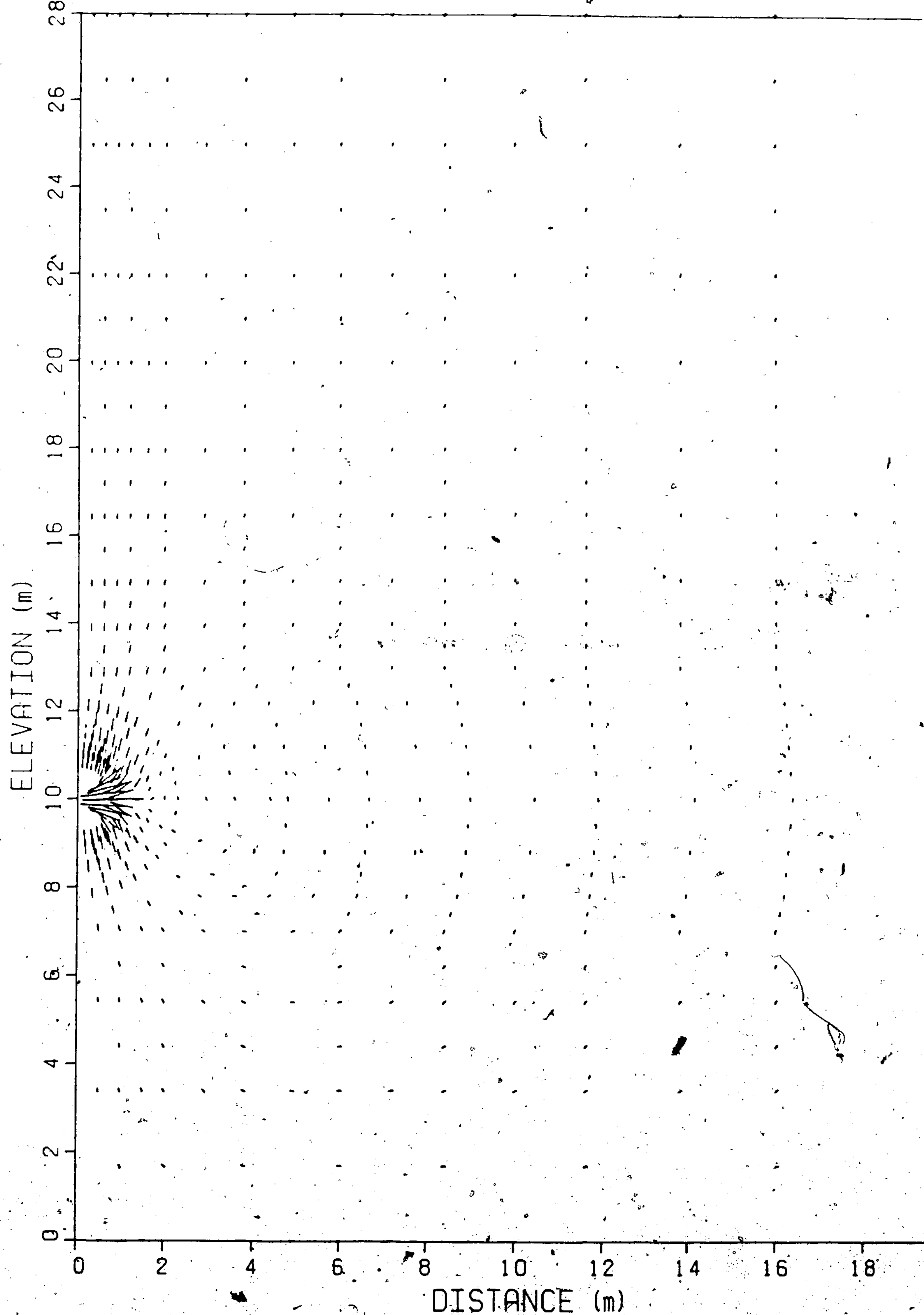

Figure B.6 Displacement Vectors (DT1)

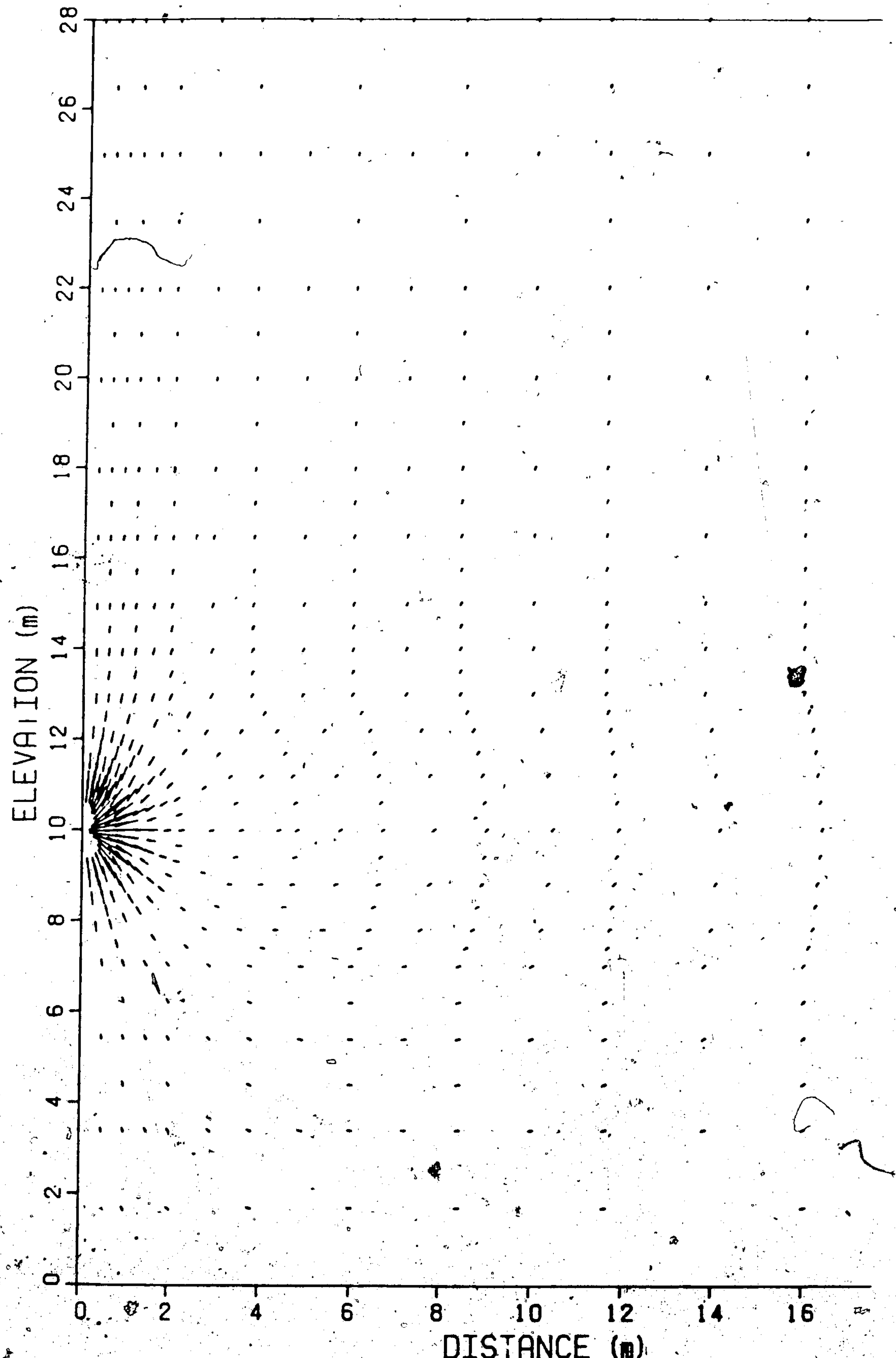

Figure B.7 Displacement Vectors (DT2)

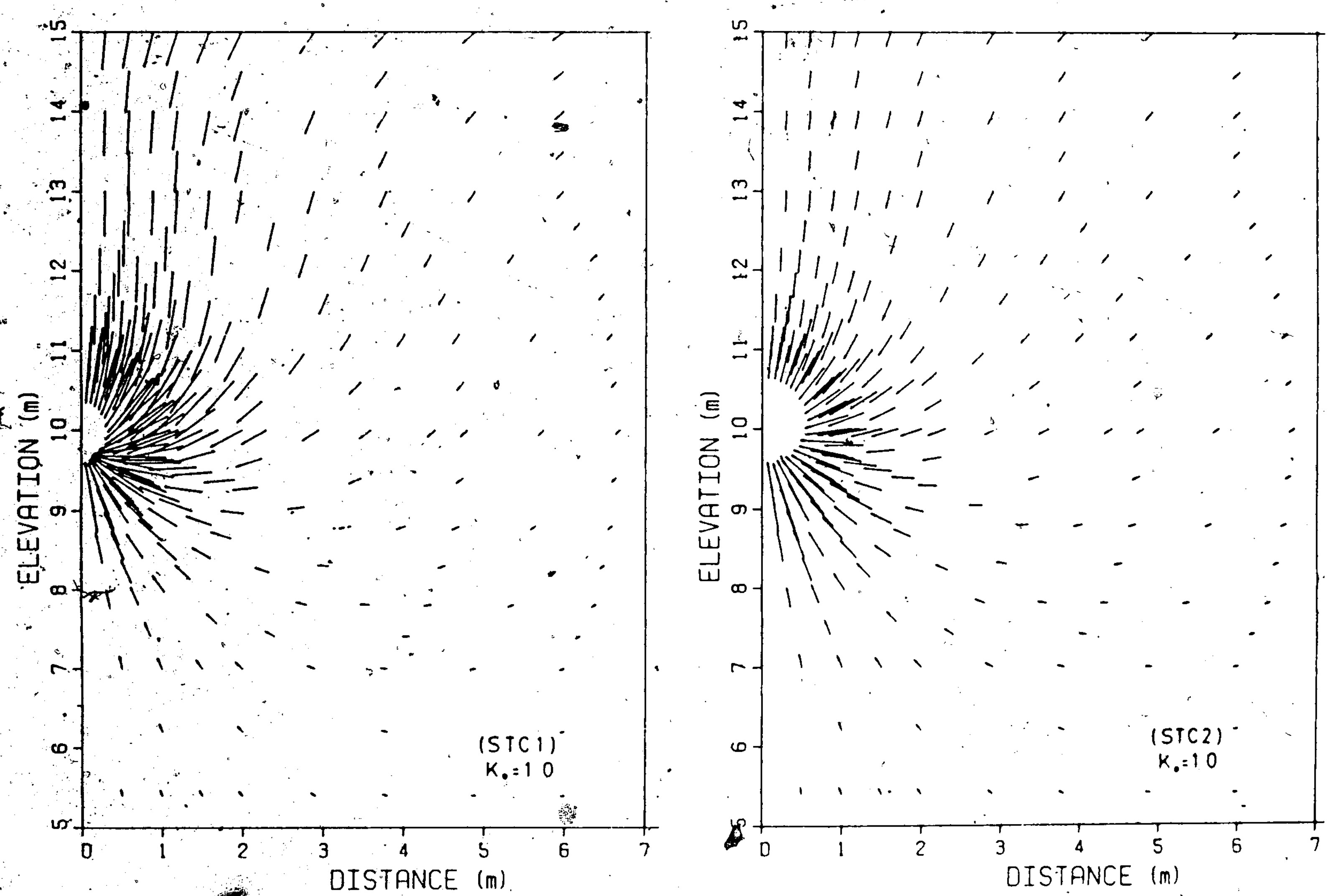

Figure B.8 Displacement Vectors (STC1 and STC2)

APPENDIX C

Tunnel Case Histories

Table C.1 Tunnel Case Histories - Cohesionless Soils

Cases	H/a	Ss/a (%)	i/a	Reference	No
London TEL, New Cross	4.8	1.0	1.8	(1)	(G)
Washington DC Metro	4.5	3.5	1.4	(1)	(I)
"	6.6	0.2	1.6	(1)	(L)
Frankfurt Shield	3.8	2.2	1.5	(1)	(M)
Brussels Metro	3.2	3.0	1.1	(1)	(T)
Mission Line BART	4.1	1.0	1.6	(1)	(1)
Toronto Subway	4.6	2.7	1.0	(1)	(2)
"	3.9	8.7	0.7	(1)	(15a)
"	5.1	11.1	0.9	(1)	(15b)
Ayrshire JD Scheme	4.3	9.3	1.0	(2)	-
Warrington Sewer	4.7	1.4	1.2	(2)	-
"	4.7	1.0	1.4	(2)	-
"	4.2	2.9	0.8	(2)	-
"	4.2	1.3	1.2	(2)	-
"	4.1	1.8	1.1	(2)	-
"	4.7	0.2	2.7	(2)	-
WNTDC Sewer	2.6	4.3	1.3	(2)	-
"	5.0	1.1	1.4	(2)	-
"	3.6	0.8	0.9	(2)	-
"	3.6	2.8	1.0	(2)	-
"	3.6	0.4	1.3	(2)	-
North West A Sewer	8.4	2.8	3.2	(2)	-
Northumbrian Sewer	7.5	4.7	4.2	(2)	-
LRT Edmonton	3.4	0.3	0.8	(3)	-
Exp Tunnel Edmonton	18.8	0.9	12.5	(4)	-
Model Test (Cambridge)	2.0	6.0	0.7	(5)	-
"	3.0	4.1	0.8	(5)	-
"	4.0	3.5	1.2	(5)	-
Model Test (Illinois)	4.9	4.1	2.2	(6)	-
"	5.7	4.9	3.6	(6)	-
"	5.7	6.[illegible]	2.0	(6)	-

* Ref.: (1) Attewell (1978), (2) O'Reilly and New (1981)
(3) Branco (1981), (4) El-Nahhas (1979)
(5) Atkinson and Potts (1977), (6) Cording et al, (1976)

Table C.2 Tunnel Case Histories - Cohesive Soils

Cases	H/a	Ss/a (%)	j/a	Cu (kPa)	Reference	No
Model Tests (Cambridge)	2.5	8.4	1.0	26	(5)	-
"	1.8	8.8	0.7	26	(5)	-
Washington Metro	4.6	4.8	1.4	75	(1)	(J)
"	3.6	8.8	0.6	75	(1)	(K)
Model Tests (Cambridge)	3.5	7.7	1.4	26	(5)	-
"	4.0	7.4	2.0	26	(5)	-
Toronto Subway	4.9	1.4	1.4	67	(1)	(12)
Chicago D-5	3.9	1.3	0.9	67	(1)	(13)
Sewerage, Belfast	3.6	1.2	2.0	10	(2)	-
BART San Francisco	3.3	1.5	1.8	10	(2)	-
Sutton Sewerage	3.8	0.4	2.3	90	(2)	-
Bristol Sewerage	3.5	1.2	2.0	18	(2)	-
NWA Seweage Scheme	7.5	0.8	3.7	73	(1)	(B)
Model Tests (Cambridge)	7.2	5.3	3.7	26	(5)	-
"	6.0	6.1	3.0	26	(5)	-
Kyoto, Tokyo Subway	6.4	0.3	15.5	72	(1)	(9)
BART San Francisco	6.5	1.7	3.2	77	(1)	(10)
NWA Sewerage	7.5	0.8	3.9	73	(2)	-
Sutton Sewerage	6.4	0.9	4.0	90	(2)	-
Stockton Council	10.0	6.9	5.5	50	(2)	-
"	9.3	8.9	5.8	50	(2)	-
Washington Metro	4.6	0.7	2.1	155-550	(1)	(N)
"	2.4	0.2	1.2	72-275	(1)	(R)
Running Tunnel	5.5	0.3	2.7	200	(2)	-
London Transport	6.8	0.2	3.8	230	(2)	-
Oxford Trunck Sewer	8.3	0.2	3.6	200-400	(2)	-
London TFL	14.1	0.3	6.1	270	(1)	(A)
"	9.4	0.3	5.0	230	(1)	(E)
"	16.4	0.2	7.3	230	(1)	(F)
Ottaw Sewer	12.0	0.4	5.2	354	(1)	(11)
Sutton Sewer	19.2	0.4	11.2	180	(2)	-

* Ref.: (1) Attewell (1978), (2) O'Reilly and New (1981), (3) Branco (1981), (4) El-Nahhas (1979), (5) Atkinson and Potts (1977), (6) Cording et al. (1976)

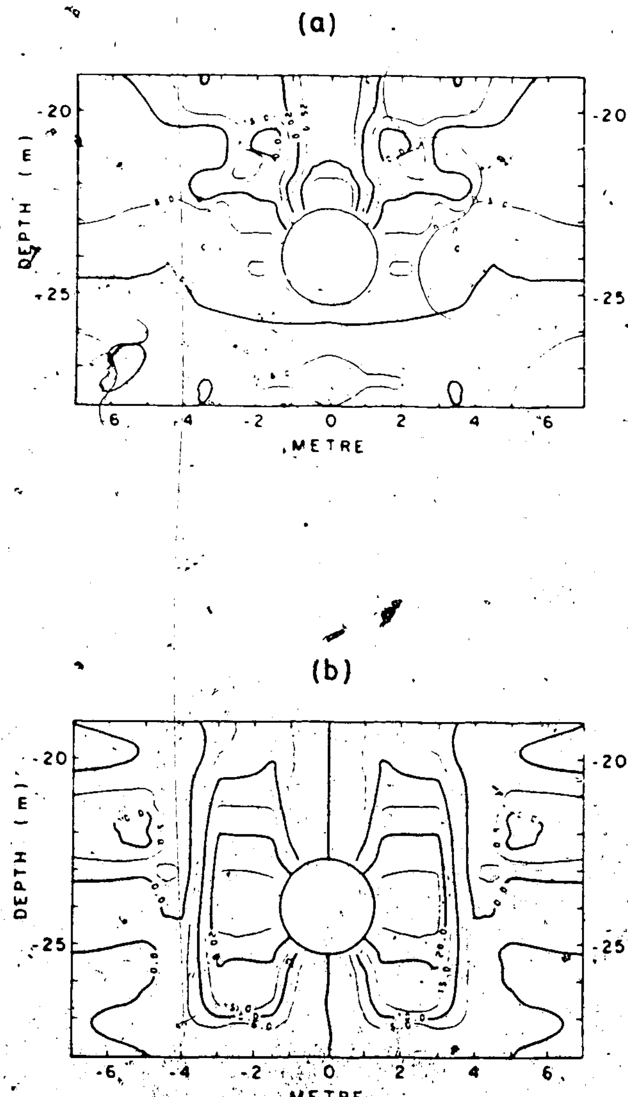

Figure C.1 Contours of Vertical and Horizontal Displacements around EXP Tunnel (modified from Eisenstein et al., 1981)

APPENDIX D

Shaft Analyses

D.1 Vertical Arching

Vertical soil arching sometimes can be referred to as "bin effect in silo" quantified by use of a horizontal differential element whose supports derive from the shear resistance on the interfaces of the stationary wall or soil mass (Fig. 4.2d). Summation of the vertical forces can be used to calculate the horizontal pressure required to maintain equilibrium of the soil mass in vertical directions. Because the shear resistances on the interfaces are derived from the frictional resistance and the shear strength of the cohesionless and cohesive materials respectively, the vertical arching action for these two types of materials is treated separately.

Cohesionless Soils

Terzaghi (1936) adopted the vertical arching action developed behind the timbering of cuts and derived a relationship between the allowed wall yielding and the lateral pressure distribution behind. However, he had to assume some linear function on the coefficient of horizontal/vertical pressure (K_s) along the depth. Recently, Handy (1985) expanded his investigation on this coefficient (K_s) and found that K_s is a function of friction angle (δ) of the wall and soil internal friction angle (ϕ) of the soil. The lateral pressure distribution calculated from the classic arching theory with adjusted K_s compared well with published data of some model and field tests. It is of practical importance that Terzaghi (1936) and Handy (1985), both assumed the plastic yielding behind the wall followed the Rankine's slip lines. However, this assumption is not applicable to the shaft case.

Vertical arching near a shaft can be quantitatively described by the same concepts as found in the two papers mentioned above, although several modifications are necessary for their generalization. These will be discussed below for the shaft behaviour.

Summation of vertical forces of a horizontal differential ring element in Fig. 4.2d gives

$$d\sigma_v = [\gamma - (2\pi\sigma_v)/A\,(K_s\mu_s R/\sin\alpha) + K_w\mu_w a)]dh \qquad \text{D.1}$$

In Eqn. D.1, the extent of the plastic zone, R can be determined from Eqn. 4.14, 4.19 or 4.25 depending on the material type and the mode of yielding. Typical values of K_s and K_w can be found in the paper by Handy (1985) for typical soil properties. These coefficients, K_s and K_w, defining the horizontal to vertical stress ratios at soil and wall, depend on the stress distribution around the shaft which in turn are functions of displacement, material types, and modes of yielding. Fig. D.5 shows stress distributions around the shaft diagrammatically, along with ranges of K_s and K_w values for yielding Modes A and B. It is important to realize that the vertical stresses calculated from Eqn. D.1

are assumed to be constant across the plastic zone. This assumption should be taken into account when estimating the K_s and K_w values. In case of the yielding Mode A ($K_o > K_{cr}$) where the vertical stress is always the intermediate stress, the K_s value at the elastic-plastic boundary is greater than K_a and less than K_o, but close to K_o. The K_w value at the wall depends on the displacement allowed, i.e., $K_w > K_a$ for small displacement and $K_w < K_a$ for excessive yielding (tangential stress equal to vertical stress). For Mode B ($K_o < K_{cr}$) where vertical stress is always the principal stress, the K_s value is slightly greater than K_a and the K_w is less than K_a. It can be seen that the K_s and K_w values vary along the depth of the shaft.

With all necessary parameters in Eqn. D.1 determined, the vertical stress distribution along the depth can be obtained by numerical integration of $d\sigma_v$ over the whole depth (see the computer program SFT2, Appendix F), and the horizontal stress due to gravity effect is given by

$$\sigma_h = p_g = K_w \sigma_v \qquad \text{D.2}$$

Cohesive Soils

The shear resistance of cohesive materials is independent of the confining pressure. Hence, applying horizontal pressure on the shaft wall does not enhance the strength of the material in the plastic zone. It is necessary to identify the possible collapse mechanism within the plastic zone and inhibit the mechanism by external forces.

Fig. D.4 shows one of the possible collapse mechanisms around the shaft. The collar within the plastic zone will cave in vertically and exert a resultant weight (W') on the conical mass beneath. To inhibit the horizontal caving in of the conical mass, horizontal pressure has to be applied. The required total force is given by considering the foroe equilibrium along the inclined failure surface of the conical mass

$$(W'+Wc)\sin a - P_g(\cos a) - F_c = 0 \qquad \text{D.3}$$

D.2 Mechanism of Shaft Behaviour in Cohesive Soil

This section contains equations governing the mechanism of shaft behaviour in cohesive soil. Equations are designated in the same sequence as those for cohesionless soil except a prefix - D. Thus, the explanations in cohesionless soil section is applicable to this appendix. The notations and symbols are given in Appendix A.

The stresses in an elastic thick walled hollow cylinder are given by:

$$\sigma_v = \gamma h = p_o \qquad \text{D.4}$$

$$\sigma_r = K_o p_o - [K_o p_o - p_i](a/r)^2 \qquad \text{D.5}$$

$$\sigma_t = K_o p_o + [K_o p_o - p_i](a/r)^2 \qquad \text{D.6}$$

For a cohesive material the strength is assumed to be constant:

$$\sigma_1 - \sigma_3 = q_u \qquad \text{D.7}$$

Hence, the support pressures for three possible modes of yield initiation are:

$$\text{For } \sigma_t - \sigma_r : p_i = K_o p_o - q_u/2 \qquad \text{D.8}$$

$$\text{For } \sigma_v - \sigma_r : p_i = p_o - q_u \qquad \text{D.9}$$

For $\sigma_t - \sigma_v$: $p_i = (2K_o - 1)p_o - q_u$ D.10

The largest value of p_i will govern the mode of yield initiation, which can be expressed in terms of required K_o:

Mode A for $\sigma_t - \sigma_r$: $q_u/(2p_o) + 1 > K_o > 1 - q_u/(2p_o)$ D.11

Mode B for $\sigma_v - \sigma_r$: $K_o < 1 - q_u/(2p_o)$ D.12

Mode C for $\sigma_t - \sigma_v$: $K_o > q_u/(2p_o) + 1$ D.13

Mode C has been neglected in the following analysis because it is of less practical significance. A critical K-value, K_{cr} is used to distinguish Mode A from Mode B, i.e., Mode A and Mode B observed for $K_o > K_{cr}$ and $K_o < K_{cr}$ respectively.

a) Mode A ($\sigma_t - \sigma_r$) at $K_o > K_{cr}$

The yielding initiates at the condition of:

$$\sigma_t - \sigma_r = 2K_o p_o - 2p_i = q_u \quad \text{D.14}$$

The magnitude of displacement corresponding to the yield initiation is:

$$u_i = [a(K_o p_o - p_i)(1+\nu)]/E \quad \text{D.15}$$

Further decrease in the internal support pressure causes propagation of the plastic zone and increase in wall convergence which are as follows:

$$R_{tr} = a\{exp[(K_o p_o - p_i)/q_u - 1/2]\} \quad D.16$$

$$u_i = a\{1-[1/(1+A_v)]^{1/2}\} \quad D.17$$

b) Mode B $(\sigma_v - \sigma_r)$ at $K_o < K_{cr}$

Yielding initiates at the condition of Eqn. D.12 and the displacement at this stage is given by:

$$p_i = \sigma_v - q_u = K_a p_o$$

$$\text{or } u_i = a[(K_o - K_a)p_o(1+\nu)]/E \quad D.18$$

As p_i is progressively reduced, the vertical stresses will also decrease due to the vertical shear stress induced by vertical downward displacement, and the tangential stress will increase until it becomes equal to the vertical stress at the wall. At this state, the radial stress in the plastic zone is given by:

$$\sigma_r = \sigma_v - q_u \text{ and } \sigma_v = p_o \quad D.20$$

Equating this stress with that in the elastic zone given by Eqn. D.5 yields the extent of plastic zone

$$R_{vr} = a\sqrt{\{(K_o p_o - p_i)/[(K_o - 1)p_o + q_u]\}} \qquad \text{D.21}$$

The corresponding wall convergence at this stage can be found by application of the model proposed by Ladanyi (1974),

$$u_i = a\{1-[1/(1+\hat{A}_v)]^{1/2}\} \qquad \text{D.22}$$

and the support pressure is

$$p_i = (K_o p_o - q_u/2) \qquad \text{D.23}$$

Further relief in support pressure induces the propagation of the plastic zone. The mode of yielding is still controlled by Mode B. But near the shaft wall, there exists a zone at which the tangential stress becomes equal to the vertical stress. Within this zone, the radial and tangential stresses governed by the failure criteria are given as Ladanyi (1974),

$$\sigma_r = p_i + q_u(\ln(r/a)) \qquad \text{D.24}$$

$$\sigma_t = p_i + q_u(1+\ln(r/a)) \qquad \text{D.25}$$

and the extent of this zone is

$$R_{tr} = a\{\exp[K_o p_o - p_i)/q_u - 1/2]\} \quad \text{D.26}$$

To calculate the extent of the plastic zone due to Mode B, one needs to know the radial stress distribution. Between the distance ($R_{tr} < r < R_{vr}$) shown in Fig. 4.9, the condition of equilibrium with tangential stress gives radial stress as

$$\sigma_r = K_o p_o - [(K_o p_o - \sigma_r')(R_{tr}/r)^2] \quad \text{D.26}$$

where: $\sigma_r' = 2K_o p_o - q_u$ at $r = R_{tr}$

Substituting $r = R_{tr}$ and σ_r' into Eqn. D.26 yields the radial stress distribution in the plastic zone ($R_{tr} < r < R_{vr}$). Continuity of radial stresses at the elastic zone boundary ($\sigma_r = K_a \sigma_v$) locates the extent of the plastic zone, R_{vr} as:

$$R_{vr} = a\sqrt{\{(K_o p_o - q_u)\exp[2((K_o p_o - p_i)/q_u - 1/2)]/[(1-K_o)p_o + q_u]\}} \quad \text{D.27}$$

The wall displacement can also be found similar to Mode A.

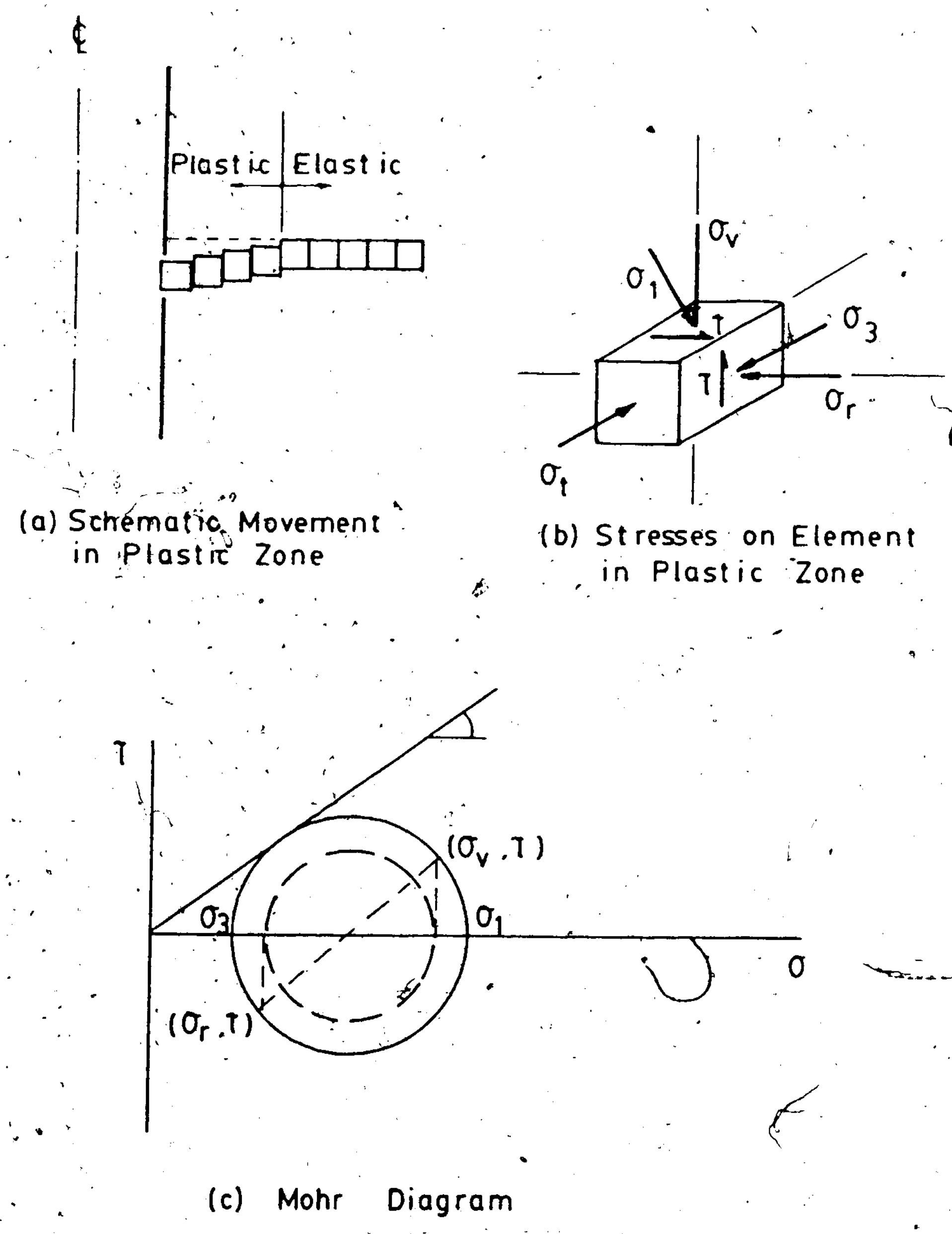

Figure D.1 Terzaghi's Method (1943)

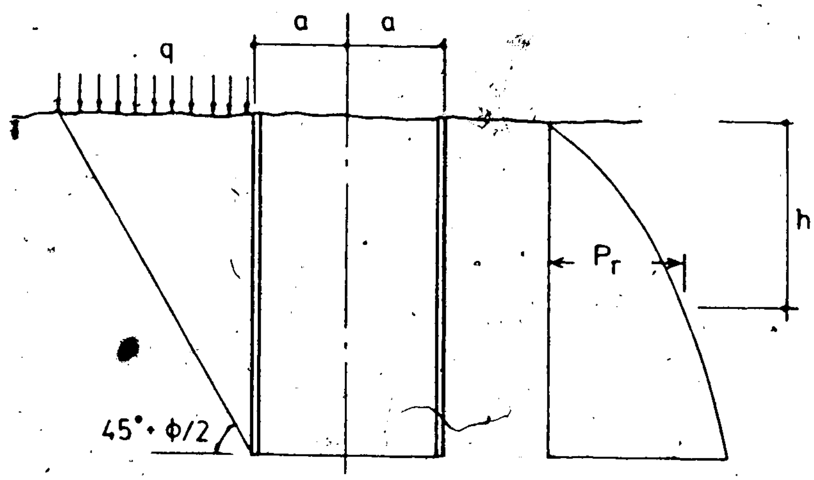

Berezantzev (1958)

Radial stresses (P_r) acting on a vertical cylindrical surface is given by:

$$P_r = a\,h\frac{\sqrt{K}}{g-1}\left(1-\left(\frac{a}{r}\right)^{g-1}\right) + q\left(\frac{a}{r}\right)^{g} + c\cot\phi\left(\left(\frac{a}{r}\right)^{g} K - 1\right)$$

where: $K = \tan^2(45^\circ - \phi/2)$
$r = a + h\sqrt{K}$
$g = 2\tan\phi\,\tan(45^\circ + \phi/2)$

Figure D.2 Berezantzev's Method (1958)

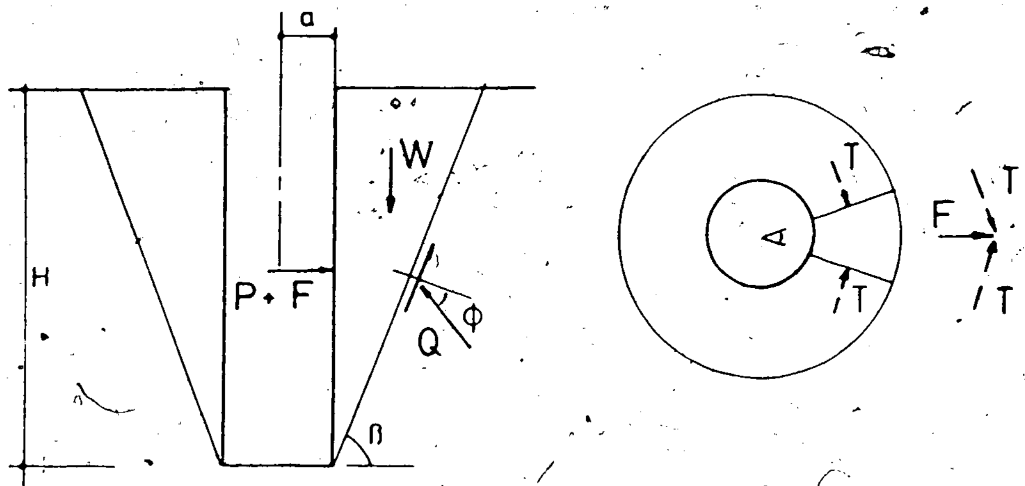

a - radius of shaft
H - depth of shaft
ß - angle between the horizontal and the failure surface of the cone
ϕ - angle of internal friction of soil

W - weight of the sliding cone
Q - reaction acting on the sliding cone
P - earth pressure acting on the shaft lining
T - tangential force which has a radial component F acting in outward direction, i.e. $F = 2 \tan(\phi/2)$

Figure D.3 Prater's Method (1977)

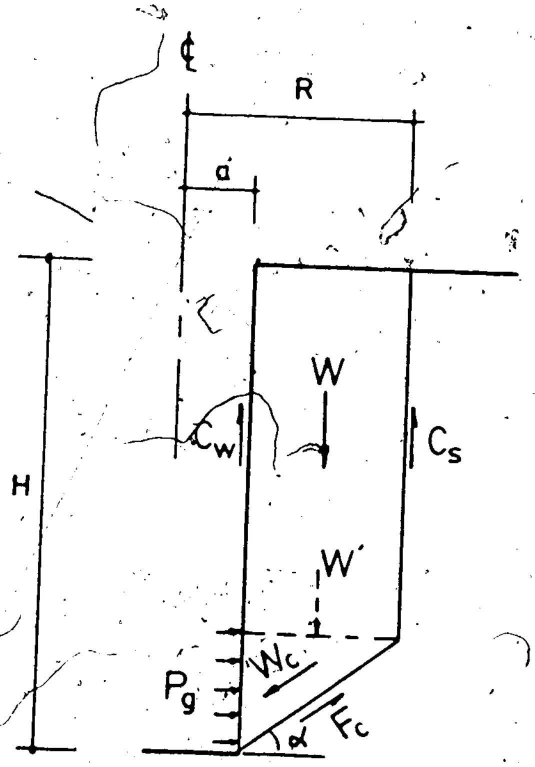

Figure D.4 Gravity Effect in Cohesive Soils

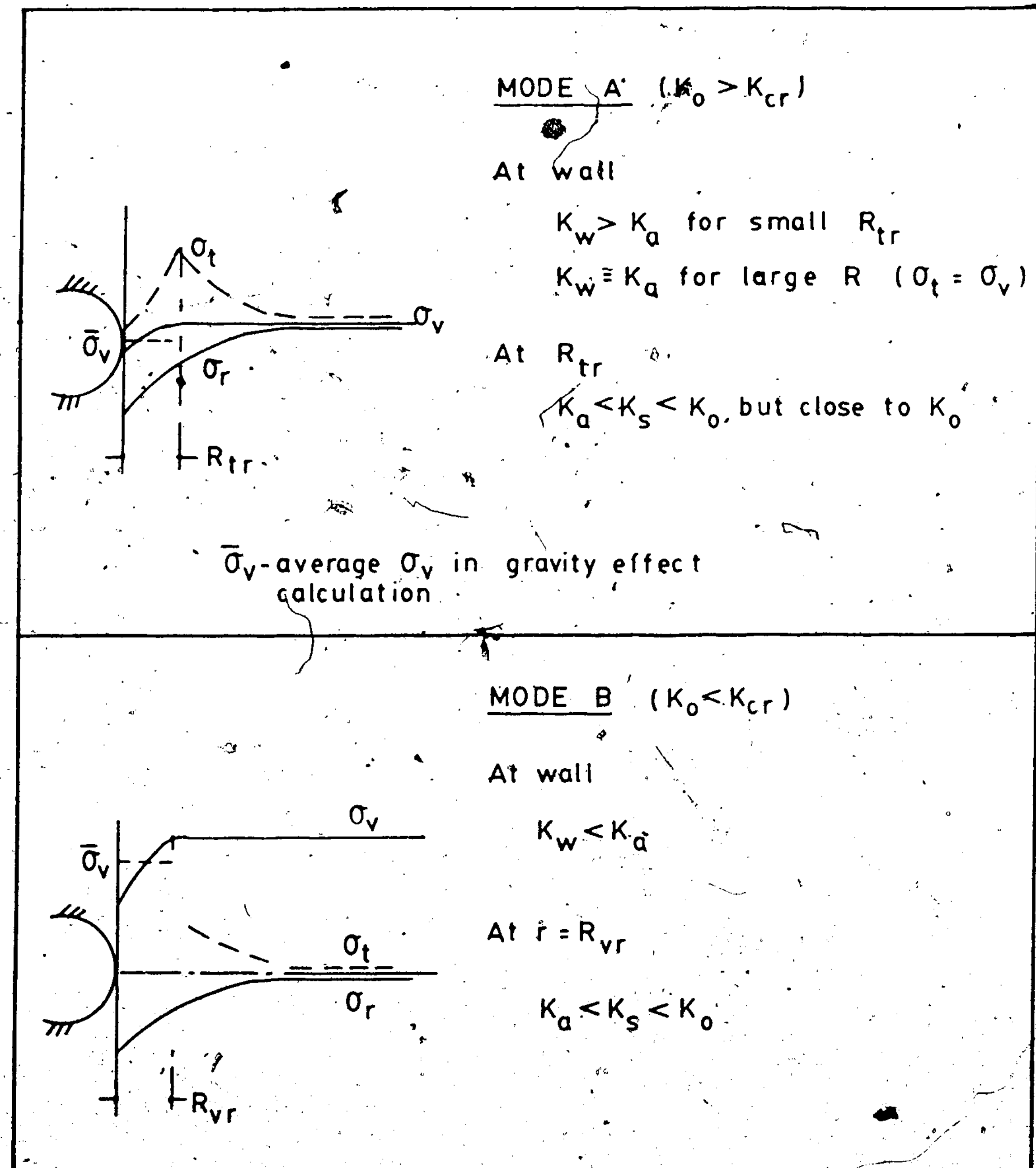

Figure D.5 Coefficients of Vertical-Radial Stress (K_s, K_w)

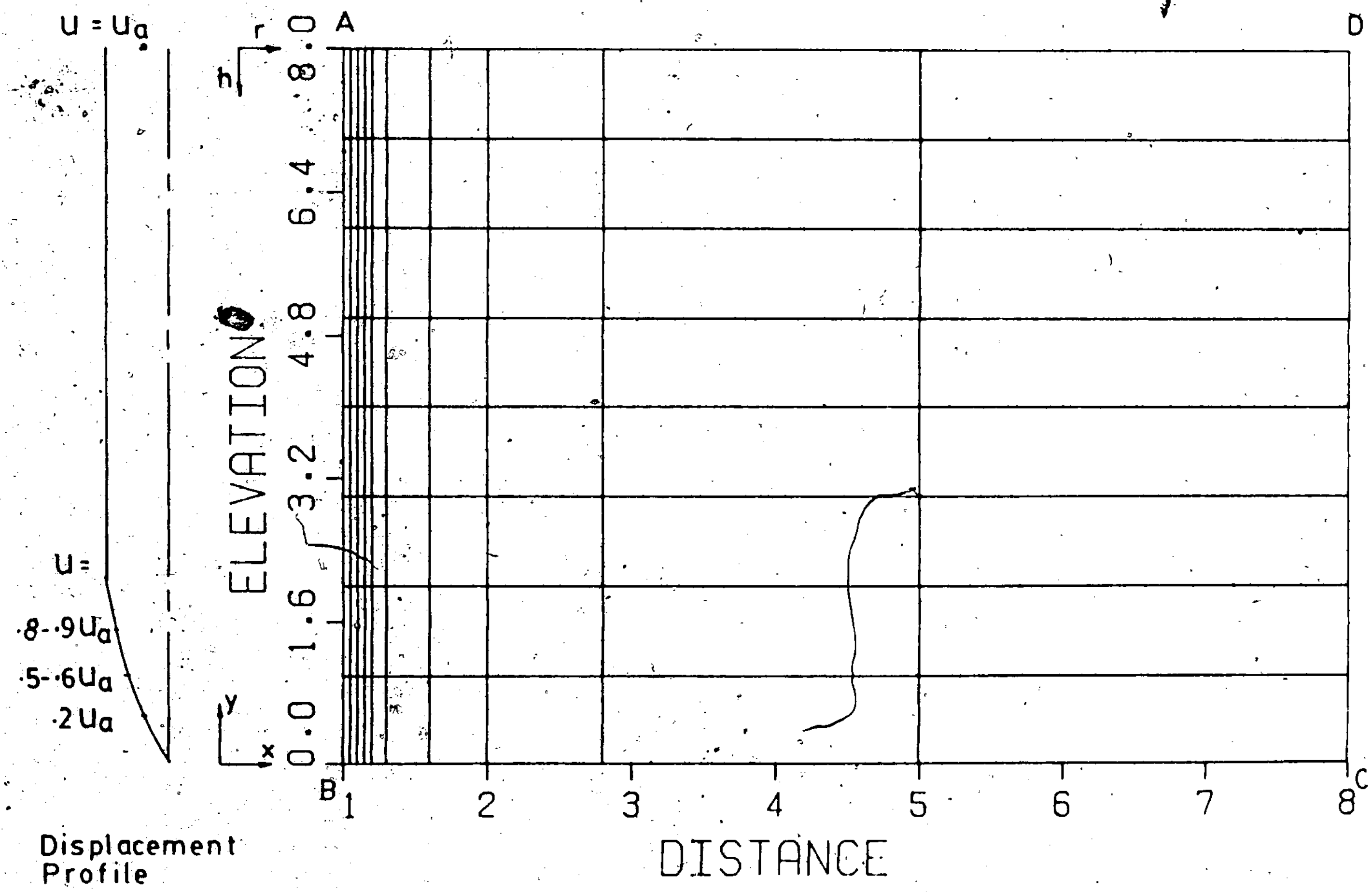

Figure D.6 Finite Element Mesh for Shaft Analysis

APPENDIX E

Shaft Case Histories

Table E.1 Properties of Melinex (Shaft Lining)

Tensile Strength	17.65 kN/sq.cm.
Yield Strength	9.81 kN/sq.cm.
Young's Modulus (at 1% strain)	430.0 kN/sq.cm.
Elongation at Yield Point	5 %
Coefficient of Thermal Expansion	17.10 $\times 10^{-6}$ cm/cm-C°

Table E.2 Properties of Leigthon Buzzard Sand 120/220

Specific Gravity	2.66
Minimum Density	12.95 kN/m3
Maximum Density	15.86 kN/m3
Average Grain Size	0.13 mm
Coefficient of Uniformity (=D60/D10)	1.40
Density in Test	1.535-1.550 kN/m3
Density Index	85%-90%
Frictional Angle	38.3 deg

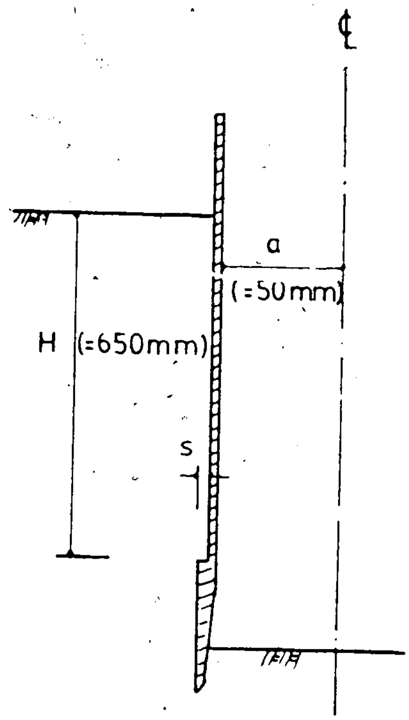

Figure E.1 Shaft Details (modified from Muller-Kirchenbauer et al., 1980)

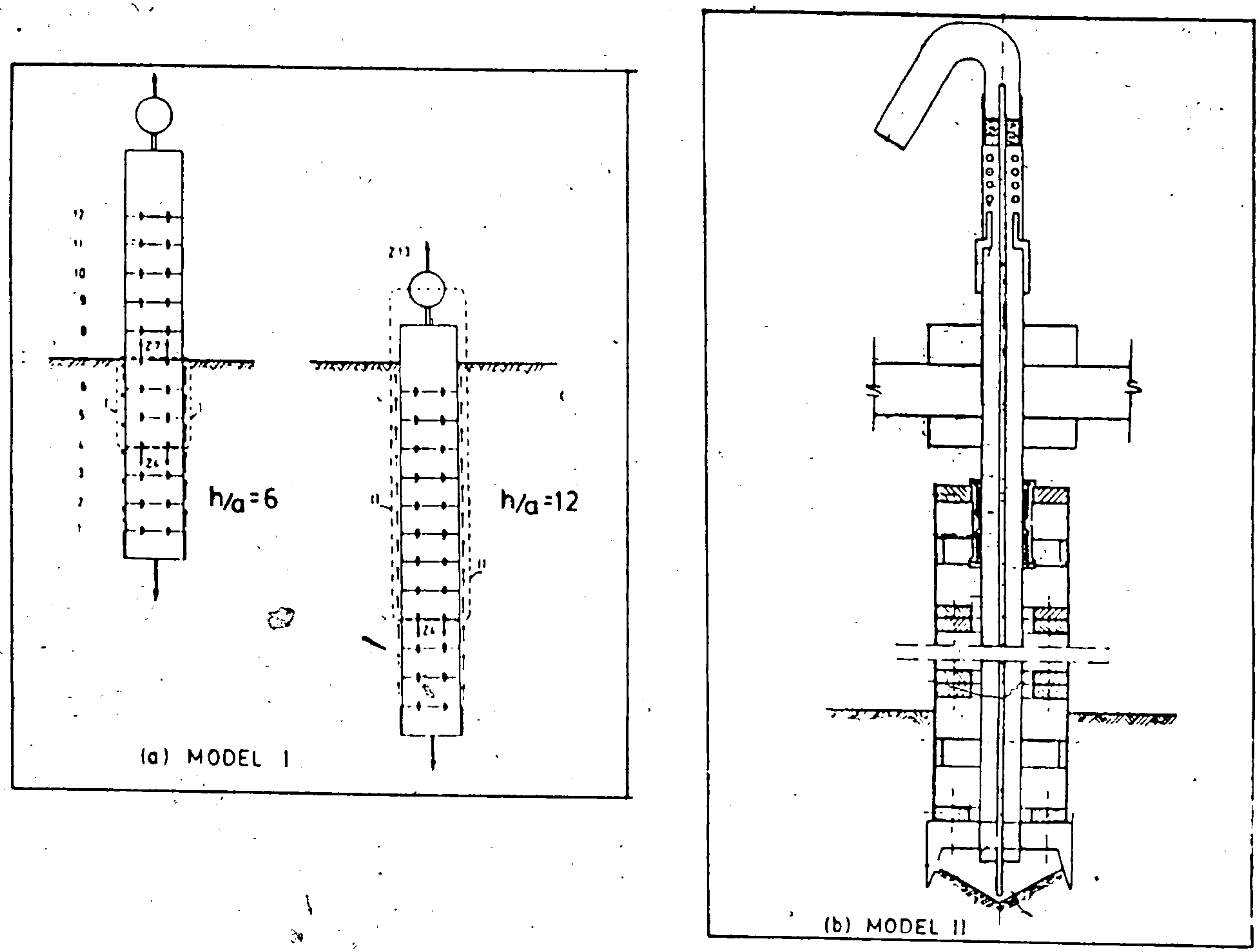

Figure E.2 Shaft Models-Types I and II (modified from Muller-Kirchenbauer et al., 1980)

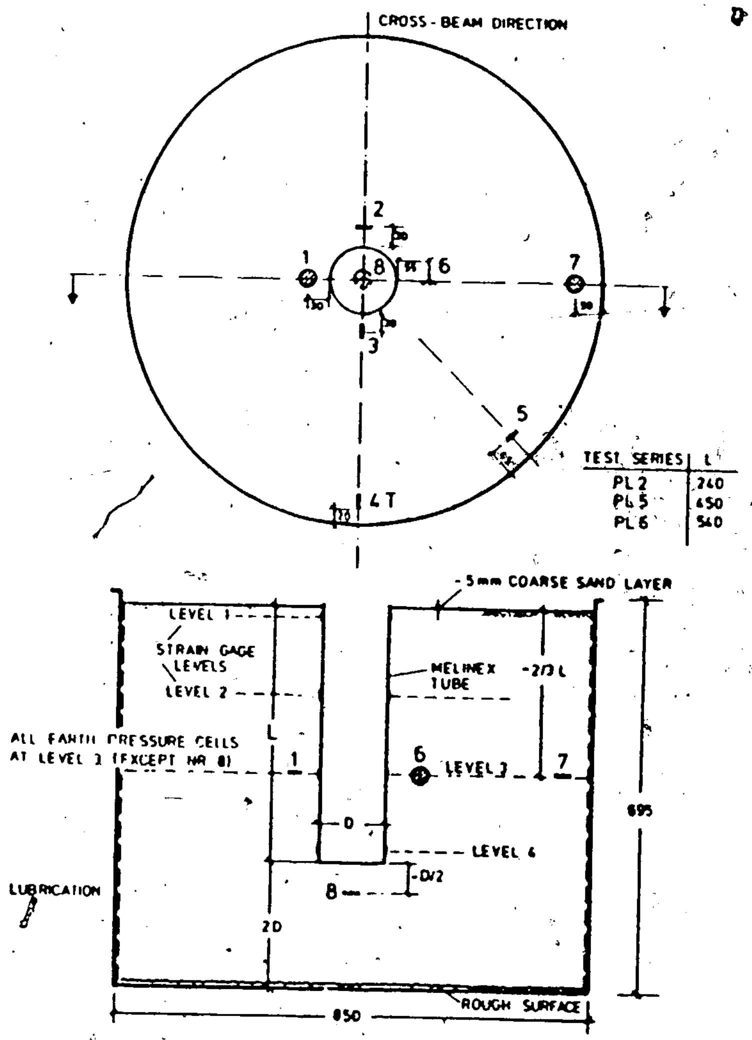

Figure E.3 Model Test Setup (modified from Lade et al., 1981)

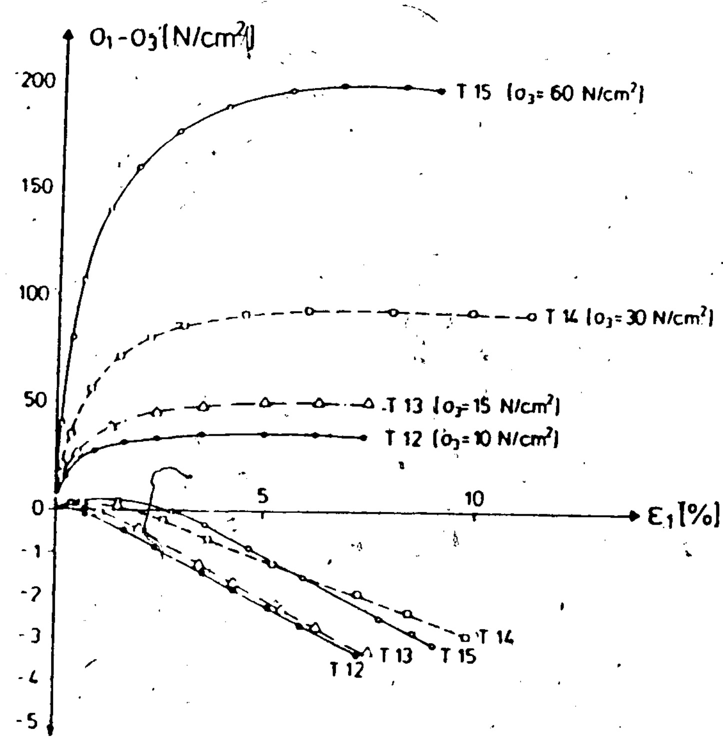

Figure E.4 Stress-Strain and Volume Change Curves from Triaxial Compression Tests on Leighton Buzzard Sand (modified from Lade et al., 1981)

APPENDIX F

Computer Program

Tunnel Analysis

TUN1 - Calculate support pressure for yield initiation at the roof (Line c-d, Fig. 2.4)

TUN2 - Calculate support pressure for yield initiation at the springline (Line h-k, Fig. 2.4)

TUN3 - Determine Regime 'J' of Mode II (Line i-l, Fig. 2.4)

TUN4 - Calculate support pressure for final equilibrium state (p_{fc})

TUN5 - Calculate support pressure for p_{ys} (LIne e-f, Fig. 2.4)

Shaft Analysis

SFT1 - Calculate Ground Convergence Curve of soil model (Ladanyi, 1974)

SFT2 - Calculate support pressure for vertical arching

```
C
C*****************************************************************
C
C*********** TUN1 ***********
C
C  CALCULATION OF SUPPORT PRESSURE(IN TERM OF YH) FOR
C     YIELD INITIATION AT ROOF IN TUNNEL
C
C*****************************************************************
C
C  USING:
C  ELASTIC STRESS DISTRIBUTION AROUND A CIRCULAR TUNNEL
C   UNDER INTERNAL PRESSURE USING SCHMIDT METHOD
C
C *************************************************************
C  INPUT FILE:
C      1. KO,PHI,DEP
C      2. EOF
C
C  OUTPUT FILE:
C      SUPPORT STRESS IN NEGATIVE
C
C
       READ(5,511) XKOO,PHIO,DEPO
 511   FORMAT(3F10.0)
C
       DXKO=0.1
       DDEP=1.
       DPHI=5.
C
       DO 11 I=1,5
       PHI=PHIO+DPHI*(I-1)
       XPHI=PHI*3.14159/180.
       XNP =(TAN(3.14159/4.+0.5*XPHI))**2.
       WRITE(6,601) PHI,XNP
 601   FORMAT(/, '  ANGLE =',F6.2,'  NP = ',F6.3)
C
       DO 22 J=1,8
       XKO=XKOO+DXKO*(J-1)
       XMIL = XKO/(1.+XKO)
C
       XN=1.0/XMIL
       D1=(1.+1./(XN-1.))*0.5
       D2=(1.-1./(XN-1.))*0.5
       XMIL1=(XN+1)*(XN-1.)/XN
       XMIL2=(XN+1)*(XN-2)/XN
       XM=-XMIL2/(4*XMIL1)
C
       WRITE(6,602) XKO,XMIL
 602   FORMAT('  KO = ',F5.3, ' POISSON RATIO =',F6.2)
C
       WRITE(6,603)
 603   FORMAT('  H/A ','    PI/YH ',/)
       DO 33 L=1,9
       DEP = DEPO +DDEP*(L-1)
C
C   AT ROOF
C
       FETA=3.14159/2.
       Q=1.0
```

```
      C
        XST=     -D1*(1.+Q)+
       &  (D1-0.5*D2-XM*Q-(XM+0.5*D2)*Q*Q)*(1./DEP)*SIN(FETA)-
       &   D2*(1.+3*Q*Q)*COS(2*(FETA))+
       &  0.5*D2*(1.-Q*Q+4*Q*Q*Q)*(1./DEP)*SIN(3*FETA)
      C
        ALPHA= XST/(XNP+1.)
      C
        WRITE(6,612) DEP   ,ALPHA
  612   FORMAT(F5.2,F10.3)
  33    CONTINUE
  22    CONTINUE
  11    CONTINUE
        STOP
        END
End of file
      C
      C*****************************************************
      C
      C*********** TUN2*********
      C
      C  CALCULATION OF SUPPORT PRESSURE(IN TERM OF YH) FOR
      C    YIELD INITIATION AT SPRINGLINE IN TUNNEL
      C
      C*****************************************************
      C
      C  USING:
      C  ELASTIC STRESS DISTRIBUTION AROUND A CIRCULAR TUNNEL
      C   UNDER INTERNAL PRESSURE USING SCHMIDT METHOD
      C
      C ************************************************
      C  INPUT FILE:
      C      1. KO,PHI,DEP
      C      2. EOF
      C
      C  OUTPUT FILE:
      C      SUPPORT STRESS IN NEGATIVE
      C
      C
        READ(5,511) XKOO,PHIO,DEPO
  511   FORMAT(3F10.0)
      C
        DXKO=0.1
        DDEP=1.
        DPHI=5.
      C
        DO 11 I=1,5
        PHI=PHIO+DPHI*(I-1)
        XPHI=PHI*3.14159/180.
        XNP =(TAN(3.14159/4.+0.5*XPHI))**2.
        WRITE(6,601) PHI,XNP
  601   FORMAT(/,'  ANGLE =',F6.2,'  NP = ',F6.3)
      C
        DO 22 J=1,8
        XKO=XKOO+DXKO*(J-1)
        XMIL = XKO/(1.+XKO)
      C
        XN=1.0/XMIL
        D1=(1.+1./(XN-1.))*0.5
        D2=(1.-1./(XN-1.))*0.5
```

```
      XMIL1=(XN+1)*(XN-1.)/XN
      XMIL2=(XN+1)*(XN-2)/XN
      XM=-XMIL2/(4*XMIL1)
C
      WRITE(6,602) XKO,XMIL
602   FORMAT('  KO = ',F5.3, ' POISSON RATIO =',F6.2)
C
      WRITE(6,603)
603   FORMAT('  H/A  ','    PI/YH  ',/)
      DO 33 L=1,9
      DEP = DEPO +DDEP*(L-1)
C
C   AT SPRINGLINE
C
      FETA=0.0
      Q=1.0
C
      XST=     -D1*(1.+Q)+
     &  (D1-0.5*D2-XM*Q-(XM+0.5*D2)*Q*Q)*(1./DEP)*SIN(FETA)-
     &   D2*(1.+3*Q*Q)*COS(2*(FETA))+
     &  0.5*D2*(1.-Q*Q+4*Q*Q*Q)*(1./DEP)*SIN(3*FETA)
C
      ALPHA= XST/(XNP+1.)
C
      WRITE(6,612) DEP   ,ALPHA
612   FORMAT(F5.2,F10.3)
33    CONTINUE
22    CONTINUE
11    CONTINUE
      STOP
      END
End of file
C*****************************************************************
C
C************** TUN3**********
C
C       STRESS DISTRIBUTION WITHIN THE PLASTIC ZONE
C                 - SOLVING CAUCHY PROBLEM
C     (INTERNAL PRESSURE WITH SHEAR IN % OF INSITU STRESS)
C                    (MARCH 21, 1985)
C*****************************************************************
C
C INPUT FILE:
C     1. RAD,HT,PI(%),ANGLE,COHESION,DENSITY,POISSON'S RATIO,TOLEN,
C     2. EOF
C
C *************
C OUTPUT INTERPRETATION
C     +VE X-AXIS POINTING DOWNWARD, +VE Y-AXIS RIGHT
C     R - RADIUS , THETA- ANGLE BETWEEN X AND R DIRECTIONS
C     DIVERGENCE OCCURED WHEN THE DIFFERENCE IN FED EXCEEDS
C     THE SPECIFED TOLERANCE,I.E. HYPERBOLIC CONDITION NOT
C     VALID AND bifurCATION INVOLVED
C
C*****************************************************************
      COMMON TUNPRS, RAD, PHI,COH ,W,
     &        X(20,20), Y(20,20),TH(20,20),SP(20,20),SR(20,20),
     &         NP,NF  , IXO,IYO, NBC,DIVAN,TOLEN
C
C W - WT OF SOIL
```

```
C TUNPRS - INTERNAL SUPPORT PRESSURE  %OF INSITU STRESS
C TOLEN - TOLERANCE ALLOWED IN CALCULATION FOR ACCURACY
C RAD - RADIUS OF TUNNEL
C HT - DEPTH OF OVERBURDEN
C PHI - INTERNAL FRICTIONAL ANGLE OF SOIL
C COH COHESION OF SOIL
C XKO - INITIAL INSITU STRESS COEFFICIENT
C P - NODAL POINT IN CHARACTERISTIC
C X - X COORDINATES
C Y - Y COORDINATES
C SP - STRESS FUNCTION
C SR - STRESS FUNNCTION
C TH -ANGLE BETWEEN X -AXIS AND PRINCIAPL STRESS
C
C  INPUT DATA
      READ(5,501) RAD,HT,TUNPRS,PHI,COH,W,XKO,TOLEN
501   FORMAT(8F10.0)
      WRITE(6,601) RAD,HT,TUNPRS, PHI,COH,W,XKO,TOLEN
601   FORMAT( ' RADIUS OF TUNNEL =',F6.2,/,
     & ' DEPTH OF OVERBURDEN = ',F6.2,/,
     & ' TUNNEL SUPPORT PRESSURE =',F10.2,/,
     & ' FRICTIONAL ANGLE =',F6.2,/,
     & ' COHESION = ', F6.2,/.
     & ' WEIGHT = ', F6.2,/,
     & ' KO = ',F6.2/,
     & ' TOL = ',F8.5,//)
C
C  INITIAL DATA
      NF=10
C  NF - NO. OF FORWARD CALCULATION (PLASTIC ZONE EXTENT)
      PHI=PHI*3.1416/180.
      XNP=TAN(0.25*3.1416+0.5*PHI)*TAN(0.25*3.1416+0.5*PHI)
C
         WRITE(6,698)
698      FORMAT(10X,' X   Y',' R',5X,'THETA',3X,'SX',3X,'SY','  SXY
     &   S1   S3   SR   ST   SSH  ',/)
C  BOUNDARY CONDITIONS
      NBC=9
C NBC - NO. OF KNOWN  BOUNDARY CONDITIONS
      IXO=1
      IYO=9
      DIVAN=3.14159/8.
      DO 11 I=1,NBC
      II=I-1
      MX=IXO+II
      NY=IYO+II
      X( MX,NY)=RAD*COS((II)*DIVAN)
      Y( MX ,NY )=RAD*SIN((II)*DIVAN)
      TH( MX ,NY )=0.5 *3.1416+(II)*DIVAN
C  INITIAL SXO ,SYO STRESSES IN X , Y DIRECTIONS
      SYO = W*(HT+X(MX ,NY))
      SXO = XKO*W*(HT+X(MX , NY))
C  INITIAL NORMAL AND SHEAR STRESSES ON THE SURFACE
      SNO = 0.5*(SXO+SYO) + 0.5*(SXO-SYO)*COS(2*TH(MX,NY))
      STO = -0.5*(SXO-SYO)*SIN(2*TH(MX,NY))
C  SUPPORT PRESSURE - % OF INSITU STRESS
      SN = SNO*TUNPRS
      ST = STO*TUNPRS
C  CALCULATION OF P , R STRESS PARAMETERS
      CX  =    COH*(1./TAN(PHI))
```

```
            VX1 = (SN*SN*SIN(PHI)*SIN(PHI)-ST*ST*COS(PHI)*COS(PHI))
            VX2 = 2*CX*SN*SIN(PHI)*SIN(PHI)+CX*CX*SIN(PHI)*SIN(PHI)
            VX3 = SQRT(VX1+VX2)
C           ROOT1=(SN+CX-VX3)/(COS(PHI)*COS(PHI))
            ROOT2=(SN+CX+VX3)/(COS(PHI)*COS(PHI))
            SP( MX,NY) =ROOT2 - CX
C           P2=ROOT1-CX
            SR( MX,NY) =SP(MX,NY)*SIN(PHI)+COH*COS(PHI)
               DTH = TH(MX, NY)*180./3.1416
               R = SQRT(X(MX,NY)*X(MX,NY)+Y(MX,NY)*Y(MX,NY))
               AN = (ATAN(Y(MX, NY)/X(MX,NY)))
               DAN = AN*180./3.1416
               SX = SP(MX,NY )+SR(MX, NY )*COS(2*TH(MX ,NY ))
               SY = SP(MX,NY )-SR(MX, NY )*COS(2*TH(MX,NY ))
               SXY = SR(MX,NY)*SIN(2*TH(MX,NY))
               S1 = (SP(MX,NY)+SR(MX,NY))
               S3 = (SP(MX,NY)-SR(MX,NY))
               SGT = SX*(SIN(AN)*SIN(AN)) +SY*(COS(AN)*COS(AN))-
          &     2*SXY*SIN(AN)*COS(AN)
               SGR = SX*(COS(AN)*COS(AN)) +SY*(SIN(AN)*SIN(AN))+
          &     2*SXY*SIN(AN)*COS(AN)
               SGSH = 0.5*(SGT-SGR)*SIN(2*AN)+SXY*(COS(2*AN))
C
             WRITE(6,612) MX, NY ,X(MX, NY),Y(MX, NY ),R,DAN,
          &     SX, SY,SXY ,S1, S3,SGR,SGT,SGSH
612        FORMAT( ' P(',I2,',',I2,') =',3F6.2, F6.1,8F7.2)
C            WRITE(6,613) CX,VX1,VX2,VX3, ROOT1 ,ROOT2
C613         FORMAT(6F10.3)
C            WRITE(6,614) SXO, SYO,SNO,STO,SN,ST ,P2
C614          FORMAT(7F10.2)
C
11         CONTINUE
C
C
              CALL NODE
C
              STOP
              END
C
C
C     SUBROUTINE NODE
            SUBROUTINE NODE
           COMMON TUNPRS, RAD, PHI,COH ,W,
          &       X(20,20), Y(20,20),TH(20,20),SP(20,20),SR(20,20),
          &       NP,NF , IXO,IYO, NBC,DIVAN,TOLEN
C
            XAN=(3.1416/4)-0.5*PHI
C
C     ICON - COUNTER TO LIMIT NO. OF ITERATION
C
            DO 10 I=1,NF
              WRITE(6,699) I
699           FORMAT(' FORWARD CAL. NO. (NF) =',I4,/)
              NNBC=NBC-1
              DO 20 II=1 ,NNBC
                ICONT1=0
                NC1=II-1
C         NC1 - COUNTER MOVING DIAGONAL DOWNARD
                IM=IXO+NC1
                JM=IYO+NC1
```

```
            IN=IXO+NC1+1
            JN=IYO+NC1+1
            XA = X(IM,JM)
            XB = X(IN,JN)
            YA = Y(IM,JM)
            YB = Y(IN,JN)
            THA=TH(IM,JM)
            THB=TH(IN,JN)
            SPA=SP(IM,JM)
            SPB=SP(IN,JN)
            SRA=SR(IM,JM)
            SRB=SR(IN,JN)
C
C FIRST ESTIMATES OF XP, YP, SRP AT POINT P
C
            XP1 = 0.5*(XA+XB)
            YP1 = 0.5*(YA+YB)
            THP1=0.5*(THA+THB)
            SPP1=0.5*(SPA+SPB)
            SRP1=0.5*(SRA+SRB)
C            WRITE(6,904) XP1,YP1,THP1,SPP1,SRP1
C904         FORMAT(5F10.3,//)
C   SOLVE FOR SPP AND THP
1000        ICONT1=ICONT1+1
            IF (ICONT1.GT.20) GO TO 999
            E1=-SIN(2*XAN)
            E2= SIN(2*XAN)
            F1=-W*SIN(2*XAN)*(XP1-XA)
            F2=-W*SIN(-2*XAN)*(XP1-XB)
            G1=SRP1+SRA
            G2=SRP1+SRB
            H1=-W*COS(2*XAN)*(YP1-YA)
            H2=-W*COS(2*XAN)*(YP1-YB)
            SPP2=(G2*(F1+H1)-G1*(F2+H2)+E1*G2*SPA-E2*G1*SPB+
     &       G1*G2*(THA-THB))/(E1*G2-E2*G1)
            THP2=(E2*(F1+H1)-E1*(F2+H2)+E1*E2*(SPA-SPB)+
     &        E2*G1*THA-E1*G2*THB)/(E2*G1-E1*G2)
            SRP2= SPP2*SIN(PHI)+COH*COS(PHI)
C            WRITE(6,901) E1, E2,F1,F2,G1,G2,H1,H2
C901        FORMAT(8F10.3,//)
C           WRITE(6,902) SPP2,THP2,SRP2
C902        FORMAT(3F10.3,//)
C
C   SOLVE FOR XP, YP
C
           A  = (0.5*(THP2+THA)-XAN)
           B = (0.5*(THP2+THB)+XAN)
           XP2 = (YB-YA+XA*TAN(A)-XB*TAN(B))/(TAN(A)-TAN(B))
           YP2= ((XB-XA)*TAN(A)*TAN(B)+YA*TAN(B)-YB*TAN(A))/
     &      (TAN(B)-TAN(A))
C           WRITE (6,905) A, B, XP2,YP2
C905        FORMAT(4F1-.3,//)
C
C  TEST FOR CONVERGENCE
C
            TEST = ABS(XP2-XP1)+ABS(YP2-YP1)+ABS(SPP2-SPP1)
     &       +ABS(THP2-THP1)
            IF (TEST .LT. TOLEN) GO TO 2000
C           WRITE(6,906) TEST
C905        FORMAT(F10.2)
```

```
              XP1 =XP2
              YP1=YP2
              SRP1 =SRP2
              SPP1 =SPP2
             GO TO 1000
      C
       2000    M=IM+1
              X( M, JM ) =XP2
              Y( M, JM ) =YP2
             TH( M, JM ) =THP2
             SP( M, JM ) =SPP2
             SR( M, JM ) =SRP2
             DTH = TH(  M, JM)*180./3.1416
             R = SQRT(X(  M, JM)*X(  M, JM)+Y(  M, JM)*Y(  M, JM))
             AN = (ATAN(Y(  M, JM)/X(  M, JM)))
             DAN = AN*180./3.1416
             SX = SP(  M, JM )+SR(  M, JM  )*COS(2*TH(  M , JM ))
             SY = SP(  M, JM )-SR(  M,  JM )*COS(2*TH(  M, JM ))
             SXY = SR(  M, JM)*SIN(2*TH(  M, JM))
             S1 =(SP(  M, JM)+SR(  M, JM))
             S3 =(SP(  M, JM)-SR(  M, JM))
             SGT = SX*(SIN(AN)*SIN(AN)) +SY*(COS(AN)*COS(AN))-
           &  2*SXY*SIN(AN)*COS(AN)
             SGR = SX*(COS(AN)*COS(AN)) +SY*(SIN(AN)*SIN(AN))+
           &  2*SXY*SIN(AN)*COS(AN)
             SGSH = 0.5*(SGT-SGR)*SIN(2*AN)+SXY*(COS(2*AN))
      C
          WRITE(6,603)   M, JM ,X(  M, JM),Y(  M,  JM ),R,DAN,
         &  SX,SY,SXY, ,S1, S3,SGR, SGT,SGSH
      603  FORMAT( ' P(',I2,',',I2,') =',3F6.2, F6.1,8F7.2)
      C
      C   INTERCHANGE IMAGES IF II=1 OR NBC-1
      C
            IF (II.EQ.1) GO TO 93
            GO TO 94
      93    X(  IM, JM-1) = X(IM+1, JM )
            Y(  IM, JM-1) =-Y(IM+1, JM )
            TH( IM, JM-1) =TH(IM+1, JM )- DIVAN
            SP( IM, JM-1) =SP(IM+1, JM )
            SR( IM, JM-1) =SR(IM+1, JM )
            MJM=JM-1
            DTH = TH(IM,MJM)*180./3.1416
            R = SQRT(X(IM,MJM)*X(IM,MJM)+Y(IM,MJM)*Y(IM,MJM))
            AN = (ATAN(Y(IM,MJM)/X(IM,MJM)))
            DAN =AN*180./3.1416
            SX = SP(IM,MJM )+SR(IM,MJM  )*COS(2*TH(IM ,MJM ))
            SY = SP(IM,MJM )-SR(IM, MJM )*COS(2*TH(IM,MJM ))
            SXY = SR(IM,MJM)*SIN(2*TH(IM,MJM))
            S1 = (SP(IM,MJM)+SR(IM,MJM))
            S3 = (SP(IM,MJM)-SR(IM,MJM))
            SGT = SX*(SIN(AN)*SIN(AN)) +SY*(COS(AN)*COS(AN))-
          &  2*SXY*SIN(AN)*COS(AN)
            SGR = SX*(COS(AN)*COS(AN)) +SY*(SIN(AN)*SIN(AN))+
          &  2*SXY*SIN(AN)*COS(AN)
            SGSH = 0.5*(SGT-SGR)*SIN(2*AN)+SXY*(COS(2*AN))
      C
          WRITE(6,604) IM,MJM ,X(IM,MJM),Y(IM, MJM ),R,DAN,
         &  SX,SY,SXY,S1,S3,SGR,SGT,SGSH
      604  FORMAT( ' P(',I2,',',I2,') =',3F6.2, F6.1,8F7.2)
      C
```

```
 94       IF (II.EQ.(NBC-1)) GO TO 95
          GO TO 20
 95       X(  IM+2, JM+1) = X(IM+1, JM )
          Y(  IM+2, JM+1) =-Y(IM+1, JM )
          TH( IM+2, JM+1) =TH(IM+1, JM )+ DIVAN
          SP( IM+2, JM+1) =SP(IM+1, JM )
          SR( IM+2, JM+1) =SR(IM+1, JM )
          NIM=IM+2
          NJM=JM+1
          DTH = TH(NIM,NJM)*180./3.1416
          R = SQRT(X(NIM,NJM)*X(NIM,NJM)+Y(NIM,NJM)*Y(NIM,NJM))
          AN = (ATAN(Y(NIM,NJM)/X(NIM,NJM)))
          DAN = AN*180./3.1416
          SX = SP(NIM,NJM )+SR(NIM,NJM  )*COS(2*TH(NIM ,NJM ))
          SY = SP(NIM,NJM )-SR(NIM, NJM )*COS(2*TH(NIM,NJM ))
          SXY = SR(NIM,NJM)*SIN(2*TH(NIM,NJM))
          SPP1 = SPP2
          S1 =(SP(NIM,NJM)+SR(NIM,NJM))
          S3 =(SP(NIM,NJM)-SR(NIM,NJM))
          SGT = SX*(SIN(AN)*SIN(AN)) +SY*(COS(AN)*COS(AN))-
     &     2*SXY*SIN(AN)*COS(AN)
          SGR = SX*(COS(AN)*COS(AN)) +SY*(SIN(AN)*SIN(AN))+
     &     2*SXY*SIN(AN)*COS(AN)
          SGSH = 0.5*(SGT-SGR)*SIN(2*AN)+SXY*(COS(2*AN))
C
        WRITE(6,605) NIM,NJM ,X(NIM,NJM),Y(NIM, NJM ),R,DAN,
     &  SX,SY,SXY,S1,S3,SGR,SGT,SGSH
 605  FORMAT( ' P(',I2,',',I2,') =',3F6.2, F6.1,8F7.2)
 20     CONTINUE
C
C COUNTER ( MOVING CENTRIOD IXO, IYO SIDEWAY RIGHT BY 1)
C
         IYO=IYO-1
C
        DO 30 LL=1, NBC
          ICONT2=0
          NC2=LL-1
C      NC2 - COUNTER MOVING DIAGONAL DOWNARD
           IM=IXO+NC2
           JM=IYO+NC2
           IN=IXO+NC2+1
           JN=IYO+NC2+1
           XA = X(IM,JM)
           XB = X(IN,JN)
           YA = Y(IM,JM)
           YB = Y(IN,JN)
           THA=TH(IM,JM)
           THB=TH(IN,JN)
           SPA=SP(IM,JM)
           SPB=SP(IN,JN)
           SRA=SR(IM,JM)
           SRB=SR(IN,JN)
C
C FIRST ESTIMATES OF XP, YP, SRP AT POINT P
C
           XP1 = 0.5*(XA+XB)
           YP1 = 0.5*(YA+YB)
           THP1=0.5*(THA+THB)
           SPP1=0.5*(SPA+SPB)
           SRP1=0.5*(SRA+SRB)
```

```
      C
      C   SOLVE FOR SPP AND THP
      3000      ICONT2=ICONT2+1
                IF (ICONT2.GT.20) GO TO 999
                E1=-SIN(2*XAN)
                E2= SIN(2*XAN)
                F1=-W*SIN(2*XAN)*(XP1-XA)
                F2=-W*SIN(-2*XAN)*(XP1-XB)
                G1=SRP1+SRA
                G2=SRP1+SRB
                H1=-W*COS(2*XAN)*(YP1-YA)
                H2=-W*COS(2*XAN)*(YP1-YB)
                SPP2=(G2*(F1+H1)-G1*(F2+H2)+E1*G2*SPA-E2*G1*SPB+
           &     G1*G2*(THA-THB))/(E1*G2-E2*G1)
                THP2=(E2*(F1+H1)-E1*(F2+H2)+E1*E2*(SPA-SPB)+
           &      E2*G1*THA-E1*G2*THB)/(E2*G1-E1*G2)
                SRP2= SPP2*SIN(PHI)+COH*COS(PHI)
      C
      C   SOLVE FOR XP, YP
      C
               A  = (0.5*(THP2+THA)-XAN)
               B  = (0.5*(THP2+THB)+XAN)
               XP2 = (YB-YA+XA*TAN(A)-XB*TAN(B))/(TAN(A)-TAN(B))
               YP2= ((XB-XA)*TAN(A)*TAN(B)+YA*TAN(B)-YB*TAN(A))/
           &    (TAN(B)-TAN(A))
      C
      C  TEST FOR CONVERGENCE
      C
                TEST = ABS(XP2-XP1)+ABS(YP2-YP1)+ABS(SPP2-SPP1)
           &     +ABS(THP2-THP1)
                IF (TEST .LT. TOLEN) GO TO 4000
                XP1 =XP2
                YP1=YP2
                SRP1 =SRP2
                SPP1 =SPP2
               GO TO 3000
      C
       4000     M=IM+1
                X( M, JM ) =XP2
                Y( M, JM ) =YP2
               TH( M, JM ) =THP2
               SP( M, JM ) =SPP2
               SR( M, JM ) =SRP2
               DTH = TH( M, JM)*180./3.1416
               R = SQRT(X( M, JM)*X( M, JM)+Y( M, JM)*Y( M, JM))
               AN = (ATAN(Y( M, JM)/X( M, JM)))
               DAN = AN*180./3.1416
               SX = SP( M, JM )+SR( M, JM )*COS(2*TH( M , JM ))
               SY = SP( M, JM )-SR( M, JM )*COS(2*TH( M, JM ))
               SXY = SR( M, JM)*SIN(2*TH( M, JM))
               S1 =(SP( M, JM)+SR( M, JM))
               S3 =(SP( M, JM)-SR( M, JM))
               SGT = SX*(SIN(AN)*SIN(AN)) +SY*(COS(AN)*COS(AN))-
           &    2*SXY*SIN(AN)*COS(AN)
               SGR = SX*(COS(AN)*COS(AN)) +SY*(SIN(AN)*SIN(AN))+
           &    2*SXY*SIN(AN)*COS(AN)
               SGSH = 0.5*(SGT-SGR)*SIN(2*AN)+SXY*(COS(2*AN))
      C
             WRITE(6,606)  M, JM ,X( M, JM),Y( M, JM ),R,DAN,
           & SX,SY,SXY,S1,S3,SGR, SGT,SGSH
```

```
606   FORMAT( ' P(',I2,',',I2,') =',3F6.2, F6.1,8F7.2)
C
30        CONTINUE
C
C   COUNTER ( MOVING CENTRIOD IXO, IYO UPWARD BY 1)
C
          IXO=IXO+1
10      CONTINUE
        GO TO 888
999     WRITE(6,610)
610     FORMAT(' SOLUTION DIVERGING',/)
888     RETURN
        END
End of file
C
C***************************************************************
C
C*************** TUN4 *********
C
C
C     VERTICAL STRESS DISTRIBUTION ALONG TUNNEL DEPTH
C     (USING BIN ARCHING THEORY,REF: HANDY, ASCE,MAR. 1985,P302)
C
C***************************************************************
C
C     INPUT FILE:
C      1. DEPTH(TUNNEL), RADIUS, INCLINED ANGLE(YIELDING EAR),
C      2. DENSITY,SOIL-SOIL COEFF.,SOIL ANGLE
C      3.  DITTO (REPEAT LINES 1 and 2)
C      4. O.,O.,
C      5  END OF FILE
C
C      OUTPUT FILE INTERPRETATION:
C      1. VERTICAL STRESS IN TERM OF PI/YH
C
C*****************************************
C
11     READ(5,1) H, RAD,ALPHA
       IF(RAD.LE.0.0) GO TO 999
1      FORMAT(3F10.0)
       READ(5,2) DEN,XK,PHI
2      FORMAT(3F10.0)
       WRITE(6,101) H,RAD,ALPHA
101    FORMAT(3X,' HEIGHT= ',F5.1,'  RADIUS=',F7.2,' INCLINED=',F6.1)
       WRITE(6,102) DEN,XK,PHI
102    FORMAT(3X,'DENSITY =',F5.2,'  XK=',F4.2,
     & '  SOIL FRICTION=',F5.1,//)
C
C  XK - COEFF. OF HORIZ. STRESS / VERTICAL STRESS AT FAILURE BOUND
C  ALPHA - INCLINED ANGLE OF THE CONE
C
       PHI=PHI*3.1416/180.
       ALPHA=ALPHA*3.1416/180.
C
       R=H*(1.0/TAN(ALPHA))
       DZ=H/20.
       SIGV=0.0
C
       WRITE(6,601)
601    FORMAT('   DEPTH ',40X,' P/DEN(Z) ',/)
```

```
      C
            DO 22 I=1,20
            Z=DZ*I
            AREA=2.*RAD+2.*(H-Z)/TAN(ALPHA)
            IF (AREA.LE.O.O) GO TO 44
            FSOIL=XK*SIGV*TAN(PHI)*DZ
            DSIGV=(1.0/AREA)*(DEN*DZ*AREA-FSOIL)
            SIGV=SIGV+DSIGV
            PV =SIGV/(DEN*Z)
      C
            WRITE(6,103) Z,AREA,FSOIL, DSIGV,SIGV,PV
      103   FORMAT(6F8.2)
      22    CONTINUE
      44    GO TO 11
      999   STOP
            END
End of file
      C.*************************************************************
      C
      C************ TUN5 ***************
      C
      C  IDENTIFY MODES OF FAILURE                  (AUG. 1985)
      C  CALCULATE FORCES DUE TO GLOBAL GRAVITY EFFECT (YIELDING
      C   ZONES REACHING SURFACE FORMING COLLAPSE MECHANISM)
      C  SPECIFY KO
      C  INCLUDING VARIATION OF STRESS ALONG TUNNEL PERIPHERY
      C  REDUCING SUPPORT PRESSURE BY PROPORTIONS ALONG POSITION
      C **************************************************************
      C INPUT FILE
      C      1. ANGLE OF FRICTION OF SOIL, KO,DEPTHRATIO,
      C          ( ALL ARE INITIAL VALUES)
      C      2. END OF FILE
      C
      C
      C OUTPUT INTERPRETATION
      C      1. GRAVITY EFFECT RESULTS ONLY IF PI/HY LESS THAN
      C         P2(I) (MODE:WEDGE)
      C      2. MAX. P2(I) GIVES THR CRITICAL YIELDING ANGLE
      C
      C
            DIMENSION P2(10),FETA(10),XFETA(10),XT(10)
            READ (5,501)  PHIO, XKOO,DEPO
      501   FORMAT(3F10.0)
      C
      C  DEP -DEPTH/RADIUS RATIO
            DDEP =1.0
            DPHI =10.
            DFETA = 10.
            DXKO=0.1
      C
            DO 11 I1=1,3
            PHI = PHIO+ DPHI*(I1-1)
            XPHI = PHI*3.1416/180.
            WRITE(6,602) PHI
      602   FORMAT(//,' ANGLE PHI =',F5.1)
      C
            DO 22 I2=1,8
            XKO=XKOO+DXKO*(I2-1)
            WRITE(6,666) XKO
      666   FORMAT(' XKO =', F5.2)
```

```
      DO 33 I3=1,9
      DEP=DEPO+DDEP*(I3-1)
      WRITE(6,601) DEP
601   FORMAT(' DEPTH RATIO = ',F5.1)
C
C
      GF = 0.5*(DEP-1.0)*(DEP-1.0)
C
      DO 55 L=1,10
      FETAO = 45.+0.5*PHI - 5.0
      FETA(L) =FETAO +(L-3)*DFETA
      XFETA(L) = FETA(L)*3.1416/180.
      XT(L) = TAN(XFETA(L)-XPHI)
55    CONTINUE
      WRITE(6,612) FETA(1),FETA(2),FETA(3),FETA(4),FETA(5),
     & FETA(6),FETA(7),FETA(8),FETA(9),FETA(10)
612   FORMAT('ANGLE',10F8.1,/)
C
C
C  CH - RATIO OF LATERAL SUPPORT STRESS TO PO
C  CV - RATIO OF VERTICAL SUPPORT STRESS TO PO
C
      CH= (1.0-0.5/DEP)*XKO
      CV= (1.0-0.5/DEP)
C
C
C   MODE 1- SLIDING WEDGES ON SIDE
C
      DO 66 M=1,10
      PART1 = 0.5*DEP*DEP*(1./TAN(XFETA(M)))+ (DEP -3.1416/4.)
      PART2 = (XKO*GF+XKO*DEP)
      P2(M) =((PART1*XT(M) - PART2)/(CH+CV*XT(M)-XKO))/DEP
66    CONTINUE
C
C
      WRITE(6,611) P2(1),P2(2),P2(3),P2(4),P2(5),
     & P2(6),P2(7),P2(8),P2(9),P2(10)
611   FORMAT('PI/YH',10F8.3)
44    CONTINUE
33    CONTINUE
      DEP =DEPO
22    CONTINUE
      XKO=XKOO
11    CONTINUE
      STOP
      END
End of file
C****************************************
C
C*********** SFT1 ***********
C
C SHAFT - GROUND REACTION CURVE FORMULATION*
C****************************************
C  SOIL MODEL - LADANYI(1974)
C           (MAY,1985)
C****************************************
C ASUMMING:
C  HOLE  IN PLATE 2-D PLANE STRAIN
C  CONSTANT VOLUME CHANGE
C  ASSOCIATED FLOW RULE
```

```
C
C  INPUT FILE:
C    1. KO, MODULUS, DENSITY, RADIUS(=1.O, NORMALISED)
C    2. PEAK ANGLE(SOIL), RESIDUAL ANGLE, PEAK COHESION,RESI. COH
C          , POISSON RATIO
C    3. DITTO
C    4. O..
C    5. END OF FILE
C
C
C APH1= SUPPORT PRESS(PI)/INT. STRESS(PO)
C APH2= COHESION(CE)/INT. STRESS(PO) ELAST
C APH3= COHESION(CP)/INT. STRESS(PO) PLAST
C CE/PO =KA**.5/2*KO
C APH4=PO/E
C FANGLE=FRICTION ANGLE ELASTIC
C PANGLE=FRICTION ANGLE PLASTIC
C XMIL=POISSON RATIO
C XKO=COEFF. EARTH PRESSURE AT REST
C E= MODULUS
C YDEN=DENSITY
C DEP=DEPTH/RADIUS OPENING
C
      DIMENSION APH(50),PSIGR(10),PSIGT(10),ESIGR(10)
      DIMENSION ESIGT(10),PXR(10),EXR(10)
      REAL NOE,NOP,NUM
      WRITE(6,7)
7     FORMAT( 'GROUND CONVERGENCE CURVE CALCULATION',/)
      READ(5,77) XKO,E,YDEN,RD
77    FORMAT(4F10.0)
      WRITE(6,777) XKO,E,YDEN,RD
777   FORMAT(3X,' KO = ',F6.2,' E = ',F8.1,' DENSITY = ',F6.2,
     & ' RADIUS = ',F6.2)
      IF(XKO.LE.0.0) GO TO 1000
C
333   READ(5,1) EANGLE,PANGLE,CE,CP,XMIL
1     FORMAT(5F10.0)
      IF (EANGLE.LE.0.0) GO TO 1000
      WRITE(6,101) EANGLE,PANGLE,CE,CP,XMIL
101   FORMAT(4X,
     &' PEAK ANGLE =',F5.2,' RESID. ANGLE =',F5.2,
     &'  CE =',F6.2,'  CP =',F6.2,
     &' POISSON RATIO =',F4.2,/)
C
      EANGLE=EANGLE*3.1416/180.
      PANGLE=PANGLE*3.1416/180.
      NOE=(1.0+SIN(EANGLE))/(1.-SIN(EANGLE))
      NOP=(1.0+SIN(PANGLE))/(1.-SIN(PANGLE))
      DEP=0.00
C    APH1 INPUT DATA
C    NAPH1 = NUMBER OF APH(I) ENTRY
      NAPH1 = 27
      APH(1)=0.0002
      APH(2)=0.0004
      APH(3)=0.0006
      APH(4)=0.0008
      APH(5)=0.0010
      APH(6)=0.0015
      APH(7)=0.002
      APH(8)=0.0025
```

```
          APH(9)=0.003
          APH(10)=0.0035
          APH(11)=0.004
          APH(12)=0.005
          APH(13)=0.006
          APH(14)=0.007
          APH(15)=0.008
          APH(16)=0.009
          APH(17)=0.01
          APH(18)=0.02
          APH(19)=0.03
          APH(20)=0.04
          APH(21)=0.05
          APH(22)=0.06
          APH(23)=0.07
          APH(24)=0.08
          APH(25)=0.09
          APH(26)=0.10
          APH(27)=0.15
C  PRINT TITLE COLUMN
          WRITE(6,601)
601       FORMAT(' ,PI/PO ',3X,' HT/RADIUS ',4X,'RP',8X,'UI',4X,
        & 'LAT PRESS',/)
C
C  DEPTH(SHAFT)/RADIUS = 15
C
          DO 44 JJ=1,15
          DEP=DEP+1.
          PO=YDEN*DEP*RD
          APH2=CE/PO
          APH3=CP/PO
          APH4=PO/E
C SCP=A (PO)
          A=APH3/TAN(PANGLE)
C SIGMAC=B (PO)
          B=APH2*2*COS(EANGLE)/(1.0-SIN(EANGLE))
C MC*SIGMAC=C (PO)
          C=(B+(NOE-1.0)*XKO)/(NOE+1.0)
C UENOS= ELASTIC DISPLACEMENT AT WALL OF NO SUPPORT
          UENOS=2.0*APH4*(1.0+XMIL)*XKO
C PLIM= PI/PO  AT PLASTIC YIELD INITIATION (=APH1)
          PLIM=XKO-C
C
          DO 999 I=1,NAPH1
          APH1=APH(I)
          IF(APH1.GE.PLIM) GO TO 44
C RP(EXTENT OF PLASTIC ZONE)=RAD(PLAST)/RAD(OPENING) (RE/RI)
          EX=1.0/(NOP-1.0)
          RP=((XKO+A-C)/(APH1+A))**EX
          IF(RP.LE.1.0) GO TO 44
C RSTS(RAD. STRESS AT ELAST/PLAST INT)=D (PO)
          RSTS=(XKO-C)
C
C  CALCULATE WALL DISPLACEMENT  UI
C
C APH4= PO/E
C
C UE=RAD. DISPLACEMENT AT ELAST/PLAST INT.
          UE=(1.0+XMIL)*C*APH4*RP
          DC= -SIN(EANGLE)
```

```
            IF(RP.GE. 1.7321) GO TO 99
            XR=2.0*DC*ALOG(RP)
            GO TO 33
      99    XR=1.1*DC
      33    DEN=2.0*((1.+XMIL)*C*APH4)*RP*RP
            NUM=((RP*RP)-1.0)*(1.0+1.0/XR)
            EAV=DEN/NUM
      C
      C UI=RAD. DISPLACEMENT AT WALL/RAD.OPENING
            AA=(2.0*UE/RP-EAV)*RP*RP
            UI=(1.0-SQRT(ABS((1.0-EAV)/(1.0+AA))))
      C
            HORP = APH1*PO
      C
            WRITE(6,602) APH1, DEP, RP, UI, HORP
      602   FORMAT(F10.6,F10.1,F10.2,F10.5,F10.3)
      C     WRITE(6,102) APH1,APH2,APH3,APH4,DEP,RP,UENOS,UI,PLIM
      C    & DEN,NUM,AA,RSTS,PLIM
      C102    FORMAT(9F8.5)
      C CALCULATE STRESS DISTRIBUTION
      C XR-WITHIN PLASTIC ZONE  XRR-WITHIN ELASTIC ZONE
      C PSIGMAR-PLASTIC STRESS RADIAL
      C     XINR=(RP-1.0)/4
      C     DO 55 IJ=1,5
      C     PXR(IJ)=1.0+XINR*(IJ-1)
      C     EXR(IJ)=(RP+IJ)
      C     PSIGR(IJ)=(APH1+A)*((PXR(IJ)**(NOP-1.0)))-A
      C     ESIGR(IJ)=XKO-C/((EXR(IJ)/RP)*(EXR(IJ)/RP))
      C     PSIGT(IJ)=NOP*(APH1+A)*((PXR(IJ))**(NOP-1.0))-A
      C     ESIGT(IJ)=XKO+C/((EXR(IJ)/RP)*(EXR(IJ)/RP))
      C 55    CONTINUE
      C      WRITE(6,104) PXR(1),PXR(2),PXR(3),PXR(4),PXR(5),EXR(1),
      C     &EXR(2),EXR(3),EXR(4),EXR(5)
      C 104   FORMAT(10F8.2)
      C      WRITE(6,105) PSIGR(1),PSIGR(2),PSIGR(3),PSIGR(4),PSIGR(5),
      C     &ESIGR(1),ESIGR(2),ESIGR(3),ESIGR(4),ESIGR(5)
      C 105   FORMAT(10F8.4)
      C      WRITE(6,106) PSIGT(1),PSIGT(2),PSIGT(3),PSIGT(4),PSIGT(5),
      C     &ESIGT(1),ESIGT(2),ESIGT(3),ESIGT(4),ESIGT(5)
      C 106   FORMAT(10F8.4)
      999   CONTINUE
      44    CONTINUE
            GO TO 333
      1000  STOP
            END
End of file
      C
      C**************************************************************
      C
      C********** SFT1***************
      C
      C     VERTICAL AND HORIZONTAL STRESS DISTRIBUTION ALONG CONE DEPTH
      C     (USING BIN ARCHING THEORY,REF: HANDY,'ASCE,MAR. 1985,P302)
      C     (PLASTIC RADIUS CAN BE VARIED IN SHAPE)
      C
      C**************************************************************
      C
      C     INPUT FILE:
      C      1. DENSITY(SOIL), SOIL-SOIL COEFF.,SOIL-WALL COEFF.,SOIL ANGLE
      C         WALL FRICTION ANGLE,
```

```
C       2. DEPTH(SHAFT), RADIUS.
C       3. NO. OF ENTRY FOR PLASTIC RADIUS(RP)
C       4. RP.
C       5. RP.
C       6. DITTO.
C       7. O.,O.,
C       8  END OF FILE
C
C
        DIMENSION RP(50)
        READ(5,1)DEN,XK,XKW,PHI,DELTA
1       FORMAT(5F10.0)
        READ(5,2) H, RAD
2       FORMAT(2F10.0)
        WRITE(6,101) H,RAD
101     FORMAT(3X,' HEIGHT= ',F5.2,'  RADIUS=',F7.3,/)
        WRITE(6,102) DEN,XK,XKW,PHI,DELTA
102     FORMAT(3X,' DENSITY=',F5.1,'  XK=',F4.2,'  XKW=',F4.2,
     & '   SOIL FRICTION=',F5.1,'  WALL FRICTION=',F5.1,//)
C
C  XK - COEFF. OF HORIZ. STRESS / VERTICAL STRESS AT FAILURE BOUND
C  XKW -                                              AT WALL
C
C
C    READ PLASTIC RADIUS (RP)
        READ(5,3) NRP
3       FORMAT(I3)
        DO 55 I=1,NRP
        READ(5,4) RP(I)
4       FORMAT(F10.0)
55      CONTINUE
C
C
        DZ=H/(NRP+1)
C
        PHI=PHI*3.1416/180.
        DELTA=DELTA*3.1416/180.
C
        SIGV=0.0
C
        WRITE(6,601)
601     FORMAT('    DEPTH ',40X,'VSTRESS',' P/DEN(Z) ',/)
C
        DO 22 I=1,NRP
        Z=DZ*I
        EXR=RP(I)
        AREA=3.1416*(EXR*EXR-RAD*RAD)
        IF (AREA.LE.0.0) GO TO 999
        FSOIL=2.0*3.1416*EXR*XK*SIGV*TAN(PHI)*DZ
        FWALL=2.0*3.1416*RAD*XKW*SIGV*TAN(DELTA)*DZ
        DSIGV=(1.0/AREA)*(DEN*DZ*AREA-FWALL-FSOIL)
        SIGV=SIGV+DSIGV
        PD=SIGV/(DEN*Z)
        HORP=XKW*SIGV
C
        WRITE(6,103) Z,RP(I),EXR,AREA,FWALL,FSOIL, DSIGV,SIGV,PD,HORP
103     FORMAT(11F8.2)
22      CONTINUE
999     STOP
        END
End of file
```